DEVELOPMENT OF IRIDIUM OXIDE CATALYSTS FOR ACIDIC WATER ELECTROLYSIS

by

Himanshi Dhawan

A thesis submitted in partial fulfillment of the requirements for the degree of

Doctor of Philosophy

in

Chemical Engineering

Department of Chemical and Materials Engineering
University of Alberta

Abstract

Scarce and expensive iridium, known for its high activity and corrosion resistance, is the most used catalyst for acidic oxygen evolution reaction (OER); however, reducing its use by enhancing catalyst performance and utilization is vital for advancing proton exchange membrane water electrolysis (PEM-WE) technology. This thesis aims to synthesize active and stable Ir-based catalysts using facile thermal decomposition methods. Rigorous physicochemical and electrochemical characterization is conducted, alongside testing in a three-electrode rotating disk electrode set-up.

The use of supports is a traditional approach in heterogeneous catalysis to increase the atom efficiency of supported metal, through increased active metal dispersion. This study proposes that active-supported Ir oxide catalysts could be synthesized without the use of conductive support and in instances where a well-connected Ir oxide network in the supported catalyst can potentially assume the role of an electron conductor. Monoclinic ZrO_2 is presented as a support for acidic OER, capable of withstanding the corrosive conditions and influencing the intrinsic catalyst activity.

Supported Ir oxide catalysts were synthesized using the incipient wetness impregnation method (IWI) using hydrogen hexachloroiridate(IV) precursor. Two different particle sizes of ZrO_2, small (S) and large (L) were used to study the effect of surface coverage on the catalyst properties and performance. Transmission electron microscopy (TEM) results showed multiple layers of Ir oxide nanoparticles forming well-connected networks in $Ir_xZr_{(1-x)}O_2/ZrO_{2(L)}$, while partial coverage with short-

range networks was observed in $Ir_xZr_{(1-x)}O_y/ZrO_{2(S)}$. X-ray diffraction (XRD) results and X-ray photoelectron spectroscopy results (XPS) suggest metal-support interactions between Zr and Ir, and the formation of $Ir_xZr_{(1-x)}O_2$ alloy, that lead to a lowered Ir oxidation state and an abundance of active Ir(III)/Ir(IV) species, which are known to be highly active for OER. $Ir_xZr_{(1-x)}O_2/ZrO_{2(L)}$ showcased remarkable specific activity, comparable to the state-of-the-art commercial IrO_x supplied by Tanaka (IrO_x TKK), and displayed a four-fold increase in intrinsic activity. On the other hand, $Ir_xZr_{(1-x)}O_y/ZrO_{2(S)}$ displayed lower activity due to a less developed Ir oxide network, underscoring the importance of a conductive network for non-conductive supports. Despite possessing high resistance to Ir dissolution compared to IrO_x TKK, ZrO_2-supported catalysts experience deactivation due to O_2 bubble accumulation and Ir(III)/Ir(IV) species transformation to anhydrous IrO_2 or higher Ir oxidation state.

During the synthesis of the aforementioned catalysts, scanning electron microscopy - energy dispersive X-ray (SEM-EDX) analysis consistently revealed the presence of chlorine in both supported and unsupported catalysts. The subsequent part of this thesis is dedicated to exploring the influence of residual Cl^- from precursors on the electrochemical and physicochemical properties of Ir oxide catalysts prepared by the thermal decomposition of H_2IrCl_6. To test this, we produced a baseline catalyst IrO_2 through the calcination of H_2IrCl_6, introduced HCl into the H_2IrCl_6 precursor followed by calcination to a chloride-rich catalyst, and incorporated NH_4OH into the precursor prior to calcination to reduce the amount of chloride.

TEM imaging of the catalysts showed that IrO_2 existed as agglomerated nanoneedles and agglomerates; the chloride-rich catalyst, IrO_2-HCl predominantly appeared as large agglomerates with minor IrO_2 needles, while the catalyst with less chloride, IrO_x-NH_4OH primarily manifested as Ir oxide nanoparticles with IrO_2 agglomerates in the minority. Selected area electron diffraction (SAED) results revealed the presence

of rutile IrO_2 across all samples, yet $IrCl_3$ phase prevailed in IrO_2-HCl, while amorphous IrO_x was evident in IrO_x-NH_4OH. These findings were also corroborated by XRD and XPS analyses. Electrochemical testing demonstrated a substantial increase in ECSA and specific activity for IrO_x-NH_4OH, exceeding that of IrO_2 by an order of magnitude. Conversely, IrO_2-HCl displayed a three-fold decline in specific and intrinsic activity in comparison to IrO_2. The stability outcomes for IrO_2-HCl also fell considerably short of those for IrO_2 and IrO_x-NH_4OH. Overall, our results underscore that residual chloride from the precursor exerts a detrimental effect on the catalyst. This study represents the first investigation into the impact of precursor-derived chloride on the OER catalysts, shedding light on how synthesis methods lacking chloride removal can inherently impede catalyst activity. This further extends to the incipient wetness impregnation method, where catalyst synthesis relies solely on calcination to eliminate of the chloride in the catalyst.

Keywords: chloride poisoning; incipient wetness impregnation; iridium oxide; oxygen evolution reaction; supported catalysts.

Preface

The introduction in Chapter 1 contains a literature review related to the presented research works. Part of Chapter 1 of this thesis has been published as H. Dhawan, M. Secanell, and N. Semagina, "State-of-the-Art Iridium-Based Catalysts for Acidic Water Electrolysis: A Minireview of Wet-Chemistry Synthesis Methods: Preparation routes for active and durable iridium catalysts", Johnson Matthey Technology Review 65 (2), 247-262. H. Dhawan was responsible for writing the original draft, editing, and review. Prof. Dr. N. Semagina and Prof. Dr. M. Secanell were the supervisory authors and helped with the manuscript concept, writing, editing, and revisions.

Chapter 2 of this thesis was submitted for publication as H. Dhawan, X. Tan, J. Shen, J. Woodford, M. Secanell, and N. Semagina, "Strong Metal - Support Interactions in ZrO_2-Supported IrO_x Catalyst for Efficient Oxygen Evolution Reaction", ChemCatChem. TEM was performed by Dr. Xuehai Tan at the nanoFAB facility at the University of Alberta. He was also involved in the concept formation and provided pivotal intellectual guidance. XRD was performed by Ms. Rebecca Funk at the Department of Earth Sciences, University of Alberta. XPS was performed by Dr. Shihong Xu at the nanoFAB facility at the University of Alberta. ICP-MS analysis was performed by Dr. Nimal De Silva at the Advanced Research Complex (ARC) in the Department of Earth Sciences, University of Ottawa. SEM-EDX was performed by Ms. Ni Yang at the Institute for Oil Sands Innovation, University of Alberta. TPD and TPR were performed and analyzed by Dr. Jing Shen. James Woodford assisted with performing experiments and analysis. Roshni Sajiv Kumar performed the BET

analysis. I was responsible for the literature review, catalyst synthesis, testing, data analysis, and manuscript writing and revision. Prof. Dr. M. Secanell and Prof. Dr. Natalia Semagina were the supervisory authors and contributed to the concept formation, provided intellectual guidance, and helped shape the manuscript objective, manuscript composition, and revisions.

Chapter 3 of this thesis is intended for submission for publication. TEM was performed by Dr. Xuehai Tan at the nanoFAB facility at the University of Alberta. XRD was performed by Ms. Rebecca Funk, XRD Technician at the Department of Earth Sciences, University of Alberta. XPS was performed by Dr. Shihong Xu at the nanoFAB facility at the University of Alberta. ICP-MS analysis was performed by Dr. Nimal De Silva at the Advanced Research Complex (ARC) in the Department of Earth Sciences, University of Ottawa. SEM-EDX was performed by Ms. Ni Yang at the Institute for Oil Sands Innovation, University of Alberta. TGA was performed and analyzed by Dr. Jing Shen. James Woodford assisted with performing experiments and analysis. I was responsible for performing a literature review, synthesizing the catalyst, testing, data interpretation, and analysis, and drafting and revising the manuscript. Prof. Dr. Natalia Semagina and Prof. Dr. Marc Secanell, my supervisors, provided discussions and feedback on experimental results, comments, and revisions for all writing work including the present thesis. The rest of the research works, such as experiments, data collection, analysis and interpretation of the experimental results, as well as writing the papers or manuscripts are my own work.

To my beloved parents

Acknowledgements

First and foremost, I would like to thank my supervisors. I am honored to have Prof. Natalia Semagina as my supervisor. Throughout the various challenges and successes of my journey through graduate school, her unwavering support and guidance have been a constant presence. Her remarkable kindness both astounds me and serves as a motivating force, urging me to strive for excellence in both my academic pursuits and personal life. She consistently boosted my confidence and ensured that I never felt isolated throughout the slightly terrifying journey that is graduate school, and for that, I am grateful.

Although Prof. Marc Secanell didn't directly choose me to be his student, I'm thankful that he was my co-supervisor. Throughout the past five years, he has invested numerous hours delving into my research, and his remarkable dedication to understanding every intricate aspect of my work has left me awestruck. He never declined to have discussions about results or experiments that were impeding my progress, irrespective of how long the discussion took. I am confident that my writing skills have undergone substantial improvement during my Ph.D., and his feedback on my writing has played a pivotal role in this growth.

I'd also like to express my gratitude to my work mom, Dr. Jing Shen, who has been a consistent source of support throughout the past five years. Sharing morning coffee with her has been a cherished daily ritual for years. She has always been there as a reliable resource to clarify things I didn't understand or found confusing, and she

has conducted numerous experiments on my behalf. I hold her in the highest esteem and admiration.

I would also like to thank Dr. Xuehai Tan, who initially served as my mentor in the research group and imparted a wealth of knowledge about my research. Even when he was no longer a member of the group, any conversation with him regarding my research proved more valuable than hours of reading research journals. He remains an indispensable part of my work. Furthermore, he characterized numerous samples for me, and each time I interacted with him, I gained knowledge that was as worthwhile, if not more so, than the actual results. I aspire to become a researcher of his caliber one day.

There are many other technicians who helped me in some capacity. Ms. Ni Yang assisted me by performing SEM-EDX for dozens of my samples and always took out time of her busy schedule to test my samples. Dr. Shihong Xu performed XPS for numerous of my samples. Ms. Rebecca Funk performed an XRD analysis for me. Dr. Nimal da Silva performed ICP-MS for me. Ms. Brittany Mackinnon helped with shipping my samples.

I would also like to thank my colleagues from both my research groups. Particularly, I would like to thank James Woodford who assisted me in performing my experiments. I would also like to thank Jasper Eitzen who lent me his equipment to perform my experiments during the hardest time of my Ph.D. journey. Luis Padilla's partnership with me, during which he evaluated my catalyst for MEA applications, helped me learn a lot about my catalyst. I would also like to thank Roshni Sajiv Kumar for performing BET for me and for her company during coffee breaks.

I also thank my colleagues in the Energy Systems Design Lab (ESDLab), for their

willingness to share their knowledge and ideas with me, offering suggestions to enhance my work, and engaging in idle chit-chat about life.

My friends have been the pillar of strength that has allowed me to finish my Ph.D. I would like to thank Shammy, Aakanksha, Karthik, Meghna, Mayank, Pallavi, Gustavo, Jose, Saeid, Shruti, Elena, Laura, Manika, Akash, Lina, Desiree, Elena, Viraj and Bishnu.

I want to express my heartfelt gratitude to my parents, Poonam Dhawan and Krishan Kumar Dhawan, for their unwavering love and support during all my years of education and throughout life.

This research was a part of the University of Alberta's Future Energy Systems research initiative and was made achievable through the generous funding provided by the Canada First Research Excellence Fund (https://futureenergysystems.ca; Grant No. T06-P04).

Table of Contents

List of Tables

List of Figures

List of Symbols

C_{dl}	Double layer capacitance, mF/cm^2
C_s	Specific capacitance, mF/cm^2
F	Faraday constant, 96, 485 C/mol
M	Molar mass, g/mol
R_{ct}	Charge transfer resistance, ohm
V	Volume, L
$[Ir]$	Concentration of Ir, g/L
$đ_{vol}$	Mean volume diameter, nm
η	Overpotential, mV
λ	Wavelength, nm
σ	Standard deviation
b	Tafel slope, mV/dec
d_i	Diameter of nanoparticle, nm
i	Current, A
i_o	Exchange current density, A/cm^2
t	Time, s
z	Number of electrons

Abbreviations

AA Alfa Aesar.

AEM-WE Anion exchange membrane water electrolyzer.

AST Accelerated stress test.

ATO Antimony tin oxide.

AWE Alkaline water electrolyzer.

BDD Boron doped diamond.

BE Binding energy.

BET Brunauer–Emmett–Teller.

CA Chronoamperometry.

CCM Catalyst coated membrane.

CER Clorine evolution reaction.

CTAB Cetyltrimethylammonium bromide.

CV Cyclic Voltammetry.

DERA German mineral resource agency.

DFT Density functional theory.

ECSA Electrochemically active surface area.

EDX Energy dispersive X-ray.

EIS Electrochemical impedance spectroscopy.

FTO Fluorine tin oxide.

FWHM Full width at half maximum.

GC Glassy carbon.

GCN Graphitic carbon nitride.

GHG Greenhouse gas.

HER Hydrogen evolution reaction.

ICP-MS Inductively coupled plasma-mass spectrometry.

IEA International Energy Agency.

IPA Isopropanol.

ITO Indium tin oxide.

IWI Incipient wetness impregnation.

JCAP Joint center for artificial photosynthesis.

LSV Linear sweep voltammetry.

MEA Membrane electrode assembly.

MMOSI Metal/metal oxide support interactions.

NP Nanoparticles.

NSTF Nanostructured thin film.

OER Oxygen evolution reaction.

PEM-WE Proton exchange membrane water electrolyzer.

PGM Platinum group metal.

PSA Pressure swing adsorption.

PTL Porous transport layer.

RDE Rotating disk electrode.

S/TEM Scanning transmission electron microscopy.

SAED Selected area electron diffraction.

SEM Scanning electron microscopy.

SMR Steam methane reforming.

SMSI Strong metal-support interactions.

SOEC Solid oxide electrolysis cells.

SSA Specific surface area.

TEM Transmission electron microscopy.

TGA Thermogravimetric analysis.

TKK Tanaka Kikinzoku Kogyo.

TOF Turnover frequency.

TPD Temperature-programmed desorption.

TPR Temperature-programmed reduction.

TTAB Tetradecyltrimethylammonium bromide.

UC Umicore.

WGS Water-gas shift reaction.

XPS X-ray photoelectron spectroscopy.

XRD X-ray diffraction.

Chapter 1

Introduction[1]

1.1 Motivation

Energy is the backbone of today's economy, with society relying on it for its day-to-day activities. The perpetual supply of energy is therefore, not only vital for the economic and social development of the society but is in fact, a necessity for the technological and industrial development of the world.[1] This growing demand has traditionally been met by carbon-based fuels such as coal, natural gas, and petroleum. However, their use is causing not only environmental but also political instability. Today, energy security has become a vexing issue. As fossil-resources are confined to finite regions of the world, their supply is administered by political and economic factors. Additionally, with the increasing focus on sustainability, there is a demand to reduce climate change-causing emissions, e.g., CO_2 and CH_4 emissions, and improve air quality. As a consequence, there is a heightened interest in exploring alternative energy strategies to fossil fuel combustion.[2]

Hydrogen, a chemical fuel, is an alluring alternative to carbon-based fuels.[3] It can be produced from both renewable (solar, wind, hydro) and non-renewable (coal, natural gas, nuclear) resources, and as long as it is produced from renewable resources, it is sustainable and can lead to the development of a de-carbonized society.[4] Hydrogen,

[1]Parts of this chapter have been published in H. Dhawan, M. Secanell, N. Semagina, *Johnson Matthey Technology Review* 2021, 65, 247.[67] Reproduced under Creative Commons Attribution 4.0 International (CC by 4.0) license.

unlike coal and petroleum, is not a primary source of energy but an "energy carrier". This means that it is generated from other sources (solar, wind, hydro, coal) and then stored for future use.[3] It has the potential of converting intermittent renewable sources of energy into storable chemical fuels.[5], [6] Hydrogen is relatively easy to store in large quantities, and although its volumetric energy in gaseous form is low, it can be transported with lower energy losses than electricity. Additionally, it has a variety of advantages over conventional fuels, including high specific energy (mass basis), no toxic and greenhouse gas emissions (no SO_x, NO_x, CO_2), from a variety of sources.[2] All this makes hydrogen a prime candidate for fueling zero-carbon-based automobiles, heavy-duty vehicles, and locomotives.

The widespread use of hydrogen faces significant limitations at present, primarily stemming from the high production costs,[7] insufficient infrastructure,[7] and general concerns about fuel safety.[8] For instance, although H_2 energy storage is technically feasible, the current technology incurs losses ranging from 60%-85% during the conversion and storage processes, affecting the overall efficiency of hydrogen energy storage systems.[9] Moreover, there are additional apprehensions about the integration of hydrogen with existing systems, particularly in the context of "sector coupling," such as the power-to-gas cycle.[10] The energy efficiency of the power-to-gas-to-power process for hydrogen remains relatively low, ranging from 15%-40%.[10]

The two most common methods of producing hydrogen include steam-methane reforming and electrolysis.[11] Other methods include, converting pyrolysis, photolytic processes that use solar energy to split water, and biological processes that use microbes, such as bacteria and microalgae, to produce hydrogen through biological reactions.[12] Steam reforming is the most commercially used process as it is technologically mature and has high energy conversion efficiencies, between 74%–85%.[13] However, in addition to the desired H_2, it also produces carbon-dioxide (CO_2).[14]

Based on the quality of the feed, 1 ton of H_2 can produce 9–12 tons of CO_2,[15] or 0.3-0.4 m^3 CO_2 per m^3 of H_2.[16] In 2020, the total carbon dioxide (CO_2) emissions into the atmosphere resulting from steam methane reforming (SMR) and coal gasification for hydrogen production reached 900 million tonnes.[17] While CO_2 sequestration can reduce emissions, it is an expensive process, and its effectiveness is questionable due to fugitive CH_4 emissions.[3] An additional problem with the hydrogen produced by this process is the presence of impurities that require multiple stages of purification via water-gas shift reaction (WGS) and pressure swing adsorption (PSA).[18], [19] Although H_2 production from fossil fuels, coupled with a carbon sequestration process, may offer a short-term solution for achieving net-zero emissions, it is crucial to prioritize carbon-neutral sources for long-term hydrogen production.[20], [21]

Research is currently focused on building a sustainable energy system for the future. Water electrolysis can play a crucial role in attaining this goal by enabling the efficient conversion of excess electricity produced by windmills, solar panels, and water turbines to storable chemical fuels such as hydrogen.[22] Water electrolyzers are electrochemical devices used to split water molecules into hydrogen and oxygen by passage of an electrical current. The produced hydrogen gas can be stored either in its compressed form or as a liquid. The oxygen is either released into the atmosphere or captured and stored for industrial utilization.[23]

A water electrolysis cell consists of two electrodes, an anode, and a cathode, along with an electrolyte. The electrolyte acts as the conduit for transporting the produced chemical charges (anions or cations) between the two electrodes. The four primary configurations of water electrolyzers include proton exchange membrane electrolyzers (PEM-WE), anion exchange membrane water electrolyzers (AEM-WE), alkaline water electrolyzers (AWE), and high-temperature electrolyzers such as solid oxide electrolysis cells (SOECs) as shown in Figure 1.1. In PEM-WE, AEM-WE, and SOECs,

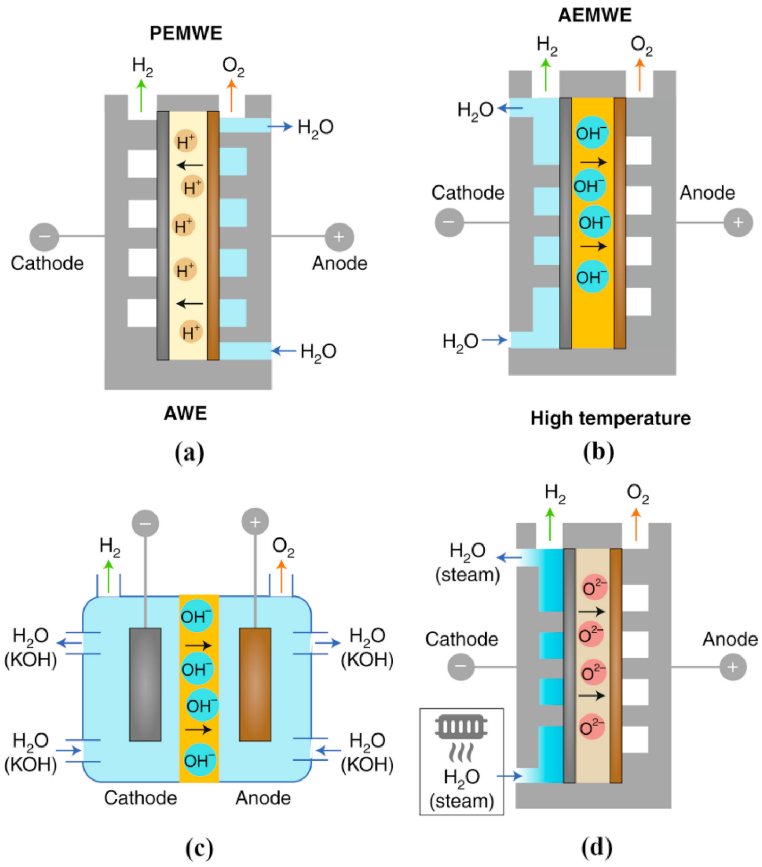

Figure 1.1: Configurations for water electrolysis: (a) proton exchange membrane water electrolyzer (PEM-WE), (b) anion exchange membrane water electrolyzer (AEM-WE), (c) alkaline water electrolyzer (AWE), (d) high-temperature water electrolyzer. Reprinted with permission from Springer Nature,[24] copyright 2020.

the anode and the cathode are separated by a solid electrolyte that does not allow the passage of electrons through it. This solid electrolyte is responsible for ion transport and produced gas separation. These types of electrolyzers eliminate the need for a liquid electrolyte solution, as ion transport takes place directly within the PEM, AEM, or SO itself. In PEM-WE, H^+ is transported, AWE conveys OH^-, and SOEC carries O^{2-}.[25] In AWE, the liquid electrolyte is responsible for transporting OH^- anions between the electrodes.[25] PEM-WE and AWE are the most mature technologies and are commonly used at an industrial scale.[26]–[29] PEM-WE, AEM-WE, and AWEs can be operated at low temperatures, $< 100°C$, while SOECs have operating temperatures in the range of 500°C-850°C.[30] PEM electrolyzers can be operated at

current densities between 2-4 $A \cdot cm^{-2}$,[30] while the AWE are limited to under 0.5 $A \cdot cm^{-2}$.[28], [30] Alkaline electrolytes also suffer from inherent drawbacks such as low ionic conductivity of OH^- ions, and sensitivity toward CO_2 poisoning.[30] Compared to PEM-WE and AWE, AEM-WE and SOECs are relatively newer technologies at a nascent stage of development.[27] SOECs are limited by the high-temperature and high-pressure operation, and AEM-WE suffers from low conductivity and stability of AEM, and poor electrode architecture. Furthermore, the OH^- ions are intrinsically slower than H^+ protons employed within PEM-WE.[25]

PEM-WE are the most actively researched technology.[30]–[33] They offer the advantage of having higher current density, higher efficiency, better gas purity, higher production rates, an acceptable transient response, smaller gas cross-over, and a more compact design when compared to a conventional alkaline electrolyzer with liquid electrolyte.[34] The heart of most PEM electrolyzers is the proton-conducting membrane, Nafion ™, a perfluorosulfonic acid polymer manufactured by DuPont.[35] It is widely used due to its exemplary stability (mechanical and chemical) and high proton conductivity. The PEM-WE operates at high potentials in the anode in an acidic environment, as a result, it is essential to use robust materials capable of withstanding these corrosive conditions, increasing the durability of PEM-WE. For instance, anodic bipolar plates which are responsible for separating single-cell stacks, conducting heat and current, and distributing the reactants within the electrolyzer are made of precious metal coated to avoid corrosion,[27], [36] contributing to the overall high cost of the PEM-WE.[27]

In a PEM-WE, the catalyst-coated membrane (CCM) comprises of the anode, cathode, and PEM. The CCM accounts for approximately 26% to 47% of the stack cost in the case of the 200-kW PEM stack and approximately 36% to 47% for the 1-MW stack.[37] This is because noble metals such as platinum and iridium are required to

form the cathode and the anode of PEM-WE to achieve good performance and durability.[38] In a CCM, iridium accounts for 24% of the total cost, making it a bottleneck to the widespread use of PEM electrolyzers.[25] The rare occurrence of Ir element, with a presence of merely 1 ppb in the Earth's crust, its exorbitant cost of $4600 per ounce, and its high price volatility, which has varied by a factor of 15 over the last 20 years, pose barriers to the future deployment of PEM water electrolyzers.[39] Bernt estimated that, in order to decarbonize the transportation sector by transitioning to fuel cell vehicles fuelled by renewable hydrogen, the metal loading on the anode of polymer electrolyte water electrolyzers should be decreased from 1 $mg_{Ir} \cdot cm^{-2}$ today to 0.05 $mg_{Ir} \cdot cm^{-2}$.[40], [41] This loading can meet the demand for approximately 150 GW/year installed capacity while using 50% of the annual Ir production. In order to meet this requirement and also use electrolysis for other needs, such as energy storage and chemical industry supply, the specific Ir activity must be increased substantially, while simultaneously reducing the catalyst layer degradation.

The primary aim of this thesis is to develop Ir oxide catalysts that exhibit both high activity and stability in acidic OER.

1.2 Literature review

1.2.1 Background

Acidic water electrolysis

Electrolysis splits water into high-purity hydrogen and oxygen. The produced hydrogen can then be stored as fuel and used at a later time. The stored hydrogen can recombine with oxygen which can then be used to generate electricity, water, and heat. Half-cell reactions for acidic water electrolysis in acidic media can be given by the simple equations:

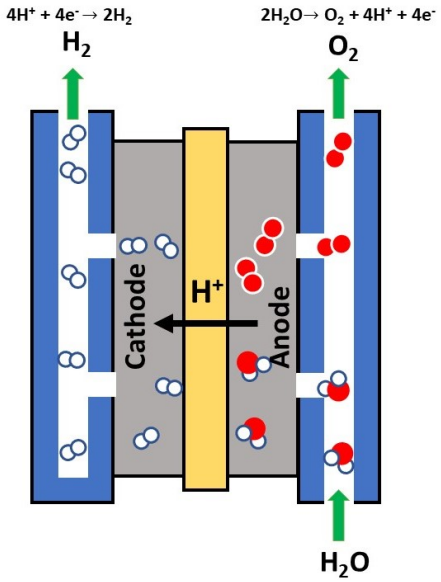

Figure 1.2: Schematic of working of PEM water electrolyzer.

Cathode Reaction:

$$4\ H^+ + 4\ e^- \longrightarrow 2\ H_2(g).....E_c^o = 0\ V \tag{1.1}$$

Anode Reaction:

$$2\ H_2O(l) \longrightarrow O_2(g) + 4\ H^+ + 4\ e^-.....E_a^o = 1.23\ V \tag{1.2}$$

The hydrogen evolution reaction (HER) takes place at the cathode and the oxygen evolution reaction (OER) occurs at the anode of a water electrolyzer. The generation of each molecule of H_2 involves the transfer of 2 electrons and O_2 requires the transfer of 4 electrons, making HER considerably faster than OER. While both HER and OER require the use of catalysts to facilitate the respective kinetics of the reaction, the activation loss of HER on the cathode side is usually ignored due to the fast kinetics on the Pt surface.[42] Since multiple transfers of electrons are not kinetically favorable, OER involves the transfer of one electron per step. This accumulation of energy barriers leads to large overpotentials and results in the sluggish kinetics of the OER.[43]–[45] Thus, the efficiency of PEM-WE is constrained by the OER acting as

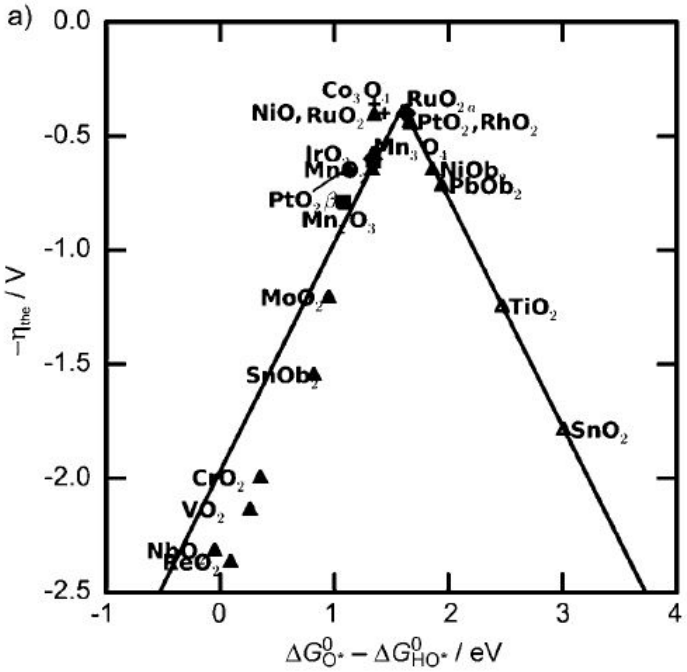

Figure 1.3: Activity trend of metal oxides towards OER. Reprinted with permission from Wiley Online Library,[55] copyright 2011.

the limiting factor. However, this limitation can be minimized by utilizing a suitable catalyst for the OER.[46]–[48]

Electrocatalysts for water splitting in acidic media

The search for an Earth-abundant OER catalyst that could combine high activity and high stability is still ongoing.[49] Non-noble metal-based catalysts cannot survive in acid-aggressive and strongly corrosive conditions present in acidic PEM-WE.[50] The existing PEM-compatible OER catalysts are scarce platinum group metals (PGM).[51]–[54]

Based on the overpotential at a geometric current density of 5 mA·cm$^{-2}_{geo}$, Miles et al. [56] and Cherevko et al. [52] reported the order of activity of noble group metals towards OER as Ru > Ir > Rh > Pt > Au. Cherevko et al. also reported the stability trend as Pt > Rh > Ir > Au ≥ Ru.[52] While they found no converse relationship

between activity and stability, the trend hints that increasing the activity decreases the stability of the catalysts.[52]

Density functional theory studies reported that the weak adsorption of OH_{ads} on the surface of catalysts limited the kinetics of OER.[48] Both ruthenium and iridium possess near optimal binding energy of OH_{ads} or OOH_{ads}, and good metallic conductivities.[57] This quality makes them the catalyst of choice for OER.[58]–[63] Even so, the use of both ruthenium and iridium as OER catalysts is limited by their scarcity and exorbitant cost. Additionally, ruthenium is unstable under acidic conditions and forms soluble RuO_4^- during OER which leads to dissolution.[46], [52], [64]

Iridium is, therefore, one of the very few metals that is both active and resistant to corrosion in highly acidic environments and has become the state-of-the-art catalyst for OER in acidic media,[47], [51], [65]–[67] and hence will be used in this study.

In terms of availability, while the mined supply of Ir is not expected to increase above 7-8 $t \cdot yr^{-1}$, a study conducted by the German Mineral Resource Agency (DERA) found that by 2040, the global annual Ir demand for PEM-WE related applications might reach 34 $t \cdot yr^{-1}$.[68] To meet the future energy demands of PEM water electrolysis without facing Ir shortage, it is imperative to increase the intrinsic activity and specific activity of the Ir based catalysts, while simultaneously reducing the catalyst layer degradation and increasing spent catalyst recycling.[68]

The catalyst-specific activity (specific current for electrocatalysis) is the product of the following catalyst characteristics, assuming ideal kinetics with no transport

limitations:

$$\begin{aligned}\text{Specific activity } [\text{A}\cdot\text{g}_{\text{Ir}}^{-1}] = \text{Intrinsic activity (Turnover frequency) } [\text{A}\cdot\text{mol}_{\text{active sites}}^{-1}]\times \\ \text{Active/surface site stoichiometry } [\text{mol}_{\text{active sites}}\cdot\text{mol}_{\text{surface atoms}}^{-1}]\times \\ \text{Ir dispersion } [\text{mol}_{\text{surface atoms}}\cdot\text{mol}_{\text{Ir total}}^{-1}]/192\ [\text{g}_{\text{Ir}}\cdot\text{mol}_{\text{Ir}}^{-1}] \quad (1.3)\end{aligned}$$

The aforementioned equation clarifies that both intrinsic activity and dispersion can contribute to improving the specific activity of the catalyst.

The activity of the catalyst is usually dependent on the OER and OH adsorption pathway, which has been shown to depend on the treatment of the Ir catalyst. In general, two mechanisms have been proposed, with the main difference being the predominant involvement of electron-deficient electrophilic oxygen (denoted as O^{I-}) and/or activated lattice oxygen in the reaction. The OER on rutile-type IrO_2 proceeds by means of the classical oxide, electrochemical oxide, or electrochemical peroxide pathways involving M-O, M-OH, and M-OOH intermediates [49], [69]:

$$(i) \quad \text{M} + \text{H}_2\text{O} \longrightarrow \text{M} - \text{OH}_{\text{ads}} + \text{H}^+ + \text{e}^- \quad (1.4)$$

$$(ii, \text{oxide}) \quad 2\text{M-OH}_{\text{ads}} \longrightarrow \text{M-O}_{\text{ads}} + \text{M} + \text{H}_2\text{O} \quad (1.5)$$

$$(ii, \text{electrochemical and peroxide}) \quad \text{M} - \text{OH}_{\text{ads}} \longrightarrow \text{M} - \text{O}_{\text{ads}} + \text{H}^+ + \text{e}^- \quad (1.6)$$

$$(iii) \quad 2\text{M} - \text{O}_{\text{ads}} \longrightarrow 2\text{M} + \text{O}_2 \quad (1.7)$$

$$(iii, \text{peroxide}) \quad \text{M} - \text{O}_{\text{ads}} + \text{H}_2\text{O} \longrightarrow \text{M} - \text{OOH}_{\text{ads}} + \text{H}^+ + \text{e}^- \quad (1.8)$$

$$(iv, \text{peroxide}) \quad \text{M} - \text{OOH}_{\text{ads}} \longrightarrow \text{M} + \text{O}_2 + \text{H}^+ + \text{e}^- \quad (1.9)$$

where M represents the metal oxide IrO_2. The peroxide pathway has recently been shown to provide trends that are in agreement with experimental observations by Schuler et al.[69] The electrochemical oxide path is highlighted in red in Figure 1.4.

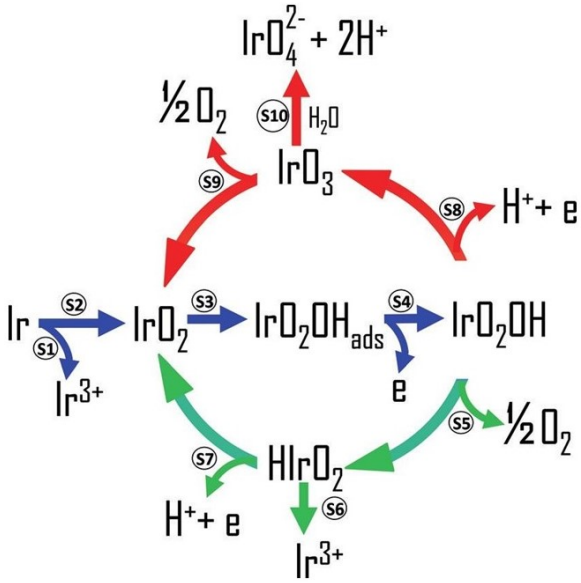

Figure 1.4: OER (green arrows) and deactivation (red arrows) pathways in acidic OER, with the green route being preferable at lower potentials, the red route at higher potentials, while the blue route is potential independent. Reprinted with permission from John Wiley and Sons, [70] copyright 2018.

Catalyst featuring an electrochemically grown porous hydrous oxide layer, also known as oxyhydroxide layer, or amorphous IrO_x catalysts, exhibit an OER mechanism that involves an electrophilic O^{I-} species and/or an activated lattice oxygen pathway.[71]–[73] According to Geiger et al.,[72] a simplified pathway highlighting the need for the outer layer of the catalyst to be involved in the reaction could be :

$$\mathrm{Ir - x - Ir + H_2O \longrightarrow Ir\text{-}O\text{-}Ir + 2H^+ + 2e^-} \tag{1.10}$$

$$\mathrm{Ir\text{-}O\text{-}Ir + H_2O \longrightarrow IrO_2 + 2H^+ + 2e^-} \tag{1.11}$$

$$\mathrm{IrO_2 \longrightarrow Ir - x - Ir + O_2,} \tag{1.12}$$

where "x" is a vacancy in the porous hydrous oxide layer. Ir-O-Ir would play a similar role to the proposed highly reactive, electrophilic oxygen O^{I-} species.[74], [75] The second step would have a similar function to the preliminary reaction proposed by Pfeifer et al., i.e., IrO_x-O + H_2O⟶ IrO_x-O-O-H + H^+ + e^-, where IrO_xO represents the iridium oxide matrix with an adsorbed oxygen.[75] The pathway involving

the electrophilic O^{I-} species is also highlighted in Figure 1.4 in green, where $HIrO_2$ would loosely represent the O^{I-} intermediate.

The OER has been shown to be more active for the pathway involving the electrophilic O^{I-} species and/or activated lattice oxygen. The electrophilic O^{I-} species are adsorbed on the surface and in the subsurface of OER-active hydrated X-ray amorphous Ir(III)/(IV) oxyhydroxides (IrO_x) can be prepared ex-situ.[6], [75], [76] Unfortunately, this pathway tends to be deactivated due to the lattice oxygen evolution leading to iridium dissolution, and the transformation of the oxyhydroxides to less active anhydrous species.[6], [72], [77], [78] Stabilization of the iridium atoms in the pathway involving the electrophilic O^{I-} intermediate via enhanced crystallinity or the use of mixed oxides could minimize stability issues.[6] Crystalline IrO_2 has a lower intrinsic activity but is more stable due to strong Ir-O bonds between IrO_6 clusters, with only the topmost layers of the rutile contributing to both processes.[77] The superior stability of thermal iridium oxide is explained by the slower kinetics of IrO_3 hydrolysis as compared to its decomposition.[70] It has been suggested that both pathways occur during the OER with the activated lattice oxygen pathway being dominant at low potential, due to its high activity, and the classical pathway (S8-S9 in Figure 1.4) being dominant at higher potential.[70] At potentials relevant to the OER, it is possible that the oxyhydroxide layer slowly transforms to anhydrous oxide with a subsequent loss in activity and enhancement in stability as recently shown by atomic probe tomography.[78]

The literature features metallic Ir with a variety of predominant crystallographic orientations, amorphous hydrous iridium oxide, crystalline rutile IrO_2, their mixtures, as well as multimetallic Ir composites. Metallic Ir may be oxidized by calcination in air, [66] or electrochemically in situ.[6], [79] Thermal iridium oxidation to IrO_2 occurs between 200°C and 500°C,[80] the higher the temperature, the higher the crystallinity

and electrochemical stability, but the surface area and the activity decrease.[81] The 400°C- 500°C region was recommended to strike a balance between activity, stability, and conductivity.[66]

Many state-of-the-art catalysts, described in the following sections, use electrochemical in-situ oxidation. The Ir(110) surface evolves into two chemically different Ir species, with an active accessible oxide-metal interface.[82] The densest Ir(111) surface is more resistant to oxidation, and once the oxide is formed, the metallic interface is buried. Although the kinetics of oxide formation and redox properties of the two surfaces are different, their final reached OER activities are rather similar. The same work [82] recommends that for the formation of a porous hydrous IrO_2, the in situ Ir(0) activation should include oxidizing-reducing cycles, instead of conventionally used electrooxidation, although another study argues that the repetitive electrochemical oxidation/reduction unavoidably leads to dissolution.[53] The electrochemical oxidation proceeds via hydroxide to the irreversible Ir(IV) oxide formation in the nanoparticles, while bulk Ir preserves its metallic subsurface with porous Ir(IV) surface layers.[51] Thus, one must be mindful of the iridium dissolution during electrochemical oxidation via hydrous iridium oxide growth.[53] When 20-nm Ir films are used for the acidic OER, their lifetime is similar to the lifetime of the hydrous iridium oxide and is significantly lower than for crystalline IrO_2.[72]

To produce highly crystalline IrO_2, which is more stable but less active than hydrous iridium oxide, preliminary annealing in air may be recommended, whenever possible. The exceptions, of course, include unsupported polymer-stabilized nanoparticles,[6] where annealing would result in particle agglomeration, as well as metal carbides, where it would lead to oxidation and loss of conductivity.[83] In such cases, the electrochemical oxidation procedure must be optimized as it affects the catalyst stability.

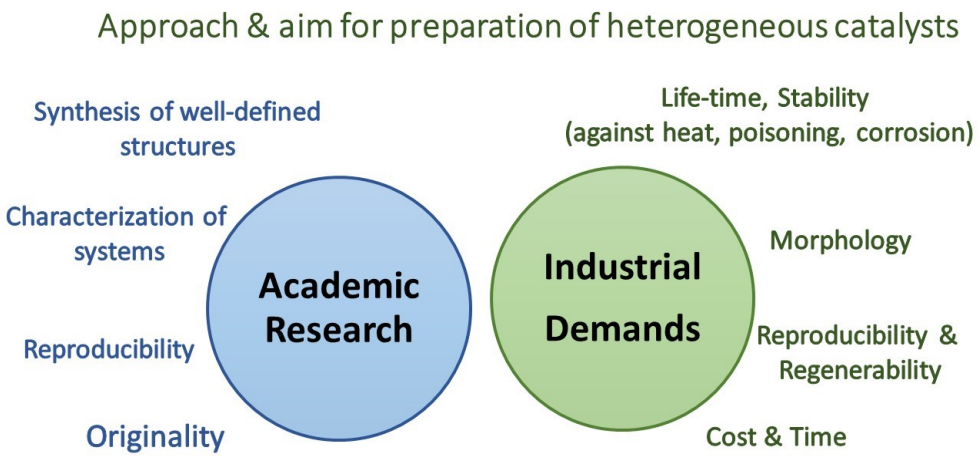

Figure 1.5: Approach & aim for preparation of heterogeneous catalysts in the academia and the industry.

Fine-tuning of the oxide crystallinity, crystallographic orientation, number of oxygen defects, and length and strength of Ir-Ir and Ir-O bonds via thoughtful synthetic approaches may diminish the gap between the active but unstable and stable but less active phases.

Therefore, the pursuit of the most efficient Ir OER catalyst involves the synthesis of catalysts that achieve a simultaneous optimization of activity and stability. Based on the above review, this thesis aims to create catalysts with bulk mixed Ir oxidation states, i.e., Ir(III)/Ir(IV) to produce catalysts with high activity and simultaneously investigate ways to improve the corrosion resistance of the synthesized catalysts.

1.2.2 Catalyst synthesis

Hundreds of research papers have been focused on the development of active and durable Ir catalysts, deposition techniques, and associated catalyst layer components, which may limit the performance of the most active Ir catalyst formulations. Recent

reviews classified Ir- containing catalysts for acidic OER [84] and the variety of methods for the synthesis of iridium oxide.[85] Commercial catalyst production methods must be scalable, preferably not require specialized equipment apart from what is available in the catalyst production industries, not produce significant waste, and lack the need for large amounts of chemicals, especially those that are hazardous to the environment. The difference in approach and aim for catalyst preparation in academia and the industry can be illustrated in Figure 1.5. With this in mind, the objective of this literature review is to select a number of the most efficient state-of-the-art Ir catalysts for acidic OER within reported wet-chemistry synthesis methods, focussing on the practicality and scalability of the techniques.

We address only wet-chemistry routes, as they are most frequently reported, being relatively accessible in a research environment. Figure 1.6 and Table 1.1 summarizes the catalyst synthetic routes and selected catalysts, addressed in this review. This is not a comprehensive summary of all possible routes and catalysts, but rather a careful selection of studies demonstrating a promising combination of activity and stability in acidic OER.

The catalyst layer preparation methods, such as deposition methods, are out of the scope of this work, although they significantly affect the catalyst performance. Gas-phase catalyst (layer) preparation techniques are omitted for the same reason, as they require specialized equipment and feature simultaneous catalyst formation and deposition.[86], [87] Herein, we aim to provide comprehensive insights into selected promising wet-synthesis methods.

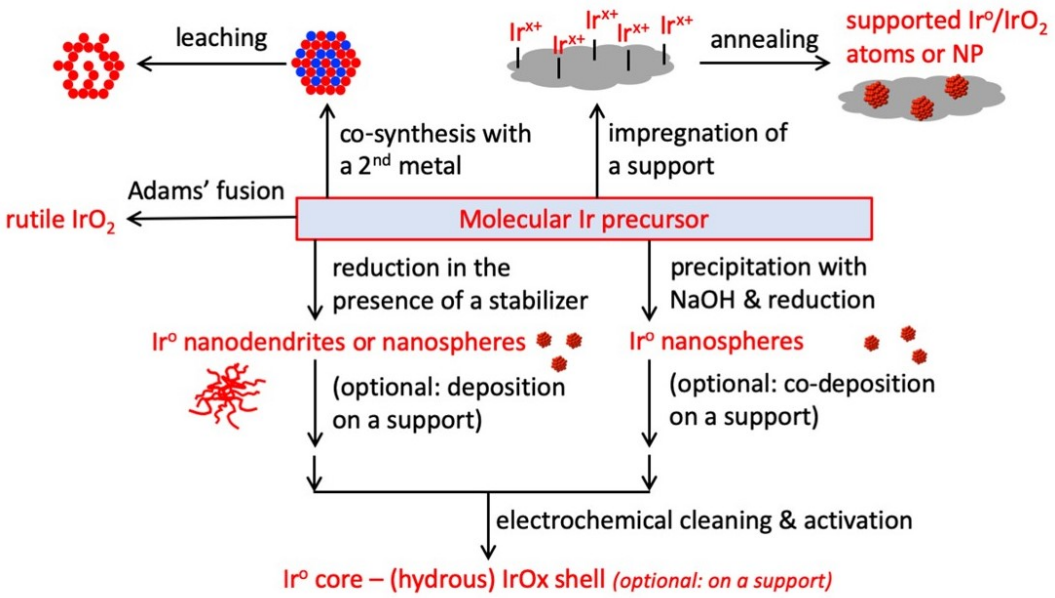

Figure 1.6: Summary of the reviewed wet-chemistry synthetic routes of state-of-the-art Ir catalysts for acidic OER. Reproduced from [67] under Creative Commons Attribution-NonCommercial-NoDerivatives 4.0 International License, published by Johnson Matthey.

Synthesis of unsupported $Ir/IrO_x/Ir$-OOH catalysts

Adams' fusion method Adams' method was originally developed to conquer the issues of irreproducible platinum catalyst synthesis; it was successfully scaled up and is used industrially for Pt (Adams') catalyst production,[93] and thus is well positioned for potential scalability. It also appears to be one of the most used methods reported for the synthesis of IrO_2 for OER, including supported and multimetallic composites. The method is based on the synthesis of iridium nitrate from an iridium molecular precursor heated in a solid mixture with sodium nitrate, followed by the iridium nitrate high-temperature decomposition to IrO_2. The side products include poisonous nitrous oxides, which release must be appropriately managed. Synthesis parameters include the temperature and duration of the calcination, the nature of the iridium precursor, and its fraction in the mixture with $NaNO_3$, all of which affect the crystallinity, oxidation state, and surface area of the produced material and thus,

Table 1.1: Summary of the state-of-the-art activities of selected catalysts prepared by wet-chemistry synthesis and tested in an RDE

Catalyst (method)	Loading on electrode, $mg_{Ir} \cdot cm^{-2}$	η at 10 $mA \cdot cm^{-2}$, mV	Activity, $A.g_{Ir}^{-1}$	Potential, V_{RHE}	Ref.
Surfactant-assisted	0.061	~290	100	1.51	[88]
Surfactant-free colloids	0.0071	345	205	1.5	[89]
Supported on GCN	0.07	278	580	1.55	[90]
Supported on TaTO	0.02	~300	250	1.51	[91]
Selective leaching	0.0277	N/A	810 3353	1.51 1.55	[92]

Note that the data are mostly reported for the fresh catalysts. Stability data, where available, are discussed in the text.

the OER performance. The higher the calcination temperature, the higher is the crystallinity of the produced oxide. However, the amount of active surface hydrous iridium oxide decreases, as well as the catalyst surface area. Although the increase in the calcination temperature leads to lower Ir dispersion (larger particle size) and lower turnover frequency due to the formation of less active crystalline IrO_2, the latter is more stable towards dissolution. This indicates the existence of the optimal calcination temperature to achieve the activity-selectivity balance for the maximized Ir utilization.[81] Electrical conductivity is also improved with increased crystallinity at annealing.[94] The highest reported surface area of an Ir oxide produced by a modified Adams' method is 350 $m^2 \cdot g^{-1}$, which was obtained from iridium acetylacetonate and calcined in air at 350°C for 30 min.[81] The oxide consists of nanodisks with a surface partially covered by active Ir(OOH), which however retained only 55% of its activity after 500 potential cycles due to mass loss and restructuring. When the original sample was further heated at 400°C for 1 h, the catalyst retained 70% of its

activity after 500 potential cycles. Increased calcination temperature, however, led to a decrease in surface area to 250 $m^2 \cdot g^{-1}$. At the catalyst loading of 0.1 $mg_{IrO_x} \cdot cm^{-2}$, the specific current of 26 $A \cdot g^{-1}_{IrO_x}$ could be achieved at 295 mV overpotential before the stability tests (0.1 M $HClO_4$). For both catalysts, the same activity loss (of 30%) occurred due to the partial oxidation of active sites, but due to the decreased leaching from the 400°C-treated sample, the latter strikes the balance between the activity and stability.[81] The increase in calcination temperature leads not only to the surface area decrease but also changes the particle morphology to rods with dominating {110} surface terminations.[95]

Among other promising reported modifications of Adams' method, the addition of cysteamine to the iridium precursor solution resulted in the formation of IrO_2 nanoneedles of 2 nm diameter 6-8 layers of (110) plane, (Figure 1.7) and 30 nm length after 450°C calcination.[96] Although the needles possessed lower BET surface area than the catalyst formed without cysteamine (141 vs. 197 $m^2 \cdot g^{-1}$), their electrical conductivity was 6-fold higher. An overpotential of 313 mV was required to achieve 10 $mA \cdot cm^{-2}$ at the catalyst loading of 0.21 $mg_{Ir} \cdot cm^{-2}$ (1.0 M H_2SO_4, 25°C) before and after a 2-h durability test. The needles were also tested in a PEM electrolyzer and found more active and stable than the spherical IrO_2 synthesized without cysteamine.[96] Most likely, the less dense and well-connected structure of Ir needles contributed to the improved porosity and electrical conductivity. Thin needles with near-zero sphericity form packed beds with the highest near-100% porosity as opposed to 40% for the spherical particles.

Adam's fusion method highlights the advantages of using the thermal decomposition methods for IrO_x/IrO_2 catalyst synthesis, such as the ability to balance activity-stability by optimizing the calcination temperature and duration. In this work, we will focus on catalyst synthesis using thermal

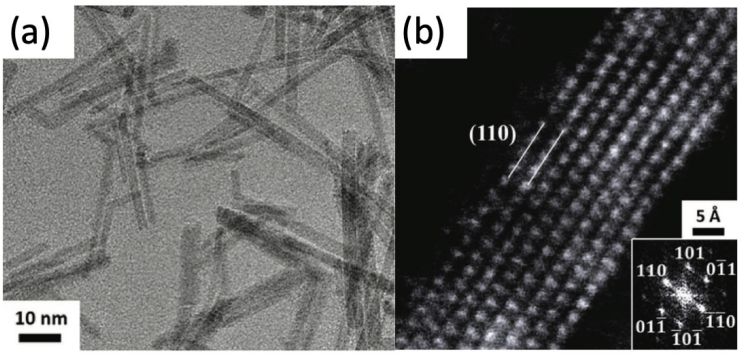

Figure 1.7: Ultrathin IrO_2 nanoneedles (a) consisting of 8 (110) layers (b). Reproduced from [96] with permission from John Wiley and Sons. Copyright 2017.

decomposition techniques, with the aim of producing catalysts that possess both activity and stability. To achieve a balance between catalyst activity and stability, the catalysts will be subjected to a selected calcination temperature of 400°C for a duration of 2 h. Additionally, efforts will be directed toward identifying thermal decomposition methods that are characterized by enhanced safety profiles and reduced resource requirements.

Iridium nanoparticles stabilized by a capping agent If one has to produce monodisperse near-spherical nanoparticles with high dispersion (>50%, i.e., smaller than ca. 2 nm), to increase metal utilization or form anisotropic nanostructures to increase the catalyst layer porosity or promote the formation of certain crystal terminations, colloidal synthesis in the presence of a capping agent is a popular method in academic research.[97] Halogen-containing stabilizers, such as CTAB, are known to act also as a growth-directing agent by the halogen selective adsorption on (100) surfaces resulting in rod-like structures. The produced structures are usually pre-washed from the excess chemicals, while the in-situ electrochemical preconditioning removes the surfactant, for example, by 50 potential sweeps from 0.05 to 1.5 V_{RHE}.[79] Since the metallic Ir is oxidized electrochemically, it is likely to possess a higher proportion of activity-relevant hydrous Ir oxide on the surface, as opposed to calcined rutile IrO_2.

One of the most successful examples in this category is the 2.0±0.4 nm Ir nanoparticles formed by $IrCl_3$ reduction in ethanol with excess $NaBH_4$ in the presence of CTAB.[88] $NaBH_4$ is a strong and fast-reducing agent to produce metallic nanoparticles and is often used in colloidal synthesis. In a protic solvent, borohydride decomposes to gaseous hydrogen, which, depending on the conditions, may proceed in a violent manner. To reach 10 $mA \cdot cm^{-2}$ current, ca. 290 mV overpotential was required at only 0.061 $mg_{Ir} \cdot cm^{-2}$ loading in an RDE (0.5 M H_2SO_4, 25°C). The catalyst demonstrated a similar Tafel slope of ca. 40 mV/dec as the calcined catalyst prepared by the Adams' fusion method.[81] However, the specific current at 1.51 V was an order of magnitude higher (100 $A \cdot g_{Ir}^{-1}$). The nanoparticles formed a nanoporous structure with well-connected particles, which retained their metallic core but featured an active thin surface oxide layer, as shown in Figure 1.8 (a, b). The authors stressed the importance of complete $IrCl_3$ removal by adding an excess reducing agent to prevent inhibition of electron transfer.

The use of TTAB during IrO_2 precipitation from H_2IrCl_6 by NaOH, followed by reduction by $NaBH_4$, resulted in the formation of 1.7 metallic Ir seeds that self-assembled into nanodendrites with 34% porosity at 39 $m^2 \cdot g^{-1}$ BET surface area.[79] The high crystallinity favored stability toward dissolution. The 10 $mA \cdot cm^{-2}$ current was achieved at 410 mV overpotential (RDE, 0.05 M H_2SO_4) but at only 0.0102 $mg_{Ir} \cdot cm^{-2}$ loading. At 1.51 V, the catalyst activity was 70 $A \cdot g_{Ir}^{-1}$.

When a slow-reducing agent is used for synthesis (such as glucose [6]), the CTAB suppressed the grain growth in (100) directions; the nanodendrites self-assembled into nanopompons, as shown in Figure 1.8 (d-f). Those highly crystalline structures with a high proportion of low-index crystal terminations were relatively resistant to dissolution but showed lower activity as compared to the hydrous iridium oxide.[6]

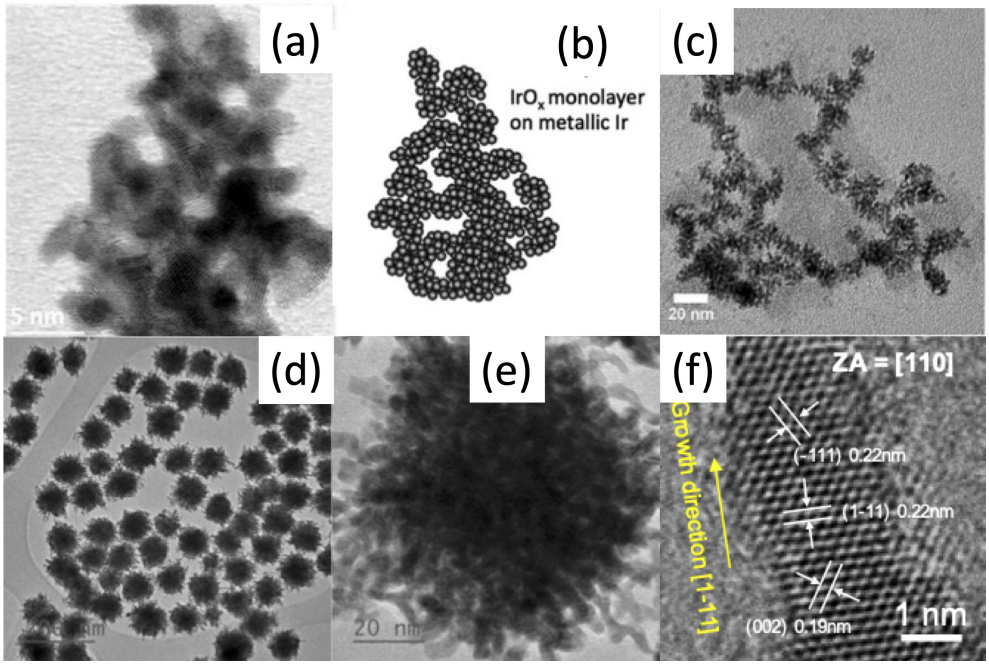

Figure 1.8: (a, b) Stabilized interconnected Ir nanoparticles [88]; (c) Ir nano-dendrites [79] (reproduced from [88] and [79] under a Creative Commons Attribution 3.0 Unported License, published by The Royal Society of Chemistry); and (d-f) highly-crystalline nanopompons [6] (reproduced from [6] under a Creative Commons License, published by Elsevier).

The stabilizer-assisted synthesis techniques are easy to implement in a wet laboratory without specialized equipment for academic research. This method of Ir synthesis is also used to perform Ir nanostructures prior to their deposition on support. However, one must be mindful of a typically low metal concentration in the synthesis solution, and the relatively large use of solvents, reductants, stabilizers, and washing solutions, many of which are manufactured from fossil resources, are expensive and must be removed by multiple washes. Such synthesis methods are usually too cumbersome for industrial production, the improvements being feasible though for certain stabilizers,[98] and hence, will not be pursued in this work. A key objective in the thesis is to identify a catalyst synthesis method that minimizes waste production, utilizes limited resources effectively, and can

be used for catalyst synthesis by the industry.

Stabilizer-free wet chemical synthesis methods This category features one of the most active catalysts reported to date, although the electrodes were fabricated without Nafion. Synthesis of 1.6±0.3 nm Ir particles was performed without a stabilizer by heating a solution of $IrCl_3$ in methanol, which reduces IrO_2 precipitated by the co-added NaOH; the resulting solution was used without purification.[89], [99] At the loading of 0.0071 mg/cm^2 achieved by drop casting of the native solution, the particles formed a uniform layer on a GC disk. In 0.1 M $HClO_4$, in an RDE, the catalyst demonstrated an outstanding 205 A$\cdot g_{Ir}^{-1}$activity at 1.5 V_{RHE} and 1130A$\cdot g_{Ir}^{-1}$at 1.55 V_{RHE}.[99] The ECSA was found to be 140 $m^2 \cdot g^{-1}$ (at the loading of 0.0071 $mg_{Ir} \cdot cm^{-2}$). The overpotential to reach 10 mA$\cdot$cm^{-2} was 345 mV at the 0.0071 $mg_{Ir} \cdot cm^{-2}$ loading, or 325 mV at the 0.0143 $mg_{Ir} \cdot cm^{-2}$ loading.[89] The Ir loading on the electrode was of vital importance: the loading increase above 0.0071 mg/cm^2 resulted in a significant drop of the ECSA and thus specific current.[89] The specific activity at the optimal loading surpasses the activity for the surfactant-mediated catalysts, and features a significantly easier, cheaper, and scalable preparation.[88] In addition to being surfactant-free and using a low-boiling recoverable solvent, the method is scalable to high metal concentrations (5 g$\cdot L^{-1}$). [99] The fate of Na^+ (10:1 Na: Ir) is to be investigated, as well as the catalyst durability and performance in a PEM electrolyzer.

Ruiz Esquius et al. synthesized IrO_x catalysts by hydrothermal method and evaluated the effect of using different alkali metal bases (Li_2CO_3, LiOH, Na_2CO_3, NaOH, K_2CO_3, KOH) on the catalyst surface area, particle morphology, and the concentration of surface hydroxyl groups and the catalyst activity and stability for OER. They observed that while adding a Li-containing base resulted in improved catalytic activity towards OER, the use of Na^+ and K^+-containing bases possibly poisoned the

active sites.[100], [101]

Many studies feature a similar Ir nanoparticle synthesis without a surfactant with the use of a base (NaOH) in other reducing solvents, but typically such particles are deposited on a support and are discussed in Section 1.2.2.

The use of a stabilizer-free wet chemical synthesis method to produce well-dispersed IrO_x/Ir is promising.

Synthesis of mixed metal oxides

The development of multimetallic Ir-containing catalysts has recently attracted considerable attention as a means of enhancing the OER catalyst performance, as it has been proven beneficial for the catalyst development for fuel cells and alkaline water electrolysis. However, with Ir being the most corrosion-resistant metal and still dissolving under acidic OER conditions, any other metal would have an even higher dissolution rate. A rather popular combination of Ir and Ru features high activities due to the higher OER activity of Ru than that of Ir but is not practical because of the low corrosion resistance of Ru, which is also a scarce and expensive metal. The studies of the mixed oxide OER catalysts do typically address (and inevitably show) the dissolution of the catalyst components, but there is a lack of studies on the effect of the leached ions on the PEM system level. It is likely that the non-Ir cations may not only ion-exchange on Nafion changing its properties,[102] but may also travel to the cathode side and poison the Pt cathode as was shown for Ir.[103] Membrane degradation may also occur due to the attack of HO• and other radicals, whose formation is catalyzed by transition metal cations.[104] For example, iron and copper ions were shown to dramatically enhance membrane degradation.[105]

Thus, a practical mixed oxide catalyst for an acidic OER application may be envi-

sioned as one of the following composites, as shown in Figure 1.9: (i) an IrO_x shell fully covering the core with an earth-abundant metal increasing the iridium dispersion; in this case, electrolyte contamination with the second metal may be delayed as compared to the mixed alloys until the iridium shell atoms leach exposing the core atoms; ii) Ir nanostructures produced by the preliminary removal of a sacrificial second component from a bimetallic composite, either by potential cycling or chemically. The selective leaching of the second component leads to surface restructuring,[106] porosity enhancement,[107] formation of lattice vacancies,[108] and ECSA increase.[109] Lattice vacancy formation via secondary metal leaching is a unique opportunity to modify the electrophilicity and Ir-O bond length leading to enhanced OER activity as compared to IrO_x synthesized only from an Ir precursor.[108], [110] Some works report, though, that Ir leaching from the composites may even increase due to the created lattice vacancies, as compared to monometallic Ir catalysts.[107]

Below, we provide some examples for such catalyst synthesis and performance. We note that the direct deposition methods, such as reactive sputtering and physical vapor deposition, are very frequently used for mixed oxide studies,[107], [109]–[113] because they ensure structures with well-controlled composition and stoichiometry, thus, enabling the fundamental understanding of the composite's behavior.

Core-shell bimetallic nanoparticles Multimetallic composites can be synthesized using all the techniques applicable for monometallic catalyst synthesis (see Section 1.2.2) with the addition of the second precursor and by the fine-tuning of the reaction conditions. Very often, both precursors are added together during the synthesis. Simultaneous reduction of different ions with different redox potentials leads to the formation of either mixed alloy particles or core/shell nanoparticles.[114] For the core-shell synthesis, methods like ionic substitution (galvanic replacement) can be used,[115] where a precursor of the second metal is deposited onto the metallic

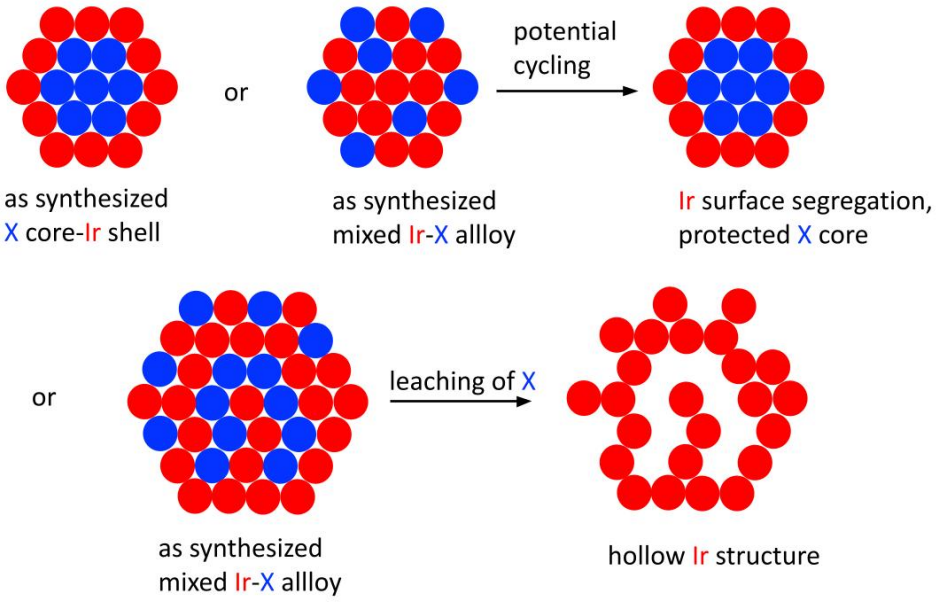

Figure 1.9: Mixed metal oxides for the acidic OER catalyst preparation. Reproduced from [67] under Creative Commons Attribution-NonCommercial-NoDerivatives 4.0 International License, published by Johnson Matthey.

nanoparticles of the other metal based on the standard electrochemical potential,[116] or a hydrogen-sacrificial method,[117] where a core metal is hydrogenated, followed by the second ion reduction by the surface hydrides and shell formation. It is important to understand that thermodynamically unstable bimetallic structures can be synthesized (in terms of metal distribution) but how fast they rearrange into thermodynamically stable composites (for example, where a metal with lower cohesive energy segregates to the surface) depends on temperature, chemical, and electrical environment. Metals can even change their location in situ depending on the catalyzed reaction or treatment conditions via so-called adsorbate-induced segregation.[118]–[120]

According to the Hume-Rothery substitution rule, in order to form a continuous solid solution, it is imperative that the difference between the atomic radii of the solvent and the solute not exceed 15% of each other and they should possess similar crystal structures.[121] One of the most common metals alloyed with Ir is Ru, but

regardless of the efforts being made to inhibit Ru leaching, literature reports continuous Ru dissolution, irrespective of methods of synthesis and structure of the mixed metals oxides. Ruban et al. reported a comprehensive table of surface segregation energies in transition-metal alloys, which can help predict the final dealloyed structure of Ir composites.[122] In bimetallic alloys with Ir, metals such as Cu, Zr, Rh, Pd, Ag, Hf, Pt, and Au would segregate to the surface, while Ir would surface-segregate from alloys with Ti, V, Cr, Mn, Fe, Co, Ni, Nb, Mo, Tc, Ru, Ta, W, Re, and Os.[122] Indeed, for example, in Ru-Ir alloys Ir formed a protective shell, offering extended stability to Ru.[123]

Another example, conforming to the Ir surface segregation prediction, relates to the Ir-Ni composite. Bimetallic 7-nm $IrNi_{3.2}$ alloy nanoparticles were prepared by a simultaneous reduction of Ir and Ni precursors in the presence of a stabilizer.[108] The following potential cycling from 0.05 to 1.5 V_{RHE} for 50 cycles resulted in partial Ni leaching, dealloying, and oxidation with the formation of a metallic IrNi alloy(core)-IrO_x(shell) nanostructure. The IrO_x shells are doped with holes (originated from Ni leaching); they feature shorter Ir-O bonds and are more electrophilic than conventional iridium oxide, which affects the rate of O-O bond formation during OER and enhanced intrinsic activity per Ir site. A specific current of 676 $A \cdot g_{Ir}^{-1}$ was reported at 300 mV overpotential with 0.0102 $mg_{Ir} \cdot cm^{-2}$ loading, which is one of the highest in the above-presented examples.[108] This example shows an extraordinary combination of increased Ir utilization due to its preferential location in the nanoparticle shell, as well as its beneficial electronic and thus catalytic activity modification upon dealloying.

Selective leaching of the sacrificial component (hard templating) When a secondary metal in bimetallic composites with Ir is selectively removed, the process

results in the formation of porous Ir nanostructures with highly accessible active site density and/or modified IrO_x electronic and geometric properties, which cannot be achieved via a monometallic Ir catalyst synthesis. Some examples of sacrificial metal are Ni,[92], [124] Co,[124], and Os.[107] Among different leaching methods, the most common is acid leaching [92] and potential cycling.[107], [109] For example, Ir was deposited on Ni nanowires via galvanic displacement, followed by the nanowires ("hard template") removal by acid leaching.[92] The residual composite with 90.5 wt.% Ir demonstrated a specific current of 1650 $A \cdot g_{Ir}^{-1}$ at 0.0306 $mg \cdot cm^{-2}$ loading at 300 mV overpotential in RDE in 0.1 M $HClO_4$. A parent mixed metal structure can be prepared as stabilized nanoparticles in a colloidal solution, such as an Ir-Os oxide.[107] The potential cycling resulted in dealloying and fast Os dissolution, leaving behind a nanoporous architecture of iridium metal core and IrO_x shell with optimized stability and conductivity.[107] An important observation was that a high amount of Os-Ir bonds in the parent alloy led to the maximum Ir dissolution upon fast Os leaching.

This category features some of the most architecturally sophisticated porous nanostructures, such as hollow nanocrystals synthesized via the formation of a Ir-Co-Ni solid nanoparticles, followed by Co and Ni etching with Fe^{3+},[124] or double-layered nanoframes produced in a solution via reduction of Ni, Cu and two types of Ir precursors with different reduction kinetics followed by acid leaching.[125] Theoretically, this approach may produce highly porous connected Ir-only nanostructures, but its practical implementation is complicated by the nuances in the size and structure control, as well as secondary component complete leaching without the structure collapse.

It appears that the main achievement of the selective etching is not in the improvement of Ir surface area and dispersion, as the thus-synthesized catalysts do not feature areas above 100 $m^2 \cdot g^{-1}$ as compared with monometallic IrO_2 synthesized by Adams' method with 250 $m^2 \cdot g^{-1}$.[81] Instead, the etching allows for modification

of the IrO_x electronic structure and vacancies, affecting its OER activity and stability.

Under OER conditions, restructuring may be expected to be an ongoing process with transient equilibrium states due to the different rates of metal dissolution in a mixed-metal oxide, which might make it difficult to develop an understanding of the catalyst performance and deactivation. Additionally, there is a risk where selective leaching of Earth-abundant metal in mixed-metal oxide might trigger Ir leaching as well. Based on the literature review, it was decided that iridium would be used as the primary electrocatalyst in this study due to its exceptional corrosion resistance and good activity toward OER.

Wet synthesis of Ir catalysts on powdered supports

In heterogeneous catalysis, supports, typically with a high specific surface area are used to stabilize highly dispersed active metal nanoparticles, both during the catalyst synthesis and to ensure their stability against agglomeration during a reaction. Additionally, this leads to an increase in the number of active sites when compared to an unsupported catalyst for a fixed mass of the active metal.[47] Choice of suitable support can further affect the chemical environment of the active site and cause a d-band shift, thereby influencing the intrinsic activity of the catalyst.[47] The extent to which the active metal binds to the support surface depends upon the interaction between them. These interactions can range from electrostatic attraction to the formation of chemical bonds and even an overlayer on the support [126] and are termed as "strong metal-support interactions (SMSI)".[127] Pan et al. defined interfacial phenomena that involve chemical reactions and charge redistribution during the formation of metal-support interface as the cornerstones of SMSI.[128] The effects that result from the formation of strong interactions between metals and supports include electronic, geometric, and bifunctional effects.[128] A schematic of the three effects is

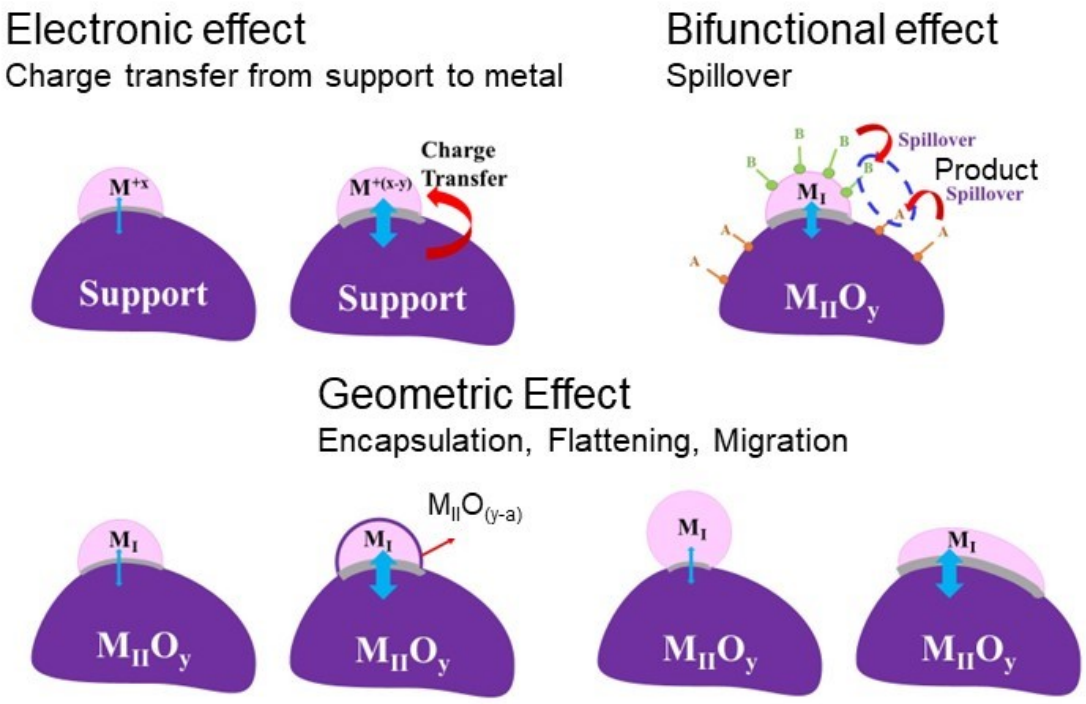

Figure 1.10: Electronic effect, geometric effect, and bifunctional effect on particle morphology resulting from strong metal-support interactions (SMSI).

shown in Figure 1.10. SMSI have the ability to influence the activity of the supported catalyst and can alter the electron density around the catalyst surface. For example, Shi et al. reported a partial covering of a thin porous oxide overlayer of TiO_2 on the platinum surface acted like an anchor, preventing particle detachment, and thereby increasing the stability of the supported catalyst.[129] Plessow et al. investigated and confirmed the increased stability using DFT.[130] A change in the adsorption energy of metal atoms (Ti) of an oxide (TiO) supported on a metal (Ir) was observed due to SMSI.

Sharma et al. had previously reported an interesting phenomenon for platinum deposited on oxide support.[131] They observed a significant lowering of the binding energy of platinum deposited on metal-oxide support in comparison to platinum

supported on carbon. The authors tried to explain this occurrence with 2 possibilities:

1. A change in the lattice energy due to the formation of an alloy between the oxide support and platinum.

2. Partial charge transfer from the oxide to platinum leading to an increased activity towards oxygen reduction reaction.

Similarly, enhanced performance of the supported catalyst was observed when Antimony tin oxide (ATO) support was added to the catalyst (IrO_x) during the Ir oxide nanoparticle synthesis in contrast to the deposition of the support on pre-synthesized Ir nanoparticle. Oh et al. reported a reduced effective oxide thickness on the IrO_x/ATO as compared to IrO_x/C with a reduction in the average oxidation state of IrO_x (+3.2 for IrO_x/ATO vs. +4.0 for IrO_x/C).[132] They proposed the occurrence of this reduction in Ir oxidation state as a result of charge donation from ATO to IrO_x. The presence of amorphous IrO_xH_y surface species was also observed, a feature that was not detected in IrO_x/C. It has been widely accepted that the presence of iridium hydroxides on the catalyst surface is mandatory for catalyst activity. They termed the interactions between the active catalyst and metal/metal oxide supports as metal/metal oxide support interactions (MMOSI) and asserted that the stability of IrO_x/support is a function of its oxidizability. Oh et al. proposed that the higher the oxidation state of the metal, the more prone it is to dissolution. Thus, the charge transfer caused by MMOSI helps stabilize the supported metal catalyst.

In the case of electrolyzers, the supports can also be used to enhance the electrode's electrical conductivity as they will reduce the contact resistance between particles. The acidic OER environment dictates specific requirements for the type of support: it must be resistant to chemical and electrochemical dissolution and preferably must have a high electronic conductivity. The latter need is mandatory if Ir loading is low; however, if iridium oxide covers most of the support, it may provide sufficient

percolative transport for the electrons.[133] The film, however, must be as thin as possible to provide advantages over unsupported iridium oxide nanoparticles. In this subsection, we focus on the wet synthesis of Ir catalysts on powdered supports, which could be mixed with a Nafion solution for catalyst layer preparation.

According to a recent literature review conducted by Clapp et al., among the different Ir-based catalysts tested on MEAs, supported nanoparticles have one of the highest effectiveness in reducing future Ir-power density targets.[68] Several substrates, including but not limited to carbon, metal oxides, metal nitrides, and metal carbides, have been investigated for their potential as supports for water-splitting electrocatalysts.[47], [84], [134], [135] Metal oxides such as tin based oxide supports (SnO_2, doped-SnO_2: ATO, ITO, FTO etc.),[79], [91], [136]–[148] titanium-based oxide supports (TiO_x, $Ti_nO_{(2-n)}$, doped titanium oxide),[138], [149]–[156] Ta_2O_5,[157] Nb-based oxides,[158]–[161] are by far the most popular metal oxide supports due to their stability under oxidative conditions, and the tunable electrical conductivity and possible metal-support interactions.[47]

In recent years, carbon and metal carbides have been receiving less and less attention because of the carbon oxidation and volatilization to CO_2 at high applied potentials.[158] As a notable exception, one of the most active Ir catalysts reported so far features a carbon-based support.[90] A 40 wt.% Ir catalyst was prepared by impregnation of graphitic carbon nitride (GCN) nanosheets with the metal precursor followed by annealing in air at 350°C. Thus embedded IrO_2 possesses compressed Ir-Ir bonds and decreased coordination numbers of Ir-O and Ir-Ir, which was suggested to weaken the adsorption of oxygen intermediates leading to increased OER activity. The reported specific currents are 580 $A \cdot g_{Ir}^{-1}$ at 1.55 V and 1493 $A \cdot g_{Ir}^{-1}$ at 1.6 V. The catalyst required the overpotential of 278 mV at 10 $mA \cdot cm^{-2}$ at 0.07 $mg_{Ir} \cdot cm^{-2}$ loading (in RDE in 0.5 M H_2SO_4). Authors demonstrated only a 35 mV potential

increase at 20 mA·cm^{-2} for 4 h in an RDE; 78.5% current retention in a laboratory water-splitting device after a 24 h operation at 1.6 V. The fate of GCN was assessed by holding 2.2 V_{RHE} for 2 h with intermediate CV measurements between 0.4 and 0.6 V_{RHE}; the double-layer capacitance decreased by 10% in the first 0.5 h and remained stable up to 2 h; apparently, the graphitic support nature with nitrogen heteroatom provides its stability in acidic electrolysis.[90] Given the high catalyst activity, and rather easy and potentially scalable preparation of GCN and Ir/GCN, studies of the catalyst durability and performance in a PEM electrolyzer are warranted.

From the catalyst synthesis viewpoint, one must be mindful that the support's chemical composition may change during the synthesis, affecting the electrochemical performance. For example, if Adams' method involving high-temperature calcination is used to produce IrO_2 on carbide support, the support oxidation leads to the loss of conductivity (e.g., TaC lost its conductivity from 120 S·cm^{-1} to 10-8 S·cm^{-1} at such circumstances).[83] A similar carbide oxidation to a less-conductive oxide was reported for the Ir nanoparticle synthesis in the presence of support by a polyol method (heating in a reducing ethylene glycol with precipitating NaOH).[158]

Among oxidation-resistant conductive metal oxide supports, tin dioxide doped with antimony (ATO), indium (ITO), and fluorine (FTO) have been the focus of most research because of their relatively high conductivity. Unfortunately, the dopant's corrosion brings down the conductivity, increasing ohmic losses and decreasing energy efficiency.[162] Dissolved cations may also ion exchange with the membrane and lead to its degradation.[104] A recent study observed neither activity nor stability benefits from the dopant addition.[142] Although FTO possesses the lowest conductivity, it was found to be the most stable material between -0.34 V_{RHE} and 2.7 V_{RHE}, followed by ITO and ATO. The stability is assigned to the oxygen atom exchange in SnO_2 with F, instead of cation exchange in the case of ATO and ITO synthesis.[162] ATO,

in turn, was suggested to mitigate Ir dissolution by preserving it in lower oxidation states.[132] Commercially available samples usually feature low surface areas; several synthetic techniques were suggested in the literature for the preparation of mesoporous doped SnO_2 with relatively high areas (for example, between 125 $m^2 \cdot g^{-1}$ and 263 $m^2 \cdot g^{-1}$).[163] To deal with toxic NH_4F for the FTO synthesis, safety measures must be in place, as in any chemical and engineering process. A number of Ir catalysts supported on doped SnO_2 with high activities and low overpotentials at low Ir loadings were recently reported.

Another example is when SnO_2 was doped with tantalum (TaTO) and used to deposit preformed 1.7 nm IrO_x nanoparticles at 11-18 wt.% Ir loading, the OER activity of the fresh catalysts after electrochemical conditioning approached 250 $A \cdot g_{Ir}^{-1}$at overpotentials of 280 mV and 370 mV at 0.020 $mg_{Ir} \cdot cm^{-2}$ loading (25°C, 0.05 M H_2SO_4).[91] Although the electronic conductivity of TaTO was two orders of magnitude lower than that of ATO, its use did not result in decreased activity, which was ascribed to the conducting role of well-dispersed IrO_x nanoparticles. In accelerated aging tests at 1.2 V-1.6 V potential steps, the IrO_x/TaTO catalysts demonstrated between 70% and 90% activity retention vs. 60% for the ATO-supported catalyst. The loss of the dopant was one to two orders of magnitude lower for Ta as compared to Sb, while the loss of Sn was not affected. The Ir dissolution was found dependent on the Ta loading: the higher loading decreased the Ir oxidation state contributing to its dissolution, while at lower loadings tantalum shell suppressed IrO_x nanoparticle detachment. This study also demonstrates that the use of support contributes to enhanced Ir leaching, as compared to commercial IrO_2.[91] As a result, although the activity of unsupported IrO_2 is significantly lower than that of the developed catalysts, its stability to dissolution contributes to high S-numbers (ratio of evolved oxygen to dissolved iridium),[72] such as the S-number for IrO_2 was twice higher than that for selected IrO_x/TaTO catalysts at 1.6 V and similar at 1.5 V.[91] When

hydrous IrO_x was supported on ATO, its S-number was also lower than the one for unsupported IrO_x, but the calcined supported samples demonstrated up to two orders of magnitude higher S-number as compared to IrO_2.[142] Moreover, Ir, Sn, and In oxides may form mixed oxides; the lattice vacancies are thus produced upon Sn and In in situ dissolution, improving the initial activity but jeopardizing the durability due to enhanced Ir dissolution.[141]

A key objective of this thesis is to develop an active and stable supported IrO_x electrocatalyst for OER. Due to the lack of conductive supports that can show strong resistance to deactivation at OER-relevant potentials, this study will instead focus on selecting support with inherent corrosion resistance (stability) alongside its capacity for synergistic interactions with Ir.

A popular method for the preparation supported Ir OER catalysts, is colloidal precipitation of IrO_2 from an iridium molecular precursor by means of NaOH; the synthesis may proceed in ethylene glycol,[79] which serves both as a solvent and a reducing agent, or, for example, in a hydrothermal microwave reactor.[134], [164] Small 2-3 nm particles may be obtained,[132] or even smaller (1.5±0.2 nm) if a stabilizer is added.[165] The support may be added to the colloidal dispersion either during synthesis or after the nanoparticle formation. The use of high-boiling ethylene glycol, though, complicates the potential process scale-up because solvent removal under vacuum is usually used,[99] instead of centrifugation or filtration of highly diluted suspensions, as practiced in the laboratories.

When the surfactant-stabilized Ir nanodendrites (39 $m^2 \cdot g^{-1}$ area) mentioned in Section 1.2.2 were deposited on high-surface-area ATO (235 $m^2 \cdot g^{-1}$), an initial overpotential of 260 mV at 10 $mA \cdot cm^{-2}$ at only 0.0102 $mg_{Ir} \cdot cm^{-2}$ loading (RDE, 0.05 M H_2SO_4) was observed while accelerated durability test showed a minor overpotential

increase by 30 mV over 15 h compared to an abrupt increase for other tested catalysts at earlier times.[79] The specific current at 280 mV overpotential was reported at 70 $A \cdot g_{Ir}^{-1}$ vs. 8 $A \cdot g_{Ir}^{-1}$ for Ir black. In a PEM electrolyzer, the catalyst demonstrated the current density of 1.5 $A \cdot cm^{-2}$ at 1.8 V and 1 $mg \cdot cm^{-2}$ loading compared to 0.8 $A \cdot cm^{-2}$ for Ir black.

An atomically dispersed Ir on ITO with ultimate Ir dispersion was developed by grafting 0.86 wt.% Ir as an organometallic Ir complex followed by calcination in air at 400°C.[166] The specific current of 156 $A \cdot g_{Ir}^{-1}$ was reached at 280 mV overpotential and 0.021 $mg_{Ir} \cdot cm^{-2}$ loading (0.1 M $HClO_4$). An overpotential of 350 ± 20 mV was required to drive the 10 $mA \cdot cm^{-2}$ current at such low metal loadings over the course of 2 h; some Ir agglomeration was observed in the used catalyst and its consequences on the long-term performance require further analysis.

As a myriad of more or less sophisticated methods emerge to develop a supported catalyst, to develop a catalyst that can be commercialized, one must keep in mind the method's practicality, safety, ease, and scalability, and that it must use as few resources and produce as little waste as possible. This, most likely, precludes the use of surfactant-assisted routes of the wet catalyst synthesis and might jeopardize the stabilizer-free colloidal synthesis in vast amounts of organic solvents.

In the incipient wetness impregnation method (IWI), a support is impregnated with a precursor-containing solution and dried. The resultant dry product is then subjected to additional activation treatments, such as calcination and/or reduction, to achieve the desired catalyst. IWI method is widely favored in various industries because of its technical simplicity, cost-effectiveness, and minimal waste generation.[167] However, its application in the context of water splitting remains largely unexplored or overlooked.

The undertaken approach in this work is to synthesize active and stable catalysts for OER applications using the incipient wetness impregnation method.

A common feature between all the wet-chemistry methods, both unsupported and supported catalysts described above, is that the majority of them use a precursor. The selection of Ir precursors is a crucial step in the synthesis that is seldom discussed in the literature. Examples of precursors include Ir(IV) based precursors like H_2IrCl_6,[6], [168] $IrCl_4$,[169] K_2IrCl_6,[170], [171] Na_2IrCl_6,[172] $(NH_4)_2IrCl_6$[173]; Ir (III) based precursors like $IrCl_3$,[168], [174] Na_3IrCl_6,[175] and $Ir(acac)_3$;[95] and Ir(I) based precursors like $[Ir(COD)_2]BF_4$.[176], [177] The majority of the aforementioned precursors contain chloride ligands. The presence of chloride atoms in the catalysts is often associated with active site poisoning.[178] For example, in supported Ru catalysts, residual chlorine has also been shown to reduce the active surface area.[179]

Several attempts have been made in the scientific community to remove chloride from catalysts. Bowker et al. synthesized catalysts by modifying the conventional incipient wetness impregnation method and simultaneously adding the halide-based precursor ($AuCl_4.3H_2O$) and a base (1.0 M Na_2CO_3) to the support (TiO_2) in an effort to remove chlorine from the lattice of the Au catalyst into the solution followed by repetitive Na_2CO_3 and water washes. An improved activity toward CO oxidation was reported as a result of chloride removal. The authors also recommended further optimization of the process by using other routes to increase the pH in the supports by replacing Na_2CO_3 with ammonia. Ruiz Esquise et al. have used a modified hydrothermal method, which is focused on driving the Cl^- ions in abundant solution, followed by washing of the catalyst, often using $>$ 2 L of water per mmol $IrCl_3$.[100]

Okada et al. focused on removing the residual chlorine from V_2O_5/TiO_2 synthesized using the deposition of $VOCl_3$ precursors by flowing NH_3 at 623 K.[180] They recommended NH_4OH washing for compounds that are not soluble in NH_4OH. Narita et al. studied the removal of chloride from the Ru/Al_2O_3 catalyst surface by washing the catalyst with dilute 0.1 M NH_4OH followed by a reduction in H_2 at 600 K. Their findings indicated that this treatment led to a twofold increase in the chemisorption of H_2 and CO_2 compared to the reduction in H_2 at 600 K alone.[181]

Another key objective of this thesis is to develop a fundamental understanding of the influence of residual chloride from the precursor on the catalyst's physicochemical and electrochemical properties, and the development of methodologies to mitigate the chloride content within the catalyst's lattice, facilitating the production of catalysts that are simultaneously active and stable. Furthermore, given that the primary limitations of catalyst synthesis using IWI are limited control of the particle size of the deposited active metal and the presence of counterions from the precursor, e.g., as chlorides from common halide-based precursors which are retained in the catalyst after drying,[182] this work will focus on developing ways of chloride removal/mitigation that can be complementary to the IWI in the future and do not require excessive resources.

1.2.3 Electrochemical testing

Reliable assessment of the performance of the electrocatalyst towards OER is of utmost importance. A membrane electrode assembly (MEAs) is typically used to accurately predict the electrolyzer system performance. However, the evaluation of electrocatalysts using MEA necessitates a significant amount of time for preparation and testing, along with costly instrumentation and the need for precise control of reaction conditions, including gas pressure, flow rate, temperature, and relative hu-

midity.[183]

Additionally, for the preliminary evaluation of new electrocatalysts, which are often available in limited quantities, typically just a few milligrams, utilizing MEAs becomes not only cumbersome but also wasteful.[183] Small-scale testing of electrocatalysts can be easily performed using convective-flow-based techniques such as rotating disk electrode (RDE),[184] the channel flow double-electrode,[185] and gas diffusion electrode.[186] Of the methods mentioned earlier, the one most commonly used is the RDE.[187], [188] RDE requires small quantities of electrocatalysts, only a few micrograms of catalysts per square centimeter,[183] to estimate the activity of different electrocatalysts.[188] While RDE cannot entirely replace the necessity for catalyst evaluation in an MEA, it is valuable for the preliminary evaluation of electrocatalysts and can provide valuable information regarding the kinetics of the reaction.

RDE will be employed to study the electrocatalysts in this work.

RDE set-up

A rotating disk electrode is a half-cell set-up consisting of a three-electrode cell along with an electrolyte. A traditional three-electrode set-up consists of working, counter, and reference electrodes placed in the same electrolyte solution. During experiments, the current flow occurs between the working electrode and the counter electrode. The potential of the working electrode is measured with respect to the reference electrode. The rotation of the working electrode minimized transport losses which allow the extraction of kinetic parameters for electrolyzer reactions.[183], [189] The schematic representation of a 3-electrode set-up is shown in Figure 1.11.

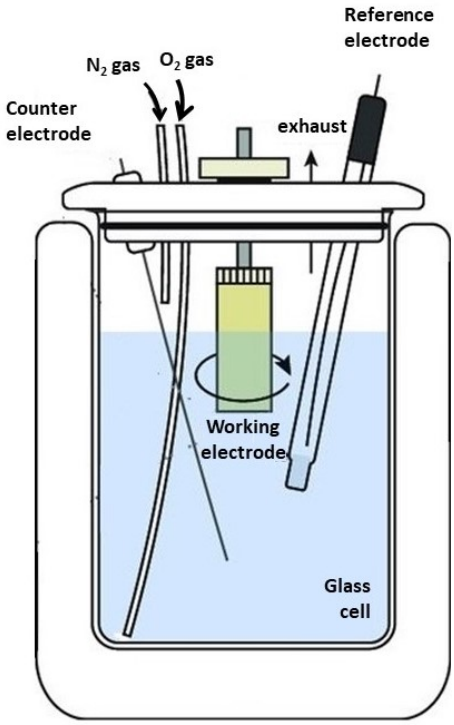

Figure 1.11: Schematic of a rotating disk electrode set-up

Working electrode: The powdered catalysts are deposited on the nonporous surface of a conductive substrate, i.e., a working electrode.[190] The rotation of the working electrode establishes a 5-50 μm thick diffusion layer from which the kinetics of OER can be extracted.[183], [189] The choice of the electrode is particularly important while performing the electrochemical activity and stability assessments since surface passivation of the substrate surface can be misinterpreted as catalyst degradation.[190] Glassy carbon is the most widely used backing electrode material for ORR and OER. However, it can easily passivate under OER conditions. Geiger et al. reported an exponential rise in the electrode potential at 2.3 V_{RHE} with minimum catalyst dissolution or particle detachment.[190] This steep rise was attributed to increasing contact resistance at the backing interface. In order to overcome the issues with backing electrode degradation, a material that resists passivation and dissolution should be used. Gold and boron-doped diamond as appropriate backing electrode

materials.[191] However, Cherevko et al. showed that gold suffers from acute dissolution at OER potentials and BDD is limited due to its exorbitant cost.[52] Thus, the use of an alternate backing electrode material can aid in understanding catalyst degradation, but cannot substitute for glassy carbon electrodes.

Due to the lack of a better alternative, a glassy carbon electrode will be used as the backing electrode in this study. Moreover, in this study, the working electrode is subjected to a maximum potential of 1.60 V_{RHE} to minimize surface passivation.

Reference electrode: Using a reference electrode within a three-electrode system allows investigation of the charge transfer characteristics of a half-cell, rather than the data of a two-electrode system associated with the full-cell behavior. A viable reference electrode should possess a constant electrochemical potential at low current density. Due to the passage of negligible current through the electrode, the decrease in the effective potential applied to the electrochemical double layer (iR-drop) is small.[192]

Among the different reference electrodes available, the hydrogen reference electrode is considered the most reliable. The standard hydrogen electrode consists of a platinized Pt electrode, either a wire, sheet, or mesh.[193] In an acidic solution having a unit activity of H^+ proton, H_2 gas is supplied at a fugacity of 1 bar in the form of small bubbles, such that the electrolyte becomes saturated with H_2 gas.[193] The standard hydrogen reference electrode can also be used to calibrate other reference electrodes. It can be used in both alkaline and acidic solutions. Its use is also preferred as it prevents contamination of the working electrode. Furthermore, it removed inaccuracies introduced by miscalibration and potential drift during testing. Other commonly used reference electrodes include chloride-based electrodes such as

silver chloride (Ag/AgCl) electrodes, saturated calomel electrodes, and sulfate-based electrodes.

In this work, a standard hydrogen electrode and a double-junction Ag/AgCl electrode will be used as reference electrodes.

Counter electrode: The counter electrode, also known as the auxiliary electrode, is used to facilitate the current required to balance the current at the working electrode, without engaging in the reaction itself. It achieves this by altering its potential.[191] Nobel metals such as Pt and Au are used to form counter electrodes. Platinum is the most commonly used electrode due to its robustness, high electrocatalytic activity, and excellent electrical conductivity.[194]

In this work, a helical Pt counter electrode will be used as a counter electrode.

Electrochemical characterization

Electrochemical characterization of the catalyst aims at measuring (1) electrochemical surface area (ECSA); (2) catalyst activity and Tafel slope, and (3) stability of the catalyst.

1. **Estimation of the electrochemical surface area using cyclic voltammetry (CV)**

   Cyclic voltammetry is used to calculate the ECSA of the catalysts. The electrochemical surface area (ECSA) of metallic Ir may be estimated by estimating the integral charges of underpotentially deposited hydrogen (H_{upd}), and its desorption in the potential range of 0–0.35 V_{RHE} of a CV profile, including a correction

for double-layer charging. [6]

$$ECSA = \frac{Q_{H_{\mathrm{UPD}}}}{q_{H_{\mathrm{UPD}}}} \tag{1.13}$$

where $q_{H_{UPD}}$ is the charge constant associated with underpotentially deposited hydrogen on Ir, assumed to be 179 C·cm^{-2}.[6]

The calculation of ECSA of Ir-oxide catalysts presents difficulties owing to the lack of hydrogen adsorption. Various approaches are employed in the literature for its determination.[6], [187], [195]–[201] One of the commonly accepted approaches to determining ECSA of IrO_x/IrO_2 catalysts is as follows:

The double-layer capacitance (C_{dl}) is calculated using cyclic voltammetry scans at different scan rates in the non-faradaic region. The slope of the current (mA) vs. scan rate (V·s^{-1}) is used to calculate the value of C_{dl}. C_s is the specific capacitance, which is the double layer of a polished GC with no catalyst. C_s is calculated using the same approach as C_{dl}. The ratio of C_{dl} and C_s provided the ECSA of the catalyst.[96], [194], [197]

$$\mathrm{ECSA} = \frac{C_{\mathrm{dl}}}{C_{\mathrm{s}}} \tag{1.14}$$

Another approach to estimate ECSA is based on measuring $Q_{\mathrm{deprotonation}}$, the total anodic charges of the CV profiles in the potential range of 0.4 to 1.25 V, where Ir deprotonation is expected, corrected for double layer charging and normalized to the geometric area of the GC electrode surface.[6], [202] Then, the ECSA is given by

$$\mathrm{ECSA} = \frac{Q_{\mathrm{deprotonation}}}{q_{\mathrm{deprotonation}}} \tag{1.15}$$

where $q_{deprotonation}$ is 440 $\pm$ 14 μC.cm$^{-2}{}_{\mathrm{ECSA}}$ based on the work of Tan et al. [6]

In this work, the latter methodology, developed by Tan et al., will be used to calculate the ECSA of the catalysts.[6]

2. **Estimation of initial activity using linear sweep voltammetry (LSV) and Tafel slope**

Linear sweep voltammetry is performed in an oxygen-saturated environment to estimate the catalyst activity. LSV refers to linear sweep in voltage from a lower potential to an upper potential limit.

The activity is given as the current produced at a given potential and is usually reported with respect to the geometric area. To compare various catalyst performances quantitatively, it is essential to calculate the specific activity of the catalyst at a constant potential, denoted as activity normalized by the mass of Ir/IrO_x employed ($A{\cdot}g^{-1}_{Ir/IrO_x}$). Higher specific activity of the catalyst (or mass activity) is associated with increased Ir utilization, decreased Ir consumption, and subsequently reduced catalyst costs.[68] Specific activity is a function of dispersion (ECSA) and intrinsic activity.[67] The intrinsic activity of the catalyst can be determined by normalizing the activity of the catalyst at a constant potential by the ECSA of the catalyst ($mA{\cdot}cm^{-2}_{ECSA}$). Here, the resultant activity of individual catalyst active sites is contingent upon the nature of the active site and not on the number of active sites/dispersion.

Another metric used to compare the catalyst performance is the overpotential (η) required to achieve the current density of 10 $mA{\cdot}cm^{-2}_{geo}$, where η for OER is given by equation 1.16,[189] as follows:

$$\eta = E - E_o \tag{1.16}$$

where E_o is the thermodynamic potential (or equilibrium potential) for OER

(1.23 V_{RHE}). The lower the overpotential, the better the performance of the catalyst.

Tafel analysis is performed to compare the electrocatalytic activity among different catalysts and to uncover the underlying reaction mechanism. During Tafel analysis, the sensitivity of the current output to the applied potential is analyzed, which provides information associated with the rate-determining steps. Current and voltage are related by Tafel equation. At high overpotential, the Tafel equation can be expressed as:

$$\eta = b \log_{10} \left(\frac{i}{i_o} \right) \tag{1.17}$$

where, b is the Tafel slope ($mV \cdot dec^{-1}$), i is the current density, i_o is the exchange current density and η is the overpotential. The experimentally observed Tafel slopes can be compared with the theoretically derived slopes assuming different rate-determining steps based on microkinetic models.[203]

In this work, the initial catalyst activity will be estimated using LSV and normalized on the basis of the geometric surface area of the working electrode, mass of Ir, and ECSA of Ir deposited on the working electrode. Tafel slopes will also be calculated for all the catalysts in the kinetically relevant potential windows.

3. **Study of corrosion stability, deactivation mechanisms, and activity regeneration**

In addition to understanding the deterioration of catalyst activity, it is equally important to discern the loss of stability of the catalyst. Due to the very long lifetimes of PEMWE catalysts, in the range of 50,000 h-100,000 h, it is not feasible to perform long-term stability tests.[132], [183] Loss of activity over time might be due to a) Ir dissolution, b) Ir oxidation/Ir phase transformation, and c) bubble accumulation displacing liquid water from the reaction site. Knowledge of Ir dissolution is the most widely discussed while estimating the stability

of IrO_x catalyst. In a PEM electrolyzer, iridium dissolution might result in both iridium ions in the water feed, and migration and redeposition at the anode/membrane interface, membrane [103], [204], [205] and possible deposition on the cathode leading to Pt deactivation, especially at high current densities and overpotentials.[103]

For RDE experiments, Joint Center for Artificial Photosynthesis Photosynthesis (JCAP) group recommended the use of an increase in potential (ΔE) after 2 h of galvanic polarization at 10 mA/cm^2_{geo} (chronopotentiometry) as the benchmarking stability protocol for OER catalysts.[126], [206] While this protocol is widely used, it suffers from serious limitations.[190] Evaluating a catalyst at a controlled current means that the catalysts are not evaluated under the same electro-oxidative conditions. This is because a catalyst with higher activity will operate at a lower potential and appear to be more stable.[6] The rise in potential (ΔE) does not necessarily indicate stability issues. Causes such as electrode passivation [190] or blocking of active sites by oxygen bubbles,[207]–[209] all bring about the increase in operating potential. The display of a constant overpotential over a long time (2 h-15 h) also does not represent a stable catalyst. The leaching of mixed metal oxides in the electrolyte and the revelation of the fresh inner layer of the catalyst post-leaching can both increase the catalyst activity. This can provide constant potential over drawn-out time despite the degradation of the material. The catalyst loading on the working electrode is left ambiguous as per the JCAP protocol. This suggests that the higher the catalyst loading, the more stable the catalyst will appear. To add to the issue, the current produced (10 mA/cm^2_{geo}) is based on the geometric surface area of the working electrode, not the active surface area of the catalyst.

A catalyst's lifetime depends on its operating current density and overpotential. It may be estimated using the stability number (S-number), i.e., the ratio of evolved oxygen to dissolved Ir at constant overpotential.[72]

$$\text{S-number} = \frac{n_{\text{O}_2}}{n_{\text{Ir}}} \tag{1.18}$$

The authors calculated the number of moles of O_2 evolved by integrating current during current or potential hold,[91] as presented in equation 1.19

$$n_{\text{O}_2} = \frac{1}{zF} \int i(t)\text{d}t \tag{1.19}$$

where z is the number of the moles of electrons transferred during OER, which is 4; F is the Faraday constant (96 485.3329 A·s·mol^{-1}), and t is the length of the test (seconds), i attributed exclusively to the OER reaction.

The number of moles of Ir dissolved can be estimated using equation 1.20,

$$n_{\text{lr}} = \frac{[\text{Ir}] \times V}{M_{\text{lr}}} \tag{1.20}$$

where [Ir] is the Ir concentration, i.e., Ir dissolved in the electrolyte ([Ir] in g·L^{-1}), V is the volume of the electrolyte and M_{Ir} is the molar mass of Ir, i.e., 192.217 g·mol^{-1}.

Finally, Tan et al. suggested a novel method to evaluate the corrosion stability of the catalyst using chronoamperometry (CA) at 1.53 V or 1.6 V_{RHE} while performing electrochemical impedance spectroscopy (EIS) and cyclic voltammetry (CV) at regular time intervals throughout CA.[6] The potentials were consciously selected to ensure a slow rate of electrode passivation.[190] This would also ensure similar electro-oxidative conditions for different electrocatalysts. The main drawback is that the more active catalyst would produce more current, which according to Geiger et al. would result in higher dissolution, suggesting Ir dissolution is proportional to the current (S-number).[72]

Massué et al. observed that Ir/IrO_x electrocatalysts deactivate in two steps: a gradual increase in anodic potential due to the depletion of OER-relevant active Ir species, and (2) a sharp increase in anodic potential due to the loss of ECSA through Ir dissolution.[134] Tan's study also noted this pattern and directed their attention on decoupling the two deactivation mechanisms. This was achieved by the following:

(a) **Detecting loss of intrinsic activity**

Chronoamperometry was performed to measure catalyst stability. EIS was used to monitor the rise in charge transfer resistance (R_{ct}) throughout the chronoamperometric cycle. An increase in the value of R_{ct} was considered a direct indicator of catalyst deactivation/depletion of OER relevant Ir species from the surface of the catalyst. CV analysis was performed at regular intervals. Performing multiple CVs at each interval was used to estimate ECSA and to partially recover the activity of the catalyst lost due to the transformation of OER-relevant Ir(III)/Ir(IV) species to anhydrous IrO_2 or higher oxidation state(s) of Ir.

The part of the activity that was not recovered by performing CV is presumed to be lost due to passivation of the catalyst surface or be irreversibly phase transformation of performance-relevant species. XPS was used to interpret the phase transformation-induced activity loss by determining the oxidation state of the catalyst and shift in binding energy post the stability test.[6]

(b) **Detecting loss due to anodic dissolution**

Tan et al. established a relationship that allows for the estimation of IrO_x depletion caused by the dissolution of Ir by evaluating the decline in the

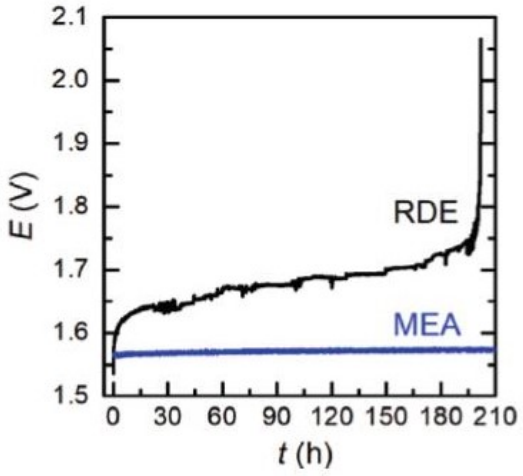

Figure 1.12: Evaluation of IrO_2/TiO_2 catalyst stability in an RDE and MEA at 70 $A \cdot g_{Ir}^{-1}$; reprinted from [41] under the Creative Commons Attribution License, copyright 2019.

ECSA of the catalyst over the course of the CA cycle. Inductively coupled plasma mass spectrometry (ICP-MS) analysis was performed before and after the CA cycle to validate these findings.[6]

While the aforementioned methodology is very useful in decoupling the catalyst deactivation mechanisms, Tan et al. did not address all the catalyst deactivation mechanisms in their study.

According to Trogisch et al., the build-up of small oxygen bubbles generated at OER-relevant potentials can also cause blockage of active sites, inhibiting electrolyte contact with the catalyst surface, and hindering the participation of active sites in OER.[207] They emphasize that bubble accumulation is capable of shielding over 90% of the active sites forcing the fraction of active sites present at the catalyst-electrolyte interface to provide all the current resulting in less current at a given cell voltage, which leads to an apparent reduction in activity and increases in R_{ct}. It might

also possibly trigger catalyst deactivation either by Ir dissolution,[207], [210] or phase transformation.[6] As shown in Figure 1.12; for example, oxygen bubble accumulation, could make the stability studies, not a reliable predictor for the catalyst lifetime in a PEM electrolyzer long-term behavior.[41]

A few different ways to promote bubble removal reported in the available literature focus either on altering the structure of the catalyst and surface wettability to facilitate O_2 removal [210]–[213] or using external equipment, such as sonicator,[209] magnetic fields,[214], [215] super-gravity [216]–[218] to remove the bubbles. However, the introduction of auxiliary equipment and redesigning the catalysts is a cumbersome process that might introduce additional variables, for example, a temperature increase in the electrolyte due to continuous sonication. There is a need to develop a facile technique or methodology to account for the deactivation experienced by the catalyst layer due to microscopic O_2 bubble accumulation.

In this work, we aim to modify the stability testing procedure developed by Tan et al.,[6] to include the estimation of losses attributed to the buildup of microscopic O_2 bubbles within the catalyst layer.

1.3 Thesis objectives

The overarching objective of this thesis is the development of stable and active Ir catalysts for acidic OER.

To achieve this goal, the following sub-projects were identified:

1. Synthesis of Ir-oxide-based catalysts using a simple synthesis approach, with a

focus on scalability and relevance to industrial use. This entails the preparation of different supported catalysts using the incipient wetness impregnation method (IWI) with a molecular commercial Ir precursor H_2IrCl_6.

2. Exploration of non-conductive supports to develop active and stable Ir-oxide-based catalyst. Ir oxide was deposited on many supports using IWI and ZrO_2 was identified the most suitable support. The supported catalysts' performance was assessed on an RDE set-up using metrics such as ECSA, Tafel slope, intrinsic and specific activity, as well as stability. Strong metal-support interactions (SMSI) between Ir oxide and ZrO_2 support were investigated to elucidate the drivers of enhanced activity and deactivation mechanisms. This was achieved by performing a thorough physicochemical characterization of the catalyst using different techniques.

3. Analysis of the influence of residual chloride from the H_2IrCl_6 precursor on the physicochemical and electrochemical performance of the catalysts. This involved altering synthesis parameters to modulate chloride content in IrO_2 catalysts prepared through thermal decomposition, followed by a comprehensive analysis of resulting differences in physicochemical properties and electrochemical performance.

The sub-projects of this thesis are based on the following key observations:

1. Academic research has focused on novel and well-defined catalytic structures that are often too complex for industrial synthesis. The use of a simple technique, such as incipient wetness impregnation method should be investigated as an alternative approach that would enable easy scale-up.

2. Supports influence the performance of OER catalysts by adding or reducing the electron density to the catalyst surface and/or altering morphology (SMSI),

increasing active metal dispersion, and mitigating Ir dissolution. Therefore, there is a need to search for suitable support.

3. Non-conductive supports can be used to synthesize active catalysts, contingent on the ability of the Ir oxide network to undertake electron transfer responsibilities. This implies that the search for a suitable support should not be confined to electrically conductive supports.

4. Most of the wet-chemistry methods of synthesis use a chloride-based precursor. The impact of residual chlorine from the precursors on the physicochemical and electrochemical properties of the catalyst should be investigated.

1.4 Structure of the thesis

This thesis is organized into four chapters. Chapter 1 has provided the motivation and goal of the work. A thorough literature review was also conducted in order to identify knowledge gaps. In Chapter 2, the incipient wetness impregnation method used for the synthesis of supported catalysts is discussed; monoclinic ZrO_2 is introduced as a novel support; physicochemical and electrochemical characterization is performed on diverse catalysts, including state-of-the-art IrO_x TKK, which is used as a benchmark and obtained results, analysis, and discussion are described in detail. In Chapter 3, the effect of residual chlorine from the H_2IrCl_6 precursor is studied in Ir oxide catalysts prepared by thermal decomposition. The chapter provides an overview of the synthesis method, coupled with a discussion of observed differences in the physicochemical and electrochemical characteristics of the catalysts. Finally, Chapter 4 summarizes the findings of this work and provides an outlook on the future directions.

Chapter 2

Strong metal - support interactions in ZrO_2-supported IrO_X catalyst for efficient oxygen evolution reaction

2.1 Introduction

The International Energy Agency (IEA) estimated that in order to meet the net zero scenarios by 2050, approximately 320 million tonnes of H_2 per year need to come through electrolysis.[219] The declining cost of renewable electricity over the years, the use of simpler designs for water electrolyzers, and the improving efficiency and durability of electrolyzers are critical for producing green hydrogen at a competitive price.[220] Proton-exchange membrane water electrolyzers (PEM-WE) are one of the most mature technologies currently present, however, they require expensive Ir-based catalysts to achieve good performance and durability.[38] In a catalyst-coated membrane (CCM), iridium accounts for 24% of the total cost, making it a bottleneck to the widespread use of PEM electrolyzers.[25] The rare occurrence of Ir element, with a presence of merely 1 ppb in the Earth's crust, its exorbitant cost of $4600 per ounce, and its high price volatility which has varied by a factor of 15 over the last 20 years pose barriers to the future of PEM water electrolyzers.[39]

One of the best ways to reduce Ir usage is to boost catalyst utilization in the CCM. This can be achieved by increasing Ir dispersion using high surface area sup-

ports,[47]use of different Ir morphologies,[6], [95], [96], [107], [110], [171], [174], [221]–[225] and use of promoters.[226]–[230] Among the available options, using supported catalysts offers an appealing solution to meet the demands of practical large-scale applications while simultaneously reducing the amount of precious metal needed for catalyst synthesis.[47] To be considered as a suitable support for oxygen evolution reaction (OER) in PEM-WE, the material must offer high stability in an acidic environment, a high surface area, and good electrical conductivity. The availability and affordability of the support are also significant factors to take into consideration.

So far, several materials, including but not limited to carbon, metal oxides, metal nitrides, and metal carbides, have been investigated for their potential as supports for water-splitting electrocatalysts.[47], [84], [134], [135] Tin based oxide supports (SnO_2, doped-SnO_2: antimony doped tin oxide , indium doped tin oxide, fluorine doped tin oxide etc.),[79], [91], [136]–[148], [231] titanium-based oxide supports (TiO_x, $Ti_nO_{(2-n)}$, doped titanium oxide),[138], [149]–[156] Ta_2O_5,[157] Nb-based oxides,[158]–[161] are by far the most popular metal oxide supports due to their stability under oxidative conditions, and the tunable electrical conductivity for some, and possible metal-support interactions.[47] For instance, Oh et al. reported a reduced effective oxide thickness in IrO_2/ATO as compared to IrO_x/C, with an observable reduction in the Ir oxidation state as a result of charge donation from ATO to IrO_x.[132] The presence of performance-relevant amorphous IrO_xH_y surface species was also observed, a feature that was not detected in IrO_x/C.

ATO has been extensively utilized and endorsed in literature, ever since its discovery, and in most cases, it is favored over SnO_2 due to higher conductivity resulting from doping Sb in the lattice of SnO_2. Several studies have highlighted its usefulness.[132], [139], [144], [232]–[234] However, recent work by DaSilva et al. showed that in IrO_2/ATO, the presence of dopants (F, In, Sb) in SnO_2 resulted in increased

Sn dissolution in comparison to the materials supported on the pristine SnO_2.[142] Furthermore, the specific use of Sb seemed to destabilize the IrO_x phase, leading to a higher Ir dissolution. Jang et al. discovered that under reductive synthesis conditions, the interactions between ATO and Ir led to an impediment in the electrocatalytic activity of the catalyst towards OER.[235] They observed that the variable oxidation state of Sb led to a decrease in the electrical conductivity of Ir/ATO, and deteriorated the electron transfer through the support, negatively affecting its performance. Taking the aforementioned observations into consideration, it would be valuable to explore the potential of other electrocatalyst supports that may offer superior performance compared to ATO.

Karimi et al. suggested that while electronic conductivity is a crucial factor in the selection of supports for OER catalysts, it is considered a lower priority compared to support surface area and the nature of the support in the hierarchy of desirable properties.[158] Maźur et al. also demonstrated that in the case of Ir-based catalyst dispersed on non-conductive TiO_2 support, the compact Ir layer deposited on TiO_2 took over the role of electron conductor, supporting the aforementioned hypothesis of Karimi et al., thereby eliminating the need to solely focus on conductive supports.[236] Similar studies were also undertaken by Nikiforov [237] and Polonsky,[238] who used non-conductive SiC-Si and ceramics (TaC, Si_3N_4, WB and Mo_2B_5) as supports for water electrolyzers. Polonsky et al. emphasized that once IrO_2 concentration exceeded the percolation level, the electrical conductivity of the support does not remain a critical quantity.[238]

Given this precedence, we prioritized the stability and nature of the support materials while selecting them for our study, including both conductive and non-conductive supports like ATO, SnO_2, Nb_2O_5, TiO_2, Ta_2O_5, and ZrO_2. While use of ATO, SnO_2, Nb_2O_5, Ta_2O_5 as supports has been documented in the literature, the use of ZrO_2 as

a support for an OER electrocatalyst is a new development. ZrO_2 support was chosen due to its synergistic relationship with Ir observed in studies conducted on IrO_2-ZrO_2 bimetallic alloys.[239]–[241] Shao et al. investigated the impact of ZrO_2 on the electrochemical activity and structure of IrO_2-ZrO_2 binary alloy and discovered that the addition of ZrO_2 limited the crystallization of IrO_2, resulting in a shift towards an amorphous structure of IrO_2-ZrO_2 as ZrO_2 content increased, while proton conductivity also increased.[241] Zhao et al. used Hf, an element with a similar electronic structure to Zr, as a modifier to create an $IrHf_xO_y$ alloy demonstrating activity an order of magnitude higher than IrO_x.[242] They suggested that a combination of early and late transition metals could selectively tune the relative energies of the OER reaction intermediates (such as M-OH, M=O, and MOOH), resulting in lower barriers for the OER reaction.[242] Ir and Zr belong to the class of Brewer-Engel intermetallics, elements known for their synergism and improved activity in the alloy form.[243] This information, coupled with the high stability of ZrO_2 in acidic and corrosive environments prompted us to explore ZrO_2 as support. A 2023 study performed by Lee et al. has described the synthesis of IrO_x/Zr_2ON_2 as promising support due to its stability and conductivity. However, they did not observe any interaction between Ir and Zr, which could be attributed to the use of the polyol synthesis method for Ir, which may have impeded interactions as already prepared Ir nanoparticles were deposited on the support.[244]

In this work, we aim to investigate the properties of ZrO_2, and its suitability as a support for Ir-catalyzed OER in acidic media. To achieve this, we selected five catalysts, namely $Ir_xZr_{(1-x)}O_2/ZrO_{2(L)}$, $Ir_xZr_{(1-x)}O_y/ZrO_{2(S)}$, IrO_2/ ATO, $(IrO_2 + Ir)_U$ (unsupported), and commercial benchmark IrO_x TKK. The subscripts (L) and (S) denote ZrO_2 particle sizes of less than 5 μm (large) and less than 100 nm (small) respectively, as reported in Table 2.1. IrO_2/ATO was of particular interest due to its reported promise as a support in the scientific literature.[47], [143], [145], [245], [246]

The activity and stability of these catalysts were evaluated by electrochemical testing of the catalysts in a rotating disk electrode set-up. A combination of linear sweep voltammetry (LSV), chronoamperometry (CA), operando electrochemical impedance spectroscopy (EIS), and cyclic voltammetry (CV) were used to evaluate the stability of the catalysts under identical electrooxidative conditions. Physicochemical characterization including transmission electron microscopy (TEM), selected area electron diffraction (SAED), X-ray diffraction (XRD), X-ray photoelectron spectroscopy (XPS), energy dispersive X-ray analysis (EDX) coupled with TEM and SEM were performed on selected catalysts. Temperature-programmed desorption (TPD) experiments of water and oxygen were implemented to investigate a correlation between the catalysts' activity during OER and the binding energy pattern of the OER-relevant species, such as water and oxygen on the catalyst.

2.2 Experimental

2.2.1 Catalyst synthesis

Three supported catalysts were synthesized using the incipient wetness impregnation method (dry impregnation). $H_2IrCl_{6\cdot x}H_2O$ (hydrogen hexachloroiridate (IV) hydrate, 99.9% trace metals basis, CAS 110802-84-1) was used as the Ir metal precursor, and ultrapure Milli-Q water (18.2 MΩ.cm) water was used as a compatible solvent. Three supports, namely $ZrO_{2(S)}$(< 100 nm nanopowder, CAS No. 1314-23-4), $ZrO_{2(L)}$ (<5 μm, 99% trace metals basis, CAS No. 1314-23-4) and antimony-doped tin oxide referred to hereafter as ATO (<50 nm nano-powder, 99.5% trace metals basis) were used in this study. All the chemicals and supports used in this study were procured from Millipore Sigma, U.S.A. unless stated otherwise. IrO_x, hereafter called IrO_x TKK (PN: ELC-0110 SA = 100), was supplied by Tanaka Kikinzoku Kogyo, Japan. The supplier stated that IrO_x TKK has an Ir content of 75.23% and a surface area of 100 $m^2 \cdot g^{-1}$.

Following the impregnation of the precursor on the support, the catalyst was dried in a vacuum furnace at 21°C and <10 mm Hg pressure. Then this catalyst was ground to a powdered form prior to calcination at 400°C for 2 h in a muffle furnace.[66], [247] After the 2 h temperature hold, the catalysts were allowed to cool down and were stored in the oven at 60°C. The powdered samples were then ground to produce finely powdered samples and then stored in air-tight sample vials.

The unsupported IrO_x catalyst was synthesized by adding Milli-Q water (18.2 MΩ.cm) water to the precursor to form a homogeneous solution, drying this solution under the aforementioned vacuum oven and then calcining the mixture at 400°C for 2 hours in static air. The unsupported Ir oxide catalyst, $(IrO_2 + Ir)_U$, served as the scientific benchmark catalyst and was included in this study to understand the effect of supports. The elemental composition of Ir in the supported and unsupported catalyst was determined by performing SEM-EDX on the prepared powdered samples and has been reported in Table 2.2.

2.2.2 Materials characterization

Bright-field and dark-field transmission electron microscopy (TEM), selected area electron diffraction (SAED), and energy-dispersive X-ray analysis (EDX) in scanning mode (STEM) were conducted on a JEOL JEM Atomic Resolution ARM 200cf S/TEM at the accelerating voltage of 200 kV. TEM-EDX was used for the local nanostructure study of the catalysts. In order to prepare the TEM sample, a dilute solution of the catalysts was prepared in Milli-Q water. Approximately 10 μL of the ink was drop-casted on the TEM grids with Ultrathin Carbon Film on Lacey Carbon Support Film, 400 mesh, Copper (Ted Pella, P.N. 01824). The grid was allowed to dry for 24 hours at room temperature. The average diameter and the standard deviation were calculated by counting over 160 particles using the ImageJ software.

To evaluate Ir composition in all of the powdered samples, energy dispersive X-Ray analysis (EDX) was used coupled to scanning electron microscope (SEM). Quanta 250 Mineral Liberation Analyzer (FEI company) SEM fitted with a tungsten filament was equipped with Bruker Xflush (133 eV) detector for the elemental analysis. To maintain result consistency, the average composition was determined by calculating the mean of 10 distinct locations. Images and composition was taken at a magnification of 600x using an electron beam intensity of 25 keV. Conductive carbon tape was used to mount the finely powdered samples onto SEM sample stubs. Any excess powder was removed using N_2 spray gun before inserting it into the equipment.

X-ray diffraction (XRD) analysis was carried out on a Rigaku Ultima IV D/max-RB diffractometer with D/Tex Ultra detector with Fe Filter (K-beta filter) using Co radiation (λ= 0.178900 nm) operated at 38 kV and 38mA for $Ir_xZr_{(1-x)}O_2/ZrO_{2(L)}$ and $Ir_xZr_{(1-x)}O_y/ZrO_{2(S)}$. Data was converted using JADE MDI 9.6 software and phase identification was done using DIFFRAC.EVA software with the 2022/2023 ICDD PDF 4 + and PDF 4+/Organics databases. Rigaku Ultima IV (Nanofab) using Cu-Kα radiation (λ = 0.15406 nm) with scintillation counter plus graphite crystal monochromator or a Nickel K- filter, operated at 40 kV and 44 mA was used for the rest of the catalyst samples (IrO_x TKK, $(IrO_2 + Ir)_U$, and IrO_2/ATO). Continuous X-ray scans were carried out from 10° to 80° (5° to 80° for) with a step width of 0.02 and a scan speed of 1.2°/min. Refer to section A.1.3 for detailed information.

Photoemission measurements were performed in Kratos AXIS Ultra Imaging spectrometer with a 1486.6 eV Al K source. The XPS spectra were analyzed using CasaXPS, where all peaks were calibrated to the main C 1s signal at 284.8 eV. A Shirley-type background was applied and the peaks were fitted with a DS(0.05,230) SGL(55) profile and the satellite peaks were fitted using GL(0). All the Ir 4f peaks were constrained to a doublet separation of 3 eV, the area ratio of $4f_{7/2}$:$4f_{5/2}$ = 4:3,

and a doublet FWHM ratio of 1.

Inductively coupled plasma mass spectrometry (ICPMS) analysis was performed on Agilent 8800 Triple Quadrupole Inductively Coupled Plasma Mass Spectrometer with iridium limit of detection of 0.0002 ppb. The minimum measured concentration in this work was at least 0.4 ppb, which is 3 orders of magnitude higher than the detection limit.

N_2 adsorption–desorption measurements were carried out at 77 K using an Autosorb-iQ-XR for $ZrO_{2(L)}$. The specific surface area was calculated by the Brunauer– Emmett–Teller (BET) method.

Temperature-programmed desorption (TPD) and temperature-programmed reduction (TPR) experiments were performed in a Micromeritics AutoChem 2950 HP instrument equipped with an online Pfeiffer Vacuum Thermostar GSD 320 spectrometer. The mass spectrometer was calibrated for H_2O (m/z = 18), O_2 (m/z = 32), H_2 (m/z = 2) using an internal standard He (m/z = 4) before the following characterization experiments. All samples were treated in H_2O at 120 °C for 4 h in an autoclave. Then, 0.1 g of H_2O-treated iridium oxide sample was packed in a quartz U-tube and assembled into Autochem equipment. Prior to the TPD experiments, samples were treated in a flow of He at 120°C (50 mL/min) for 2 h to eliminate physically adsorbed H_2O molecules. During the 2 h wait time, mass spectrometer signal for He was stabilized. The TPD was performed from 120°C to 700°C with a desired ramping rate, for example, 5°C/min, in He (50 mL/min), while the concentrations of H_2O, O_2 and He were collected every 5 s by the mass spectrometer. TPD experiments were repeated at different ramping rates (β = 2, 3, 5, 7, 10, 15, 20°C/min) for all the samples. A new sample was used for each TPD ramping rate.

TPR experiments of the iridium oxide samples were performed with an 5% H_2/He gas mixture using the spent sample in H_2O and O_2-TPD analyses. The H_2 consumption and H_2O evolution were monitored by the mass spectrometer. After the sample was cooled down in He, TPR was started from room temperature to 500°C with a ramping rate of 10°C/min in 5% H_2/He gas mixture (20 mL/min); the sample was held at 500°C for 10 min. After reduction, the sample was cooled to room temperature in He.

2.2.3 Catalyst ink and electrode preparation

To prepare the working electrode, 9.5 mg of the catalyst powder was added to 1 mL of Milli-Q (deionized) water and 0.5 mL of isopropanol (IPA). The geometric loading of the total catalyst deposited on the working electrode was kept uniform for the three supported catalysts, $Ir_xZr_{(1-x)}O_y/ZrO_{2(S)}$, $Ir_xZr_{(1-x)}O_2/ZrO_{2(L)}$, and IrO_2/ATO, irrespective of Ir loading to mitigate mass transfer limitations. For $(IrO_2 + Ir)_U$, 3 mg of the catalyst powder was added to the ink solution, while for IrO_x TKK 2.4 mg of the catalyst powder was added to the ink solution. Nafion^{TM} (diluted to 5 wt.%, Ion Power) was added to this solution in a drop-wise manner (each drop = 10-20 μL). The total Nafion added to the ink corresponded to 15 wt.% of the total solid mass (support + IrO_x) suspended in the ink. The catalyst ink solution was then sonicated in an ultrasonic bath for 30 minutes followed by sonication using a probe sonicator (Qsonica S4000, 20 kHz 600 W, 2 min ON 1 min OFF, 5% amplitude) for 10 min. The total sonication time was selected to maintain a balance between homogeneous dispersion since longer irradiation could be detrimental to its composition and morphology, mainly due to cavitation and sonolysis phenomena.[248] In both cases (bath and probe sonication), the catalyst was sonicated in a 2 mL plastic vial steadily placed in an ice bath. This was done to avoid overheating of the ink since power ultrasound is known to yield a rapid increase in temperature ΔTs of up to 50°C per hour when starting from room temperature.[248]

Glassy carbon (Pine Instruments) disc electrode (diameter = 5 mm) embedded in a Teflon cylinder was used as the working electrode. The GC electrode was polished to a mirror-like finish before casting the ink, with polishing paper (Buehler, P.N. 40-7218) and 0.05 μm alumina oxide paste (Al_2O_3, supplied by Allied High Tech Products, P.N. 90-187505) in an ultrasonic bath (frequency 20kHz, 2 sec ON- 2 sec OFF) in water followed by alternate washing with ultrapure Milli-Q water (18.2 MΩ.cm) and IPA for 10 minutes each. The working electrode (GC) was cast by pipetting a 10 μL aliquot of catalyst ink on the glassy carbon surface to achieve geometric loading of 60 $\mu g_{Ir} \cdot cm^{-2}$. These values ultimately varied with the catalyst as loading was decided based on the targeted Ir composition of 20 wt.% in the supported catalysts. For clarity, the actual mass of Ir on GC, calculated on the basis of SEM-EDX results has been reported in the results. The working electrode was then dried using the rotational drying technique at 600 rpm under air for 1.5 hr to form uniform and reproducible films followed by drying in the oven at 60°C in air for 30 min.

2.2.4 Electrochemical measurements

Electrochemical measurements were carried out using a potentiostat (BioLogic Science Instruments SP-200) on a standard rotating-disk electrode (RDE) system (PINE Research MSR Rotator), and a three-electrode cell. Helical Pt wire electrode was used as the counter electrodes. Double-junction silver chloride (Ag/AgCl) electrode (supplied by Pine Research Instrumentation, Inc.) calibrated against reference hydrogen electrode (ET070 Hydroflex™, supplied by eDAQ) was used as a reference electrode to test IrO_x TKK and $Ir_xZr_{(1-x)}O_2/ZrO_{2(L)}$. The hydrogen reference electrode was used to test $Ir_xZr_{(1-x)}O_y/ZrO_{2(S)}$ and $(IrO_2 + Ir)_U$ catalysts. The reference electrode calibration data has been provided in Figure A.9.

Sulfuric acid (Optima grade, Fisher Scientific) diluted to 1.0 M H_2SO_4 with Milli-Q

water (18.2 MΩ.cm) was used as the electrolyte.[50] All electrochemical measurements were carried out at room temperature using research-grade gases N_2 and O_2 (99.999%, Praxair). The glassware was cleaned by storing it overnight in 1.0 M H_2SO_4, followed by multiple washes with deionized water.

The potentials are reported relative to the reversible hydrogen electrode (RHE) scale based on the equation. This is done to remove the impact of pH on applied potential as it ensures that the theoretical potential for OER remains constant, i.e., 1.23 V_{RHE}.[249] All the experiments were recorded in the potential corresponding to E vs. Ag/AgCl and have been reported in this paper after normalization to E vs. RHE using Equation 2.1:

$$E(V \text{ vs. RHE}) = E(Ag/AgCl) + 0.199 + (0.059 \times pH) \tag{2.1}$$

iR compensation at 85% was applied using Biologic EC-Lab software while recording LSV and CV. Cyclic voltammetry (CV) was carried out in a deoxygenated environment by saturating the electrolyte with N_2. CV is performed at a scan rate of 40 mV s^{-1} in an unstirred electrolyte unless stated otherwise.

All Ir samples were preconditioned prior to oxygen evolution reaction (OER) electrochemical testing by recording 500 cyclic voltammograms from 0 V_{RHE} to 1.53 V_{RHE} at a voltage scan rate of 500 mV·s^{-1}. This electrochemical preconditioning was followed by performing 5 CV from 0 V_{RHE}-1.53 V_{RHE} at the scan rate of 40 mV.s^{-1}. The ECSA was estimated by calculating the total anodic charges of the CV profile in the potential range of 0.4V_{RHE} -1.25 V_{RHE} with acceptable double-layer correction. The electrical charge constant associated with the anodic processes within this potential range was taken as 440 $\mu C \cdot cm_{ECSA}^{-2}$.[6] The entire process of calculating ECSA has been previously discussed in the work of Tan et al.[6] Further information regarding the estimation of charges can be obtained from the following references.[107], [126],

[250]

Anodic linear sweep voltammetry (LSV) was performed between 1.0 V_{RHE} and 1.6 V_{RHE} in an O_2-saturated environment to measure the OER at a rotational speed of 1600 rpm and a scan rate of 10 $mV \cdot s^{-1}$. The potential range was selected to curtail the effect of change in hydrogen concentration at lower potentials. To ensure O_2 saturation, the electrolyte was continuously bubbled with research-grade O_2 for 10 minutes (99.999%, Praxair).

The corrosion stability of the electrocatalysts was evaluated using chronoamperometry (CA) at 1.6 V_{RHE} under O_2 saturated environment at a rotational speed of 1600 rpm. The potential is deliberately selected to mitigate GC electrode surface passivation.[190] Catalysts' stability evaluation under identical electrode potential ensures that they are fairly exposed to similar electrooxidative conditions. Potentiostatic operando electrochemical impedance spectroscopy was performed before, during, and after each CA cycle to investigate the change in charge transfer resistance (R_{ct}). EIS was measured at the potential of CA in the frequency range of 200 kHz to 30 mHz, with a potential perturbation amplitude of 10 mV. The diameter of the semicircle observed in the high-to-medium frequency region is representative of the charge transfer resistance of the electrocatalytic OER.

A combination of CA, EIS and CV analyses, was used to understand the effect of catalyst deactivation on charge transfer resistance and the ability of catalyst regeneration.[6] The stability test protocol is described as follows: Catalyst stability was measured by performing CA at 1.6 V_{RHE} for 2 hours in an O_2-saturated environment with the electrode rotating at 1600 rpm. One CV cycle was performed every 30 minutes to clean the surface of the catalyst in the potential range of 0 V_{RHE}-1.53 V_{RHE} was performed initially at t=0, and then periodically after every 30 minutes in

Table 2.1: Properties of commercial $ZrO_{2(L)}$, $ZrO_{2(S)}$ and ATO used in the study

Support	Average particle size (nm) [a]	Specific surface area ($m^2.g^{-1}$)
$ZrO_{2(L)}$	<5000	4 [b]
$ZrO_{2(S)}$	<100	25 [a]
ATO	<50	47 [a]

[a] Provided by a commercial supplier, Sigma Aldrich [b] Measured by BET analysis. The isotherm is reported in Figure A.1.

the cycle. After every CA cycle (2 h), the process of bubble removal was initiated, where the working electrode rotated at 1600 rpm for 30 min at zero current under atmospheric conditions. At the end of every 2 hour cycle, the catalyst was then regenerated by performing 20 CV cycles in the potential range of 0 V_{RHE}-1.53 V_{RHE} in an N_2-saturated environment without stirring. The electrochemical cell was saturated with N_2 gas bubbling for 10 minutes prior to the regeneration steps.

2.3 Results and discussion

2.3.1 Materials characterization

Transmission electron microscopy (TEM) and selected area electron diffraction (SAED)

TEM images of the catalysts are shown in Figure 2.1 and Figure A.2. The measurement process for determining the diameter of individual IrO_x particles (d_i) was guided by utilizing the grain boundary (crystal lattice) of the particles in high-resolution TEM images, as shown by yellow circles in Figure 2.1. d_i was used to calculate the mean volume diameter ($đ_{vol}$) of IrO_x particles as described in Equation A.1.

The $đ_{vol}$ reported for different samples were as follows: 4.5 ± 3.5 nm for $Ir_xZr_{(1-x)}O_y$/$ZrO_{2(S)}$, 3.7 ± 3.3 nm for $Ir_xZr_{(1-x)}O_2$/$ZrO_{2(L)}$, 1.5 ± 0.7 nm for IrO_2/ATO, 30.3 nm

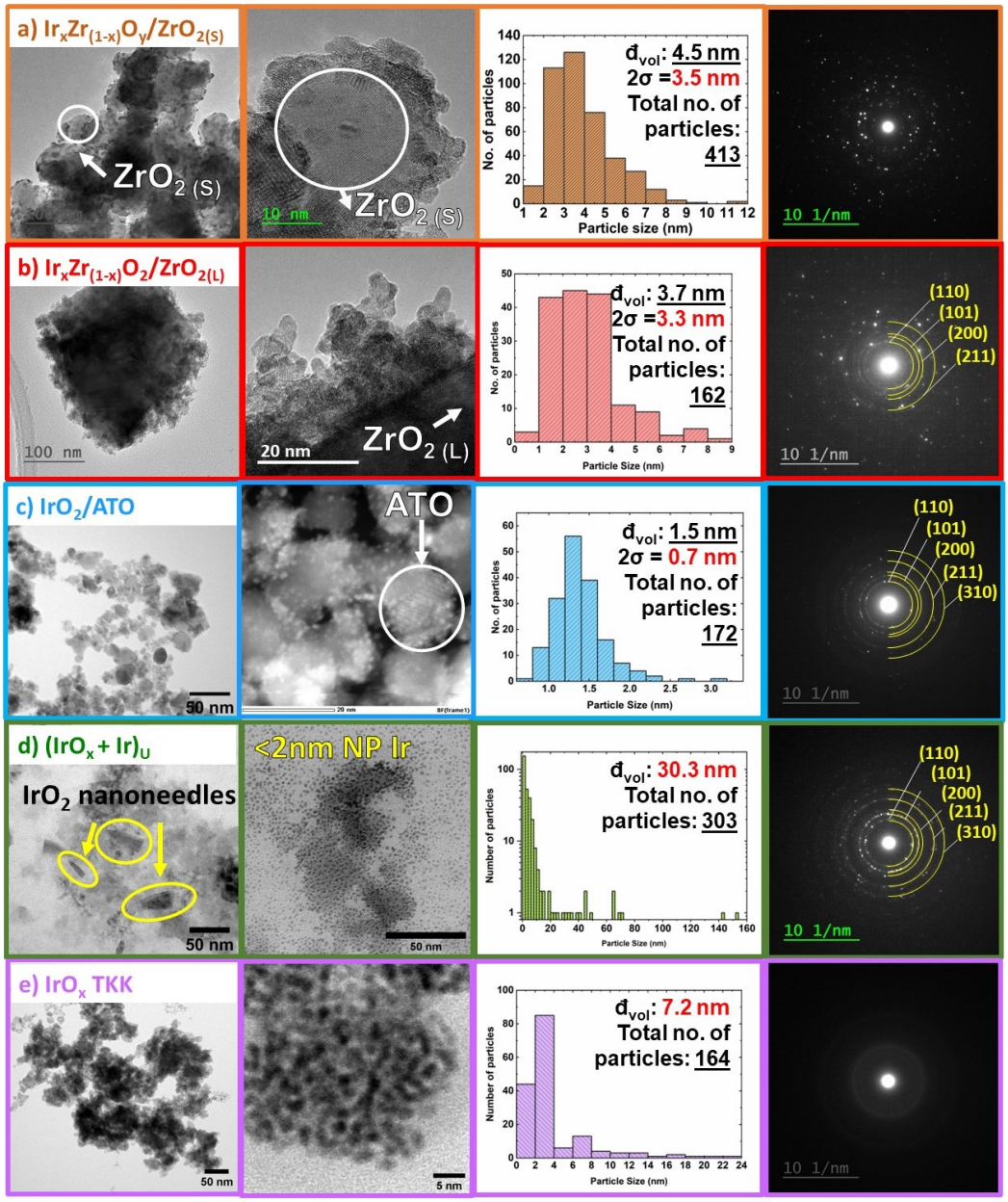

Figure 2.1: TEM images, IrO_x size distribution histograms, and SAED patterns of (a) $Ir_xZr_{(1-x)}O_y/ZrO_{2(S)}$, (b) $Ir_xZr_{(1-x)}O_2/ZrO_{2(L)}$, (c) IrO_2/ATO, (d) $(IrO_2 + Ir)_U$, and (e) IrO_x TKK, where $\bar{d}_{vol}$ is the volume-mean particle size of IrO_x and σ is the associated standard deviation (2σ represents the corresponding associated 95% confidence interval).

for $(IrO_2 + Ir)_U$, and 7.2 nm for IrO_x TKK. Note that the standard deviation could be calculated only for particle size distribution histograms following the normal distribution and not for right-skewed histograms, IrO_x TKK and $(IrO_2 + Ir)_U$.

Figure 2.1 (a) shows the TEM images of IrO_x dispersed on $ZrO_{2(S)}$ nanoparticles. The nanoparticles tend to form a short-ranged network of IrO_x over $ZrO_{2(S)}$ support. The SAED pattern of $Ir_xZr_{(1-x)}O_y/ZrO_{2(S)}$ could not be identified as a single phase.

Figure 2.1 (b) shows the microstructure of IrO_x deposited on $ZrO_{2(L)}$. Multiple layers of distinct IrO_x nanoparticles that are potentially porous, seem to cover a majority of the external surface area of $ZrO_{2(L)}$ support. Notwithstanding the considerable difference in particle size and specific surface area of $ZrO_{2(L)}$ and $ZrO_{2(S)}$ supports, the volume mean particle size ($đ_{vol}$) of IrO_x deposited on them were relatively similar as reported in Figure 2.1 (a). The thickness of IrO_x layer enveloping the $ZrO_{2(L)}$ was estimated to be 28 nm as shown in Figure A.3. The SAED of $Ir_xZr_{(1-x)}O_2/ZrO_{2(L)}$ matched well with rutile IrO_2 as shown in Figure A.4.

The TEM-EDX analysis of Ir, O, and Zr was inconclusive due to the overlap between Ir and Zr at 2 keV, as shown in Figures A.5 and A.6.

Figure 2.1 (c) shows IrO_2 dispersed on ATO. The average particle size of IrO_2 nanoparticles was 1.5 ± 0.7 nm. IrO_2 nanoparticles were uniformly distributed over the surface of the ATO support. In contrast to $Ir_xZr_{(1-x)}O_2/ZrO_{2(L)}$ and $Ir_xZr_{(1-x)}O_y/ZrO_{2(S)}$, where the IrO_x particles exhibit a network-like arrangement on the support, the dispersed IrO_x particles on the higher surface area ATO (with an SSA of 47 $m^2 \cdot g^{-1}$) did not. The ring pattern observed through SAED also corresponds to that of rutile IrO_2, as shown in Figure A.4.

$(IrO_2 + Ir)_U$ catalyst exhibited a bimodal particle size distribution, containing two distinct types of particles: nanoparticles with sizes <2 nm and large needle-shaped structures, as depicted in Figure 2.1 (d). The nanoneedles accounted for 49% of the 303 particles recorded in the TEM images obtained for this study. The volume mean diameter of $(IrO_2 + Ir)_U$ ($đ_{vol} \leq$ 30 nm) was greater than for for any supported catalyst. The SAED patterns of $(IrO_2 + Ir)_U$ matched with the rutile IrO_2 structure (Figure A.4).

As shown in Figure 2.1 (e), IrO_x TKK possessed a more uniform particle size distribution with > 78 % of the particles being less than 4 nm in diameter based on the trend observed from 164 particles recorded in the TEM images. IrO_x particles were well connected and porous in nature, in accordance with the high BET surface area of the catalyst. (SSA of 100 $m^2 \cdot g^{-1}$).[6] The SAED pattern of IrO_x is X-ray amorphous and shows a single ring that is very diffused, which is in line with literature data for IrO_x TKK.[6]

The TEM results indicate that the incorporation of support, irrespective of its nature and size, led to a more uniform particle size distribution of IrO_x which is supported by comparing the skewness of the particle size distribution histograms of supported and unsupported catalysts as shown in Figure 2.1. All the histograms were skewed to the right, however, the increasing order of skewness can be represented in the following trend: $Ir_xZr_{(1-x)}O_2/ZrO_{2(L)} < Ir_xZr_{(1-x)}O_y/ZrO_{2(S)} < IrO_x/ATO < IrO_x$ TKK $< (IrO_2 + Ir)_U$.

X-ray diffraction (XRD)

XRD was performed for all five fresh catalysts that were calcined at 400°C in the air, except IrO_x TKK. The results for IrO_x/ZrO_2 and IrO_2/ATO samples are shown in Figure 2.2, Figure 2.3, and Figure 2.4. For $(IrO_2 + Ir)_U$ and IrO_x TKK samples, the

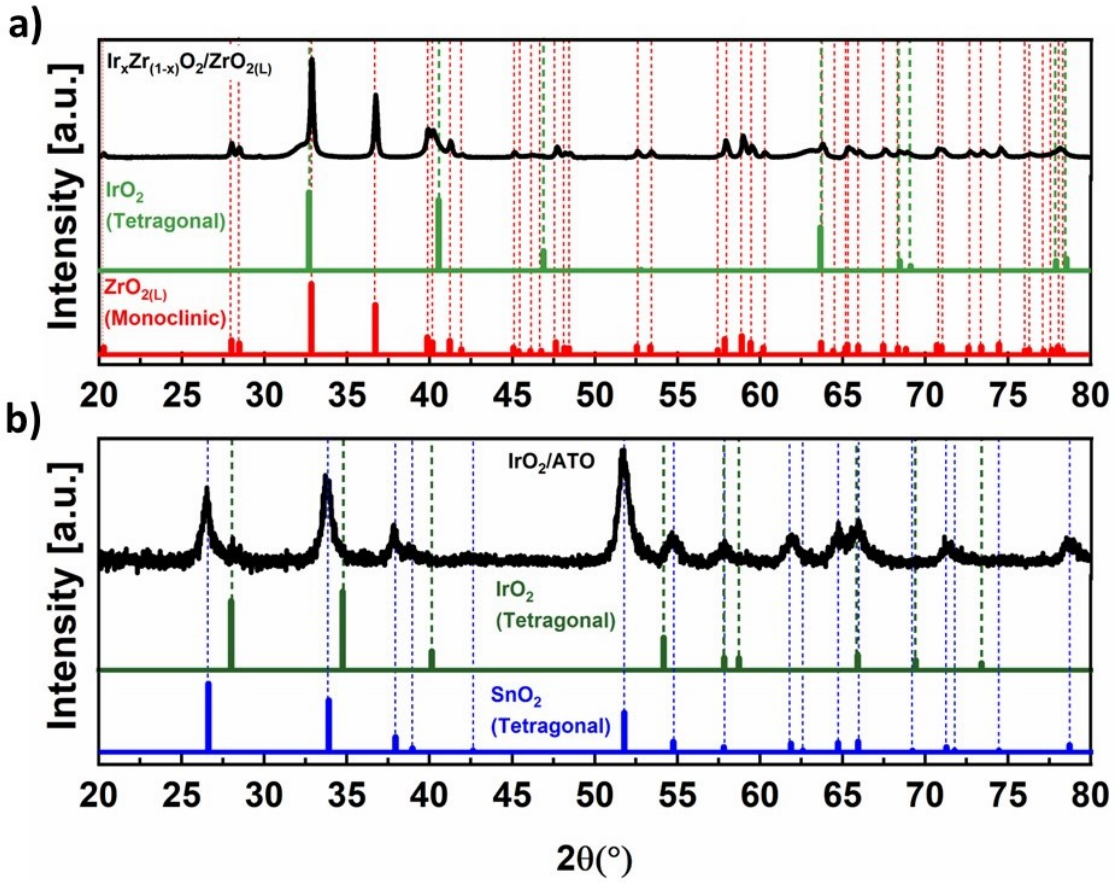

Figure 2.2: XRD diffraction peaks: (a) $Ir_xZr_{(1-x)}O_2/ZrO_{2(L)}$. References for ZrO_2 (PDF 04-004-4339, X-ray: Co radiation, (λ= 0.178900 nm)), IrO_2 (PDF 00-015-0870, X-ray: Co radiation, (λ= 0.178900 nm)); (b) IrO_2/ ATO. References for SnO_2 (PDF 00-041-1445, X-ray: Cu-Kα radiation (λ = 0.15406 nm)) and IrO_2 (JCPDS 15870, X-ray: Cu-Kα radiation (λ = 0.15406 nm)). Selected enlarged regions are shown in Figure 2.3.

results are shown in Figure A.7. The diffraction pattern of $(IrO_2 + Ir)_U$ corresponds to the crystallographic structure of tetragonal IrO_2, with two peaks corresponding to Ir. For IrO_x TKK, the observed peak broadening in XRD and SAED pattern (Figure 2.1 (e)) suggests the presence of an amorphous structure and its profile matches the quasi-amorphous Ir(III)/Ir(IV) oxide species reported in the literature.[6], [75], [101], [251]

Strong metal support interactions (SMSI) were identified in the diffraction pat-

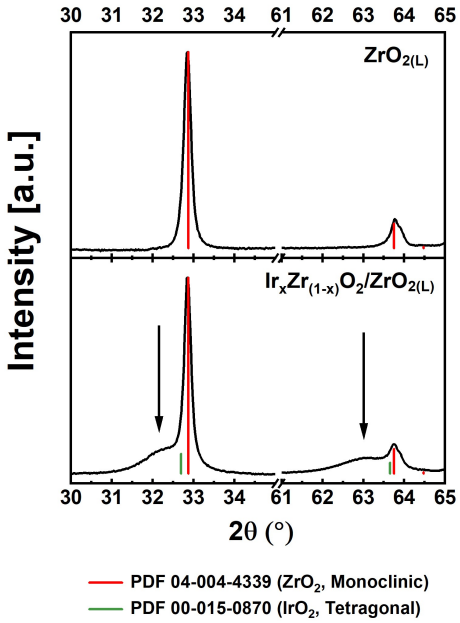

Figure 2.3: XRD diffraction peak of (a) ZrO_2 (top) and $Ir_xZr_{(1-x)}O_2/ZrO_{2(L)}$ (bottom) calcined at 400°C for 2h. Arrows show peak shift of IrO_2 in $Ir_xZr_{(1-x)}O_2/ZrO_{2(L)}$ References for ZrO_2 (PDF 04-004-4339, X-ray: Co radiation, (λ= 0.178900 nm)) and IrO_2 (PDF 00-015-0870, X-ray: Co radiation, (λ= 0.178900 nm)).

tern of $Ir_xZr_{(1-x)}O_2/ZrO_{2(L)}$ catalyst. As seen in Figure 2.2 (a), $Ir_xZr_{(1-x)}O_2/ZrO_{2(L)}$ demonstrated the emergence of new peaks at lower diffraction angles, to the left of the expected IrO_2 peak position. Figure 2.3 illustrates the two most significant peak shifts observed in $Ir_xZr_{(1-x)}O_2/ZrO_{2(L)}$. A comparison is made between the peak characteristics of monoclinic $ZrO_{2(L)}$ calcined at 400°C in the air for 2 hours and those of the $Ir_xZr_{(1-x)}O_2/ZrO_{2(L)}$ catalyst. This comparison helps to verify that any observed shift is due to the synthesized catalyst and not the $ZrO_{2(L)}$ support. Kondoh et al. also observed a similar peak on the left side of the established ZrO_2 peak, resulting from the incorporation of larger Y ions in a solid solution due to the lattice distortion of ZrO_2.[252] Similarly, in $Ir_xZr_{(1-x)}O_2/ZrO_{2(L)}$, the deviation of the IrO_2 peak to lower diffraction angles also suggests the expansion of the IrO_2 lattice due to the introduction of larger Zr ions.[241], [253], [254] The theory of solid solutions suggests that a substitutional-type solid solution can be formed when creating alloys,

given that the difference in radius between the solute and solvent is less than 15%. In this particular scenario, the ionic radius of Ir^{4+} is 62.5 pm, while Zr^{4+} has a radius of 72 pm, resulting in a disparity of 15.3%.[241], [255], [256] Thus, it is plausible that a substitutional-type solid solution, $Ir_xZr_{(1-x)}O_2$, is formed during the synthesis process. $Ir_xZr_{(1-x)}O_2$ alloy formation with different Ir:Zr ratios was also confirmed by first-principles calculations,[241] and experimentally by thermal decomposition of Ir and Zr precursors in the air at 400°C by Shao et al. and Liu et al.[240], [241] Furthermore, this peak shift was not identified in IrO_2/ATO sample. The diffraction profile of IrO_2/ATO predominately resembles that of tetragonal SnO_2 with shoulder peaks of tetragonal IrO_2 that were identified at their anticipated peak positions, as shown in Figure 2.2 (b), suggesting that no alloy was formed in IrO_2/ATO samples.

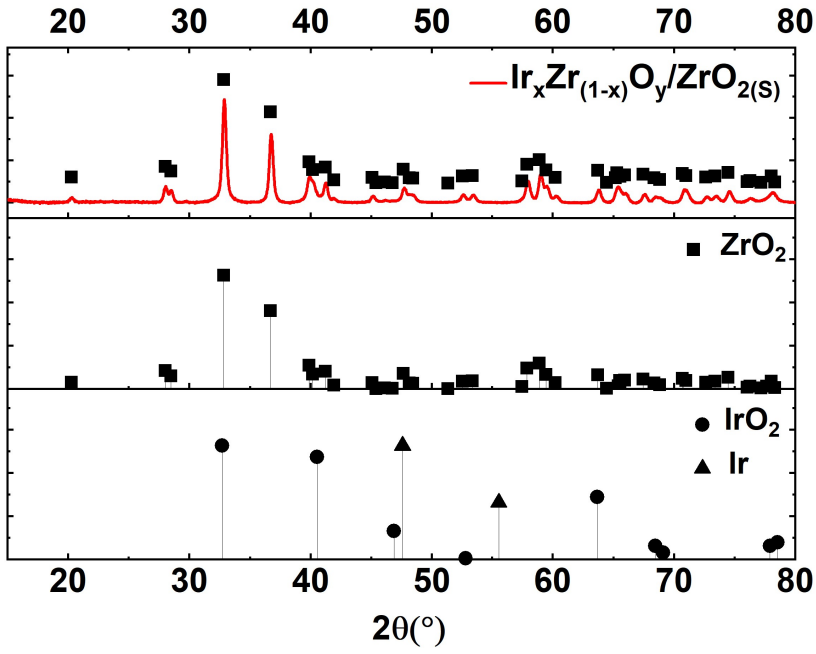

Figure 2.4: XRD diffraction pattern of $Ir_xZr_{(1-x)}O_y/ZrO_{2(S)}$. References for ZrO_2 (PDF 04-004-4339, X-ray: Co radiation, (λ= 0.178900 nm)), IrO_2 (PDF 00-015-0870, X-ray: Co radiation, (λ= 0.178900 nm)), and Ir (PDF 00-006-0598, X-ray: Co radiation, (λ= 0.178900 nm)).

In $Ir_xZr_{(1-x)}O_y/ZrO_{2(S)}$, where a larger surface area $ZrO_{2(S)}$ supports a thinner

layer of IrO_2 compared to $ZrO_{2(L)}$, the IrO_2 peaks were absent, as shown in Figure 2.4. The lack of definitive SAED results also makes it difficult to characterize $Ir_xZr_{(1-x)}O_y/ZrO_{2(S)}$. It is, however, plausible that the amorphous IrO_x was formed in $Ir_xZr_{(1-x)}O_y/ZrO_{2(S)}$. Shao et al., reported that in IrO_2-ZrO_2 binary alloy system, the presence of ZrO_2 restricted the crystal growth of IrO_2, leading to an increase in the extent of the amorphous IrO_x phase as the content of ZrO_2 increased. [241]

In summary, the effect of SMSI was manifested differently in both $Ir_xZr_{(1-x)}O_y/ZrO_{2(S)}$ and $Ir_xZr_{(1-x)}O_2/ZrO_{2(L)}$ samples. In $Ir_xZr_{(1-x)}O_2/ZrO_{2(L)}$, tetragonal IrO_2 peaks were identified along with monoclinic ZrO_2, albeit at a lower diffraction angle. In $Ir_xZr_{(1-x)}O_y/ZrO_{2(S)}$, no IrO_2 peaks were observed, a phenomenon previously associated with alloy formation in the literature. These findings align well with the SAED patterns of both catalysts. Importantly, it is worth noting that no such anomaly was observed in IrO_2/ATO, indicating the absence of SMSI in that case.

X-ray photoelectron microscopy (XPS) of fresh catalysts

XPS analysis was performed both for fresh and used catalyst samples, the latter is discussed in Catalyst stability section. For fresh samples, XPS analysis was used to identify the possible differences in the Ir oxidation state on the catalyst surface. Peak deconvolution was performed using an established doublet fit, as shown in Figure 2.5 and described in detail in the Experimental section. The analysis revealed that irrespective of the amorphous or crystalline structure observed using TEM and XRD, the surface of all the supported catalysts and IrO_x TKK were found to be composed of a mixture of Ir(IV) and Ir(III) species. $Ir_xZr_{(1-x)}O_y/ZrO_{2(S)}$ was composed of approximately 48% Ir(IV) species and 52% Ir(III) species, while $Ir_xZr_{(1-x)}O_2/ZrO_{2(L)}$and IrO_x TKK were composed of 57% Ir(IV) and 42% Ir(III) species. The species distribution is similar given the uncertainty of deconvolution. IrO_2/ATO was composed of 54% Ir(IV) species and 46% Ir(III) species. Previous studies in the literature have

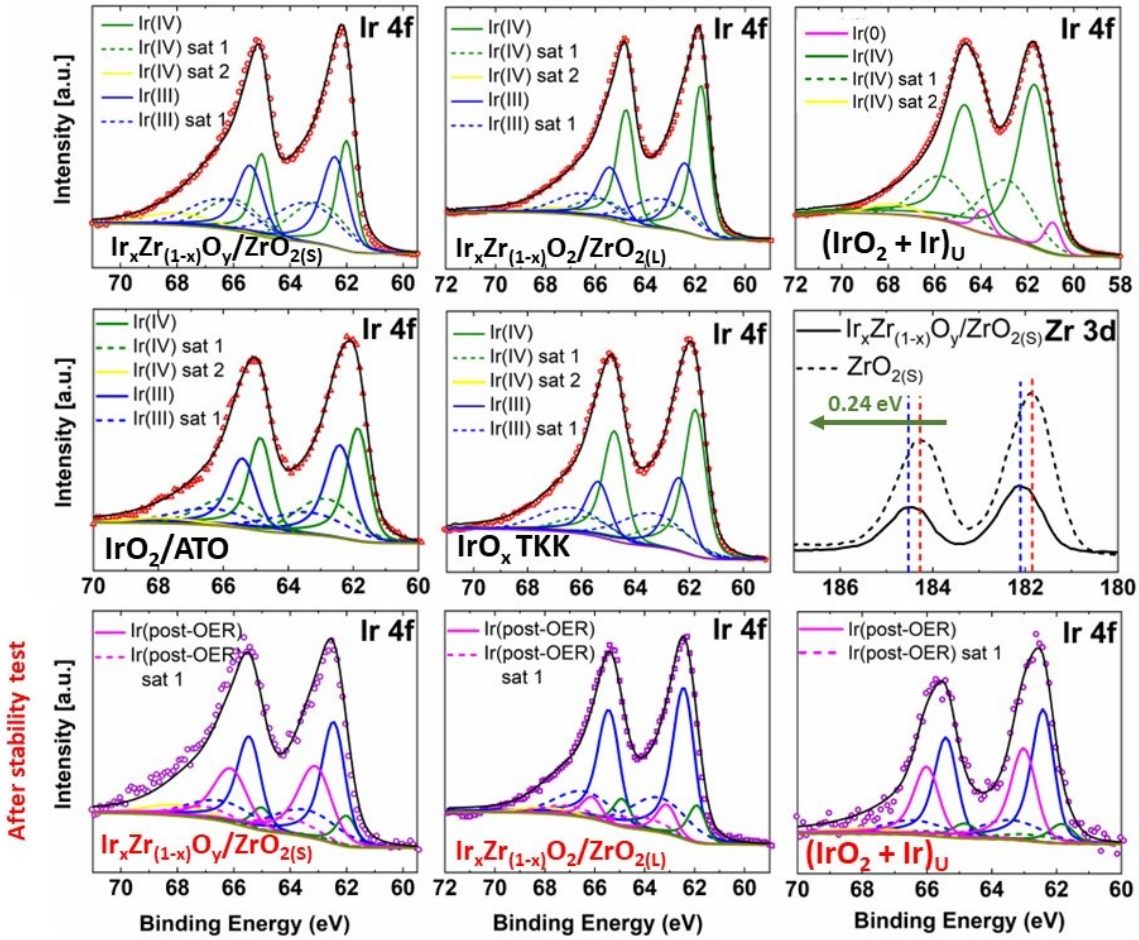

Figure 2.5: XPS spectra of the fresh and spent (after stability test) catalysts. All the samples except IrO_x TKK have been calcined in air at 400° for 2 h. The fit parameters have been reported in section A.1.4.

indicated that having a mixed oxidation state of Ir, especially Ir(III)/Ir(IV), can be beneficial in improving the performance of OER.[75], [134], [257], [258] $(IrO_2 + Ir)_U$ was predominantly composed of Ir(IV) with a minor presence of Ir(0). Tables A.1-A.5 contain the quantitative values of various Ir oxidation states and their corresponding satellite peaks for all the catalysts.

XPS was also used to assess the presence of SMSI between IrO_x and ZrO_2 in both the $Ir_xZr_{(1-x)}O_2/ZrO_{2(L)}$ and $Ir_xZr_{(1-x)}O_y/ZrO_{2(S)}$. For this purpose, changes in the Zr 3d binding energy (B.E.) profiles of $Ir_xZr_{(1-x)}O_y/ZrO_{2(S)}$ and $ZrO_{2(S)}$ were investigated, as shown in Figure 2.5 (f). A shift of +0.24 eV towards higher B.E. was observed in the Zr 3d peak of $Ir_xZr_{(1-x)}O_y/ZrO_{2(S)}$ compared to that of $ZrO_{2(S)}$. This observation implied that electron transfer occured from Zr to Ir. The ionization energy values of 6.63 eV for Zr and 9.1 eV for Ir are in line with the direction of electron transfer from Zr to Ir.[259], [260] A similar, but less pronounced shift (+0.14 eV) was also noticed in the Zr 3d peak of $Ir_xZr_{(1-x)}O_2/ZrO_{2(L)}$, as depicted in Figure A.8. A greater shift in the binding energy of Zr showed a direct correlation with the Ir(III) to Ir(IV) ratio in both the $Ir_xZr_{(1-x)}O_y/ZrO_{2(S)}$ and $Ir_xZr_{(1-x)}O_2/ZrO_{2(L)}$ samples. Since there was a more significant charge transfer from $ZrO_{2(S)}$ to IrO_x in the $Ir_xZr_{(1-x)}O_y/ZrO_{2(S)}$ compared to the $Ir_xZr_{(1-x)}O_2/ZrO_{2(L)}$ sample, a higher proportion of Ir(III) species was observed in the $Ir_xZr_{(1-x)}O_y/ZrO_{2(S)}$ sample as opposed to the $Ir_xZr_{(1-x)}O_2/ZrO_{2(L)}$ sample.

In summary, the findings from SAED, XRD, and XPS analyses collectively indicate the existence of SMSI between IrO_x and ZrO_2 supports in the fresh catalysts, albeit in different capacities. Ir oxide phase in $Ir_xZr_{(1-x)}O_2/ZrO_{2(L)}$ sample exhibits a SAED pattern resembling that of IrO_2, suggesting the presence of a rutile oxide phase. From XRD, the noticeable peak shift to a lower angle, compared to that of IrO_2, indicates lattice expansion of the rutile oxide. This is induced by significant Zr incorporation

Table 2.2: Summary of electrochemical properties of different catalysts studied in this work

Sample	Specific ECSA ($m^2 \cdot g_{Ir}^{-1}$)	Ir (wt.%)[a]	Tafel slope (mV/dec) [c]	j_{mass} at 1.60 V_{RHE} ($A \cdot g_{Ir}^{-1}$)	j_{ECSA} at 1.60 V_{RHE} ($mA \cdot cm_{Ir\ ECSA}^{-2}$)
$Ir_xZr_{(1-x)}O_y$/ $ZrO_{2(S)}$	11 ± 0.2	11.2 ± 0.6[a]	61 ± 1	290	2.6
$Ir_xZr_{(1-x)}O_2$/ $ZrO_{2(L)}$	15 ± 0.2	11.4 ± 0.3[a]	55 ± 0.5	712	4.8
IrO_x/ATO	6.5 ± 0.3	14.0 ± 0.3[a]	132 ± 0.5	24	0.4
$(IrO_2 + Ir)_U$	1 ± 0.1	62 ± 0.3 [a]	80 ± 3	11	1.1
IrO_x TKK	71 ± 0.5	75.2 [b]	49 ± 0.3	907	1.25

[a] Based on the elemental mapping of Ir performed on SEM-EDX; [b] Information provided by the supplier; [c] Within the potential window of 1.50 V_{RHE}-1.55 V_{RHE}. Data correspond to a 95% confidence level.

into the IrO_2 lattice as $Ir_xZr_{(1-x)}O_2$ alloy oxide. The argument of $Ir_xZr_{(1-x)}O_2$ alloy formation is well supported by the XPS results of both $Ir_xZr_{(1-x)}O_2/ZrO_{2(L)}$ and $Ir_xZr_{(1-x)}O_y/ZrO_{2(S)}$. The shift of Zr binding energy to a higher value, compared to bare ZrO_2, is attributed to the electron transfer from Zr to Ir in the $Ir_xZr_{(1-x)}O_2$ alloy oxide. Accepting electrons from Zr lowers the oxidation state of Ir in the rutile alloy oxide, creating a rich amount of Ir(III)/Ir(IV) active species throughout the oxide phase, a precursor to high activity in OER catalysts. The enhancement of OER activity caused by IrO_2-ZrO_2 alloys has also been discussed in the literature.[241] In contrast, similar alloy oxide formation is not observed in the IrO_2/ATO sample. The IrO_2/ATO serves as a baseline without spontaneous alloy oxide formation.

2.3.2 Electrochemical characterization

Initial electrochemical surface area (ECSA) of the catalysts

The electrocatalysts studied in this work were cleaned and activated prior to evaluation by performing 500 preconditioning cycles involving cyclic voltammetry (CV) in an N_2-saturated environment in an unstirred electrolyte (1.0 M H_2SO_4) at a scan

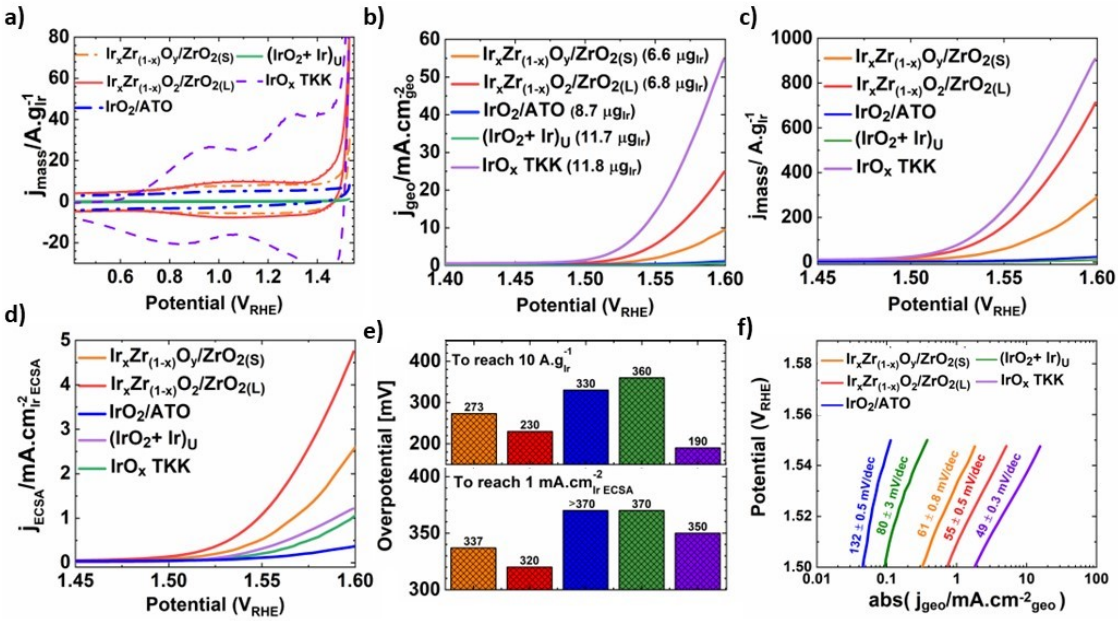

Figure 2.6: (a) Initial cyclic voltammogram (normalized by initial mass of Ir) of $Ir_xZr_{(1-x)}O_y/ZrO_{2(S)}$, $Ir_xZr_{(1-x)}O_2/ZrO_{2(L)}$, IrO_2/ATO, $(IrO_2 + Ir)_U$, and IrO_x TKK with the upper potential limit of 1.53 V_{RHE}, (b) iR-corrected OER polarization curves normalized to the geometric area, (c) iR-corrected OER polarization curves normalized to the mass of Ir, (d) iR-corrected OER polarization curves normalized to Ir ECSA, (e) Overpotential to reach 10 $A{\cdot}g_{Ir}^{-1}$ (top), and 1 $mA{\cdot}cm_{Ir\ ECSA}^{-2}$(bottom) (f) Tafel slopes.

rate of 500 $mV{\cdot}s^{-1}$ in the potential range of 0 V_{RHE}-1.53 V_{RHE}. The preconditioning step served the dual purpose of cleaning the catalyst surface and forming highly active Ir(III)/Ir(IV) oxohydroxide species.[6], [51], [53], [261], [262] Keeping the upper potential limit at 1.53 V_{RHE} ensured surface oxidation of Ir to its irreducible oxide form.[6]

Figure 2.6 (a) shows the CV profiles of the catalysts recorded after preconditioning in the potential range of 0 V_{RHE}-1.53 V_{RHE} in N_2 saturated environment in an unstirred electrolyte solution at the scan rate of 40 $mV{\cdot}s^{-1}$. The ECSA of the catalysts was estimated using the total anodic charges under the CV (forward sweep) in the potential range of 0.4 V_{RHE}- 1.25 V_{RHE}. The methodology has been described in the work of Tan et al. [6] and Section A.2.3 (Equation A.2). The total charge accumu-

lated was then appropriately corrected for the double layer and for the shift along the normalized current density axis (y-axis), as shown in Figure A.10, prior to calculating the ECSA. The schematic in Figure A.11 illustrates the difference between the CV profiles of support and supported IrO_x catalyst. The adjusted area under the CV corresponded to the charge accumulated from the deprotonation of hydrous Ir oxide.

The ECSA of all the catalysts are reported in Table 2.2. IrO_x TKK exhibited a significantly higher ECSA than the other catalysts, i.e., 71 ± 0.5 $m^2 \cdot g_{Ir}^{-1}$, despite not having the smallest IrO_x particle size as reported previously in Transmission electron microscopy (TEM) and selected area electron diffraction (SAED) section. This can be attributed to the porous nature of the IrO_x clusters observed in IrO_x TKK shown in Figure 2.1 (e) and previously discussed by Tan et al.[6] Despite having a majority of particles less than 2 nm, $(IrO_2 + Ir)_U$ exhibited a considerably smaller ECSA than IrO_x TKK, i.e., 1 ± 0.1 $m^2.g_{Ir}^{-1}$. This is likely due to the presence of large crystalline IrO_x nanoneedles and the possible lack of electrical contact between the small IrO_x nanoparticles.

Synthesis of supported catalysts offered a higher surface area available for iridium dispersion and deposition, as demonstrated by the increase in the ECSA of the supported catalysts, $Ir_xZr_{(1-x)}O_2/ZrO_{2(L)}$, $Ir_xZr_{(1-x)}O_y/ZrO_{2(S)}$ and IrO_2/ATO, in comparison to their unsupported counterpart, $(IrO_2 + Ir)_U$. We observed, however, that an increase in the specific surface area of non-porous support ZrO_2, i.e., $ZrO_{2(S)}$ (25 $m^2 \cdot g^{-1}$) and $ZrO_{2(L)}$ (4 $m^2 \cdot g^{-1}$), did not necessarily lead to a proportionate increase in the ECSA. $Ir_xZr_{(1-x)}O_y/ZrO_{2(S)}$ and $Ir_xZr_{(1-x)}O_2/ZrO_{2(L)}$ exhibited similar average IrO_x particle sizes (4.5 ± 3.5 nm vs. 3.7 ± 3.3 nm) with $Ir_xZr_{(1-x)}O_y/ZrO_{2(S)}$ having only a slightly lower Ir ECSA (15 ± 0.2 $m^2 \cdot g_{Ir}^{-1}$ vs. 11 ± 0.2 $m^2 \cdot g_{Ir}^{-1}$), which aligns well with the larger particle size observed in $Ir_xZr_{(1-x)}O_y/ZrO_{2(S)}$. The TEM profiles of these supported catalysts, however, were markedly different. $Ir_xZr_{(1-x)}O_2/ ZrO_{2(L)}$

exhibited multiple layers of IrO_x nanoparticles deposited on top of each other, while for $Ir_xZr_{(1-x)}O_y/ZrO_{2(S)}$, IrO_x nanoparticles formed short-ranged networks on the surface of the support that were a monolayer thick. Hence, the larger ECSA observed in $Ir_xZr_{(1-x)}O_2/\ ZrO_{2(L)}$ was attributed to the presence of porous IrO_x nanoparticles supported on $ZrO_{2(L)}$.[263]

IrO_2/ATO exhibited the lowest ECSA among the supported catalysts, i.e., 6.5 $\pm$ 0.3 $m^2 \cdot g_{Ir}^{-1}$. The reason behind it could possibly be the support degradation during electrochemical testing. The preconditioning cycles in the potential window 0 V_{RHE}-1.53 V_{RHE} could have resulted in the degradation of ATO conductivity due to either dissolution of Sb or surface segregation of Sb and SnO_2.[162], [264], [265] Detailed information on this topic has been provided in the Initial electrocatalyst activity section.

Initial electrocatalyst activity

Linear sweep voltammetry (LSV) was used to investigate the activity of the electrocatalysts. OER polarization curves were measured at 1600 rpm in an O_2 saturated electrolyte in the potential window of 0 V_{RHE}-1.6 V_{RHE} at a scan rate of 10 $mV \cdot s^{-1}$. Figures 2.6 (b-d) show the iR-corrected OER polarization curves for all the catalysts. These curves can be treated as initial performance indicators for the electrocatalysts. Figure 2.6 (b) shows the activity of the catalyst normalized by the geometric surface area of the electrode. An identical quantity of solids (active metal + support) were deposited on the electrode, despite variations in Ir weight loading of the supported catalysts, to exclude any activity differences due to external mass transfer limitations. The mass of Ir deposited on the working electrode was mentioned in the legend, as shown in Figure 2.6 (b). The methodology for estimating Ir loading on the working electrode is described in section A.2.4 (Equations A.3 and A.4). The desired geometric loading is not identical in all the cases because the target Ir loading set during

synthesis for supported catalysts, i.e., 20 wt.% Ir was not achieved. After synthesis, the elemental compositions of Ir were not found to be consistent in all the catalysts, and it was measured to be between 11 wt.% and 14 wt.% based on SEM-EDX analysis on the powdered samples as reported in Table 2.2.

Figures 2.6 (c) and (d) show the mass normalized activity and intrinsic activity of all the catalysts. IrO_x TKK demonstrates the highest mass normalized activity, with values of 907 $A{\cdot}g_{Ir}^{-1}$ reported at 1.60 V_{RHE}. Following closely, $Ir_xZr_{(1-x)}O_2/ZrO_{2(L)}$ demonstrated a mass activity of 712 $A{\cdot}g_{Ir}^{-1}$ at the same potential. $Ir_xZr_{(1-x)}O_2/ZrO_{2(L)}$, however, showed the highest intrinsic activity. At 1.6 V_{RHE}, the intrinsic activity of $Ir_xZr_{(1-x)}O_2/ZrO_{2(L)}$ was 4.8 $mA{\cdot}\ cm_{Ir\ ECSA}^{-2}$, which was approximately four times greater than that of IrO_x TKK, i.e., 1.25 $mA{\cdot}cm_{Ir\ ECSA}^{-2}$. This suggested that the superior mass activity of IrO_x TKK could be attributed in part, to the catalyst's well-connected network of IrO_x and relatively high ECSA. The high mass and intrinsic activity of $Ir_xZr_{(1-x)}O_2/ZrO_{2(L)}$ could possibly be due to a combination of factors, including $Ir_xZr_{(1-x)}O_2$ alloy formation with enhanced bulk Ir(III) concentration, and a well-connected IrO_x network, both of which are necessary for an active catalyst. In comparison to other studies, the intrinsic activity of $Ir_xZr_{(1-x)}O_2/ZrO_{2(L)}$ is also among the highest in the literature, as shown in Figure 2.7 and Section A.3. However, we acknowledge that ECSA normalized activity is challenging to compare due to the different methods used in the literature to calculate ECSA.[6], [187], [195]–[201] A comprehensive literature review comparing the mass (specific) activity of $Ir_xZr_{(1-x)}O_2/ZrO_{2(L)}$ with other supported catalysts in the literature has been reported in Section A.3.

For non-conductive support such as ZrO_2, the significance of establishing a percolating conductive network of IrO_x becomes evident by comparing the performance of $Ir_xZr_{(1-x)}O_2/ZrO_{2(L)}$ and $Ir_xZr_{(1-x)}O_y/ZrO_{2(S)}$. Despite showcasing stronger evi-

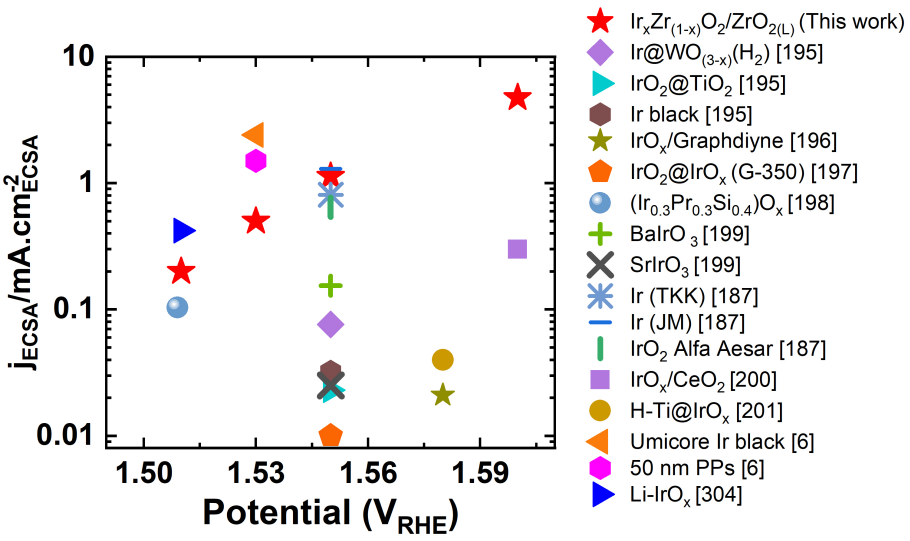

Figure 2.7: Comparison of the intrinsic activity of $Ir_xZr_{(1-x)}O_2/ZrO_{2(L)}$ catalyst with literature.

dence of SMSI and a high concentration of Ir(III) species detected by XPS known for its high electrocatalytic activity, $Ir_xZr_{(1-x)}O_y/ZrO_{2(S)}$ exhibits lower mass normalized activity (290 $A{\cdot}g_{Ir}^{-1}$ at 1.6 V_{RHE}) and intrinsic (2.6 $mA{\cdot}cm_{Ir\ ECSA}^{-2}$ at 1.6 V_{RHE}) activities compared to $Ir_xZr_{(1-x)}O_2/ZrO_{2(L)}$.[266] This is attributed to a lack of electrical conductivity. $Ir_xZr_{(1-x)}O_2/ZrO_{2(L)}$ showcased a continuous network of IrO_x nanoparticles that engulf $ZrO_{2(L)}$ particles while in $Ir_xZr_{(1-x)}O_y/ZrO_{2(S)}$, the IrO_x network is fragmented and short-ranged, due to the higher specific surface area of the $ZrO_{2(S)}$ support. The presence of a continuous conductive IrO_x network in the case of $Ir_xZr_{(1-x)}O_2/\ ZrO_{2(L)}$ might provide a continuous charge transport pathway which is crucial when using non-conductive supports, such as ZrO_2.[263], [267] A similar trend was observed by Manzur et al., where non-conductive TiO_2 with varying specific surface areas were used as support.[236] It is possible that $Ir_xZr_{(1-x)}O_y/ZrO_{2(S)}$ could achieve even better performance with higher Ir loading on the support since once a dense enough conductive Ir film is formed, good electrical conductivity could be achieved while maintaining more intimate contact with the support.

$(IrO_2 + Ir)_U$ and IrO_2/ATO, showed poor performance compared to the other catalysts. IrO_2/ATO yielded a mass normalized activity of 24 $A \cdot g_{Ir}^{-1}$ and intrinsic activity of 0.4 $mA \cdot cm_{Ir\ ECSA}^{-2}$ at 1.6 V_{RHE}. $(IrO_2 + Ir)_U$ exhibited 11 $A \cdot g_{Ir}^{-1}$ and 1.1 $mA \cdot cm_{Ir\ ECSA}^{-2}$ at 1.6 V_{RHE}. The poor mass normalized activity of $(IrO_2 + Ir)_U$ could be associated with the presence of large needle-shaped structures that cause a considerable decline in ECSA, and the occurrence of Ir in the (IV) oxidation state. Upon comparing the activity of the two unsupported catalysts, we found that $(IrO_2 + Ir)_U$ and IrO_x TKK have comparable intrinsic activities, and categorically different mass activities due to the high surface area of IrO_x TKK.

The subpar performance of IrO_2/ATO compared to $Ir_xZr_{(1-x)}O_2$/ $ZrO_{2(L)}$ and $Ir_xZr_{(1-x)}O_y/ZrO_{2(S)}$ suggests that supporting Ir on ATO did not lead to an improvement in performance. There are two potential reasons for this phenomenon: (a) there may be insufficient electrical conductivity due to the lack of a percolating IrO_x network, and (b) the commercial ATO support utilized in this study might be insufficiently conductive or unstable.

Regarding reason (a), since the difference in the extent of IrO_x dispersion on $ZrO_{2(L)}$ and $ZrO_{2(S)}$ impacted their electrochemical performance, it is plausible that the high dispersion observed for IrO_2/ATO might have affected its activity by virtue of lower connectivity between Ir oxideparticles. As shown in Figure 2.1 (c), it is evident that the Ir oxide nanoparticles are sparsely dispersed on the support. There has been extensive discussion in the literature regarding how the Ir oxide network contributes to improving the activity of supported catalysts. Ledendecker et al. showed that OER activity scales with the amount of iridium deposited on FTO with the mass-normalized activity of 20 deposition cycles matching the theoretical value of mass-normalized activity for one monolayer of rutile IrO_2.[141] Krivina et al. also reported increased activity with increased Ir loading for Sb/SnO_2 and F/SnO_2 con-

ductive oxides.[268]

In order to ascertain whether the underwhelming performance could be attributed in part to inadequate IrO_2 coverage on ATO, as opposed to the intrinsic properties of the resulting catalyst, we synthesized a higher loading of IrO_2 deposited on ATO support, 60 wt.% Ir in composition, as reported in Figure A.12 and Figure A.13. The mass activity of IrO_2/ATO (60 wt. % Ir) showed an order of magnitude reduction, due to the lower Ir dispersion and ECSA. However, the ECSA normalized activity remained unchanged, indicating that the OER mechanism remained unaffected. This suggests that the lack of a continuous IrO_2 film in 14 wt.% (Ir) IrO_2/ATO catalyst is not a dominating factor for its poor performance.

Regarding reason (b), Geiger et al. tested the stability limits of the sub-components of commercial ATO, i.e., Sb and Sn, and discovered that Sb and Sn were stable in the potential window 0.36 $V_{RHE} < E_{Sb} <$ 1.1 V_{RHE} and -0.29 $V_{RHE} < E_{Sn} <$ 1.45 V_{RHE}, respectively.[162] Beyond these potential windows, segregation of Sb and SnO_2 occurred. Given that the activity measurement follows 500 CV cycles within the potential range of 0 V_{RHE}-1.53 V_{RHE}, it is plausible that the support may have already experienced a loss in its structural stability and conductivity. In another study performed on ATO synthesized using the sol-gel route, Fabbri et al. reported a loss of Sb atoms from Sb-doped SnO_2 following an accelerated stress test (AST) comprising 1,000 potential cycles ranging from 0.5 V_{RHE} to 1.5 V_{RHE} in an O_2-saturated electrolyte.[264] The occurrence of Sb dissolution during the preconditioning cycles in this study is also possible, as the AST cycling window overlaps with the potential range of the aforementioned preconditioning cycles. The loss of Sb atoms from the ATO, either due to dissolution or segregation, would affect the support conductivity and restrict the capacity of IrO_x to exchange electrons with the ATO support, which is crucial for the activity of the catalysts supported on ATO. ATO-supported IrO_x catalysts

reported to have high activity [132], [139], [144], [232]–[234] are often self-synthesized with modified properties, such as adjusted porosity, [79], [231], [232] shape/structure, [138], [146] specific surface area, [79] conductivity [139] or composition.[147], [231] Our explanation suggests that modifications to the conductivity and stability of commercial ATO support, at least to the one used in this study, are necessary to produce IrO_2/ATO catalysts with higher activity. More successful performances reported in literature could be due to different synthesis and deposition methods, or a different Ir oxide phase.

Figure 2.6 (e) show the overpotential required to achieve the current density of 10 $A{\cdot}g_{Ir}^{-1}$, and 1 $mA{\cdot}cm_{Ir\ ECSA}^{-2}$. IrO_x TKK required the lowest overpotential to achieve 10 $A{\cdot}g_{Ir}^{-1}$, i.e., 190 mV, closely followed by $Ir_xZr_{(1-x)}O_2/ZrO_{2(L)}$, $Ir_xZr_{(1-x)}O_y/ZrO_{2(S)}$, IrO_2/ATO and $(IrO_2 + Ir)_U$ with overpotentials 230 mV, 273 mV, 330 mV and 360 mV respectively. To achieve 1 $mA{\cdot}cm_{Ir\ ECSA}^{-2}$, $Ir_xZr_{(1-x)}O_2/ZrO_{2(L)}$ required the lowest overpotential of 320 mV, followed by $Ir_xZr_{(1-x)}O_y/ZrO_{2(S)}$, IrO_x TKK, $(IrO_2 + Ir)_U$, and IrO_2/ATO with the overpotentials 337 mV, 350 mV, >370 mV, and 370 mV. Tafel slopes were also estimated in the potential window of 1.50 V_{RHE} -1.55 V_{RHE} as shown in Figure 2.6 (f). Tafel slopes of $Ir_xZr_{(1-x)}O_y/ZrO_{2(S)}$, $Ir_xZr_{(1-x)}O_2/ZrO_{2(L)}$, IrO_x TKK catalysts exhibit similar values in the range of 49-61 mV/dec in the potential window of 1.5 V_{RHE}-1.55 V_{RHE}. This indicates that the three aforementioned catalysts are likely to follow the same OER mechanism. However, $(IrO_2 + Ir)_U$, and IrO_2/ATO exhibit relatively higher Tafel slopes of 80 mV/dec and 132 mV/dec in the same potential window, suggesting a change in OER mechanism or limited charge transport.

From the initial catalyst activity analysis, we conclude that $Ir_xZr_{(1-x)}O_2/ZrO_{2(L)}$ performs exceedingly well compared to other synthesized catalysts. The high activity can be attributed to a well-connected system of $Ir_xZr_{(1-x)}O_2$ nanoparticles, and a

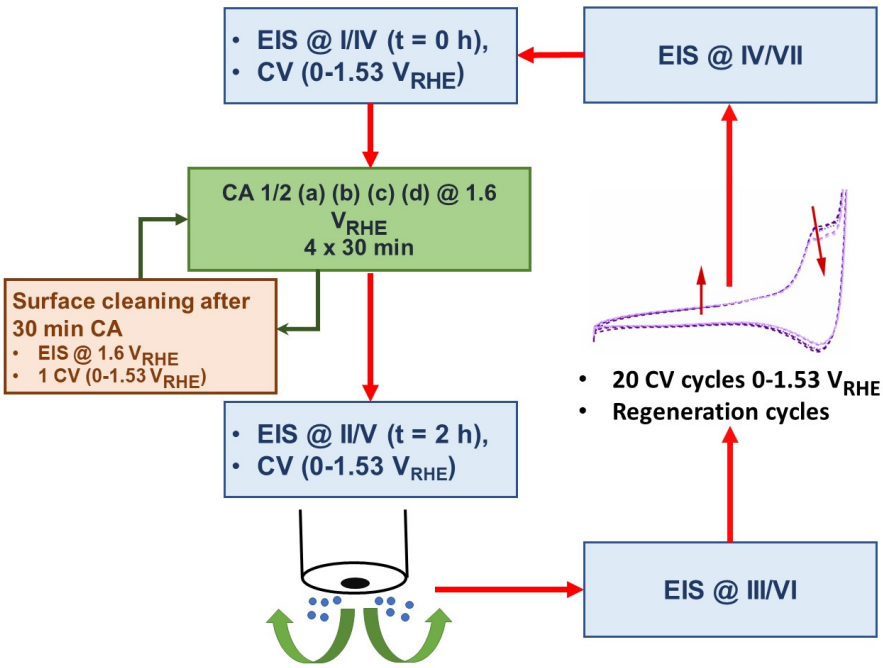

Figure 2.8: Stability test protocol- CA, EIS, bubble removal and CV regeneration cycle.

high concentration of Ir(III)/Ir(IV) OER relevant species present throughout the oxide, due to the formation of $Ir_xZr_{(1-x)}O_2$ alloy.

Catalyst stability

Chronoamperometry (CA), operando electrochemical impedance spectroscopy (EIS), and CV were used to evaluate catalyst stability by observing the drop in activity, the changes in charge transfer resistance (R_{ct}) with continuous exposure to a potential of 1.6 V_{RHE}, and the change in ECSA over each CA cycle respectively. The stability test procedure has been explained in detail in the experimental section and is shown in Figure 2.8. This study provides the stability results of IrO_x TKK, $Ir_xZr_{(1-x)}O_2/ZrO_{2(L)}$, $Ir_xZr_{(1-x)}O_y/ZrO_{2(S)}$, and $(IrO_2 + Ir)_U$.

Figure 2.9 (a) illustrates the normalized electrode current densities measured during two CA cycles, each 2 h long. The current densities are expressed in percentage

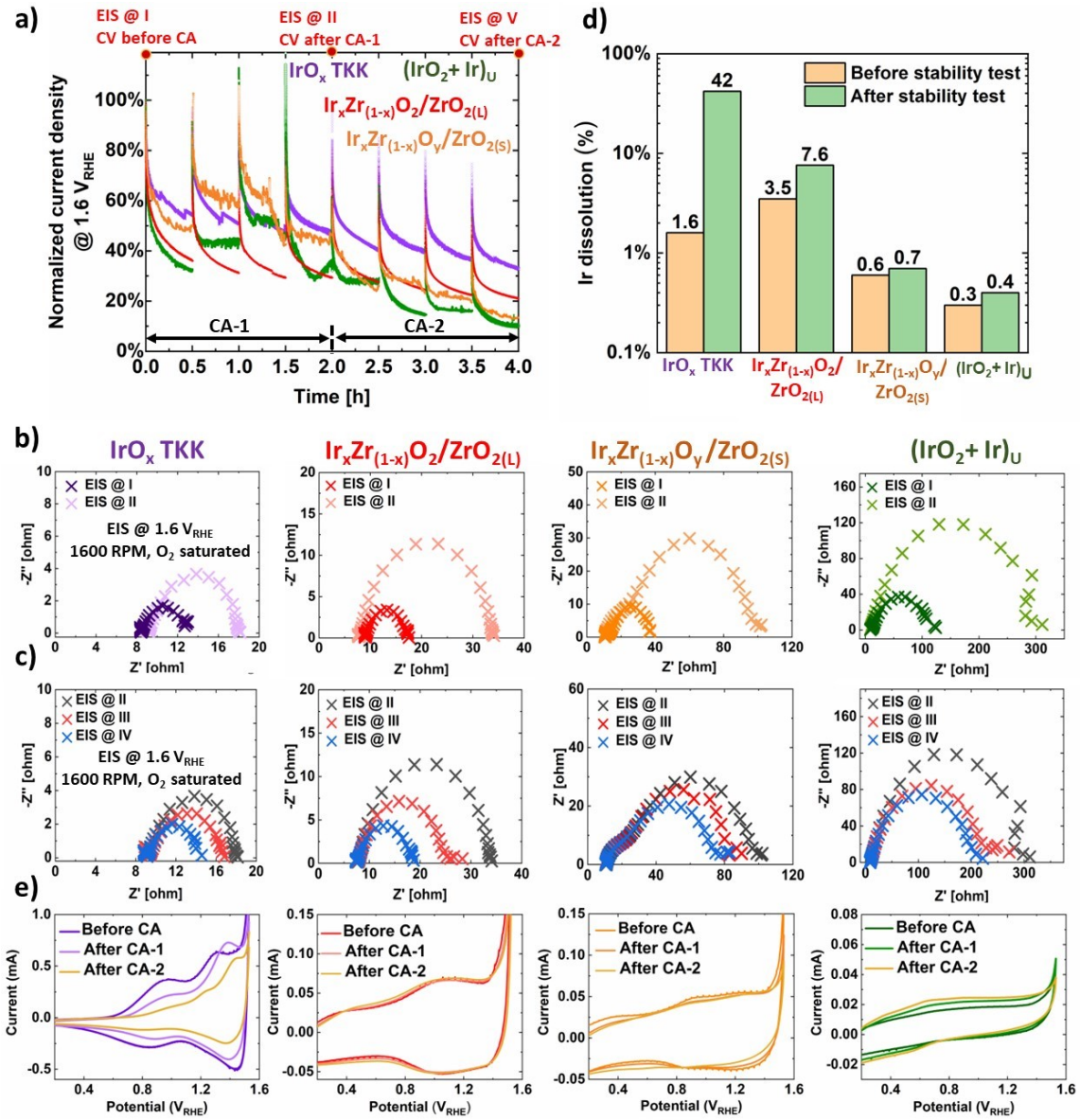

Figure 2.9: Catalyst stability of IrO_x TKK, $Ir_xZr_{(1-x)}O_2/ZrO_{2(L)}$, $Ir_xZr_{(1-x)}O_y/ZrO_{2(S)}$ and $(IrO_2 + Ir)_U$ evaluated by performing chronoamperometry (CA) at 1.6 V_{RHE}. a) Normalized current density measured as a function of time during controlled potential electrolysis. b) Electrochemical impedance spectroscopy (EIS), measured before (EIS @ I) and after (EIS @ II) the first 2 h CA analysis with minimal interference in the applied potential of the CA analysis. e) Partial recovery of charge transfer from the removal of accumulated microscopic bubbles and CV regeneration d) ICP-MS analysis of the Ir ion concentration from the electrolyte before and after the stability test. The percentage of Ir dissolution is normalized to the Ir mass on the working electrode available before stability test. e) CV profiles measured before CA-1 and after each 2 h CA analysis.

and have been normalized with respect to the current at the beginning of the stability test ($t = 0$ h). IrO_x TKK outperforms other catalysts, by maintaining approximately 40% of its activity at the end of the two CA cycles. In comparison, the performance of the other synthesized catalysts, both supported and unsupported, was inferior. $Ir_xZr_{(1-x)}O_y/ZrO_{2(S)}$ activity did not decline in the first CA cycle; but, it experienced a substantial decrease in activity during the second cycle. Both $Ir_xZr_{(1-x)}O_2/ZrO_{2(L)}$ and $(IrO_2 + Ir)_U$ showcased lower stability than the other catalysts over the two CA cycles. The noise observed in $Ir_xZr_{(1-x)}O_y/ZrO_{2(S)}$ and $(IrO_2 + Ir)_U$ is due to the use of a hydrogen reference electrode instead of Ag/AgCl electrode for measuring and not caused by the sample itself.

To gain a comprehensive understanding of the underlying cause for the observed decrease in activity during CA cycles of the four catalysts, it was imperative to identify the primary deactivation mechanism that governed the process. The potential mechanisms were hypothesized to be: (a) the accumulation of microscopic bubbles, (b) transformation of Ir(III)/Ir(IV) species on the catalyst surface, to anhydrous Ir(IV) oxide or higher oxidation state Ir, and (c) Ir dissolution.[207], [257], [269] Microscopic bubble accumulation and depletion of active species could be measured by performing EIS. It was observed in the work of Tan et al. [6] that depletion of OER-relevant species from the catalyst surface results in a gradual increase in the charge transfer resistance (R_{ct}), as evidenced by the increasing diameter of the semicircle observed from the Nyquist plots before (EIS @ I) and after the 2 h CA at 1.6 V_{RHE} (EIS @ II) in Figure 2.9 (b). Similarly, according to the work of Trogisch et al., the build-up of small oxygen bubbles generated at high current density could also cause blockage of active sites, inhibiting electrolyte contact with the catalyst surface and resulting in an apparent reduction in activity and an increase in R_{ct}.[207], [209]

In order to separate the contribution of microscopic bubble accumulation in the

increased R_{ct} observed at the end of the CA cycle, the working electrode was maintained at zero current under constant stirring at 1600 rpm for 30 minutes after each CA cycle, in order to remove at least a portion of the bubbles that might have blocked the catalyst layer. While spinning the electrode for 30 minutes does not ensure the complete removal of the bubbles, it is still a viable way to observe if the bubble accumulation affects the results. The resistance associated with bubbles is quantified as the difference between R_{ct} values before (EIS @ II) and after (EIS @ III) the bubble removal process, as seen in Figure 2.9 (c). The R_{ct} observed at point III is mostly associated with the depletion of Ir(III)/Ir(IV) species from the catalyst surface and subsequent conversion to anhydrous Ir(IV) oxide or higher oxidation state Ir species, the process is referred to as "Ir(III)/Ir(IV) phase transformation" in this paper. It is however possible to partially recover the loss of intrinsic activity of the catalyst by performing 20 CV cycles in the potential window of 0 V_{RHE}-1.53 V_{RHE}.[6] The portion of the activity that was not able to be restored through CV regeneration was regarded as lost due to Ir dissolution, irreversible phase transformation, or due to the microbubbles that could not escape the catalyst layer.[6] Ir dissolution was also studied by ECSA loss and ICP-MS.

The results of EIS performed before and after the first CA cycle are represented by the Nyquist plots displayed in Figure 2.9 (b). The increasing order of charge transfer resistance at the beginning of CA cycle (EIS @ I) is as follows: IrO_x TKK < $Ir_xZr_{(1-x)}O_2/ZrO_{2(L)}$ < $Ir_xZr_{(1-x)}O_y/ZrO_{2(S)}$ < $(IrO_2 + Ir)_U$. The sequence illustrates the degree of ease with which charge transfer occurs at 1.6 V_{RHE}, with IrO_x TKK experiencing the least resistance to charge transfer, owing to well connected IrO_x network composed entirely of oxohydroxides.[6], [270] $(IrO_2 + Ir)_U$ experiences maximum resistance to charge transfer due to the lack of bulk Ir(III)/Ir(IV) species. Taking into account the physicochemical and electrochemical characterization performed on fresh catalyst samples, the combination of well-connected IrO_x structures and the presence

of Ir(III)/Ir(IV) bulk species might be contributing to maintaining high activity and a low value of (R_{ct}), as seen in IrO_x TKK and $Ir_xZr_{(1-x)}O_2/ZrO_{2(L)}$. The presence of Ir(III)/Ir(IV) bulk species ensures easy ion mobility within the film which would ensure all Ir centers undergo OER when exposed to oxidative potentials and a well-connected $Ir_xZr_{(1-x)}O_2$ network ensures larger availability of Ir active site.[6], [257] $Ir_xZr_{(1-x)}O_y/ZrO_{2(S)}$ also possesses Ir(III)/Ir(IV) species but has a smaller number of active sites (ECSA) and short-range network of $Ir_xZr_{(1-x)}O_y$, and hence a limited supply of Ir active sites, and $(IrO_2 + Ir)_U$ does not possess Ir(III) species in the fresh catalysts, both of which could lead to a higher initial charge transfer resistance, as shown in Figure 2.9 (b) (EIS @ I). At this stage, as the catalysts have not been subjected to prolonged exposure to high potentials, it can be assumed that the buildup of microscopic bubbles is negligible. At the end of the first CA cycle, all catalysts exhibited an increase in R_{ct}, albeit with varying magnitude. The sequence of R_{ct} (EIS @ II - EIS @ I) in increasing order of magnitude is as follows: IrO_x TKK < $Ir_xZr_{(1-x)}O_2/ZrO_{2(L)}$< $Ir_xZr_{(1-x)}O_y/ZrO_{2(S)}$ < $(IrO_2 + Ir)_U$, as expected.

Despite having overall low R_{ct} values, microscopic bubble accumulation severely affected charge transfer for $Ir_xZr_{(1-x)}O_2/ ZrO_{2(L)}$, as shown in Figure 2.9 (e) and Figure A.14. After 30 minutes of bubble removal, a 30% and 40% recovery in R_{ct} was observed for $Ir_xZr_{(1-x)}O_2/ZrO_{2(L)}$ after CA-1 and CA-2 respectively. A greater recovery of R_{ct} after the bubble removal indicates that the microstructure of the catalyst makes it more challenging to remove the produced gas formed during the CA cycles, despite stirring the working electrode at 1600 rpm. This may be a result of $Ir_xZr_{(1-x)}O_2/ZrO_{2(L)}$ structure, which does not allow for the prompt removal of oxygen bubbles. $Ir_xZr_{(1-x)}O_2$ exists in the form of multiple layers of nanoparticles deposited on $ZrO_{2(L)}$. When this catalyst is exposed to high currents, the rapid production of O_2 microbubbles and entrapment between $Ir_xZr_{(1-x)}O_2$ layers might shield the majority of active Ir active sites resulting in higher localized current in

the remaining active particles.[208], [209], [271] This is supported by the fact that $Ir_xZr_{(1-x)}O_2/ZrO_{2(L)}$ exhibited better mass and ECSA-normalized activity and lower resistance to charge transfer than $Ir_xZr_{(1-x)}O_y/ZrO_{2(S)}$ and yet experiences prominent loss in activity during CA cycle. This suggests that microscopic bubble accumulation might be the dominating deactivation mechanism in $Ir_xZr_{(1-x)}O_2/ZrO_{2(L)}$. $(IrO_2 + Ir)_U$ also experienced considerable recovery in R_{ct} values. In $(IrO_2 + Ir)_U$, the presence of large nanoneedles might also exacerbate the mass transfer of O_2 bubbles away from the catalyst surface. However, bubble accumulation is not the only mode of deactivation in $(IrO_2 + Ir)_U$ as it showcases the highest R_{ct} values even after bubble removal.

Figure 2.9 (c) shows the reduction in R_{ct} observed after performing 20 regeneration CV cycles. It can be seen that $Ir_xZr_{(1-x)}O_2/ZrO_{2(L)}$ and IrO_x TKK return, approximately, to the same values as the beginning of CA cycle (EIS @ I), whereas $Ir_xZr_{(1-x)}O_y/ZrO_{2(S)}$ and $(IrO_2 + Ir)_U$ experience lesser regeneration of R_{ct}. The observed increase in R_{ct} may be caused by irreversible depletion of OER active species, likely resulting from phase transformation occurring at the end of the CA cycle and/or Ir dissolution.

XPS analysis was performed for $Ir_xZr_{(1-x)}O_2/ZrO_{2(L)}$, $Ir_xZr_{(1-x)}O_y/ZrO_{2(S)}$, and $(IrO_2 + Ir)_U$ after the stability test as shown in Figure 2.5 to investigate the aforementioned phase transformation. The film sample was collected post-CV regeneration cycles performed after CA-2. As discussed in the XPS section, the fit parameters of Ir(0), Ir(III), and Ir(IV), along with their satellite peaks obtained from the deconvolution of the fresh catalysts were used as guidelines to deconvolute the Ir 4f spectra of the spent catalysts. The Ir 4f peak could not be deconvoluted with only Ir(III) and Ir(IV) species (no Ir(0) peak was identified in the end of testing $(IrO_2 + Ir)_U$ sample), and an additional peak at higher binding energy than Ir(III) and Ir(IV) was identified.

This common phase labeled as Ir(post-OER) in Figure 2.5 was potentially Ir(>IV), owing to the higher binding energy of Ir $4f_{7/2}$ and Ir $4f_{5/2}$ peak positions located at the binding energies of 63.0 eV and 66.0 eV, as shown in Figure 2.5. The concentration of Ir(post-OER) perhaps corresponds to the fraction of Ir species on the surface of the catalysts that were irreversibly transformed to Ir(>IV) oxidation state. This additional peak was also reported by Tan et al. while studying IrO_x catalysts.[6] Previous studies discussing OER mechanisms have also reported the presence of Ir(>IV), Ir(V), and Ir(VI) species in the potential region of OER.[49], [257], [272]–[275] Based on the deconvoluted value, Ir (post-OER) phase accounts for approximately 16% of the Ir composition in $Ir_xZr_{(1-x)}O_2/ZrO_{2(L)}$ while it was 36% in $Ir_xZr_{(1-x)}O_y/ZrO_{2(S)}$ and 34% in $(IrO_2 + Ir)_U$. The appearance of Ir(post-OER) phase suggests irreversible conversion of Ir(III)/Ir(IV) species to inactive species with a higher oxidation state of Ir. The higher values for $Ir_xZr_{(1-x)}O_y/ZrO_{2(S)}$ and $(IrO_2 + Ir)_U$ also agree with their lower normalized current at the end of CA-2.[276]

The resistance to depletion of OER-relevant Ir(III)/Ir(IV) species from the surface of $Ir_xZr_{(1-x)}O_2/ZrO_{2(L)}$ may be attributed to the high ECSA and electrical conductivity, as well as electron transfer from Zr to Ir in $Ir_xZr_{(1-x)}O_2$ alloy, which potentially helps suppress the over-oxidation of Ir. This coupled with the larger number of active sites available for the reaction slows catalysts deactivation. We suspect that $Ir_xZr_{(1-x)}O_y/ZrO_{2(S)}$ experiences a similar electron transfer effect during the first CA cycle, as this catalyst maintains the best resistance to activity deterioration as shown in Figure 2.9 (a). However, given the non-conductive nature of the support, it is bottlenecked by the lack of available active sites. To affirm the durability of the $Ir_xZr_{(1-x)}O_2$ /$Ir_xZr_{(1-x)}O_y$ alloy and its ability to suppress over-oxidation following the stability test, further investigation is required. The process of anhydrous layer/higher Ir oxidation state formation may be faster in $(IrO_2 + Ir)_U$ owing to the unavailability of bulk Ir(III) species.

The XPS results of spent samples also show an elevated concentration of Ir(III) species on the catalyst surface. This was expected as the samples were taken right after CV regeneration which helps recover active species on the surface of the catalysts. In line with previous findings where $Ir_xZr_{(1-x)}O_2/ZrO_{2(L)}$ exhibited notable R_{ct} recovery following CV regeneration cycles, the XPS analysis shows that 71% of the Ir species on the catalyst surface exist at lower Ir(III) oxidation state. Although the regeneration protocols were consistently applied to all samples, Ir(III) species concentration after CV regeneration in $Ir_xZr_{(1-x)}O_y/ZrO_{2(S)}$, and $(IrO_2+Ir)_U$ were limited to 50% to 53% respectively. This shows that $Ir_xZr_{(1-x)}O_2/ZrO_{2(L)}$ surface is rich in OER-relevant species, further reinforcing its stability against phase transformation.

The third relevant deactivation mechanism is Ir dissolution. To quantify dissolution, both ECSA loss and Ir concentration in the electrolyte were measured. The ECSA loss is measured based on the decrease in total anodic charges observed in the cyclic voltammetry (CV) profile between 0.4 V_{RHE}-1.25 V_{RHE} before and after the stability cycle can be interpreted as evidence of Ir dissolution.[6] The concentration of Ir ions in the electrolyte, before and after the stability test was measured using ICP-MS to calculate the percentage of dissolution from the catalyst electrode during stability tests. The percentage of Ir dissolution during the stability test is calculated based on the initial mass of Ir deposited on the electrode and has been adjusted to account for the mass of Ir dissolved in the electrolyte prior to the stability testing. Results presented in Figure 2.9 (d) indicate a considerable loss of over 42% of the deposited Ir on the electrode during the stability testing procedure in IrO_x TKK. The fast dissolution rate in IrO_x TKK could be attributed to the presence of a high density of surface defects and quasi/amorphous structure.[6] Figure 2.9 (e) shows the CV cycles between 0 V_{RHE}-1.53 V_{RHE} before and after both 2 h cycles of controlled potential OER. It is clear that IrO_x TKK experiences a fast loss of ECSA after each

CA cycle, whereas all the other synthesized catalysts demonstrate relatively smaller ECSA loss, as only a minor change in voltammetric charge is observed. ICP-MS analysis of the synthesized catalysts corroborate with this observation and demonstrated that the stability test leads to a loss of less than 8% Ir in $Ir_xZr_{(1-x)}O_2/ZrO_{2(L)}$, while dissolution in both $Ir_xZr_{(1-x)}O_y/ZrO_{2(S)}$ and $(IrO_2 + Ir)_U$ results in a loss of less than 1% of Ir. Based on the dissolution results, the loss of activity for the synthesized catalysts could not be predominantly attributed to dissolution. The resistance to Ir dissolution in $(IrO_2 + Ir)_U$ can be attributed to its predominantly rutile structure observed in fresh catalysts, which is well-known for its resistance to dissolution.[6], [96], [169], [269], [277] $Ir_xZr_{(1-x)}O_2/ZrO_{2(L)}$ and $Ir_xZr_{(1-x)}O_y/ZrO_{2(S)}$ catalysts experience relatively smaller Ir dissolution when compared to IrO_x TKK, despite having a similar distribution of Ir(III) and Ir(IV) oxidation state in the fresh catalysts.[53] Between both the ZrO_2 supported samples, it is plausible that $Ir_xZr_{(1-x)}O_2/ZrO_{2(L)}$ experiences larger dissolution compared to $Ir_xZr_{(1-x)}O_y/ZrO_{2(S)}$, as a result of having a less intimate contact with the support. The comparative dissolution percentages of $Ir_xZr_{(1-x)}O_y/ZrO_{2(S)}$ and $(IrO_2 + Ir)_U$ show that $Ir_xZr_{(1-x)}O_y/ZrO_{2(S)}$ inherited the stability advantages of rutile IrO_2 while also maintaining higher activity than the latter. It is likely that resistance to IrO_x dissolution in ZrO_2-supported samples might be due to charge donation from the ZrO_2 support to the IrO_x.[200] However, further work is needed to understand the phenomenological reason for enhanced resistance to dissolution.

In summary, $Ir_xZr_{(1-x)}O_2/ZrO_{2(L)}$ catalyst exhibits a large resistance to Ir(III)/Ir(IV) phase transformation and Ir dissolution, however, deactivates due to microscopic bubble accumulation in its layered microstructure. The electron transfer from Zr to Ir in $Ir_xZr_{(1-x)}O_2$ alloy likely suppressed over-oxidation of Ir and simultaneously mitigated dissolution. These findings showed that there is an opportunity to optimize the loading of IrO_x on ZrO_2 to form a mono-layer of $Ir_xZr_{(1-x)}O_2$ engulfing the support

that will offer the highest resistance to Ir dissolution, possess a well-connected supply of OER-relevant Ir(III)/Ir(IV) species on the catalyst surface and in bulk, and facilitate bubble removal without affecting the $Ir_xZr_{(1-x)}O_2$ microstructure in the process. Therefore, membrane electrode assembly testing is of paramount importance to assess how critical this behavior is in limiting performance. Furthermore, support modifications to increase hydrophilicity might reduce the observed degradation. Nonetheless, additional research is required to substantiate the continual existence of $Ir_xZr_{(1-x)}O_y/Ir_xZr_{(1-x)}O_2$ throughout the stability test and to understand the phenomenological reason for enhanced resistance to dissolution.

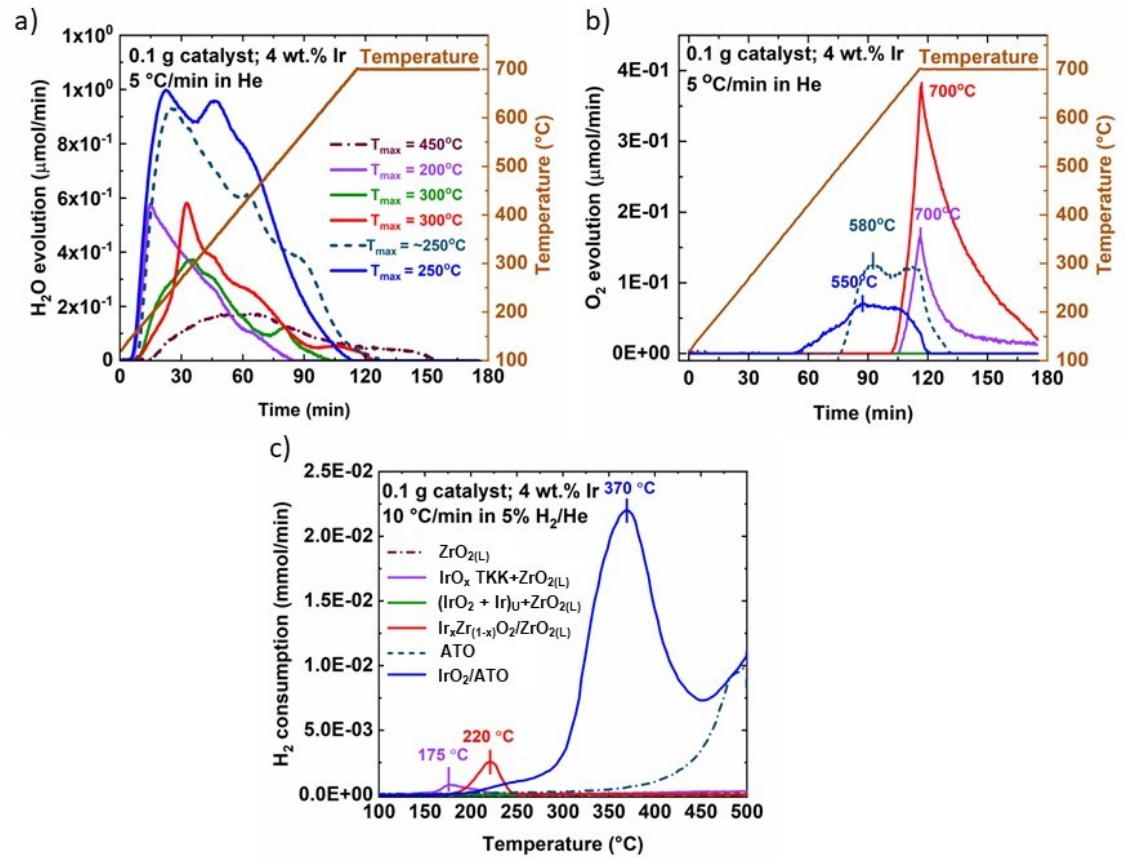

Figure 2.10: a) H_2O and b) O_2 TPD profiles ($\beta = 5°$/min in He) followed by c) H_2 consumption profile obtained by performing TPR ($\beta = 10°$/min in 5% H_2/He) of the spent catalysts. 0.1 g of catalyst sample, 4 wt.% Ir. See sections A.4.1 and A.4.3 for profiles at other heating rates.

2.3.3 Thermal desorption analyses of water and oxygen

H_2O adsorption and O_2 desorption play an essential part in the OER mechanism, as per Equations 2.2-2.5, with electrocatalytic activity being determined by the binding energies of the reaction intermediates to the catalyst surface [278]:

$$H_2O_{(l)} \longrightarrow HO^* + H^+ + e^- \tag{2.2}$$

$$HO^* \longrightarrow O^* + H^+ + e^- \tag{2.3}$$

$$O^* + H_2O_{(l)} \longrightarrow HOO^* + H^+ + e^- \tag{2.4}$$

$$HOO^* \longrightarrow O_2 + 4H^+ + e^- \tag{2.5}$$

As early as 1955, metal-OH bond energy was correlated linearly with overvoltage in OER in alkaline conditions.[279] More recently, in an acidic OER study, thermogravimetry quadrupole mass spectrometry coupled with differential scanning calorimetry showed that chemisorbed water was released only from OER-active amorphous iridium oxide but not from the less active rutile.[266] Gauthier et al. investigated the IrO_2(110)-water interface using DFT and reported that the oxide surface binds *OH and *OOH too strongly, which required a higher than 1.23 V potential to complete the OER.[280] They also suggested that *OO removal may happen chemically, not electrochemically. It is known that the higher the temperature at which species are desorbed from a catalyst during heating, the stronger the bond. By performing temperature-programmed desorption (TPD), the desorption temperature and the activation energy of desorption can be obtained, which equals the heat of non-activated adsorption or sets an upper limit to the heat of activated adsorption.[281]

Herein, we performed TPD of water-treated samples to understand if they exhibit differences in bonding oxygen and hydroxyls. The samples were treated in liquid water at 120°C in an autoclave, followed by purging in He at 120°C in a packed-bed reactor until no physisorbed water evolution was observed. Upon further heating

Table 2.3: Water and oxygen TPD of catalyst and support samples.

Sample [a]	SSA	Activity in OER[b]			H_2O desorption [c]			O_2 desorption [c]	
	$\frac{m^2}{g_{cat}}$	$j_i, \frac{A}{g_{Ir}}$	$j_k, \frac{mA}{cm^2_{Ir\ ECSA}}$	Ea, $\frac{kJ}{mol_{H2O}}$	$\frac{\mu mol\ H_2O}{g_{cat}}$	$\frac{mol\ H_2O}{mol_{Ir}}$	$\frac{\mu mol\ H_2O}{m^2_{cat}}$	$\frac{\mu mol\ O_2}{g_{cat}}$	$\frac{mol\ O_2}{mol_{Ir}}$
$ZrO_{2(L)}$	4.0	-	-	108	131(21)	-	33	0(0)	-
$Ir_xZr_{(1-x)}O_2/ZrO_{2(L)}$	4.4	712	4.8	80	237(54)	0.5	54	109(13)	0.5
IrO_x TKK+$ZrO_{2(L)}$	6.8	907	1.25	73	230(54)	0.5	34	35(6)	0.2
$(IrO_2 + Ir)_U$+$ZrO_{2(L)}$	4	11	1.1	82	161(12)	0.15	40	0(0)	0
ATO	47	-	-	54	580(18)	-	12	44(10)	-
IrO_2/ATO	45	24	0.4	52	626(68)	0.2	14	34(13)	0

[a] Ir loading is 4 wt.%; average $ZrO_{2(L)}$ particle size is 5 μm, ATO 50 nm.[b] Activities were measured at 1.6 V_{RHE}; corresponding values of IrO_x TKK and $(IrO_2 + Ir)_U$ correspond the activity of only IrO_x and not the physical mixture.[c] Data in brackets corresponds to one standard deviation.

to 700°C at different heating rates, H_2O and O_2 evolution were monitored with an online calibrated mass spectrometer. After the analyses, the samples were subjected to temperature-programmed reduction (TPR) in H_2 to evaluate the availability of remaining reducible oxygen species.

Figure 2.10 shows H_2O and O_2 TPD evolution profiles followed by TPR, and Table 2.3 summarizes the results of the H_2O and O_2 desorption analyses. Section A.4.1 and Section A.4.3 include individual profiles at different heating rates. Activation energies of water desorption were found from the slope of ln (β/T^2_{max}) vs. $1/T_{max}$, where β is a heating rate, and T_{max} is the corresponding temperature peak maximum and their graphical representation has been provided in Section A.4.2 (Equation A.5).[281] H_2O and O_2 desorption per mole of Ir was found by subtracting the amount of desorbed water by $ZrO_{2(L)}$ or ATO support from those of the Ir-containing samples.

The two ATO samples (with and without Ir) demonstrated the lowest H_2O and O_2 desorption amounts per surface area and the lowest activation energies of H_2O desorption (E_a) of 53 kJ/mol for the first peak at T_{max} of 250°C, with ATO prop-

erties governing the observed phenomena. This E_a value is similar to the heat of water vaporization of 41 kJ/mol (at 100°C), implying a significant contribution from physically adsorbed water molecules. The higher-temperature peaks for H_2O and O_2 are characteristic of chemically activated water and oxygen species on the SnO_2 surface.[282] The IrO_2/ATO catalyst also demonstrated the lowest OER activity.

$ZrO_{2(L)}$ shows the highest activation energy (E_a) of water desorption of 108 kJ/-mol and does not release O_2 at any conditions studied. When $(IrO_2 + Ir)_U$ is mixed physically with $ZrO_{2(L)}$, the E_a is reduced to 82 kJ/mol, and the T_{max} is lowered to 300°C from 450°C for $ZrO_{2(L)}$. Considering the water adsorption on $ZrO_{2(L)}$, the IrO_x contribution amounted to 0.15 mol/mol_{Ir} of released water. No O_2 was evolved from this sample either. When IrO_x was deposited on $ZrO_{2(L)}$ by impregnation ($Ir_xZr_{(1-x)}O_2/ZrO_{2(L)}$), the desorbed water amount increased 3-fold to 0.5 mol/mol_{Ir} at the same E_a of 80 kJ/mol and T_{max} of 300°C. This indicates the similarity of the M-OH bond strength of active sites, but a higher amount of the sites for $Ir_xZr_{(1-x)}O_2/ZrO_{2(L)}$ catalyst as compared to the physical mixture. The $Ir_xZr_{(1-x)}O_2/ZrO_{2(L)}$ catalyst also showed the highest O_2 evolution among the samples above 700°C, which were reducible at the following TPR at 0.5 molar ratios of H_2/Ir.

When the mixture of IrO_x TKK and $ZrO_{2(L)}$, instead of $(IrO_2 + Ir)_U$ and $ZrO_{2(U)}$ was subject to the same analysis, the T_{max} of H_2O desorption shifted to 200°C with a lower E_a of 73 kJ/mol. Pfeifer also reported that the desorption of chemisorbed hydroxyl species from amorphous IrO_x occurred at 227°C.[266] The amount of water desorbed per unit of catalyst surface area decreased by nearly half on the TKK catalyst compared to the $Ir_xZr_{(1-x)}O_2/ZrO_{2(L)}$ catalyst, which suggests that the TKK has fewer active sites available per unit surface area. O_2 desorption was also reduced almost 3-fold on the IrO_x TKK+$ZrO_{2(L)}$ catalyst vs. $Ir_xZr_{(1-x)}O_2/ZrO_{2(L)}$,

with a similar 0.4-0.5 molar ratio of H_2/Ir consumed at the following TPR but at a lower reduction temperature. The reduced O_2 desorbed amounts are concurrent with the lower OER activity of TKK of 1.25 $mA{\cdot}cm^{-2}_{ECSA}$ vs. 4.8 $mA{\cdot}cm^{-2}_{ECSA}$ for the $IrOx/ZrO_{2(L)}$ catalyst.

Thus, the observed TPD behavior of the investigated samples, when compared with their OER performance, suggests that the higher activity is concurrent with the activation energies of water desorption of about 70-80 kJ/mol, and high adsorbed H_2O ($\frac{mol\ H_2O}{mol_{Ir}}$) and desorbed O_2 ($\frac{mol\ O_2}{mol_{Ir}}$) amounts, with easier reducible oxygen species in IrO_x. The limits of this hypothesis need to be explored further, as too high adsorption energies are detrimental to catalysis, as per Sabatier's principle.

2.4 Conclusion

We have investigated the use of ZrO_2 as support for acidic OER electrocatalysts. Commercial ZrO_2 supports with 2 different particle sizes <5 μm ($ZrO_{2(L)}$) and <100 nm ($ZrO_{2(S)}$) were used. Supported IrO_x-based catalysts were synthesized using the incipient wetness impregnation method using the H_2IrCl_6 precursor followed by calcination in the air at 400°C. Commercial state-of-the-art IrO_x TKK, and unsupported IrO_2 prepared by thermal decomposition of the precursor were used as benchmarks.

At an operating voltage of 1.6 V_{RHE}, $Ir_xZr_{(1-x)}O_2/ZrO_{2(L)}$ exhibited 80 % of the mass normalized activity of IrO_x TKK catalyst, with estimated values of 712 $A.g^{-1}_{Ir}$ and 907 $A.g^{-1}_{Ir}$. $Ir_xZr_{(1-x)}O_2/ZrO_{2(L)}$ exhibited the highest intrinsic activity among all the catalysts, with a value of ~4.8 $mA{\cdot}cm^{-2}_{Ir\ ECSA}$, which was approximately 4 times higher than the most active benchmark IrO_x TKK (1.25 $mA{\cdot}cm^{-2}_{Ir\ ECSA}$) at 1.6 V_{RHE}. The analysis conducted through XRD, XPS, TPD, and TPR techniques suggests the potential existence of SMSI between Ir oxide and ZrO_2 supports. XRD results suggest the formation of $Ir_xZr_{(1-x)}O_2$ alloy demonstrated by the IrO_2 peak shift observed in

$Ir_xZr_{(1-x)}O_2/ZrO_{2(L)}$, and XPS analysis demonstrates binding energy shift observed in ZrO_2 support for both the samples, suggesting electron transfer from Zr to Ir. Catalyst stability was also studied. All catalysts exhibited loss of activity during a potential hold at 1.6 V_{RHE} with IrO_x TKK and $Ir_xZr_{(1-x)}O_2/ZrO_{2(L)}$ showing the most stable performance. The deactivation mechanism of the synthesized catalyst, both supported and unsupported was different from IrO_x TKK. IrO_x TKK deactivated via Ir dissolution, losing over 42% of active sites during the stability test. The formation of $Ir_xZr_{(1-x)}O_2$ in $Ir_xZr_{(1-x)}O_2/ZrO_{2(L)}$ confers good resistance against Ir dissolution and Ir(III)/Ir(IV) phase transformation, thereby enabling a low Ir oxidation state even in OER potentials; however, the microstructure of the $Ir_xZr_{(1-x)}O_2/ZrO_{2(L)}$ catalyst was susceptible to performance degradation due to the formation of oxygen bubbles on the catalyst surface. $(IrO_2 + Ir)_U$ and $Ir_xZr_{(1-x)}O_y/ZrO_{2(S)}$ lost activity primarily due to Ir(III)/Ir(IV) phase transformation and exhibited negligible Ir dissolution.

Finally, temperature-programmed desorption of water and oxygen from the studied catalysts followed by temperature-programmed reduction was used to establish a possible link between higher activity, lower activation energies for water desorption, higher amounts of adsorbed H_2O and desorbed O_2 species, and the presence of easily reducible remaining oxygen species in IrO_x.

The objective of this study is to establish ZrO_2 as a promising support for IrO_2-based catalysts, with the intention of facilitating future research, including optimization of its structural properties and confirmation of the stability of $Ir_xZr_{(1-x)}O_y$/ $Ir_xZr_{(1-x)}O_2$ after electrochemical testing. In the future, there is significant potential for enhancing the activity of Ir on ZrO_2 support by optimizing the Ir loading and modifying the properties of ZrO_2 support to increase Ir active area. For example, Cao et al. reported the synthesis of porous ZrO_2 with a specific surface area as high as 275 $m^2 \cdot g^{\breve{}1}$ showing that a high BET surface area of ZrO_2 particles can be

synthesized.[283]

Chapter 3

Effect of residual chlorine from catalyst precursors during the synthesis of Ir-based catalysts

3.1 Introduction

Ir oxide catalysts are the preferred catalyst choice in proton exchange membrane (PEM) water electrolyzers due to their robustness in highly corrosive acidic media and activity towards oxygen evolution reaction (OER). Wet-chemistry techniques continue to be one of the most widely reported methods of Ir oxide-based catalyst synthesis in the scientific literature, owing to their relative accessibility in a research environment and their ability to produce well-defined catalytic structures.[67], [79], [138], [139], [142], [145], [150]–[154], [158], [232], [284], [285] Numerous methods for catalyst preparation have been reported in the literature, such as the polyol method,[144], [235] the Adams fusion method,[121], [286], [287] the sol-gel method,[63], [288] and hydrothermal method,[100], [139], [247], [289]. A comprehensive review of the different synthesis methods can be found elsewhere.[67], [177] These synthesis routes may produce catalysts with large surface areas possessing suitable crystallographic structures to maximize the specific activity.[290] Selecting the appropriate metal precursor and optimizing the deposition conditions (such as solvent, active metal loading, and deposition temperature) are crucial considerations to produce the desired catalyst. The selection of Ir precursors is a crucial step in the synthesis that is seldom discussed in

the literature. Among the different precursors utilized for the preparation of Ir and IrO_x catalysts, the most extensively documented ones are Ir(IV) based precursors like H_2IrCl_6,[6], [168] $IrCl_4$,[169] K_2IrCl_6,[170], [171] Na_2IrCl_6,[172] $(NH_4)IrCl_6$.[173]; Ir (III) based precursors like $IrCl_3$,[168], [174] Na_3IrCl_6,[175] and $Ir(acac)_3$[95]; and Ir(I) based precursors like $[Ir(COD)_2]BF_4$.[176], [177] Bowker et al. reported that the presence of chloride species caused poisoning and sintering of the IrO_x active metal oxides for low-temperature CO oxidation.[178] In the case of supported noble metal (Ru) catalyst, residual chlorine has also been shown to reduce the active surface area.[179] The majority of the aforementioned precursors contain chlorine atoms. In the case of gold containing chloride precursors, it is widely accepted that the chloride ligands present in the coordination sphere of $[AuCl_4]^-$, through Cl-bridging, result in polymerization which leads to agglomeration.[291]–[294] Finally, during conditioning, there could be competition with anodic O_2 evolution due to the preferential Cl_2 evolution reaction (CER).[295]–[298] In chlorine-based electrolytes, Vos et al. studied the parallel evolution of chlorine and oxygen on IrO_x electrodes. They discovered that chloride adsorption significantly slowed down the OER by blocking sites, which increased the Tafels slope from ∼40 mV/dec to ∼120 mV/dec when CER is competing with the OER.[299]

Although these detrimental effects of chlorine in the catalyst lattice are evident, there has been limited investigation into the detailed examination of how residual chlorine from the precursor impacts the physicochemical characteristics and electrochemical performance of the catalyst in acidic water splitting conditions. Specifically, very few details are available on how this residual Cl^- from the precursor affects surface area, activity, particle size, Ir oxidation state, and concentration of active OER species required to catalyze OER.

Depending on the chosen synthesis method, it is possible to either eliminate or

retain a significant portion of chlorine within the catalyst lattice. Lettenmeirer et al., for example, synthesized IrO_x-Ir catalysts using a surfactant-assisted method and detected the presence of chlorine via XRD analysis due to unreduced $IrCl_3^-$.[174] Approximately 3 wt.% chlorine was detected even after electrochemical characterization. Ruiz Esquise et al. have used a modified hydrothermal method, which is focused on driving the Cl^- ions in abundant solution, followed by washing of the catalyst, often using $>$ 2 L of water per mmol $IrCl_3$.[100] This resulted in almost complete removal of chloride ions, as none was detected using an XPS and EDX.On the contrary, Haruta et al. reported that, while the majority of noble metal catalysts are prepared using incipient wetness impregnation, these impregnation methods are limited in their ability to produce high dispersion catalysts due to the presence of chlorine in their lattice when synthesized at a temperature lower than 600°C.[300]

In commonly employed industrial synthesis methods like incipient wetness, continuous washing of the catalyst can result in the loss of precious noble metal catalysts as a result of dissolution from the support. This makes it less appealing for large-scale production due to the potential loss of valuable active metals and increased resource demands, including higher water usage. For instance, Del Rio et al. developed a speciation-controlled incipient wetness impregnation method (ScIWI), a modification to the existing method, where they combined the use of a chemically well-defined impregnating Au solution and IWI.[293] Their hypothesis posited that altering the pH of the impregnation solution ($HAuCl_4$ precursor) through the addition of NaOH to elevate it within the range of 8-12, followed by aging the precursor base solution (with a suitable volume of 2.5 M NaOH) until achieving thermodynamic equilibrium (4 h) and incorporating intermittent ultrasonication to avert $Au(OH)_3$ precipitation, could enhance the interaction between supports and dissolved gold species with fewer Cl ligands. It was also reported that the use of the ScIWI method minimized the loss of the $HAuCl_4$ precursor.

Several studies in the current literature are focused on discovering solutions to alleviate residual chlorine contamination in Ir oxide catalysts used for OER despite the lack of knowledge about its effect.[100], [178], [300] For example, Xu et al. and Ruiz Esquise et al. reported that when the chloride-containing precursor is exposed to highly alkaline aqueous conditions, the conversion of $Ir(H_2O)_3Cl_3$ to IrO_x is hypothesized to occurs, IrO_x nanoparticles are formed, with Ir(III) and Ir(IV) species. The mechanism is described as follows [301]:

$$Ir(H_2O)_3Cl_3 + 6\ OH^- \longrightarrow [Ir(OH)_6]^{3-} + 3\ Cl^- + 3\ H_2O \tag{3.1}$$

$$2\ [Ir(OH)_6]^{3-} \longrightarrow Ir_2O_3 + 3\ H_2O + 6\ OH^- \tag{3.2}$$

$$2\ Ir_2O_3 + O_2 \longrightarrow 4\ IrO_x/4\ IrO_2 \tag{3.3}$$

As a result, chlorine atoms will be less likely to enter the crystalline structures of Ir oxide catalyst and become easier to remove.

The objective of this study is to understand the impact of residual Cl^- from precursors on the electrochemical and physicochemical properties of IrO_x catalysts prepared by thermal decomposition of hydrogen hexachloroiridate (IV) ($H_2IrCl_6.xH_2O$) precursor and recommend ways to mitigate the effect of residual chlorine poisoning. In order to find out if the OER activity of IrO_x is sensitive to the chlorine content in the precursor, a fixed amount of HCl was added to the $H_2IrCl_6.xH_2O$ precursor to form the IrO_2-HCl catalyst. In a second study, the interaction between Ir and Cl^- was disrupted by introducing NH_4OH base to the precursor, where its addition would modify the pathway of IrO_2/IrO_x formation, breaking the bond between Ir and Cl.

3.2 Experimental section

3.2.1 Catalyst synthesis

IrO_2: In this work, $H_2IrCl_6.xH_2O$ (Hydrogen hexachloroiridate(IV) hydrate, 99.9% trace metal basis, supplied by Millipore Sigma) was used as the metal precursor, and ultrapure Milli-Q water (18.2 MΩ.cm) water as a compatible solvent. The solvent volume required to dissolve the precursor crystal was added and stirring continued until a uniform solution was achieved. This solution was then dried in the fumehood overnight and then moved to a well-ventilated furnace at 120°C for the next 4 h. The catalyst was then broken into a coarse powder using a spatula. It was then subjected to calcination at 400°C for a duration of 2 h (total heating time of 2 hours and 37 minutes from room temperature) in a furnace, with the temperature increasing at a rate of 10°C/min. Following calcination, the catalyst was ground into a fine IrO_x powder using a mortar and pestle.

IrO_2-HCl: In order to find out whether the addition of excess chlorine hinders the performance of the catalyst, HCl (supplied by Fischer Scientific, CAS 7647-01-0) was added to the precursor solution. The addition of other chlorine-containing compounds, such as NaCl and KCl, would lead to the addition of non-decomposing ions, i.e., Na^+, K^+, in the catalyst which could make it difficult to isolate the effect of Cl addition from that of the other ions.[101] The target concentration of Cl^- was approximately twice the amount of Cl^- present in the desired amount of precursor (anhydrous basis) by weight. 118 μL 37% HCl (aq. solution) was added per 100 mg H_2IrCl_6 (anhydrous basis, MW: 406.95 g/mol). HCl was added directly to the precursor-deionized water solution and left to dry under the fumehood overnight. Next, it was placed in a well-ventilated furnace at 120°C over the next 4 hours. Once the catalyst was completely dry, it was then broken into coarse powder form using a spatula, after which it was calcined at 400°C for 2 h in a furnace (total heating

time of 2 hours and 37 minutes from room temperature). After being subjected to calcination, the catalyst was crushed using a mortar and pestle to obtain a fine powder of IrO_2-HCl.

IrO_x-NH_4OH: 28%-30% wt./wt. NH_4OH solution ($\sim$ 14.8 mol·L^{-1}) was added to the pre-decided $H_2IrCl_6.xH_2O$ precursor-deionized water solution to ensure a 1:1 molar ratio of Cl^- (in H_2IrCl_6) and OH^-(in NH_4OH). The precursor-base solution was stirred well using the spatula for 5-10 minutes until a homogenous solution was observed, and the mixture was left to dry under the fumehood overnight and then moved to a well-ventilated furnace at 120°C for the next 4 hours. In order to safely remove possible NH_3 (boiling point = -33.34°C) [302] and NO_x (boiling point NO_2 = 21°C) [303] generated, safe ventilation was assured throughout the process. Once the catalyst was completely dry, the catalyst was then ground into coarse powder form using a spatula. After this step, the catalyst was calcined at 400°C for 2 hours in a well-ventilated furnace (total heating time of 2 hours and 37 minutes from room temperature). Finally, the formed powder was pestled to form a fine powder.

Commercial IrO_x/IrO_2 catalysts: State-of-the-art IrO_x was supplied by Tanaka Kikinzoku Kogyo (P.N. ELC-0110 SA = 100), and will be hereafter denoted as IrO_x TKK. The supplier stated that IrO_x TKK has Ir content of 75.23 wt.% and a surface area of 100 $m^2 \cdot g^{-1}$, which was analyzed by BET in a previous study by Tan et al.[6] Commercial IrO_2 from Alfa Aesar (P.N. A17849, product purity: 99%) was used as the second benchmark catalyst. The SEM-EDX analysis revealed that the Ir content of IrO_2 AA was approximately 87%, as reported in Table B.1.

3.2.2 Catalyst ink and electrode preparation

To prepare the working electrode, 5.3 mg of the catalyst powder was added to 1 mL of Milli-Q (deionized) water and 0.5 mL of isopropanol (IPA) in a 2 mL plastic vial. 20 μL of Nafion^{TM} (diluted to 5 wt.%, EW 1100 from Ion Power) was added to

this solution in a drop-wise manner (each drop = 10 μL). The catalyst ink solution was then sonicated in an ice-cold ultrasonic bath for 30 minutes followed by probe sonication (Qsonica S4000, 20 kHz 600 W, 2 min ON 1 min OFF, 5% amplitude) for 8 minutes. The total sonication time was selected to maintain a balance between homogeneous catalyst dispersion, and solution temperature, since longer sonication could be detrimental to the catalyst composition and morphology, mainly due to cavitation and sonolysis phenomena.[248] While performing bath and probe sonication, the plastic vial containing the ink was placed in an ice bath. This precautionary measure was taken to prevent the ink from overheating, as power ultrasound has been observed to cause a swift temperature rise of up to 50°C/h when starting from room temperature.[248]

A glassy carbon (GC) disc electrode (supplied by Pine instruments with diameter = 5 mm) embedded in a Teflon cylinder was used as the working electrode. The GC electrode was polished to a mirror-like finish before casting the ink, with polishing paper (supplied by Allied High Tech Products, P.N. 90-150-230) and 0.05 μm alumina oxide paste (Al_2O_3, supplied by Allied High Tech Products) in an ultrasonic bath (Frequency= 20kHz, 2 sec on, 1 second off) in water followed by six alternate washing cycles with ultrapure Milli-Q water (18.2 MΩ.cm) and IPA for 10 minutes each. The working electrode (GC) was cast by pipetting an 8 μL aliquot of catalyst ink on the glassy carbon surface (geometric catalyst loading = $\sim$140 μg$\cdot$cm^{-2}). The working electrode was then dried using the rotational drying technique at 600 rpm under air for 1 hr to form uniform and reproducible films followed by drying in the oven at 60°C for 30 minutes to completely dry out the catalyst film.

3.2.3 Materials characterization

Scanning electron microscopy (SEM) was performed on the catalyst samples using a Quanta 250 Mineral Liberation Analyzer (FEI company) fitted with a tungsten filament and images were taken at an accelerating voltage of 10 keV. Conductive carbon tape was used to mount the finely powdered samples onto SEM sample stubs. Any excess powder was removed using an N_2 spray gun before inserting it into the equipment. SEM was equipped with a Bruker Xflush (133 eV) detector for elemental analysis. To maintain result consistency, elemental composition was determined by calculating the mean of 10 distinct locations. Images and composition were taken at a magnification of 600x using an electron beam intensity of 25 keV.

Bright-field and dark-field transmission electron microscopy (TEM), small angle electron diffraction (SAED), and energy-dispersive X-ray spectroscopy (EDX) analyses in scanning mode (S/TEM) were conducted on a JEOL JEM Atomic Resolution ARM 200cf S/TEM at the accelerating voltage of 200 kV. In order to prepare the TEM sample, a dilute solution of the catalyst was prepared in Milli-Q water (18.2 MΩ.cm). Approximately 10 μL of the ink was drop-casted on the TEM grids with Ultrathin Carbon Film on Lacey Carbon Support Film, 400 mesh, Copper (Ted Pella, P.N. 01824). The grid was allowed to dry for 24 hours. The average diameter and the standard deviation were calculated by counting over 160 particles using the ImageJ software.

X-ray diffraction (XRD) analysis was carried out on a Rigaku Ultima IV D/max-RB diffractometer with D/Tex Ultra detector with Fe Filter (K-beta filter) using Co radiation (λ= 0.178900 nm) operated at 38 kV and 38 mA. Data was converted using JADE MDI 9.6 software and phase identification was done using DIFFRAC.EVA software with the 2022/2023 ICDD PDF 4 + and PDF 4+/Organics databases.

Photoemission measurements were performed in Kratos AXIS Ultra Imaging spectrometer. The XPS spectra were analyzed using CasaXPS, where all peaks were calibrated to the main C 1s signal at 284.8 eV. A Shirley-type background was applied to all the samples. Ir 4f peaks were fitted with a DS(0.05,230) SGL(55) profile and the Ir satellite peaks were fitted using GL(0). All the Ir 4f peaks were constrained to a doublet separation of 3 eV, the area ratio of $4f_{7/2}$:$4f_{5/2}$ = 4:3, and a doublet FWHM ratio of 1. The O1s spectrum was deconvoluted using the GL(30) peak profile. For the deconvolution of Cl 2p peaks, GL(30) profile was used, with a double separation of 1.6 eV, and the area ratio of $2p_{3/2}$: $2p_{1/2}$ of 2:1, and doublet FWHM ratio of 1.

Thermogravimetric analysis (TGA) was performed on Thermo Cahn 400. The precursor solutions (H_2IrCl_6 + DI water for IrO_2; H_2IrCl_6+ aq. HCl for IrO_2-HCl; H_2IrCl_6+ aq. NH_4OH for IrO_x-NH_4OH) were initially heated in a well-ventilated furnace at 120°C for 4 h to evaporate the water. 20 mg of the dried samples were then heated from room temperature to 750°C in the TGA apparatus at a heating rate of 10°C/min under the air atmosphere.

3.2.4 Electrochemical characterization

Electrochemical measurements were carried out using a potentiostat (BioLogic Science Instruments SP-200) on a standard rotating-disk electrode (RDE) system (PINE Research MSR Rotator), and a three-electrode cell. Helical Pt wire and reference hydrogen electrode (ET070 Hydroflex™, supplied by eDAQ) were used as the counter and reference electrodes, respectively. Sulfuric acid (Optima grade, Fisher Scientific) diluted to 1.0 M H_2SO_4 with Milli-Q water (18.2 MΩ.cm) was used as the electrolyte.[50] All electrochemical measurements were carried out at room temperature using research-grade N_2 and O_2 gases (99.999%, Praxair).

The glassware was cleaned by storing it overnight in 1.0 M H_2SO_4, followed by multiple washes with deionized water.

The potentials reported in this study are relative to the reversible hydrogen electrode (RHE) scale. iR compensation at 85% was applied using Biologic EC-Lab software while recording LSV and CV.

Cyclic voltammetry (CV) was carried out in a deoxygenated environment by saturating the electrolyte with N_2 at a scan rate of 40 $mV{\cdot}s^{-1}$ in an unstirred electrolyte unless stated otherwise. All IrO_x samples were preconditioned prior to oxygen evolution reaction (OER) electrochemical testing by recording 50 cyclic voltammograms from 0.05 V_{RHE} to 1.53 V_{RHE} at a voltage scan rate of 500 $mV{\cdot}s^{-1}$. This electrochemical preconditioning was followed by performing 10 CVs from 0-1.53 V_{RHE} at the scan rate of 40 $mV{\cdot}s^{-1}$ to calculate ECSA. The ECSA was estimated by calculating the total anodic charges of the CV profile in the potential range of 0.4 V_{RHE}-1.25 V_{RHE} with double-layer correction. The average ECSA of the last 5 CV cycles out of the 10 CVs described above has been reported in this work. The electrical charge constant associated with the anodic processes within this potential range was taken as 440 $\mu C{\cdot}cm^{-2}_{ECSA}$.[6] The entire process of calculating ECSA has been previously discussed in the work of Tan et al.[6] Further information regarding the estimation of charges can be obtained from the following references.[107], [126], [250]

Anodic linear sweep voltammetry (LSV) was performed between 1.0 V_{RHE} and 1.6 V_{RHE} at a scan rate of 10 $mV{\cdot}s^{-1}$ in an O_2-saturated environment to measure the OER. The working electrode was set to rotate at a speed of 1800 rpm. The potential range (1.0 V_{RHE}- 1.6 V_{RHE}) was selected to curtail the effect of change in hydrogen concentration at lower potentials. To ensure O_2 saturation, the electrolyte was continuously bubbled with research-grade O_2 (99.999%, Praxair).

3.3 Results and discussions

3.3.1 Materials characterization

Scanning electron microscopy (SEM) and energy-dispersive x-ray spectroscopy (EDX)

Figure 3.1 (a-e) displays the SEM micrographs of (a) IrO_x, (b) IrO_2-HCl, (c) IrO_x-NH_4OH, (d) IrO_2 AA and (e) IrO_x TKK respectively. Among the synthesized catalysts, IrO_2 and IrO_2-HCl particles exhibited flat surfaces with visible pores resembling pitting. The observed pore sizes were larger in IrO_2-HCl, as compared to IrO_2. One of the possible reasons for the pitting is the evaporation of HCl and H_2O, which might occur during the synthesis process when the catalyst undergoes calcination (Figure B.1). The surface of IrO_x-NH_4OH appears to have been modified by the addition of NH_4OH base, resulting in higher surface roughness. Additionally, the IrO_x-NH_4OH catalyst also showcased a highly porous morphology, as shown in Figure 3.2 (c). Commercial IrO_2 AA resembled an intermediate surface morphology between IrO_2 and IrO_x-NH_4OH, as IrO_2 flakes possess higher surface roughness than the synthesized IrO_2. IrO_x TKK also possessed high surface roughness and visibly smaller particles.

SEM-EDX was performed to evaluate the elemental composition of the synthesized catalysts in, IrO_2, IrO_2-HCl, and IrO_x -NH_4OH, as shown in Table 3.1 Special attention was paid to the changes in the Cl content. While IrO_2 contained approximately $44 \pm 11\%$ chlorine by atomic percentage, this value increased to $51 \pm 6\%$ in IrO_2-HCl, as expected due to the intentional addition of chlorine to the sample during synthesis. Although the quantity of HCl added during the synthesis aimed to achieve a two-fold increase in the Cl concentration observed in IrO_2, only a fraction of the introduced chlorine became incorporated into the lattice structure. It is possible that a significant portion of the HCl might have evaporated during the synthesis process. IrO_x-NH_4OH

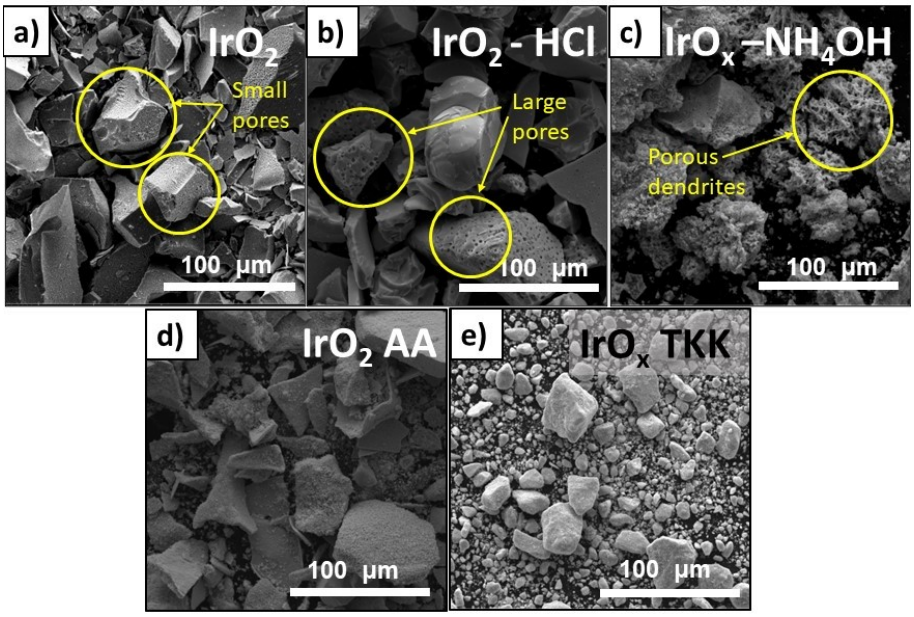

Figure 3.1: SEM images of (a) IrO_2, (b) IrO_2-HCl, (c) IrO_x-NH_4OH, (d) IrO_2, and (e) IrO_x TKK.

exhibits a decreased chlorine content, with an average Cl atomic composition of 32 ± 5% compared to 44 ± 11 % for IrO_2. An increase in the atomic percentage of oxygen was also observed in IrO_x-NH_4OH (50 ± 7 %) sample compared to IrO_2 (34 ± 12 %) and IrO_2-HCl (30 ± 7%), suggesting that NH_4OH addition to the Ir precursor (H_2IrCl_6) assisted in the transformation of Ir-Cl species to Ir-oxide species. Nitrogen could not be detected using SEM-EDX technique. In summary, the Cl to Ir atomic ratio increased from 2:1 observed in IrO_2 to 2.7:1 in IrO_2-HCl, and reduced to 1.8:1 in IrO_x-NH_4OH, confirming chlorine removal from the IrO_x-NH_4OH in bulk.

Transmission electron microscopy (TEM), selected area electron diffraction (SAED), and scanning transmission electron microscopy - energy-dispersive X-ray spectroscopy (S/TEM-EDX)

Figure 3.2 shows the TEM images of the 5 catalysts studied in this work. Figures 3.2 (a,b) depict the structure of IrO_2, consisting of a cluster of needle-shaped IrO_2. It was difficult to estimate the size of each needle due to the complex structure, however, an effort was made to produce a range of IrO_2 particle sizes from Figure 3.2. The length

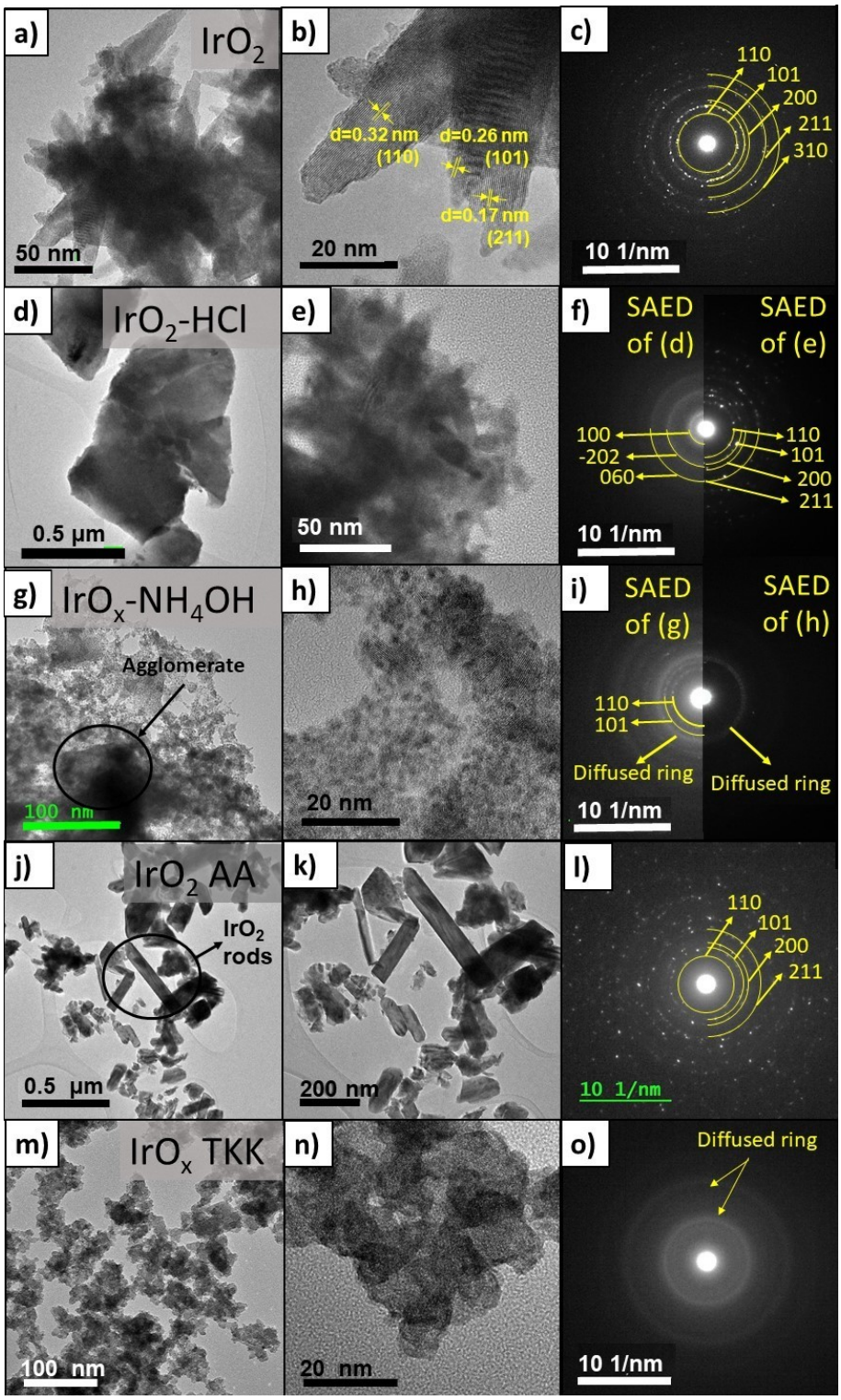

Figure 3.2: TEM bright field images and SAED of (a-c) IrO_2, (d-f) IrO_2-HCl, (g-i) IrO_x-NH_4OH, (j-l) IrO_2 AA, and (m-o) IrO_x TKK.

Table 3.1: Summary of the elemental composition of catalysts obtained using SEM-EDX

Samples	Atomic %			Weight %			Atomic Ratios	
	Ir	Cl	O	Ir	Cl	O	Cl:Ir	O:Ir
IrO_2	22±2	44±11	34±12	66±1	27±3	8±3	2	1.5
IrO_2-HCl	19±1	51±6	30±7	61±1	31±2	8±3	2.7	1.6
IrO_x-NH_4OH	18±2	32±5	50±7	63±2	22±1	15±3	1.8	2.8

Atomic and weight percentages are calculated by averaging 10 values of the bulk composition obtained by performing SEM-EDX on the powdered samples.

of the protruding needles from the agglomerate's edge was measured, and needles ranging from 10 nm to 100 nm in length were detected. While these measurements are not precise, they are still helpful in estimating the size of the particles. Agglomerates were also observed in IrO_2 sample, as shown in Figure 3.3. The SAED pattern of IrO_2 matched the rutile phase of IrO_2, as shown in Figure 3.2 (c).

Figures 3.2 (d,e) show the structural features of IrO_2-HCl. Alongside the needle-shaped rutile IrO_2, also seen in the IrO_2 sample (Figure 3.2 (a,b)), larger chunks/agglomerates were identified, as shown in Figure 3.2 (d). SAED analysis of the IrO_2-HCl agglomerate shown in Figure 3.2 (d) revealed that the rings align with the profile of $IrCl_3$, while the cluster of IrO_2 nanoneedles shown in Figure 3.2 (e) resembles tetragonal IrO_2.

IrO_x-NH_4OH was composed of IrO_x small nanoparticles, that were predominantly present on the surface of large agglomerates, as shown in Figure 3.2 (g). The volume mean diameter ($\bar{d}_{vol}$) of these nanoparticles was calculated to be 4.0±3.5 nm, based on 165 particles recorded in the TEM images. The formula to calculate volume mean diameter has been provided in Section B.1.2. The particle size distribution has

been provided in Figure B.2. The presence of 2 distinct phases was also observed in IrO_x-NH_4OH, as shown in Figure 3.2 (g). The low-resolution images display a large agglomerate along with IrO_x nanoparticles that surround and encapsulate it. The corresponding SAED also shows a ring pattern corresponding to a combination of rutile IrO_2 with a single diffused ring. Upon increasing the magnification to focus only on the nanoparticles, as shown in Figure 3.2 (h), the SAED shows a single diffused ring. This ring matched the diffused ring in the SAED of Figure 3.2 (g). This diffused ring suggests that the IrO_x nanoparticles observed in TEM are amorphous in nature.[6], [304]

Commercial IrO_2 AA is composed of IrO_2 rods, with some measuring around 0.5 μm in length, along with irregularly shaped particles, as depicted in Figures 3.2 (j,k). Its SAED matched well with rutile IrO_2, as shown in Figure 3.2 (l).

IrO_x TKK is composed of a well-connected network of IrO_x nanoparticles, somewhat similar to IrO_x-NH_4OH. The volume mean diameter ($\hat{d}_{vol}$) of the nanoparticles was approximately 7.2 nm derived from analyzing 164 particles. The particle size distribution has been provided in Figure B.2. The SAED pattern of IrO_x TKK is X-ray amorphous, similar to the nanoparticles observed in IrO_x-NH_4OH and to the SAED pattern reported by Tan et al.[6]

In summary, the TEM results presented in Figure 3.2 show the thermal decomposition of $H_2IrCl_6.xH_2O$ results in the development of agglomerates in all synthesized samples. In IrO_2, the agglomerates are composed of IrO_2 nanoneedles. The addition of chlorine, as observed in IrO_2-HCl promotes the formation of larger agglomerates where $IrCl_3$ dominated the composition. The elimination of chlorine from the lattice structure, as seen in the case of IrO_2-NH_4OH, induced the formation of amorphous IrO_x nanoparticles. Although present in significantly lower quantities compared to

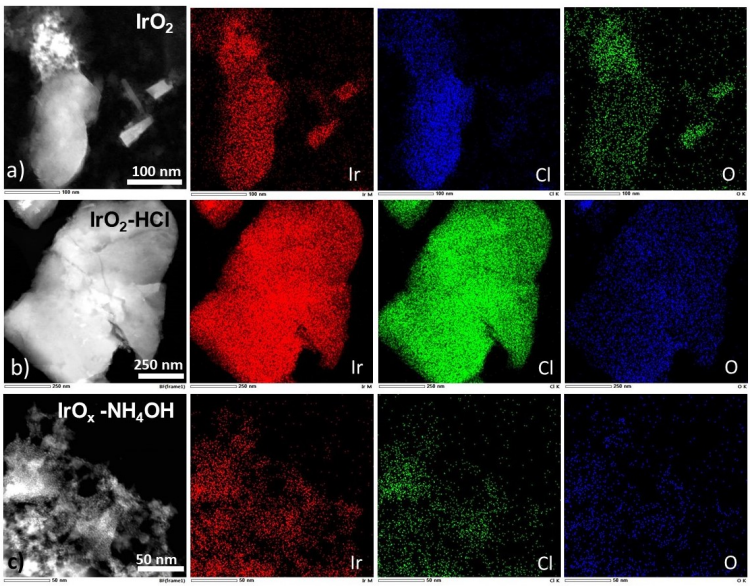

Figure 3.3: Dark field image and S/TEM–EDX signal maps for IrO_2, IrO_2-HCl, and IrO_2 NH_4OH.

the other synthesized catalysts, agglomerates with a rutile nature were still observable. IrO_x TKK and IrO_2 AA were used as benchmarks, each possessing distinct microstructures, where IrO_x TKK consisted entirely of potentially amorphous IrO_x, while IrO_2 was composed of entirely rutile IrO_2.

To obtain the local nanoscale elemental composition of IrO_2, IrO_2-HCl and IrO_x-NH_4OH, STEM-EDX was performed, as shown in Figure 3.3. The signal maps obtained from S/TEM-EDX analysis provide clear evidence of the presence of Ir, Cl, and O in all three samples, thus confirming the existence of chlorine. Notably, the presence of chlorine is notably more prominent in the IrO_2 and IrO_2-HCl samples when compared to the IrO_x-NH_4OH sample. Additionally, it is evident that Ir is more uniformly distributed in IrO_x-NH_4OH sample than in their counterparts. The chlorine signals are detected to be significantly higher in agglomerates, as shown in Figure 3.3 (a) and (b).

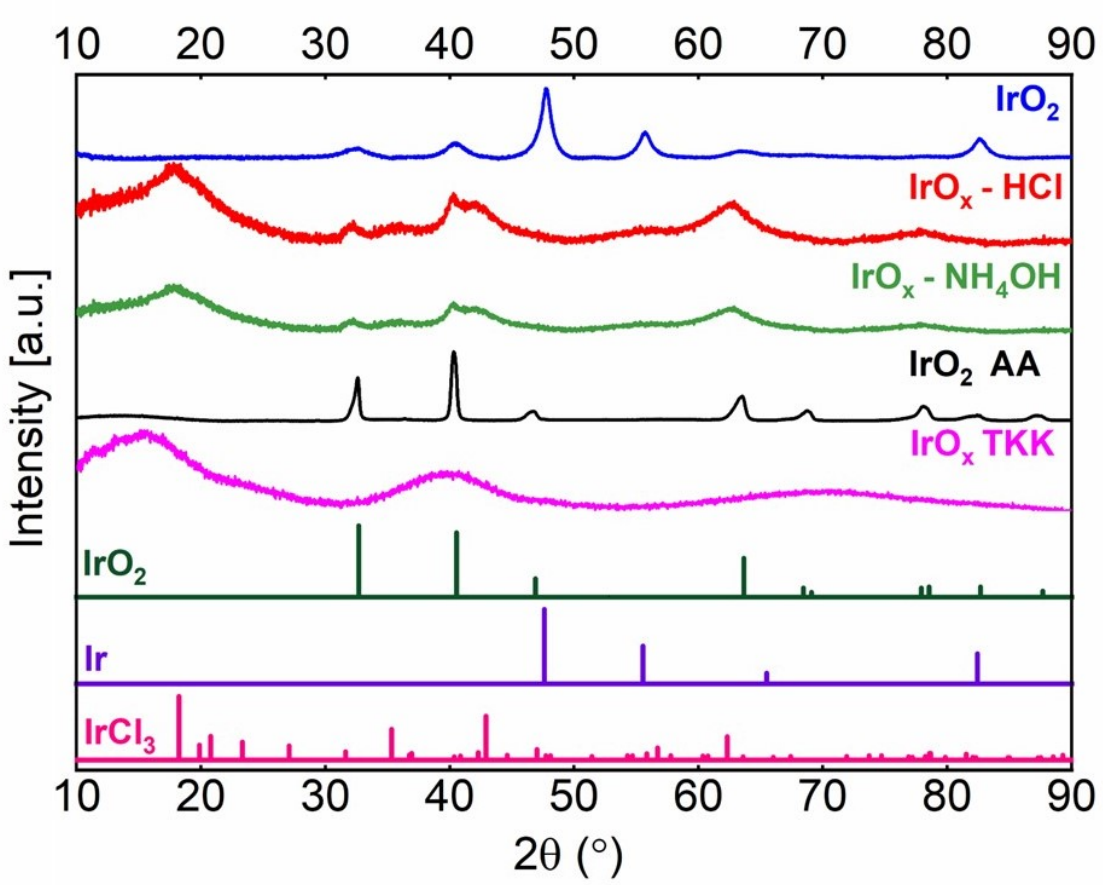

Figure 3.4: XRD diffraction peaks of IrO_2, IrO_2-HCl, and IrO_x-NH_4OH, IrO_2 AA and IrO_x TKK. References for IrO_2 (PDF 00-015-0870), Ir (PDF 00-006-0598), and $IrCl_3$ (PDF 04-005-4686).

X-ray diffraction (XRD)

The crystal structure of the catalysts was examined using XRD, as shown in Figure 3.4. The diffraction pattern of IrO_2 corresponds to a combination of rutile IrO_2 (PDF 00-015-0870) and metallic state Ir peaks (PDF 00-006-0598). The presence of metallic Ir in commercial IrO_2 samples has also been previously reported in the literature.[286], [304] In contrast, the XRD profile of IrO_2-HCl displays broad peaks associated with both IrO_2 and $IrCl_3$ (PDF 04-005-4686), in line with the SAED results shown in Figure 3.2. The broader peaks imply that the addition of HCl to the precursor during synthesis potentially induced lattice defects in the IrO_2-HCl sample. The

XRD peaks of IrO_x-NH_4OH also matched with rutile IrO_2 and $IrCl_3$. The broader peaks observed may be attributed to either lattice defects or the smaller particle size. The contribution of $IrCl_3$ peaks is less significant in IrO_x-NH_4OH compared to that observed in IrO_2-HCl.

The XRD profile of commercial IrO_2 AA exhibited sharp peaks that were strongly indexed to tetragonal IrO_2 (PDF 00-015-0870). IrO_x TKK showcased broad peaks and can be considered XRD amorphous. The X-ray diffraction patterns of all the catalysts are in line with the SAED findings reported in Section 3.3.1.

X-ray photoelectron spectroscopy (XPS)

The oxidation state of Ir, O, and Cl, along with the surface composition of the five catalysts were evaluated by XPS. Figure 3.5 (a,b) shows the deconvoluted Ir 4f and O 1s spectra of IrO_2, IrO_2-HCl, IrO_x-NH_4OH, IrO_2 AA, and IrO_2 TKK (top to bottom). Iridium is present in Ir(III) and Ir(IV) oxidation states in all the catalysts. The asymmetric line peak of Ir $4f_{7/2}$ (Ir $4f_{5/2}$) in Ir(IV) is located at 62.0 ± 0.25 eV (65.0 ± 0.25 eV), while that of Ir(III) is located at 62.5±0.2 eV (65.5±0.2 eV) in all the samples. The fitting parameters used for deconvolution have been provided in Sections B.1.4 and B.1.4. Commercial IrO_2 AA showed the highest contribution from Ir(IV), at nearly 67%, while IrO_2-HCl showed the least contribution, at 13.5%. The atomic ratios of Ir(IV) and Ir(III) have been provided in Figure 3.7 (a). The increasing order of the atomic ratio of Ir(III)/Ir(IV) is as follows: IrO_2 AA < IrO_x TKK < IrO_2 < IrO_x-NH_4OH< IrO_2-HCl. Even though the atomic composition of Ir(III) is highest in IrO_2-HCl, it might be attributed to the contribution from $IrCl_3$, since Ir exists in the Ir(III) oxidation state in both IrOOH and $IrCl_3$, and the binding energies of hydrated IrO_2 and $IrCl_3$ are nearly identical, making them challenging to distinguish.[305] SAED and XRD analysis have previously identified a notable presence of

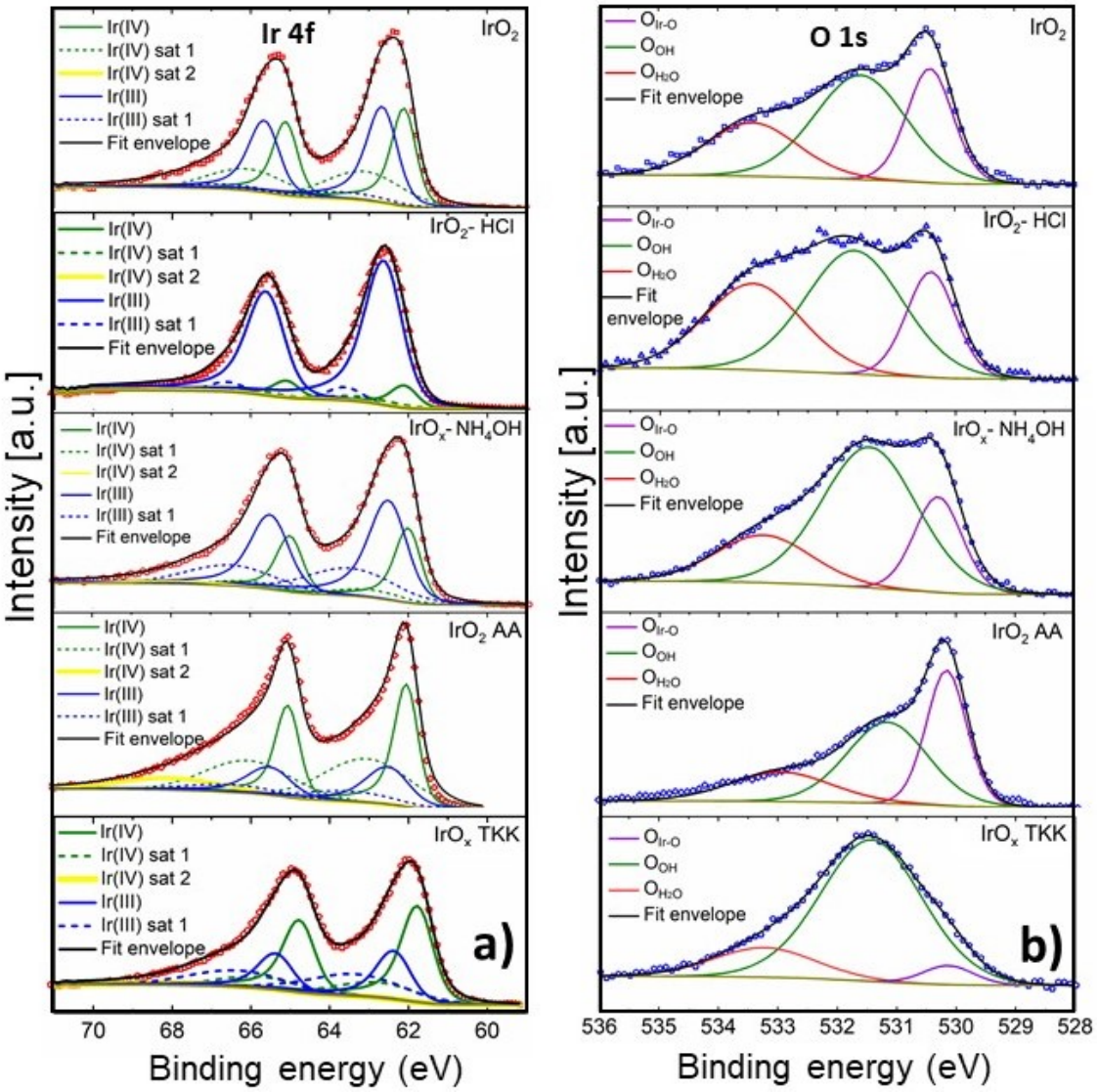

Figure 3.5: XPS profiles (a) Ir 4f; (b) O 1s of IrO_2, IrO_2-HCl, IrO_x-NH_4OH, IrO_2 AA and IrO_x TKK fresh.

$IrCl_3$ in IrO_2-HCl. In IrO_x- NH_4OH, the Ir(III) species constitute 70% of the overall surface composition. As a result of the reduced presence of chlorine in IrO_x-NH_4OH, the Ir(III) species could predominantly be associated with IrOOH, which is known for its high activity.[6], [306]

The key differences between the five samples were detected by deconvoluting the O 1s peaks into three peaks, the lattice oxygen (O_{Ir-O}); oxygen in the hydroxyl group/-coordinatively unsaturated oxygen (O_{OH}); [304] and absorbed water (O_{H_2O}). The three peaks were located at 530.3 ± 0.2 eV, 531.5 ± 0.3 eV, and 533.2 ± 0.3 eV in all the samples as shown in Figure 3.5.[305], [307] The percentage composition of the different oxygen species has been reported in Figure 3.7 (b). The atomic percentages of O_{Ir-O}, O_{OH} , and O_{H_2O} in commercial IrO_2 AA are 36%, 44%, and 20% respectively, where IrO_2 AA constitutes the maximum contribution from O_{Ir-O} among all the samples. In contrast, amorphous IrO_x TKK contains 79% O_{OH}, while O_{Ir-O} contributes only 5% and O_{H_2O} accounts for 16%. In the literature, a direct correlation was observed between higher O_{OH} concentration and superior activity, while a higher O_{Ir-O} concentration was associated with limited activity.[77], [100], [304] In the case of IrO_x-NH_4OH, the predominant species is O_{OH}, accounting for 60% of the O 1s spectra, higher than in IrO_2 (48%) and IrO_2-HCl (47%). Even though IrO_x-NH_4OH exhibited features of both rutile IrO_2 and amorphous IrO_x in the SAED results, a high concentration O_{OH} species in IrO_x-NH_4OH is promising, as it is considered essential for achieving high OER activity.[100], [306], [308] IrO_2 and IrO_2-HCl possess a similar percentage of O_{Ir-O}, however, IrO_2-HCl possesses a slightly larger contribution from O_{H_2O} (33% vs. 25%) which may be attributed to the presence of $IrCl_3$.[305] The literature has reported the presence of O_{H_2O} in both hydrous and anhydrous forms of $IrCl_3$.[305]

Deconvolution of the Cl 2p spectra exhibited two distinct states, namely Ir-Cl and

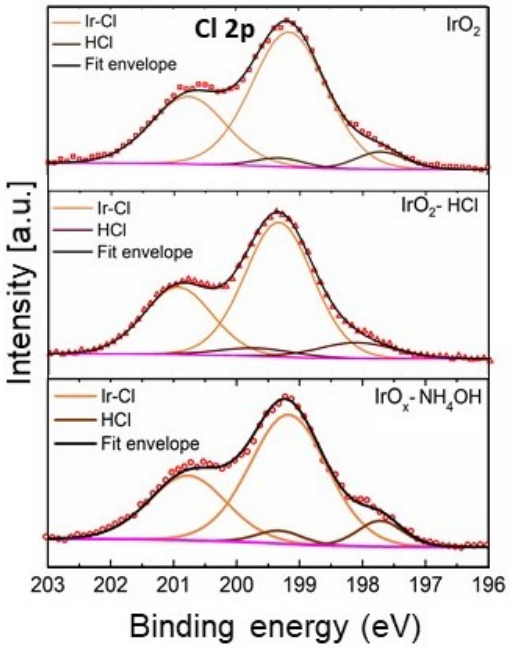

Figure 3.6: Cl 2p spectra of IrO_2, IrO_2-HCl, IrO_x-NH_4OH fresh catalysts detected by XPS.

HCl, as shown in Figure 3.6. Ir-Cl species was the most prevalent species in all the samples, as shown by the Cl $2p_{3/2}$ peaks observed at a binding energy of 199.4 $\pm$ 0.1 eV. The binding energy of the HCl peak in IrO_2-HCl, situated at 198.1 eV, differs from the values observed at 197.7 eV in IrO_2 and IrO_x-NH_4OH. The difference in binding energies may be attributed to the nature of HCl found in the samples. According to a similar study performed on $RuCl_3$ by Morgan, the HCl peak observed in IrO_2-HCl, might be attributed to solvated HCl while those in IrO_2 and IrO_x-NH_4OH may be attributed to physisorbed HCl.[309] Nonetheless, the Cl($2p_{3/2}$) signal at $\sim$ 198 eV is attributed to excess surface chloride, assigned as HCl.[305]

Atomic elemental composition of the surface of the synthesized catalysts IrO_2, IrO_2-HCl, and IrO_x-NH_4OH was obtained from the XPS survey spectra of the catalysts and has been reported in Table 3.2. The results quantitatively agree with the SEM-EDX findings reported in Section 3.3.1, Cl to Ir ratio increased on the surface of

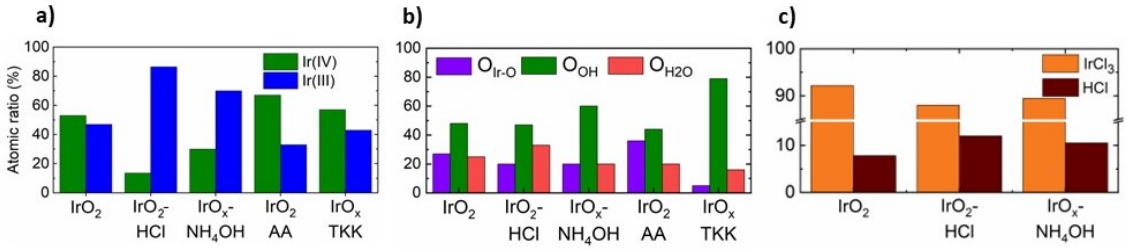

Figure 3.7: (a) Atomic ratio of Ir (III) and Ir(IV) in Ir 4f species detected by XPS; (b) Atomic ratio of O_{Ir-O}, O_{OH}, and O_{H_2O} in O 1s species; (c) Atomic ratio of Ir-Cl and HCl in Cl 2p species in the five catalysts.

Table 3.2: Summary of the elemental atomic composition of catalysts obtained using XPS survey spectra

Samples	Atomic % from XPS survey spectra				Cl:Ir	O:Ir
	Ir	Cl	O	N		
IrO_2	24.4	32.5	42	—	1.3	1.7
IrO_2-HCl	22.1	39.3	38.6	—	1.8	1.7
IrO_x-NH_4OH	22.8	23.7	48.3	5.2	∼1	2.1
IrO_2 AA	28.7	6	65.3	—	0.2	2.3
IrO_x TKK	22	—	77	—	—	3.5

the IrO_2-HCl sample compared to the synthesized IrO_2 sample. On the other hand, the Cl to Ir ratio decreased in the IrO_x-NH_4OH sample treated with NH_4OH. These results confirm that in IrO_2-HCl and IrO_x-NH_4OH samples, chlorine was added and removed from both the catalyst surface and the bulk respectively when compared to the IrO_2 catalyst.

3.3.2 Thermogravimetric analysis (TGA)

TGA was used to monitor the mass loss/gain of the H_2IrCl_6 precursors as a function of increasing temperature in air from room temperature to 750°C. This approach aimed to gain insights into the various pathways involved in the synthesis of IrO_2, IrO_2-HCl, and IrO_x-NH_4OH. The TGA profiles of IrO_2, IrO_2-HCl, and IrO_x-NH_4OH samples are shown in Figure 3.8 (a) and Figure B.3 (a-c). Derivative thermogravimetry (DTG)

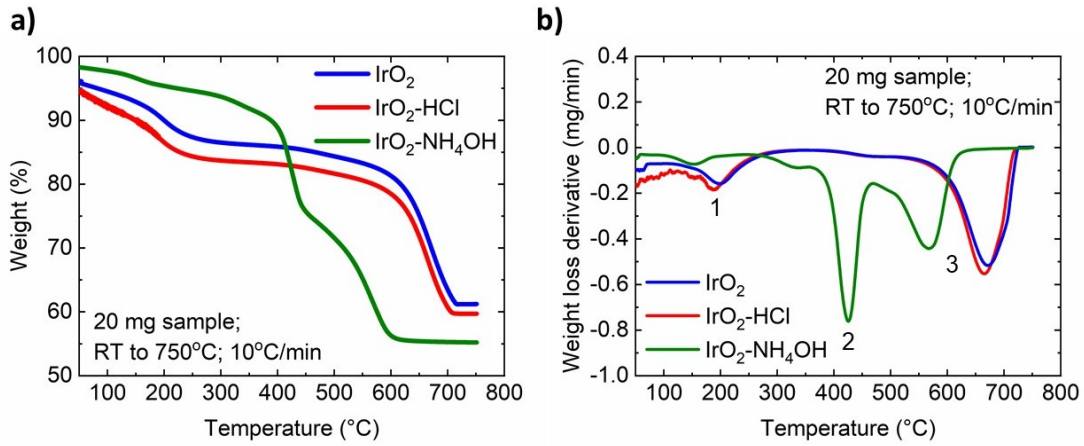

Figure 3.8: (a) TGA of IrO_2 (H_2IrCl_6 heated at 120°C for 4 h), IrO_2 -HCl (H_2IrCl_6 + HCl heated at 120°C for 4 h), and IrO_x-NH_4OH (H_2IrCl_6 + NH_4OH heated at 120°C for 4 h); (b) Derivative thermogravimetry (DTG). Decomposition of 20 mg of the dried precursor samples in air (flow rate = 50 ml/min) from room temperature to 750 °C, at the heating rate of 10 °C·min^{-1}.

of the samples has been plotted in Figure 3.8 (b) and Figure B.3 (a-c). Based on the study performed by Jang et al.,[310] the decomposition of H_2IrCl_6 under air proceeds in the form of the following reactions:

$$H_2IrCl_6 \cdot nH_2O \longrightarrow IrCl_3 + 2\ HCl + \frac{1}{2}\ Cl_2 + n\ H_2O \tag{3.4}$$

$$IrCl_3 + O_2 \longrightarrow IrO_2 + \frac{3}{2}\ Cl_2 \tag{3.5}$$

$$IrCl_3 \longrightarrow Ir + \frac{3}{2}\ Cl_2 \tag{3.6}$$

Reaction in equation 3.4 takes place between 25°C-300°C, while reaction in equation 3.5 and equation 3.5 are competing reactions occurring in the temperature window of 450°C-650°C.

As shown in Figure 3.8 (b), the thermal decomposition of H_2IrCl_6 and H_2IrCl_6+HCl can be divided into two steps [310]: weight loss from 25°C-300°C occurs as a result of loss of H_2O, accompanied by the loss of HCl and Cl_2 (Peak 1); (2) oxidative degradation of anhydrous $IrCl_3$ (Peak 3) to IrO_2 and Cl_2 between 450°C-650°C. Incomplete

decomposition can compete with oxidative degradation to produce Ir, along with IrO_2. The presence of iridium has been identified in the X-ray diffraction analysis of IrO_2, as shown in Figure 3.4. Two distinct peaks were observed in the TGA profiles of IrO_2 and IrO_2-HCl at 190°C-200°C (Peak 1), and 665°C-675°C (Peak 3). These peaks were likewise detected in the IrO_x-NH_4OH sample, albeit occurring at a reduced temperature of 150°C and 570°C, potentially due to the smaller particle size, as indicated by TEM findings. In addition, a distinct peak between 375°C-475°C was detected, which was preceded by a shoulder peak at 340°C. Previous studies attribute the peak formation between 400°C and 500°C to the transition of iridium oxohydroxide ($IrO_x(OH)_y$) to iridium oxide IrO_x.[247], [311] Massué et al. associated the peak observed between 150°C to 500°C with hydroxyl decomposition.[101]

The precursor in H_2IrCl_6 loses approximately 7.4 wt.% of its mass between room temperature and 750°C. Water desorption accounted for approximately 2.2 wt. % of the weight loss, while the decomposition of $IrCl_3$ to Cl_2 and IrO_2, or into Ir and Cl_2, depending on the nature of the decomposition, accounted for 5.2 wt. % of the weight loss. H_2IrCl_6 + HCl exhibited an overall water loss percentage of 8%, 2.8 wt.% for the first peak at 190°C, and 5.2 wt.% for the second. In IrO_x-NH_4OH, physisorbed water accounted for only 0.7% of the total water loss, while hydroxyl decomposition/ transformation of Ir oxohydroxide ($IrO_x(OH)_y$) to iridium oxide IrO_x accounted for 4.4 wt. % of the weight loss.[101] This falls in line with the XPS results presented earlier where IrO_x-NH_4OH surface was found to be rich in O_{OH} species.

In summary, the TGA profiles of IrO_2, IrO_2-HCl, and IrO_x-NH_4OH indicate that while IrO_2 and IrO_2-HCl share a common synthesis route involving the decomposition of H_2IrCl_6 to $IrCl_3$ and volatiles, followed by the decomposition of $IrCl_3$ to IrO_2 and volatiles (as described by Equations 3.4, 3.5, and 3.6); IrO_x-NH_4OH follows a similar route but in addition, also exhibits significant weight loss due to the decomposition

of $IrO_x(OH)_y$ to IrO_x. Notably, decomposition in IrO_x-NH_4OH occurs at a lower temperature than in IrO_2 and IrO_2-HCl, likely due to the smaller particle size.

Physicochemical characterization of the catalysts such as EDX, SEM, TEM, XRD, XPS, and TGA was used to obtain crucial insights into a catalyst's structural, compositional, and surface properties, that might influence their behavior and performance in OER catalysis. The intended modulation in chlorine content in different samples, in the increasing order of IrO_x-NH_4OH < IrO_2 < IrO_2-HCl was confirmed by SEM-EDX and XPS. SEM also showed increased pitting in IrO_2-HCl and increased surface roughness in IrO_x-NH_4OH, as compared to the IrO_2 sample. According to the TEM observations, IrO_2 and IrO_2-HCl were primarily made up of needle clusters and agglomerates, with IrO_2 having a higher percentage of needle clusters. The agglomerates detected in IrO_2-HCl were rich in $IrCl_3$, which was confirmed by SAED. IrO_x-NH_4OH showcased a network of amorphous Ir oxide nanoparticles and rutile IrO_2 agglomerates that are entirely encapsulated by the nanoparticles. The presence of small IrO_x nanoparticles potentially caused the peak broadening of the XRD profile of IrO_x-NH_4OH. The addition of NH_4OH to the H_2IrCl_6 precursor in IrO_x-NH_4OH, potentially resulting in lattice defects, could also explain the observed peak broadening, since a similar phenomenon was observed in IrO_2-HCl, despite the presence of larger agglomerates and the absence of IrO_x nanoparticles. XRD profile of IrO_2 detected a significant presence of Ir along with tetragonal IrO_2, the former could be formed as a result of incomplete decomposition of the precursor. XPS showed a rich presence of both Ir(III)/Ir(IV) species and O_{OH} species in IrO_x-NH_4OH, crucial for OER. In contrast, IrO_2-HCl exhibited a notable abundance of Ir(III) species but lacked a proportional O_{OH} presence, indicating that the elevated Ir(III) content is likely attributed to the presence of $IrCl_3$. The TGA profiles of IrO_2 and IrO_2-HCl align with the two-step decomposition pathway of H_2IrCl_6 to IrO_2 and Ir, as previously documented in Jang et al.'s work.[310] However, IrO_x-NH_4OH exhibits a third

peak, indicating the decomposition of $IrO_x(OH)_y$ to IrO_x, which is not present in the previously mentioned catalysts. This demonstrates the coexistence of two distinct types of active sites in IrO_x-NH_4OH, generated by the decomposition of $IrO_x(OH)_y$ and $IrCl_3$.

3.3.3 Electrochemical characterization

Initial electrochemical surface area (ECSA) of the catalysts

The electrocatalysts were activated prior to electrochemical characterization. During catalyst preconditioning, 50 cycles of cyclic voltammetry (CV) were performed in N_2 saturated environment in an unstirred electrolyte (1.0 M H_2SO_4) at a scan rate of 500 $mV{\cdot}s^{-1}$ in the potential range of 0.05 V_{RHE} to 1.53 V_{RHE}. The preconditioning step served the purpose of cleaning the catalyst surface as well as forming highly active hydrous Ir(III)/Ir(IV) species on the catalyst surface.[6], [51], [53], [261], [262] Keeping the upper potential limit at 1.53 V_{RHE} ensured surface oxidation of any Ir on the surface to its irreducible oxide form.[6]

Figures 3.9 (a,b) show the CV profiles of the catalysts recorded after preconditioning in the potential window of 0 V_{RHE}-1.53 V_{RHE} at the scan rate of 40 $mV{\cdot}s^{-1}$. The measurements were conducted in an unstirred electrolyte solution under constant N_2 bubbling. Using the average of 5 CV profiles, the electrochemical surface area (ECSA) of the catalysts was estimated by measuring the total anodic charge under the cyclic voltammogram in the potential window of 0.4 V_{RHE}-1.25 V_{RHE}. The total charge in the potential window was corrected for double-layer capacitance. The anodic charges correspond to the chemisorption of oxygenated species or/and deprotonation of hydrous iridium oxide. The detailed method has been described in the work of Tan et al.[6]

The ECSA of the three synthesized catalysts is reported in Table 3.3, and can be

Table 3.3: Summary of electrochemical performance of the catalysts

Sample	ECSA ($m^2.g_{Ir}^{-1}$)	Loading, $\mu g_{Ir} \cdot cm_{geo}^{-2}$	j_{geo}, ($mA \cdot cm_{geo}^{-2}$)	j_{mass}, ($A \cdot g_{Ir}^{-1}$)	j_{ECSA}, ($mA \cdot cm_{Ir\ ECSA}^{-2}$)
IrO_2	1.4	92	0.4	4	0.3
IrO_2-HCl	1.4	85.5	0.15	1.4	0.1
IrO_x-NH_4OH	11.7	89.5	6	64	0.5
IrO_2 AA	1.1	123.5	0.6	5	0.4
IrO_x TKK	78	100	65	650	0.8

Note: Measured at a potential of 1.55 V_{RHE}

arranged in increasing order as IrO_2-HCl (1.4 $m^2 \cdot g_{Ir}^{-1}$) = IrO_x (1.4 $m^2 \cdot g_{Ir}^{-1}$) < IrO_x-NH_4OH (11.7 $m^2 \cdot g_{Ir}^{-1}$). The ECSA of IrO_x-NH_4OH was an order of magnitude higher than its synthesized counterparts. This may be attributed to the presence of porous IrO_x nanoparticles in IrO_x-NH_4OH that increase the number of active sites on the surface of the catalyst that are available for OER.[312] The ECSA of IrO_2 AA (1.1 $m^2 \cdot g_{Ir}^{-1}$) was comparable to that of IrO_2 and IrO_2-HCl. The state-of-the-art IrO_x TKK exhibited exceptionally high ECSA (78 $m^2 \cdot g_{Ir}^{-1}$) compared to the other catalysts in this study. The high ECSA might be related to the porous nature of a well-connected network of IrO_x nanoparticles which allows for higher catalyst utilization as shown in Figure 3.2.[6] While IrO_x-NH_4OH displays a similar microstructure, composed of IrO_x nanoparticles, it also possesses large rutile agglomerates that are often surrounded by the IrO_x nanoparticles. Due to the presence of larger agglomerates, the surface-to-volume ratio of IrO_x-NH_4OH is notably inferior to that observed in IrO_x TKK, leading to a reduction in ECSA by a factor of seven.

Initial electrochemical activity

Linear sweep voltammetry (LSV) was used to determine the electrocatalysts' performance. iR-corrected (85%) polarisation curves were measured at 1800 rpm in O_2-

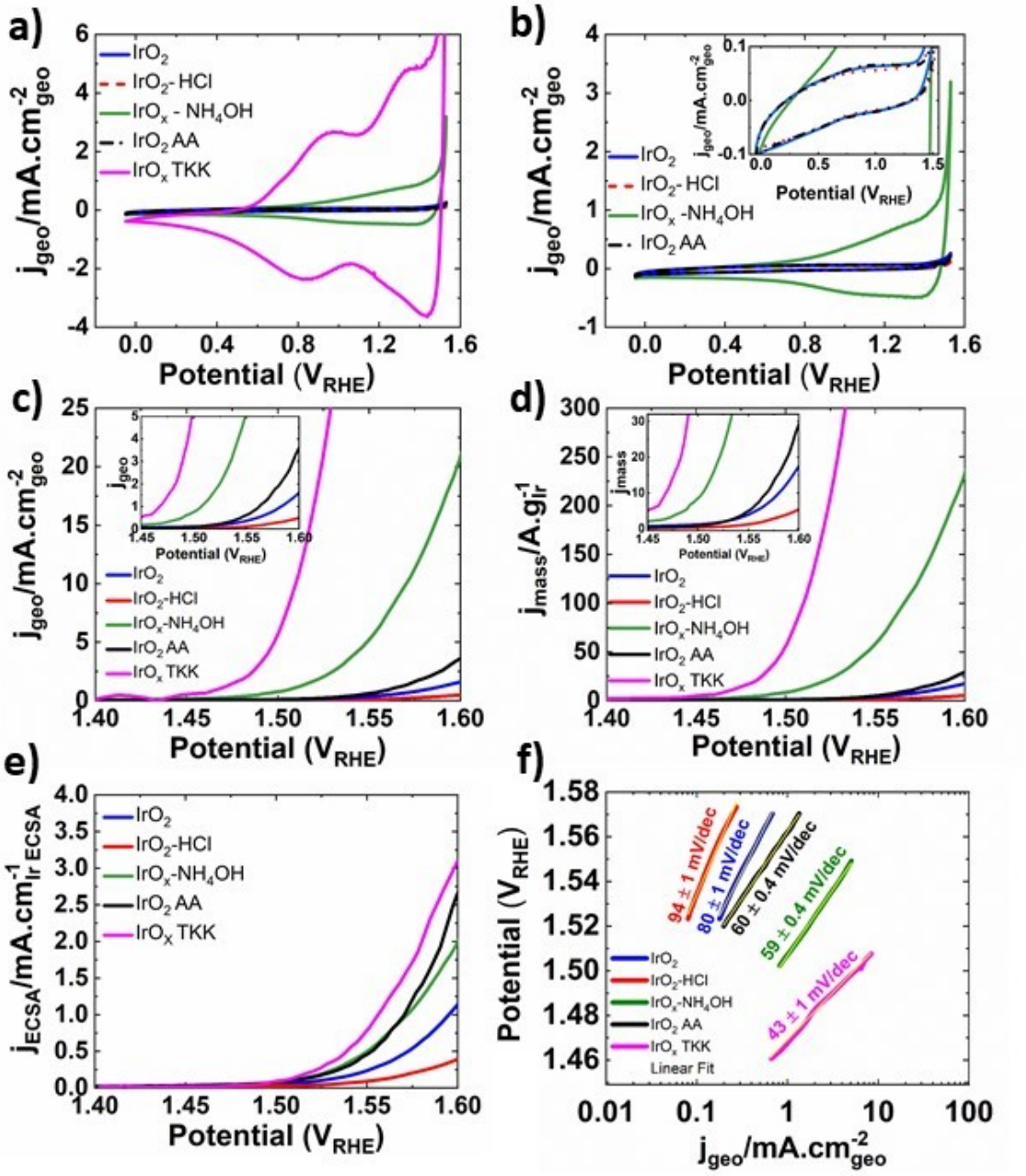

Figure 3.9: (a,b) Initial cyclic voltammograms of the catalysts measured at a scan rate of 40 $mV \cdot s^{-1}$ with the upper potential limit of 1.53 V_{RHE} in N_2 saturated environment (c) iR-corrected (85%) polarization curves measured at a scan rate of 10 $mV \cdot s^{-1}$ in O_2 saturated electrolyte, normalized to the geometric area (d) iR-corrected (85%) normalized to the mass of Ir (specific activity) (e) iR-corrected polarization curves normalized by Ir ECSA (f) Tafel slope measured between 1.50 V_{RHE}-1.55 V_{RHE}.

saturated electrolyte between 1.0 V_{RHE}-1.6 V_{RHE} at a scan rate of 10 $mV{\cdot}s^{-1}$. The polarization curves can be treated as initial performance indicators of the electrocatalysts.

Figure 3.9 (c) shows the activity of the catalyst normalized by the geometric area of the working electrode (0.196 cm^2). Near identical quantities of the total catalyst were deposited on the electrode to mitigate differences due to external mass transfer limitations. Figures 3.9 (d) and (e) show the mass normalized activity (specific activity) and Ir ECSA normalized activity (intrinsic activity) of the catalysts. The synthesized catalysts can be arranged in the order of increasing geometric, intrinsic, and mass activity as follows: IrO_2-HCl < IrO_2 < IrO_x-NH_4OH. IrO_x-NH_4OH exhibited the highest mass activity of 64 $A{\cdot}g_{Ir}^{-1}$ at 1.55 V_{RHE} among the synthesized catalysts. IrO_2 and IrO_2-HCl exhibited an order of magnitude lower activity, measuring at 4 $A{\cdot}g_{Ir}^{-1}$ and 1.4 $A{\cdot}g_{Ir}^{-1}$ respectively. The higher mass-normalized activity of IrO_x-NH_4OH is directly associated with the increase in the number of accessible active Ir sites (ECSA) for OER in IrO_x-NH_4OH.[6], [72], [100] Hence, state-of-the-art IrO_x TKK, owing to its even higher ECSA, exhibited an order of magnitude higher mass activity of 650 $A.g_{Ir}^{-1}$ at 1.55 V_{RHE}. Comparing IrO_2 and IrO_2-HCl, there is a clear disparity in the mass activity of the catalysts despite having identical ECSA. It is possible that owing to the larger presence of Cl in IrO_2-HCl, it experiences larger poisoning of Ir active sites that result in lower activity of the IrO_2-HCl compared to IrO_2. The performance of IrO_2 was also compared to commercial IrO_2 AA catalysts, owing to their similar physicochemical properties. Their mass activities of 4 $A.g_{Ir}^{-1}$ and 5 $A.g_{Ir}^{-1}$ show a similar order of magnitude at 1.55 V_{RHE}, which are notably lower than that of IrO_x TKK and IrO_x-NH_4OH.

Figure 3.9 (d) shows that IrO_x-NH_4OH exhibited the highest intrinsic activity among the synthesized catalysts, reaching a value of 0.5 $mA{\cdot}cm_{Ir\ ECSA}^{-2}$ at 1.55 V_{RHE}.

The improved intrinsic activity of IrO_x-NH_4OH may be attributed to the presence of Ir(III)/Ir(IV) species and larger concentration of surface hydroxyl species (O_{OH}), prerequisites for highly activity OER catalysts as reported in the X-ray photoelectron spectroscopy (XPS) section.[75], [100], [266], [313] In comparison, IrO_2 was able to achieve 0.3 $mA{\cdot}cm^{-2}_{Ir\ ECSA}$ at 1.55 V_{RHE} respectively. Among the catalysts studied in this work, IrO_2-HCl demonstrated the worst specific activity, reaching only 0.1 $mA{\cdot}cm^{-2}_{Ir\ ECSA}$ at 1.55 V_{RHE} respectively. The observed poor intrinsic activity of IrO_2-HCl provides additional evidence supporting the notion that the Ir(III) species detected in the XPS results may not be associated with Ir-oxyhydroxides, but rather with $IrCl_3$. The intrinsic activity of IrO_2-HCl suffered, possibly due to the larger Cl: Ir ratio, as reported in Table 3.2.[299], [314]

Commercial benchmarks IrO_2 AA and IrO_x TKK exhibited intrinsic activity of 0.4 $mA{\cdot}cm^{-2}_{Ir\ ECSA}$ and 0.8 $mA{\cdot}cm^{-2}_{Ir\ ECSA}$ respectively. The reason behind the sudden increase in the intrinsic activity of IrO_2 AA above 1.57 V_{RHE}, surpassing the surface Ir(III) and O_{OH}-rich IrO_x-NH_4OH catalyst is not clear and requires further probing. However, looking at the kinetic region at a lower potential, <1.57 V_{RHE} it is clear that the activity of the IrO_2 AA and IrO_x-NH_4OH follow a similar trend. It is possible that the activity of IrO_x-NH_4OH suffers at higher potential (above 1.57 V_{RHE}) due to mass transfer limitations, such as O_2 bubble formation which blocks the active sites of the catalyst.[207] On the other hand, the performance of IrO_x TKK exceeds all the other catalysts, including commercial rutile IrO_2 AA studied in this work, in agreement with the work of Tan et al.[6]

Tafel slopes of the catalysts tested in this study have been reported in Figure 3.9 (f) and Table 3.3. Tafel slope analysis was conducted within a specific kinetic potential window of the OER for each catalyst. The selected potential window for IrO_2 and IrO_2 was 1.52 V_{RHE}-1.57 V_{RHE} for IrO_2, IrO_2-HCl and IrO_2 AA. The kinetic window

for IrO_x TKK was 1.46 V_{RHE}-1.51 V_{RHE} and for IrO_x NH_4OH was 1.50 V_{RHE}-1.55 V_{RHE}. The Tafel slopes of IrO_2, IrO_2-HCl, and IrO_x-NH_4OH were as follows: 80±2 mV/dec, 94±4 mV/dec, and 59±0.4 mV/dec. The reduction in the Tafel slope value observed for IrO_x-NH_4OH suggests a different OER mechanism when compared to IrO_2 sample. Commercial IrO_2 AA showcases a Tafel slope of 60±1 mV/dec. At low current densities, Tafel slopes for IrO_2 are generally observed in the range of 60 mV/dec.[315]–[317] IrO_x TKK possesses the lowest Tafel slope, with a value of 43±1 mV/dec, showing the fastest kinetics among the studied catalysts. IrO_2-HCl, on the other hand, showcases the highest Tafel slope. Vos et al. investigated the parallel evolution of chlorine and oxygen on IrO_x electrodes in chlorine-based electrolytes and found that chloride adsorption significantly slowed down the OER, by blocking sites which led to an increase in the Tafels slope from ∼40 mV/dec to ∼120 mV/dec when CER is competing with the OER. Although a direct correlation cannot be inferred from these findings, they do provide some insight into the elevated Tafel slope observed in IrO_2 and IrO_2-HCl.[299]

3.4 Conclusions

Herein, we investigated the effect of residual chlorine from the H_2IrCl_6 precursor on the physicochemical and electrochemical properties of the catalysts. This was achieved by studying three variations of Ir oxide catalyst produced by the thermal decomposition of H_2IrCl_6 at 400°C for 2 h, namely IrO_2, IrO_2-HCl, and IrO_x-NH_4OH. In IrO_2-HCl, HCl was added to the precursor solution to increase the chloride content in the catalyst, while in IrO_x-NH_4OH, NH_4OH was added to reduce the chloride content.

Both SEM-EDX and XPS survey spectra show an increase in chloride content in IrO_2-HCl and a decrease in chloride content in IrO_x-NH_4OH. Modification in the ratio

of NH_4OH to the H_2IrCl_6 may help further reduce the amount of chloride content in the catalyst. Commercial catalysts, IrO_2 AA and IrO_x TKK were also studied as rutile IrO_2 and amorphous IrO_x benchmarks. TEM of the catalysts revealed that chlorine species hinder the appropriate control of the particle shape and size during the synthesis of Ir-oxide. While IrO_2 consists mainly of rutile IrO_2 nanoneedles that often form agglomerates, the addition of HCl led to the formation of much larger agglomerated particles in addition to IrO_2 nanoneedles. SAED analysis of the samples showed that these agglomerates primarily consisted of $IrCl_3$. IrO_x-NH_4OH consisted predominantly of 4 nm IrO_x nanoparticles and a smaller proportion of rutile IrO_2 agglomerates. XRD analysis confirmed the presence of rutile IrO_2 in all three catalysts. However, the XRD profile of IrO_2-HCl showed much broader peaks than IrO_2, with key peaks corresponding to $IrCl_3$.

XPS analysis of IrO_x-NH_4OH suggests the presence of mixed Ir(III)/Ir(IV) species with a high Ir(III) to Ir(IV) ratio as well as high concentrations of O_{OH} species, the basic constituents of iridium oxohydroxides ($IrO_x(OH)_y$) and precursors for achieving high catalytic activity in OER. TGA results also confirm the presence of the presence of iridium oxohydroxides ($IrO_x(OH)_y$) in IrO_x-NH_4OH. In the case of IrO_2-HCl, a high ratio of Ir(III) to Ir(IV) was observed, but this phenomenon can be attributed not to Ir oxohydroxides but to the existence of $IrCl_3$ in the Ir(III) oxidation state.

Electrochemical analysis of the catalysts indicated a substantial improvement in both activity and stability for IrO_x-NH_4OH, compared to IrO_2, while IrO_2-HCl exhibited a decline in activity. There appears to be a very good correlation between the level of Cl measured by XPS and EDX for the catalysts studied, and the activity. Compared to IrO_2, IrO_x-NH_4OH exhibited more than an order-of-magnitude increase in Ir ECSA (11.7 $m^2 \cdot g_{Ir}^{-1}$ vs 1.4 $m^2 \cdot g_{Ir}^{-1}$) and mass activity of the catalyst (65 $A \cdot g_{Ir}^{-1}$ vs. 4 $A \cdot g_{Ir}^{-1}$ at 1.55 V_{RHE}), while activity decreased by almost three-fold (4 $A \cdot g_{Ir}^{-1}$

vs. 1.4 $A \cdot g_{Ir}^{-1}$ at 1.55 V_{RHE}) in IrO_2-HCl. The Ir ECSA of IrO_2 and IrO_2-HCl were identical.

This study underscores the significance of eliminating residual chloride from the catalysts and proposes an approach to accomplish this without resorting to intricate synthesis methods or subjecting the catalysts to excessively high temperatures that could irreversibly alter their morphology. Subsequent research, such as employing suitable support to mitigate the dissolution of IrO_x-NH_4OH, could pave the way for the development of active and durable catalysts in the future.

Chapter 4

Conclusions and future work

4.1 Conclusions

The presented thesis focused on the development of Ir oxide-based catalysts for acidic OER.

In this study, the following research objectives were successfully completed:

1. Synthesis of supported Ir-oxide catalyst using incipient wetness impregnation method (IWI) of commercial supports with commercial molecular Ir precursor (H_2IrCl_6).

2. Development of a supported Ir oxide-based catalyst using non-conductive ZrO_2 support. Study of the strong metal-support interactions between IrO_x and ZrO_2, and evaluation of catalyst performance in a three-electrode rotating disk electrode set-up.

3. Investigation of the impact of residual chloride from H_2IrCl_6 precursor on the physicochemical properties of IrO_2 catalyst, prepared by thermal decomposition.

The findings of this study underscore the viability of using incipient wetness impregnation method (IWI) with molecular Ir precursor (H_2IrCl_6) to synthesize electrocatalysts that exhibit both high activity and stability. Notably, the IWI, a technique widely used in the industry for its scalability, versatility, and cost-effectiveness, had

not been reported in literature for the synthesis of OER electrocatalysts prior to this investigation.

Additionally, the use of ZrO_2 to synthesize a supported IrO_x catalyst for OER had not been explored. We chose ZrO_2 support for its stability in acidic media and the possibility of synergistic interactions with Ir oxide.[241], [242], [318]

The use of ZrO_2, a non-conductive support also calls into question the long-held paradigm of using a conductive support to synthesize supported catalysts for PEM-WE applications. In the scientific community, there is an ever-increasing focus on fine-tuning support structures for enhanced conductivity, often involving doping with a variety of elements. SnO_2, for instance, is frequently doped with elements like Sb, In, Nb, Ta, and F.[79], [91], [136]–[148], [231], [319] The doping of stable SnO_2 support seems a good strategy to improve the activity of the IrO_x nanoparticles and their utilization. However, the stability of such doped supports is questionable.[72]

The use of ZrO_2 as support addresses two key challenges in the development of supported catalysts for acidic OER: firstly, it eradicates the need to synthesize conductive supports, that often succumb to in-situ degradation, and secondly, the presence of strong-metal support interactions prevalent between Ir and Zr improved the intrinsic properties of Ir in favour of OER, extending the benefits of using a support to beyond just offering higher dispersion. This comprises of the formation of $Ir_xZr_{(1-x)}O_2/Ir_xZr_{(1-x)}O_y$ alloy and a rich amount of Ir(III)/Ir(IV) active species throughout the oxide phase, a precursor to high activity in OER catalysts. The study of two different sizes of ZrO_2 support, $ZrO_{2(L)}$ with large particle size and smaller specific surface area (5 μm, 4 $m^2 \cdot g^{-1}$), and $ZrO_{2(S)}$ with smaller particle size and larger SSA (100 nm, 25 $m^2 \cdot g^{-1}$) enabled us to develop an understanding of the importance of Ir surface coverage of Ir ZrO_2 supports. TEM results showed a well-connected

network of Ir oxide composed of multiple layers of Ir oxide nanoparticles on the surface of $ZrO_{2(L)}$. On the other hand, a short-ranged network of Ir oxide nanoparticles with partial support coverage was observed in $Ir_xZr_{(1-x)}O_y/ZrO_{2(S)}$. A comparison was made between the performance of $Ir_xZr_{(1-x)}O_2/ZrO_{2(L)}$, $Ir_xZr_{(1-x)}O_y/ZrO_{2(S)}$, and the state-of-the-art IrO_x TKK. When compared to state-of-the-art IrO_x TKK, $Ir_xZr_{(1-x)}O_2/ZrO_{2(L)}$ exhibited comparable specific activity (Ir mass normalized activity), but substantially lower dissolution when subjected to a constant potential of 1.6 V_{RHE}. Between $Ir_xZr_{(1-x)}O_2/ZrO_{2(L)}$ and $Ir_xZr_{(1-x)}O_y/ZrO_{2(S)}$, we hypothesized that because of the higher SSA of $ZrO_{2(S)}$, its surface coverage would be low, causing it to be less active than the $Ir_xZr_{(1-x)}O_2/ZrO_{2(L)}$ catalyst, thereby demonstrating the importance of a percolative Ir oxide network. However, due to the more intimate contact of IrO_x with $ZrO_{2(S)}$ in $Ir_xZr_{(1-x)}O_y/ZrO_{2(S)}$, it would exhibit higher resistance to Ir dissolution. Evidently, $Ir_xZr_{(1-x)}O_2/ZrO_{2(L)}$ outperformed $Ir_xZr_{(1-x)}O_y/ZrO_{2(S)}$ in terms of activity but also exhibited higher Ir dissolution, substantiating the validity of our hypothesis. It is possible that $Ir_xZr_{(1-x)}O_y/ZrO_{2(S)}$ could achieve even better performance with higher Ir loading on the support since once a dense enough conductive Ir film is formed, good electrical conductivity could be achieved while maintaining more intimate contact with the support.

Another important contribution of this thesis to the body of knowledge is the use of temperature-programmed desorption (TPD) of water and oxygen from the investigated catalysts, followed by temperature-programmed reduction as a screening tool for active catalysts. Using the methods described above, a relationship was established between high catalyst activity and lower activation energies for water desorption (70-80 kJ/mol), higher levels of adsorbed H_2O and desorbed O_2 species seen during TPD, and the presence of reducible oxygen species even after TPD.

This thesis also enhances our understanding related to the impact of residual chlo-

ride poisoning from H_2IrCl_6 precursor commonly used for the wet-chemistry synthesis of supported and unsupported IrO_x catalysts. We hypothesized that residual chloride from the precursor could negatively impact the properties of the Ir oxide active sites synthesized using thermal decomposition methods that use chloride precursors without applying rigorous washing or treatment either during or post-synthesis. This work provides strong evidence to confirm that this is indeed true. To test this, we produced a baseline catalyst IrO_2 by calcining H_2IrCl_6 at 400°C for 2 h, introduced HCl into the H_2IrCl_6 precursor followed by calcination to synthesize IrO_2-HCl, and incorporated NH_4OH into the precursor prior to calcination to generate IrO_x-NH_4OH, aiming to reduce the amount of bulk and surface chloride. IrO_2-HCl showed significant contributions from $IrCl_3$, in addition to IrO_2, while IrO_x shows key contributions from IrO_x, along with IrO_2. On the other hand, IrO_x-NH_4OH, with reduced chloride content, possessed a high concentration of desirable Ir oxyhydroxides, and electrochemical tests revealed improved activity/stability compared to IrO_2, while IrO_2-HCl showcased reduced activity. The study highlights the need to remove residual chloride for catalyst efficacy. Future work, like using appropriate supports to mitigate IrO_x-NH_4OH dissolution, could enhance catalyst development.

In summary, the following are the key takeaway messages from this work:

1. Incipient wetness impregnation of supports with commercial molecular precursor (H_2IrCl_6) offers a straightforward and versatile wet-chemistry approach for producing IrO_x electrocatalysts for OER.

2. Non-conductive supports, such as ZrO_2, show promise in the development of supported Ir oxide catalysts given that the IrO_x loading on the support is sufficient to form a percolative network.

3. A strategic approach to support selection entails selecting supports that can

change the intrinsic properties of IrO_x active sites to favor OER, specifically by inducing strong metal-support interactions that boost catalyst activity and prevent Ir dissolution.

4. Residual chlorine from the precursors can act as an active site poison and be detrimental to the activity and stability of the catalyst. Addressing this concern in future catalyst synthesis, whether via thermal decomposition for unsupported catalysts or incipient wetness impregnation method for supported catalysts could unlock their potential to produce even more active and stable catalysts.

4.2 Future work

4.2.1 Optimizing Ir oxide loading on ZrO_2 support for scale-up

In Chapter 2, IrO_x/ZrO_2 support was synthesized using commercial ZrO_2 supports of different surface areas. Due to the smaller surface area of $ZrO_{2(L)}$ (SSA: 4 $m^2g_{Ir}^{-1}$), multi-layer coverage of IrO_x nanoparticles was observed. On the other hand, for $Ir_xZr_{(1-x)}O_y/ZrO_{2(S)}$ with a relatively higher surface area (SSA: 25 $m^2g_{Ir}^{-1}$), a short-range network of IrO_x was observed that did not completely cover the surface of the $ZrO_{2(S)}$. $Ir_xZr_{(1-x)}O_2/ZrO_{2(L)}$ exhibited superior activity compared to $Ir_xZr_{(1-x)}O_y/ZrO_{2(S)}$ due to improved electrical conductivity. To address the obstacles posed by the non-conductive nature of the ZrO_2 support, it is crucial to exceed the percolation threshold of the IrO_x network on the support. This ensures that the electrical conductivity of the support does not hinder the overall performance. Thus, there is a need to optimize the loading of IrO_x on ZrO_2 support such that a monolayer of well-connected IrO_x is formed.

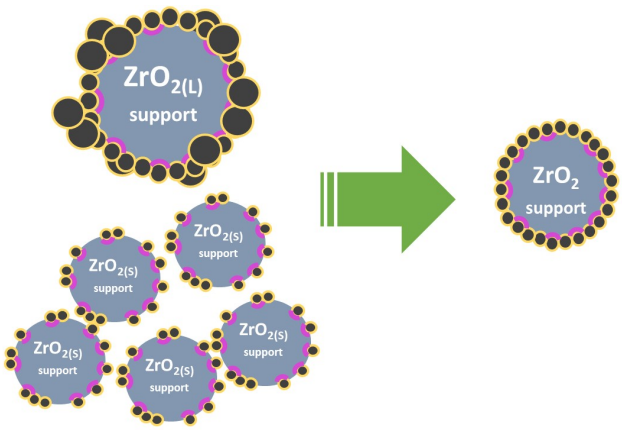

Figure 4.1: Schematic showing the optimized Ir oxide loading on ZrO_2.

4.2.2 Improving incipient wetness impregnation method for supported IrO_x catalyst synthesis

In Chapter 3, the addition of NH_4OH to the H_2IrCl_6 precursor prior to thermal decomposition was studied as a means to decrease the amount of chlorine in the bulk and surface of the catalyst and form well-dispersed IrO_x nanoparticles. In the future, we would like to investigate the synthesis of ZrO_2-supported IrO_x using the speciation-controlled incipient wetness impregnation method (ScIWI) with NH_4OH as a base.[293]

The loss of the expensive H_2IrCl_6 precursor during supported IrO_x synthesis has been a key observation when using the incipient wetness impregnation method. Reducing this loss would be a good way to overcome another barrier to the widespread use of the emerging wetness method that has yet to be addressed in this work.

Another pivotal consideration for enhancing the efficacy of incipient wetness impregnation method involves utilizing a chloride-free precursor, iridium(III) acetylacetonate ($Ir(acac)_3$), for synthesizing supported catalysts. Our investigations showed that directly decomposing the chloride-free precursor ($Ir(acac)_3$) in a furnace at 400°C

Figure 4.2: Mirror-like finish formed on the walls of the crucible due to evaporation and deposition of Ir when calcined in the furnace directly at 400°C.

for 2 hours resulted in the formation of a reflective film on the crucible, indicating the evaporation of Ir prior to decomposition on the support. In contrast, decomposing the precursor-support mixture at 280°C for 1 hour followed by a subsequent 2-hour decomposition at 400°C did not exhibit this issue, facilitating successful precursor decomposition on the support. Although beyond the scope of this study, discussing these findings as a prospective avenue for future research holds significance.

Bibliography

[1] *Comparing the Sustainability Parameters of Renewable, Nuclear and Fossil Fuel Electricity Generation Technologies (Conference)*. URL: https://www.osti.gov/etdeweb/biblio/21396864.

[2] A. Midilli, M. Ay, I. Dincer, et al. "On Hydrogen and Hydrogen Energy Strategies: I: Current Status and Needs". In: *Renewable and Sustainable Energy Reviews* 9.3 (2005), pp. 255–271. DOI: 10.1016/j.rser.2004.05.003.

[3] P. P. Edwards, V. L. Kuznetsov, W. I. F. David, et al. "Hydrogen and Fuel Cells: Towards a Sustainable Energy Future". In: *Energy Policy*. Foresight Sustainable Energy Management and the Built Environment Project 36.12 (2008), pp. 4356–4362. DOI: 10.1016/j.enpol.2008.09.036.

[4] Mobilite Hydrogene France (France). "H_2 Mobilite France - Study for a Fuel Cell Electric Vehicle national deployment plan". In: (2014). URL: http://inis.iaea.org/Search/search.aspx?orig_q=RN:45104849.

[5] S. Chu, Y. Cui, and N. Liu. "The Path towards Sustainable Energy". In: *Nature Materials* 16.1 (2017), pp. 16–22. DOI: 10.1038/nmat4834.

[6] X. Tan, J. Shen, N. Semagina, et al. "Decoupling Structure-Sensitive Deactivation Mechanisms of Ir/IrO_x Electrocatalysts toward Oxygen Evolution Reaction". In: *Journal of Catalysis* 371 (2019), pp. 57–70. DOI: 10.1016/j.jcat.2019.01.018.

[7] C. Tarhan and M. Al. Çil. "A Study on Hydrogen, the Clean Energy of the Future: Hydrogen Storage Methods". In: *Journal of Energy Storage* 40 (2021), p. 102676. DOI: 10.1016/j.est.2021.102676.

[8] E. Abohamzeh, F. Salehi, M. Sheikholeslami, et al. "Review of Hydrogen Safety during Storage, Transmission, and Applications Processes". In: *Journal of Loss Prevention in the Process Industries* 72 (2021), p. 104569. DOI: 10.1016/j.jlp.2021.104569.

[9] T. Egeland-Eriksen, A. Hajizadeh, and S. Sartori. "Hydrogen-Based Systems for Integration of Renewable Energy in Power Systems: Achievements and Perspectives". In: *International Journal of Hydrogen Energy* 46.63 (2021), pp. 31963–31983. DOI: 10.1016/j.ijhydene.2021.06.218.

[10] D. Parra, L. Valverde, J. Pino, et al. "A Review on the Role, Cost and Value of Hydrogen Energy Systems for Deep Decarbonisation". In: *Renewable and Sustainable Energy Reviews* 101 (2019), pp. 279–294. DOI: 10.1016/j.rser.2018.11.010.

[11] *Production of Hydrogen - U.S. Energy Information Administration (EIA)*. URL: https://www.eia.gov/energyexplained/hydrogen/production-of-hydrogen.php.

[12] *Hydrogen Production Processes*. Energy.gov. URL: https://www.energy.gov/eere/fuelcells/hydrogen-production-processes.

[13] P. Nikolaidis and A. Poullikkas. "A Comparative Overview of Hydrogen Production Processes". In: *Renewable and Sustainable Energy Reviews* 67 (2017), pp. 597–611. ISSN: 1364-0321. DOI: 10.1016/j.rser.2016.09.044.

[14] C. M. Kalamaras and A. M. Efstathiou. *Hydrogen Production Technologies: Current State and Future Developments*. 2013. DOI: 10.1155/2013/690627. URL: https://www.hindawi.com/journals/cpis/2013/690627/.

[15] G. Collodi. "Hydrogen Production via Steam Reforming with CO_2 Capture". In: *Chemical Engineering Transactions* 19 (2010), pp. 37–42. DOI: 10.3303/CET1019007.

[16] N. Muradov. "Hydrogen via Methane Decomposition: An Application for Decarbonization of Fossil Fuels". In: *International Journal of Hydrogen Energy* 26.11 (2001), pp. 1165–1175. DOI: 10.1016/S0360-3199(01)00073-8.

[17] *What Is the Major Drawback of Steam Methane Reforming*. 2022. URL: https://www.hydrogennewsletter.com/what-is-the-major-drawback-of-steam-methane-reforming/.

[18] R. O'Hayre, S. W. Cha, W. Colella, et al. *Fuel Cell Fundamentals*. John Wiley & Sons, 2016. eprint: O2JYCwAAQBAJ.

[19] A. Basile, S. Liguori, and A. Iulianelli. "2 - Membrane Reactors for Methane Steam Reforming (MSR)". In: *Membrane Reactors for Energy Applications and Basic Chemical Production*. Woodhead Publishing, 2015, pp. 31–59. DOI: 10.1016/B978-1-78242-223-5.00002-9.

[20] R. M. Navarro, M. A. Peña, and J. L. G. Fierro. "Hydrogen Production Reactions from Carbon Feedstocks: Fossil Fuels and Biomass". In: *Chemical Reviews* 107.10 (2007), pp. 3952–3991. DOI: 10.1021/cr0501994.

[21] T. Nguyen, Z. Abdin, T. Holm, et al. "Grid-Connected Hydrogen Production via Large-Scale Water Electrolysis". In: *Energy Conversion and Management* 200 (2019), p. 112108. DOI: 10.1016/j.enconman.2019.112108.

[22] A. Buttler and H. Spliethoff. "Current Status of Water Electrolysis for Energy Storage, Grid Balancing and Sector Coupling via Power-to-Gas and Power-to-Liquids: A Review". In: *Renewable and Sustainable Energy Reviews* 82 (2018), pp. 2440–2454. DOI: 10.1016/j.rser.2017.09.003.

[23] *What Is an Electrolyzer and What Is It Used for? | Accelera*. 2023. URL: https://www.accelerazero.com/news/what-is-an-electrolyzer-and-what-is-it-used-for.

[24] W. Tong, M. Forster, F. Dionigi, et al. "Electrolysis of Low-Grade and Saline Surface Water". In: *Nature Energy* 5.5 (2020), pp. 367–377. DOI: 10.1038/s41560-020-0550-8.

[25] *Green Hydrogen Cost Reduction*. 2020. URL: https://www.irena.org/publications/2020/Dec/Green-hydrogen-cost-reduction.

[26] R. Abbasi, B. P. Setzler, S. Lin, et al. "A Roadmap to Low-Cost Hydrogen with Hydroxide Exchange Membrane Electrolyzers". In: *Advanced Materials* 31.31 (2019), p. 1805876. DOI: 10.1002/adma.201805876.

[27] K. Zhang, X. Liang, L. Wang, et al. "Status and Perspectives of Key Materials for PEM Electrolyzer". In: *Nano Research Energy* 1.3 (2022), e9120032. DOI: 10.26599/NRE.2022.9120032.

[28] K. E. Ayers, E. B. Anderson, C. Capuano, et al. "Research Advances towards Low Cost, High Efficiency PEM Electrolysis". In: *ECS Transactions* 33.1 (2010), pp. 3–15. DOI: 10.1149/1.3484496.

[29] J. Chi and H. Yu. "Water Electrolysis Based on Renewable Energy for Hydrogen Production". In: *Chinese Journal of Catalysis* 39.3 (2018), pp. 390–394. DOI: 10.1016/S1872-2067(17)62949-8.

[30] S. Shiva Kumar and H. Lim. "Recent Advances in Hydrogen Production through Proton Exchange Membrane Water Electrolysis – a Review". In: *Sustainable Energy & Fuels* 7.15 (2023), pp. 3560–3583. DOI: 10.1039/D3SE00336A.

[31] F. Barbir. "PEM Electrolysis for Production of Hydrogen from Renewable Energy Sources". In: *Solar Energy*. Solar Hydrogen 78.5 (2005), pp. 661–669. DOI: 10.1016/j.solener.2004.09.003.

[32] M. Little, M. Thomson, and D. Infield. "Electrical Integration of Renewable Energy into Stand-Alone Power Supplies Incorporating Hydrogen Storage". In: *International Journal of Hydrogen Energy* 32.10 (2007), pp. 1582–1588. DOI: 10.1016/j.ijhydene.2006.10.035.

[33] K. W. Harrison, G. D. Martin, T. G. Ramsden, et al. *Wind-To-Hydrogen Project: Operational Experience, Performance Testing, and Systems Integration*. NREL/TP-550-44082. National Renewable Energy Lab. (NREL), Golden, CO (United States), 2009. DOI: 10.2172/951802.

[34] M. Carmo, D. L. Fritz, J. Mergel, et al. "A Comprehensive Review on PEM Water Electrolysis". In: *International Journal of Hydrogen Energy* 38.12 (2013), pp. 4901–4934. DOI: 10.1016/j.ijhydene.2013.01.151.

[35] H. Ito, T. Maeda, A. Nakano, et al. "Properties of Nafion Membranes under PEM Water Electrolysis Conditions". In: *International Journal of Hydrogen Energy*. International Conference on Hydrogen Production (ICH2P)-2010 36.17 (2011), pp. 10527–10540. DOI: 10.1016/j.ijhydene.2011.05.127.

[36] S. Lædre, O. E. Kongstein, A. Oedegaard, et al. "Materials for Proton Exchange Membrane Water Electrolyzer Bipolar Plates". In: *International Journal of Hydrogen Energy* 42.5 (2017), pp. 2713–2723. DOI: 10.1016/j.ijhydene.2016.11.106.

[37] A. Steinbach, M. Ulsh, and H. Xi. *Low-Cost, High Performance Catalyst Coated Membranes for PEM Water Electrolyzers (Final Technical Report)*. DOE-3M-0008425. 3M Company, Maplewood, MN (United States), 2022. DOI: 10.2172/1863440.

[38] K. Ayers. "High Efficiency PEM Water Electrolysis: Enabled by Advanced Catalysts, Membranes, and Processes". In: *Current Opinion in Chemical Engineering* 33 (2021), p. 100719. DOI: 10.1016/j.coche.2021.100719.

[39] *Iridium Price | Umicore Precious Metals Management*. URL: https://pmm.umicore.com/en/prices/iridium/.

[40] Ma. Bernt, A. Siebel, and H. A. Gasteiger. "Analysis of Voltage Losses in PEM Water Electrolyzers with Low Platinum Group Metal Loadings". In: *Journal of The Electrochemical Society* 165.5 (2018), F305. DOI: 10.1149/2.0641805jes.

[41] M. Bernt, A. Hartig-Weiß, M. F. Tovini, et al. "Current Challenges in Catalyst Development for PEM Water Electrolyzers". In: *Chemie Ingenieur Technik* 92.1-2 (2020), pp. 31–39. DOI: 10.1002/cite.201900101.

[42] H. Liu, H. B. Tao, and B. Liu. "Kinetic Insights of Proton Exchange Membrane Water Electrolyzer Obtained by Operando Characterization Methods". In: *The Journal of Physical Chemistry Letters* 13.28 (2022), pp. 6520–6531. DOI: 10.1021/acs.jpclett.2c01341.

[43] V. I. Birss, A. Damjanovic, and P. G. Hudson. "Oxygen Evolution at Platinum Electrodes in Alkaline Solutions II . Mechanism of the Reaction". In: *Journal of The Electrochemical Society* 133.8 (1986), pp. 1621–1625. DOI: 10.1149/1.2108978.

[44] L. A. De Faria, J. F. C. Boodts, and S. Trasatti. "Electrocatalytic Properties of Ternary Oxide Mixtures of Composition $Ru_{0.3}Ti_{(0.7x)}Ce_xO_2$: Oxygen Evolution from Acidic Solution". In: *Journal of Applied Electrochemistry* 26.11 (1996), pp. 1195–1199. DOI: 10.1007/BF00243745.

[45] E. Antolini. "Iridium As Catalyst and Cocatalyst for Oxygen Evolution/Reduction in Acidic Polymer Electrolyte Membrane Electrolyzers and Fuel Cells". In: *ACS Catalysis* 4.5 (2014), pp. 1426–1440. DOI: 10.1021/cs4011875.

[46] I. Katsounaros, S. Cherevko, A. R. Zeradjanin, et al. "Oxygen Electrochemistry as a Cornerstone for Sustainable Energy Conversion". In: *Angewandte Chemie International Edition* 53.1 (2014), pp. 102–121. DOI: 10.1002/anie.201306588.

[47] L. Moriau, M. Smiljanić, A. Lončar, et al. "Supported Iridium-based Oxygen Evolution Reaction Electrocatalysts - Recent Developments". In: *ChemCatChem* 14.20 (2022), e202200586. DOI: 10.1002/cctc.202200586.

[48] H. Dau, C. Limberg, T. Reier, et al. "The Mechanism of Water Oxidation: From Electrolysis via Homogeneous to Biological Catalysis". In: *ChemCatChem* 2.7 (2010), pp. 724–761. DOI: 10.1002/cctc.201000126.

[49] T. Reier, H. N. Nong, D. Teschner, et al. "Electrocatalytic Oxygen Evolution Reaction in Acidic Environments – Reaction Mechanisms and Catalysts". In: *Advanced Energy Materials* 7.1 (2017), p. 1601275. DOI: 10.1002/aenm.201601275.

[50] C. C. L. McCrory, S. Jung, Jo. C. Peters, et al. "Benchmarking Heterogeneous Electrocatalysts for the Oxygen Evolution Reaction". In: *Journal of the American Chemical Society* 135.45 (2013), pp. 16977–16987. DOI: 10.1021/ja407115p.

[51] T. Reier, M. Oezaslan, and P. Strasser. "Electrocatalytic Oxygen Evolution Reaction (OER) on Ru, Ir, and Pt Catalysts: A Comparative Study of Nanoparticles and Bulk Materials". In: *ACS Catalysis* 2.8 (2012), pp. 1765–1772. DOI: 10.1021/cs3003098.

[52] S. Cherevko, A. R. Zeradjanin, A. Topalov, et al. "Dissolution of Noble Metals during Oxygen Evolution in Acidic Media". In: *ChemCatChem* 6.8 (2014), pp. 2219–2223. DOI: 10.1002/cctc.201402194.

[53] S. Cherevko, S. Geiger, O. Kasian, et al. "Oxygen Evolution Activity and Stability of Iridium in Acidic Media. Part 1. – Metallic Iridium". In: *Journal of Electroanalytical Chemistry* 773 (2016), pp. 69–78. DOI: 10.1016/j.jelechem.2016.04.033.

[54] N. Danilovic, R. Subbaraman, K.-C. Chang, et al. "Activity–Stability Trends for the Oxygen Evolution Reaction on Monometallic Oxides in Acidic Environments". In: *The Journal of Physical Chemistry Letters* 5.14 (2014), pp. 2474–2478. DOI: 10.1021/jz501061n.

[55] I. C. Man, H.-Y. Su, F. Calle-Vallejo, et al. "Universality in Oxygen Evolution Electrocatalysis on Oxide Surfaces". In: *ChemCatChem* 3.7 (2011), pp. 1159–1165. DOI: 10.1002/cctc.201000397.

[56] M. H. Miles and M. A. Thomason. "Periodic Variations of Overvoltages for Water Electrolysis in Acid Solutions from Cyclic Voltammetric Studies". In: *Journal of The Electrochemical Society* 123.10 (1976), pp. 1459–1461. DOI: 10.1149/1.2132619.

[57] R. Hutchings, K. Müller, R. Kötz, et al. "A Structural Investigation of Stabilized Oxygen Evolution Catalysts". In: *Journal of Materials Science* 19.12 (1984), pp. 3987–3994. DOI: 10.1007/BF00980762.

[58] S. Song, H. Zhang, X. Ma, et al. "Electrochemical Investigation of Electrocatalysts for the Oxygen Evolution Reaction in PEM Water Electrolyzers". In: *International Journal of Hydrogen Energy* 33.19 (2008), pp. 4955–4961. DOI: 10.1016/j.ijhydene.2008.06.039.

[59] F. Cheng and J. Chen. "Metal–Air Batteries: From Oxygen Reduction Electrochemistry to Cathode Catalysts". In: *Chemical Society Reviews* 41.6 (2012), pp. 2172–2192. DOI: 10.1039/C1CS15228A.

[60] *Ruthenium Dioxide-Based Film Electrodes | SpringerLink*. URL: https://link.springer.com/article/10.1007/BF00617671.

[61] C. P. De Pauli and S. Trasatti. "Composite Materials for Electrocatalysis of O_2 Evolution: IrO_2+SnO_2 in Acid Solution". In: *Journal of Electroanalytical Chemistry* 538–539 (2002), pp. 145–151. DOI: 10.1016/S0022-0728(02)01055-0.

[62] S. Trasatti. "Electrocatalysis in the Anodic Evolution of Oxygen and Chlorine". In: *Electrochimica Acta* 29.11 (1984), pp. 1503–1512. DOI: 10.1016/0013-4686(84)85004-5.

[63] F. I Mattos-Costa, P de Lima-Neto, S. A. S Machado, et al. "Characterisation of Surfaces Modified by Sol-Gel Derived $Ru_xIr_{1x}O_2$ Coatings for Oxygen Evolution in Acid Medium". In: *Electrochimica Acta* 44.8 (1998), pp. 1515–1523. DOI: 10.1016/S0013-4686(98)00275-8.

[64] R. Kötz, H. J. Lewerenz, P. Brüesch, et al. "Oxygen Evolution on Ru and Ir Electrodes: XPS-studies". In: *Journal of Electroanalytical Chemistry and Interfacial Electrochemistry* 150.1 (1983), pp. 209–216. DOI: 10.1016/S0022-0728(83)80203-4.

[65] E. Fabbri, A. Habereder, K. Waltar, et al. "Developments and Perspectives of Oxide-Based Catalysts for the Oxygen Evolution Reaction". In: *Catalysis Science & Technology* 4.11 (2014), pp. 3800–3821. DOI: 10.1039/C4CY00669K.

[66] S. Geiger, O. Kasian, B. R. Shrestha, et al. "Activity and Stability of Electrochemically and Thermally Treated Iridium for the Oxygen Evolution Reaction". In: *Journal of The Electrochemical Society* 163.11 (2016), F3132. DOI: 10.1149/2.0181611jes.

[67] H. Dhawan, M. Secanell, and N. Semagina. "State-of-the-Art Iridium-Based Catalysts for Acidic Water Electrolysis: A Minireview of Wet-Chemistry Synthesis Methods". In: *Johnson Matthey Technology Reviews* 65.2 (2021), pp. 247–262. DOI: 10.1595/205651321X16013966874707.

[68] M. Clapp, C. M. Zalitis, and M. Ryan. "Perspectives on Current and Future Iridium Demand and Iridium Oxide Catalysts for PEM Water Electrolysis". In: *Catalysis Today* 420 (2023), p. 114140. DOI: 10.1016/j.cattod.2023.114140.

[69] T. Schuler, T. Kimura, T. J. Schmidt, et al. "Towards a Generic Understanding of Oxygen Evolution Reaction Kinetics in Polymer Electrolyte Water Electrolysis". In: *Energy & Environmental Science* 13.7 (2020), pp. 2153–2166. DOI: 10.1039/D0EE00673D.

[70] O. Kasian, J.-P. Grote, S. Geiger, et al. "The Common Intermediates of Oxygen Evolution and Dissolution Reactions during Water Electrolysis on Iridium". In: *Angewandte Chemie International Edition* 57.9 (2018), pp. 2488–2491. DOI: 10.1002/anie.201709652.

[71] V. A Saveleva, L. Wang, W. Luo, et al. "Uncovering the Stabilization Mechanism in Bimetallic Ruthenium–Iridium Anodes for Proton Exchange Membrane Electrolyzers". In: *The Journal of Physical Chemistry Letters* 7.16 (2016), pp. 3240–3245. DOI: 10.1021/acs.jpclett.6b01500.

[72] S. Geiger, O. Kasian, M. Ledendecker, et al. "The Stability Number as a Metric for Electrocatalyst Stability Benchmarking". In: *Nature Catalysis* 1.7 (2018), pp. 508–515. DOI: 10.1038/s41929-018-0085-6.

[73] A. Grimaud, A. Demortière, M. Saubanère, et al. "Activation of Surface Oxygen Sites on an Iridium-Based Model Catalyst for the Oxygen Evolution Reaction". In: *Nature Energy* 2.1 (2016), pp. 1–10. DOI: 10.1038/nenergy.2016.189.

[74] V. A. Saveleva, Li Wang, D. Teschner, et al. "Operando Evidence for a Universal Oxygen Evolution Mechanism on Thermal and Electrochemical Iridium Oxides". In: *The Journal of Physical Chemistry Letters* 9.11 (2018), pp. 3154–3160. DOI: 10.1021/acs.jpclett.8b00810.

[75] V. Pfeifer, T. E. Jones, J. J. Velasco Vélez, et al. "The Electronic Structure of Iridium Oxide Electrodes Active in Water Splitting". In: *Physical Chemistry Chemical Physics* 18.4 (2016), pp. 2292–2296. DOI: 10.1039/C5CP06997A.

[76] J. Rossmeisl, Z. -W. Qu, H. Zhu, et al. "Electrolysis of Water on Oxide Surfaces". In: *Journal of Electroanalytical Chemistry* 607.1 (2007), pp. 83–89. ISSN: 1572-6657. DOI: 10.1016/j.jelechem.2006.11.008.

[77] O. Kasian, S. Geiger, T. Li, et al. "Degradation of Iridium Oxides via Oxygen Evolution from the Lattice: Correlating Atomic Scale Structure with Reaction Mechanisms". In: *Energy & Environmental Science* 12 (2019), pp. 3548–3555. DOI: 10.1039/C9EE01872G.

[78] T. Li, O. Kasian, S. Cherevko, et al. "Atomic-Scale Insights into Surface Species of Electrocatalysts in Three Dimensions". In: *Nature Catalysis* 1.4 (2018), pp. 300–305. DOI: 10.1038/s41929-018-0043-3.

[79] H.-S. Oh, H. N. Nong, T. Reier, et al. "Oxide-Supported Ir Nanodendrites with High Activity and Durability for the Oxygen Evolution Reaction in Acid PEM Water Electrolyzers". In: *Chemical Science* 6 (2015), pp. 3321–3328. DOI: 10.1039/C5SC00518C.

[80] B. J. Kip, J. Van Grondelle, J. H. A. Martens, et al. "Preparation and Characterization of Very Highly Dispersed Iridium on Al_2O_3 and SiO_2". In: *Applied Catalysis* 26 (Jan. 1, 1986), pp. 353–373. DOI: 10.1016/S0166-9834(00)82564-6.

[81] M. Povia, D. F. Abbott, J. Herranz, et al. "Operando X-ray Characterization of High Surface Area Iridium Oxides to Decouple Their Activity Losses for the Oxygen Evolution Reaction". In: *Energy & Environmental Science* 12.10 (2019), pp. 3038–3052. DOI: 10.1039/C9EE01018A.

[82] E. Özer, I. Sinev, A. Mingers, et al. "Ir-Ni Bimetallic OER Catalysts Prepared by Controlled Ni Electrodeposition on Irpoly and Ir(111)". In: *Surfaces* 1.1 (2018), pp. 165–186. DOI: 10.3390/surfaces1010013.

[83] A. V. Nikiforov, C. B. Prag, J. Polonský, et al. "Development of Refractory Ceramics for the Oxygen Evolution Reaction (OER) Electrocatalyst Support for Water Electrolysis at Elevated Temperatures". In: *ECS Transactions* 41.42 (2012), p. 115. DOI: 10.1149/1.4718004.

[84] C. Wang, F. Lan, Z. He, et al. "Iridium-Based Catalysts for Solid Polymer Electrolyte Electrocatalytic Water Splitting". In: *ChemSusChem* 12.8 (2019), pp. 1576–1590. DOI: 10.1002/cssc.201802873.

[85] H. Jang and J. Lee. "Iridium Oxide Fabrication and Application: A Review". In: *Journal of Energy Chemistry* 46 (2020), pp. 152–172. DOI: 10.1016/j.jechem.2019.10.026.

[86] H. Yu, N. Danilovic, Y. Wang, et al. "Nano-Size IrO_x Catalyst of High Activity and Stability in PEM Water Electrolyzer with Ultra-Low Iridium Loading". In: *Applied Catalysis B: Environmental* 239 (2018), pp. 133–146. DOI: 10.1016/j.apcatb.2018.07.064.

[87] J. M. Roller, M. J. Arellano-Jiménez, R. Jain, et al. "Oxygen Evolution during Water Electrolysis from Thin Films Using Bimetallic Oxides of Ir-Pt and Ir-Ru". In: *Journal of The Electrochemical Society* 160.6 (2013), F716. DOI: 10.1149/2.121306jes.

[88] P. Lettenmeier, J. Majchel, L. Wang, et al. "Highly Active Nano-Sized Iridium Catalysts: Synthesis and Operando Spectroscopy in a Proton Exchange Membrane Electrolyzer". In: *Chemical Science* 9.14 (2018), pp. 3570–3579. DOI: 10.1039/C8SC00555A.

[89] F. Bizzotto, J. Quinson, A. Zana, et al. "Ir Nanoparticles with Ultrahigh Dispersion as Oxygen Evolution Reaction (OER) Catalysts: Synthesis and Activity Benchmarking". In: *Catalysis Science & Technology* 9.22 (2019), pp. 6345–6356. DOI: 10.1039/C9CY01728C.

[90] J. Chen, P. Cui, G. Zhao, et al. "Low-Coordinate Iridium Oxide Confined on Graphitic Carbon Nitride for Highly Efficient Oxygen Evolution". In: *Angewandte Chemie International Edition* 58.36 (2019), pp. 12540–12544. DOI: 10.1002/anie.201907017.

[91] S. Abbou, R. Chattot, V. Martin, et al. "Manipulating the Corrosion Resistance of SnO_2 Aerogels through Doping for Efficient and Durable Oxygen Evolution Reaction Electrocatalysis in Acidic Media". In: *ACS Catalysis* 10.13 (2020), pp. 7283–7294. DOI: 10.1021/acscatal.0c01084.

[92] S. M. Alia, S. Shulda, C. Ngo, et al. "Iridium-Based Nanowires as Highly Active, Oxygen Evolution Reaction Electrocatalysts". In: *ACS Catalysis* 8.3 (2018), pp. 2111–2120. DOI: 10.1021/acscatal.7b03787.

[93] R. Adams and R. L. Shriner. "Platinum oxide as a catalyst in the reduction of organic compounds III. Preparation and properties of the oxide of platinum obtained by the fusion of chloroplatinic acid with sodium nintrate". In: *Journal of the American Chemical Society* 45.9 (1923), pp. 2171–2179. DOI: 10.1021/ja01662a022.

[94] E. Rasten, G. Hagen, and R. Tunold. "Electrocatalysis in Water Electrolysis with Solid Polymer Electrolyte". In: *Electrochimica Acta*. Electrocatalysis:From Theory to Industrial Applications 48.25 (2003), pp. 3945–3952. DOI: 10.1016/j.electacta.2003.04.001.

[95] D. F. Abbott, D. Lebedev, K. Waltar, et al. "Iridium Oxide for the Oxygen Evolution Reaction: Correlation between Particle Size, Morphology, and the Surface Hydroxo Layer from Operando XAS". In: *Chemistry of Materials* 28.18 (2016), pp. 6591–6604. DOI: 10.1021/acs.chemmater.6b02625.

[96] J. Lim, D. Park, S. S. Jeon, et al. "Ultrathin IrO_2 Nanoneedles for Electrochemical Water Oxidation". In: *Advanced Functional Materials* 28.4 (2018), p. 1704796. DOI: 10.1002/adfm.201704796.

[97] N. Semagina and L. Kiwi-Minsker. "Recent Advances in the Liquid-Phase Synthesis of Metal Nanostructures with Controlled Shape and Size for Catalysis". In: *Catalysis Reviews* 51.2 (2009), pp. 147–217. DOI: 10.1080/0161494080248-0379.

[98] Witte, P.T., Berben, P.H., Boland, S., et al. "BASF NanoSelect$^{(TM)}$ Technology : Innovative Supported Pd- and Pt-based Catalysts for Selective Hydrogenation Reactions". In: *Topics in Catalysis* 55.7-10 (2012), pp. 505–511. DOI: 10.1007/s11244-012-9818-y.

[99] J. Quinson, S. Neumann, T. Wannmacher, et al. "Colloids for Catalysts: A Concept for the Preparation of Superior Catalysts of Industrial Relevance". In: *Angewandte Chemie* 130.38 (2018), pp. 12518–12521. DOI: 10.1002/ange.201807450.

[100] J. Ruiz Esquius, D. J. Morgan, I. Spanos, et al. "Effect of Base on the Facile Hydrothermal Preparation of Highly Active IrO_x Oxygen Evolution Catalysts". In: *ACS Applied Energy Materials* 3.1 (2020), pp. 800–809. DOI: 10.1021/acsaem.9b01642.

[101] C. Massué, X. Huang, A. Tarasov, et al. "Microwave-Assisted Synthesis of Stable and Highly Active Ir Oxohydroxides for Electrochemical Oxidation of Water". In: *ChemSusChem* 10.9 (2017), pp. 1958–1968. DOI: 10.1002/cssc.201601864.

[102] S. Shi, A. Z. Weber, and A. Kusoglu. "Structure-transport relationship of perfluorosulfonic-acid membranes in different cationic forms". In: *Electrochimica Acta* 220 (2016), pp. 517–528. DOI: 10.1016/j.electacta.2016.10.096.

[103] H. Yu, N. Danilovic, C. Capuano, et al. "Iridium Oxide/Nafion Catalyst for Oxygen Evolution Reaction and Proton Exchange Membrane Water Electrolyzer". In: *Meeting Abstracts* MA2017-01.30 (2017), pp. 1387–1387. DOI: 10.1149/MA2017-01/30/1387.

[104] U. Babic, M. Suermann, F. N. Büchi, et al. "Critical Review—Identifying Critical Gaps for Polymer Electrolyte Water Electrolysis Development". In: *Journal of The Electrochemical Society* 164.4 (2017), F387. DOI: 10.1149/2.1441704jes.

[105] T. Kinumoto, M. Inaba, Y. Nakayama, et al. "Durability of Perfluorinated Ionomer Membrane against Hydrogen Peroxide". In: *Journal of Power Sources* 158.2 (2006), pp. 1222–1228. DOI: 10.1016/j.jpowsour.2005.10.043.

[106] C. Spöri, P. Briois, H. N. Nong, et al. "Experimental Activity Descriptors for Iridium-Based Catalysts for the Electrochemical Oxygen Evolution Reaction (OER)". In: *ACS Catalysis* 9.8 (2019), pp. 6653–6663.

[107] Y.-T. Kim, P. P. Lopes, S.-A. Park, et al. "Balancing Activity, Stability and Conductivity of Nanoporous Core-Shell Iridium/Iridium Oxide Oxygen Evolution Catalysts". In: *Nature Communications* 8.1 (2017), p. 1449. DOI: 10.1038/s41467-017-01734-7.

[108] H. N. Nong, T. Reier, H. S. Oh, et al. "A Unique Oxygen Ligand Environment Facilitates Water Oxidation in Hole-Doped $IrNiO_x$ Core–Shell Electrocatalysts". In: *Nature Catalysis* 1.11 (2018), pp. 841–851. DOI: 10.1038/s41929-018-0153-y.

[109] O. Kasian, S. Geiger, M. Schalenbach, et al. "Using Instability of a Non-stoichiometric Mixed Oxide Oxygen Evolution Catalyst As a Tool to Improve Its Electrocatalytic Performance". In: *Electrocatalysis* 9.2 (2018), pp. 139–145. DOI: 10.1007/s12678-017-0394-6.

[110] L. C. Seitz, C. F. Dickens, K. Nishio, et al. "A Highly Active and Stable $IrO_x/SrIrO_3$ Catalyst for the Oxygen Evolution Reaction". In: *Science* 353.6303 (2016), pp. 1011–1014. DOI: 10.1126/science.aaf5050.

[111] A. W. Jensen, G. W. Sievers, K. D. Jensen, et al. "Self-Supported Nanostructured Iridium-Based Networks as Highly Active Electrocatalysts for Oxygen Evolution in Acidic Media". In: *Journal of Materials Chemistry A* 8.3 (2020), pp. 1066–1071. DOI: 10.1039/C9TA12796H.

[112] A. L Strickler, R. A. Flores, L. King, et al. "Systematic Investigation of Iridium-Based Bimetallic Thin Film Catalysts for the Oxygen Evolution Reaction in Acidic Media". In: *ACS Applied Materials Interfaces* 11.37 (2019), pp. 34059–34066. DOI: 10.1021/acsami.9b13697.

[113] O. Kasian, S. Geiger, P. Stock, et al. "On the Origin of the Improved Ruthenium Stability in RuO_2–IrO_2 Mixed Oxides". In: *Journal of The Electrochemical Society* 163.11 (2016), F3099–F3104. DOI: 10.1149/2.0131611jes.

[114] N. Toshima. "Core/Shell-Structured Bimetallic Nanocluster Catalysts for Visible Light-Induced Electron Transfer". In: *Pure and Applied Chemistry* 72.1-2 (2000), pp. 317–325. DOI: 10.1351/pac200072010317.

[115] C. Wang, Y. Sui, G. Xiao, et al. "Synthesis of Cu–Ir Nanocages with Enhanced Electrocatalytic Activity for the Oxygen Evolution Reaction". In: *Journal of Materials Chemistry A* 3.39 (2015), pp. 19669–19673. DOI: 10.1039/C5TA05384F.

[116] B. Coq and F. Figueras. "Bimetallic Palladium Catalysts: Influence of the Co-Metal on the Catalyst Performance". In: *Journal of Molecular Catalysis A: Chemical* 173.1 (2001), pp. 117–134. DOI: 10.1016/S1381-1169(01)00148-0.

[117] Hessam Ziaei-Azad and Natalia Semagina. "Nickel Boosts Ring-Opening Activity of Iridium". In: *ChemCatChem* 6.3 (2014), pp. 885–894. DOI: 10.1002/cctc.201300844.

[118] F. Tao, M. E. Grass, Y. Zhang, et al. "Reaction-Driven Restructuring of Rh-Pd and Pt-Pd Core-Shell Nanoparticles". In: *Science* 322.5903 (2008), pp. 932–934. DOI: 10.1126/science.1164170.

[119] X. Liu, A. Wang, L. Li, et al. "Structural Changes of Au–Cu Bimetallic Catalysts in CO Oxidation: In Situ XRD, EPR, XANES, and FT-IR Characterizations". In: *Journal of Catalysis* 278.2 (2011), pp. 288–296. DOI: 10.1016/j.jcat.2010.12.016.

[120] K. J. J. Mayrhofer, V. Juhart, K. Hartl, et al. "Adsorbate-Induced Surface Segregation for Core–Shell Nanocatalysts". In: *Angewandte Chemie International Edition* 48.19 (2009), pp. 3529–3531. DOI: 10.1002/anie.200806209.

[121] C Felix, T Maiyalagan, S Pasupathi, et al. "Synthesis, Characterisation and Evaluation of IrO_2 Based Binary Metal Oxide Electrocatalysts for Oxygen Evolution Reaction". In: *International Journal of Electrochemical Science* 7 (2012), p. 14.

[122] A. V. Ruban, H. L. Skriver, and J. K. Nørskov. "Surface Segregation Energies in Transition-Metal Alloys". In: *Physical Review B* 59.24 (1999), pp. 15990–16000. DOI: 10.1103/PhysRevB.59.15990.

[123] N. Danilovic, R. Subbaraman, K. C. Chang, et al. "Using Surface Segregation To Design Stable Ru-Ir Oxides for the Oxygen Evolution Reaction in Acidic Environments". In: *Angewandte Chemie International Edition* 53.51 (2014), pp. 14016–14021. DOI: 10.1002/anie.201406455.

[124] J. Feng, F. Lv, W. Zhang, et al. "Iridium-Based Multimetallic Porous Hollow Nanocrystals for Efficient Overall-Water-Splitting Catalysis". In: *Advanced Materials* 29.47 (2017), p. 1703798. DOI: 10.1002/adma.201703798.

[125] J. Park, Y. J. Sa, H. Baik, et al. "Iridium-Based Multimetallic Nanoframe@Nanoframe Structure: An Efficient and Robust Electrocatalyst toward Oxygen Evolution Reaction". In: *ACS Nano* 11.6 (2017), pp. 5500–5509. DOI: 10.1021/acsnano.7b00233.

[126] C. Spöri, J. T. H. Kwan, A. Bonakdarpour, et al. "The Stability Challenges of Oxygen Evolving Catalysts: Towards a Common Fundamental Understanding and Mitigation of Catalyst Degradation". In: *Angewandte Chemie International Edition* 56.22 (2017), pp. 5994–6021. DOI: 10.1002/anie.201608601.

[127] S. J. Tauster, S. C. Fung, and R. L. Garten. "Strong Metal-Support Interactions. Group 8 Noble Metals Supported on Titanium Dioxide". In: *Journal of the American Chemical Society* 100.1 (1978), pp. 170–175. DOI: 10.1021/ja00469a029.

[128] C.-J. Pan, M.-C. Tsai, Wei-Nien Su, et al. "Tuning/Exploiting Strong Metal-Support Interaction (SMSI) in Heterogeneous Catalysis". In: *Journal of the Taiwan Institute of Chemical Engineers* 74 (2017), pp. 154–186. DOI: 10.1016/j.jtice.2017.02.012.

[129] X. Y. Shi, W. Zhang, C. Zhang, et al. "Real-space observation of strong metal-support interaction: state-of-the-art and what's the next". In: *Journal of Microscopy* 262.3 (2016), pp. 203–215. DOI: 10.1111/jmi.12366.

[130] P. N. Plessow, M. Bajdich, J. Greene, et al. "Trends in the Thermodynamic Stability of Ultrathin Supported Oxide Films". In: *The Journal of Physical Chemistry C* 120.19 (2016), pp. 10351–10360. DOI: 10.1021/acs.jpcc.6b01404.

[131] S. Sharma and B. G. Pollet. "Support Materials for PEMFC and DMFC Electrocatalysts—A Review". In: *Journal of Power Sources* 208 (June 2012), pp. 96–119. DOI: 10.1016/j.jpowsour.2012.02.011.

[132] Hyung-Suk Oh, Hong Nhan Nong, Tobias Reier, et al. "Electrochemical Catalyst–Support Effects and Their Stabilizing Role for IrO_x Nanoparticle Catalysts during the Oxygen Evolution Reaction". In: *Journal of the American Chemical Society* 138.38 (2016), pp. 12552–12563. DOI: 10.1021/jacs.6b07199.

[133] K. A. Lewinski, D. van der Vliet, and S. M. Luopa. "NSTF Advances for PEM Electrolysis - the Effect of Alloying on Activity of NSTF Electrolyzer Catalysts and Performance of NSTF Based PEM Electrolyzers". In: *ECS Transactions* 69.17 (2015), p. 893. DOI: 10.1149/06917.0893ecst.

[134] C. Massué, V. Pfeifer, X. Huang, et al. "High-Performance Supported Iridium Oxohydroxide Water Oxidation Electrocatalysts". In: *ChemSusChem* 10.9 (May 9, 2017), pp. 1943–1957. DOI: 10.1002/cssc.201601817.

[135] J. Zhang, Q. Zhang, and X. Feng. "Support and Interface Effects in Water-Splitting Electrocatalysts". In: *Advanced Materials* 31 (2019), p. 1808167. DOI: 10.1002/adma.201808167.

[136] J. Xu, G. Liu, J. Li, et al. "The Electrocatalytic Properties of an IrO_2/SnO_2 Catalyst Using SnO_2 as a Support and an Assisting Reagent for the Oxygen Evolution Reaction". In: *Electrochimica Acta* 59 (2012), pp. 105–112. DOI: 10.1016/j.electacta.2011.10.044.

[137] S. Delgado, P. Lakhtaria, E. Sousa, et al. "Towards Stable and Highly Active IrO_2 Catalysts Supported on Doped Tin Oxides for the Oxygen Evolution Reaction in Acidic Media". In: *E3S Web of Conferences* 334 (2022), p. 03001. DOI: 10.1051/e3sconf/202233403001.

[138] L. Solà-Hernández, F. Claudel, F. Maillard, et al. "Doped Tin Oxide Aerogels as Oxygen Evolution Reaction Catalyst Supports". In: *International Journal of Hydrogen Energy* 44.45 (2019), pp. 24331–24341. DOI: 10.1016/j.ijhydene.2019.07.152.

[139] A. Hartig-Weiss, M. Miller, H. Beyer, et al. "Iridium Oxide Catalyst Supported on Antimony-Doped Tin Oxide for High Oxygen Evolution Reaction Activity in Acidic Media". In: *ACS Applied Nano Materials* 3.3 (2020), pp. 2185–2196. DOI: 10.1021/acsanm.9b02230.

[140] H. P. Tran, H. N. Nong, H.-S. Oh, et al. "Catalyst–Support Surface Charge Effects on Structure and Activity of IrNi-Based Oxygen Evolution Reaction Catalysts Deposited on Tin-Oxide Supports". In: *Chemistry of Materials* 34.21 (2022), pp. 9350–9363. DOI: 10.1021/acs.chemmater.2c01098.

[141] M. Ledendecker, S. Geiger, K. Hengge, et al. "Towards Maximized Utilization of Iridium for the Acidic Oxygen Evolution Reaction". In: *Nano Research* 12.9 (2019), pp. 2275–2280. DOI: 10.1007/s12274-019-2383-y.

[142] G. C. da Silva, S. I. Venturini, S. Zhang, et al. "Oxygen Evolution Reaction on Tin Oxides Supported Iridium Catalysts: Do We Need Dopants?" In: *ChemElectroChem* 7.10 (2020), pp. 2330–2339. DOI: 10.1002/celc.202000391.

[143] B. Han, M. Risch, S. Belden, et al. "Screening Oxide Support Materials for OER Catalysts in Acid". In: *Journal of The Electrochemical Society* 165.10 (2018), F813. DOI: 10.1149/2.0921810jes.

[144] F. Karimi and B. A. Peppley. "Comparison of Conventional versus Microwave Heating for Polyol Synthesis of Supported Iridium Based Electrocatalyst for Polymer Electrolyte Membrane Water Electrolysis". In: *International Journal of Hydrogen Energy* 42.8 (2017), pp. 5083–5094. DOI: 10.1016/j.ijhydene.2017.01.090.

[145] V. K. Puthiyapura, M. Mamlouk, S. Pasupathi, et al. "Physical and Electrochemical Evaluation of ATO Supported IrO_2 Catalyst for Proton Exchange Membrane Water Electrolyser". In: *Journal of Power Sources* 269 (2014), pp. 451–460. DOI: 10.1016/j.jpowsour.2014.06.078.

[146] G. Liu, J. Xu, Y. Wang, et al. "An Oxygen Evolution Catalyst on an Antimony Doped Tin Oxide Nanowire Structured Support for Proton Exchange Membrane Liquid Water Electrolysis". In: *Journal of Materials Chemistry A* 3.41 (2015), pp. 20791–20800. DOI: 10.1039/C5TA02942B.

[147] H. Li, Y. Xu, N. Lv, et al. "Ti-Doped SnO_2 Supports IrO_2 Electrocatalysts for the Oxygen Evolution Reaction (OER) in PEM Water Electrolysis". In: *ACS Sustainable Chemistry & Engineering* 11.3 (2023), pp. 1121–1132. DOI: 10.1021/acssuschemeng.2c06368.

[148] J.-A. Hoffman, Z. Rajan, D. Susac, et al. "Influence of Support Physicochemical Properties on the Oxygen Evolution Reaction Performance of ITO-Supported IrO_x Nanoparticles". In: *The Journal of Physical Chemistry C* 127.2 (2023), pp. 894–906. DOI: 10.1021/acs.jpcc.2c06501.

[149] M. Bele, P. Jovanovič, Ž. Marinko, et al. "Increasing the Oxygen-Evolution Reaction Performance of Nanotubular Titanium Oxynitride-Supported Ir Nanoparticles by a Strong Metal–Support Interaction". In: *ACS Catalysis* 10.22 (2020), pp. 13688–13700. DOI: 10.1021/acscatal.0c03688.

[150] S. Zhao, A. Stocks, B. Rasimick, et al. "Highly Active, Durable Dispersed Iridium Nanocatalysts for PEM Water Electrolyzers". In: *Journal of The Electrochemical Society* 165.2 (2018), F82. DOI: 10.1149/2.0981802jes.

[151] D. Böhm, M. Beetz, C. Gebauer, et al. "Highly Conductive Titania Supported Iridium Oxide Nanoparticles with Low Overall Iridium Density as OER Catalyst for Large-Scale PEM Electrolysis". In: *Applied Materials Today* 24 (2021), p. 101134. DOI: 10.1016/j.apmt.2021.101134.

[152] G. Li, H. Jia, H. Liu, et al. "Nanostructured IrO_x Supported on N-doped TiO_2 as an Efficient Electrocatalyst towards Acidic Oxygen Evolution Reaction". In: *RSC Advances* 12.45 (2022), pp. 28929–28936. DOI: 10.1039/D2RA05374H.

[153] W. Hu, S. Chen, and Q. Xia. "IrO_2/Nb–TiO_2 Electrocatalyst for Oxygen Evolution Reaction in Acidic Medium". In: *International Journal of Hydrogen Energy* 39.13 (2014), pp. 6967–6976. DOI: 10.1016/j.ijhydene.2014.02.114.

[154] T. Wang, Y. Zeng, M. Xu, et al. "Effect of B-Doping and Manifestation on TiO_2-Supported IrO_2 for Oxygen Evolution Reaction in Water Electrolysis". In: *Langmuir* 39.11 (2023), pp. 4005–4014. DOI: 10.1021/acs.langmuir.2c03345.

[155] E. Oakton, D. Lebedev, M. Povia, et al. "IrO_2-TiO_2: A High-Surface-Area, Active, and Stable Electrocatalyst for the Oxygen Evolution Reaction". In: *ACS Catalysis* 7.4 (2017), pp. 2346–2352. DOI: 10.1021/acscatal.6b03246.

[156] D. Bernsmeier, M. Bernicke, R. Schmack, et al. "Oxygen Evolution Catalysts Based on Ir–Ti Mixed Oxides with Templated Mesopore Structure: Impact of Ir on Activity and Conductivity". In: *ChemSusChem* 11.14 (2018), pp. 2367–2374. DOI: 10.1002/cssc.201800932.

[157] C. Baik, J. I. Cha, and C. Pak. "Enhanced Oxygen Evolution Reaction Activity of Iridium Nanostructure Supported on Mesoporous Tantalum Oxide By the SMSI Effect". In: *ECS Meeting Abstracts* MA2022-02.44 (2022), p. 1646. DOI: 10.1149/MA2022-02441646mtgabs.

[158] F. Karimi and B. A. Peppley. "Metal Carbide and Oxide Supports for Iridium-Based Oxygen Evolution Reaction Electrocatalysts for Polymer-Electrolyte-Membrane Water Electrolysis". In: *Electrochimica Acta* 246 (2017), pp. 654–670. DOI: 10.1016/j.electacta.2017.06.048.

[159] Z. Shi, J. Li, J. Jiang, et al. "Enhanced Acidic Water Oxidation by Dynamic Migration of Oxygen Species at the $Ir/Nb_2O_{(5x)}$ Catalyst/Support Interfaces". In: *Angewandte Chemie International Edition* 61.52 (2022), e202212341. DOI: 10.1002/anie.202212341.

[160] S. Shanmugapriya, P. Zhu, C. Yan, et al. "Multifunctional High-Performance Electrocatalytic Properties of Nb_2O_5 Incorporated Carbon Nanofibers as Pt Support Catalyst". In: *Advanced Materials Interfaces* 6.17 (2019), p. 1900565. DOI: 10.1002/admi.201900565.

[161] L. A. Albiter, J. F. G. Salomon, M. E. Urena, et al. "Niobium Oxide Aerogel-Supported Bifunctional Oxygen Electrocatalysts for Unitized Regenerative Fuel Cells". In: *ECS Meeting Abstracts* MA2021-01.38 (2021), p. 1235. DOI: 10.1149/MA2021-01381235mtgabs.

[162] S. Geiger, O. Kasian, A. M. Mingers, et al. "Stability Limits of Tin-Based Electrocatalyst Supports". In: *Scientific Reports* 7.1 (2017), p. 4595. DOI: 10.1038/s41598-017-04079-9.

[163] H.-S. Oh, H. N. Nong, and P. Strasser. "Preparation of Mesoporous Sb-, F-, and In-Doped SnO_2 Bulk Powder with High Surface Area for Use as Catalyst Supports in Electrolytic Cells". In: *Advanced Functional Materials* 25.7 (2015), pp. 1074–1081. DOI: 10.1002/adfm.201401919.

[164] F. Bizzotto, J. Quinson, J. Schröder, et al. "Surfactant-Free Colloidal Strategies for Highly Dispersed and Active Supported IrO_2 Catalysts: Synthesis and Performance Evaluation for the Oxygen Evolution Reaction". In: *Journal of Catalysis* 401 (2021), pp. 54–62. DOI: 10.1016/j.jcat.2021.07.004.

[165] D. Lebedev and C. Copéret. "Small, Narrowly Distributed Iridium Nanoparticles Supported on Indium Tin Oxide for Efficient Anodic Water Oxidation". In: *ACS Applied Energy Materials* 2.1 (2019), pp. 196–200. DOI: 10.1021/acsaem.8b01724.

[166] D. Lebedev, R. E. Ezhov, J. Heras-Domingo, et al. "Atomically-Dispersed Iridium on Indium Tin Oxide Efficiently Catalyzes Water Splitting". In: *ACS Central Science* 6 (7 2020), pp. 1189–1198. DOI: 10.1021/acscentsci.0c00604.

[167] J. Sietsma, A. Jos van Dillen, P. E. de Jongh, et al. "Application of Ordered Mesoporous Materials as Model Supports to Study Catalyst Preparation by Impregnation and Drying". In: *Studies in Surface Science and Catalysis*. Ed. by E. M. Gaigneaux, M. Devillers, D. E. De Vos, et al. Vol. 162. 2006, pp. 95–102. DOI: 10.1016/S0167-2991(06)80895-5.

[168] A. Goel and S. Sharma. "Synthesis of Colloidal Iridium Nanoparticles and Their Role as Catalyst in Homogeneous Catalysis – An Approach to Green Chemistry". In: *Chemistry of Phytopotentials: Health, Energy and Environmental Perspectives*. Ed. by L. D. Khemani, M. M. Srivastava, and Shalini Srivastava. Springer, 2012, pp. 357–361. DOI: 10.1007/978-3-642-23394-4_76.

[169] Y. Lee, J. Suntivich, K. J. May, et al. "Synthesis and Activities of Rutile IrO_2 and RuO_2 Nanoparticles for Oxygen Evolution in Acid and Alkaline Solutions". In: *The Journal of Physical Chemistry Letters* 3 (2012), pp. 399–404. DOI: 10.1021/jz2016507.

[170] P.G. Hoertz, Y.-I. Kim, W.J. Youngblood, et al. "Bidentate Dicarboxylate Capping Groups and Photosensitizers Control the Size of IrO_2 Nanoparticle Catalysts for Water Oxidation". In: *Journal of Physical Chemistry B* 111.24 (2007), pp. 6845–6856. DOI: 10.1021/jp070735r.

[171] Y. Zhao, E. A. Hernandez-Pagan, N. M. Vargas-Barbosa, et al. "A High Yield Synthesis of Ligand-Free Iridium Oxide Nanoparticles with High Electrocatalytic Activity". In: *The Journal of Physical Chemistry Letters* 2.5 (2011), pp. 402–406. DOI: 10.1021/jz200051c.

[172] H. Hirai, Y. Nakao, and N. Toshima. "Preparation of Colloidal Transition Metals in Polymers by Reduction with Alcohols or Ethers". In: *Journal of Macromolecular Science: Part A - Chemistry* 13.6 (1979), pp. 727–750. DOI: 10.1080/00222337908056685.

[173] A. Iwase, H. Kato, and A. Kudo. "A Novel Photodeposition Method in the Presence of Nitrate Ions for Loading of an Iridium Oxide Cocatalyst for Water Splitting". In: *Chemistry Letters* 34.7 (2005), pp. 946–947. DOI: 10.1246/cl.2005.946.

[174] P. Lettenmeier, L. Wang, U. Golla-Schindler, et al. "Nanosized IrO_x–Ir Catalyst with Relevant Activity for Anodes of Proton Exchange Membrane Electrolysis Produced by a Cost-Effective Procedure". In: *Angewandte Chemie International Edition* 55.2 (2016), pp. 742–746. DOI: 10.1002/anie.201507626.

[175] German Mills and Arnim Henglein. "Radiation Chemical Formation of Colloidal Iridium and Mechanism of Catalysed Hydrogen Formation by Radicals". In: *Radiation Physics and Chemistry* 26.4 (1985), pp. 385–390. DOI: 10.1016/0146-5724(85)90226-2.

[176] P. Migowski, D. Zanchet, G. Machado, et al. "Nanostructures in Ionic Liquids: Correlation of Iridium Nanoparticles' Size and Shape with Imidazolium Salts' Structural Organization and Catalytic Properties". In: *Physical Chemistry Chemical Physics* 12.25 (2010), pp. 6826–6833. DOI: 10.1039/B925834E.

[177] J. Quinson. "Iridium and IrO_x Nanoparticles: An Overview and Review of Syntheses and Applications". In: *Advances in Colloid and Interface Science* 303 (2022), p. 102643. DOI: 10.1016/j.cis.2022.102643.

[178] M. Bowker, A. Nuhu, and J. Soares. "High Activity Supported Gold Catalysts by Incipient Wetness Impregnation". In: *Catalysis Today* 122.3 (2007), pp. 245–247. DOI: 10.1016/j.cattod.2007.01.021.

[179] P. G. J. Koopman, A. P. G. Kieboom, and H. van Bekkum. "Characterization of Ruthenium Catalysts as Studied by Temperature Programmed Reduction". In: *Journal of Catalysis* 69.1 (1981), pp. 172–179. DOI: 10.1016/0021-9517(81)90139-1.

[180] K. Okada, A. Satsuma, T. Hattori, et al. "NH_3 Treatment for Removal of Residual Chlorine from Supported Catalysts". In: *Zeitschrift für Physikalische Chemie* 162.1 (1989), pp. 125–127. DOI: 10.1524/zpch.1989.162.Part_1.125.

[181] T. Narita, H. Miura, M. Ohira, et al. "The Effect of Reduction Temperature on the Chemisorptive Properties of Ru/Al_2O_3: Effect of Chlorine". In: *Applied Catalysis* 32 (1987), pp. 185–190. DOI: 10.1016/S0166-9834(00)80624-7.

[182] B. A. T. Mehrabadi, S. Eskandari, U. Khan, et al. "Chapter One - A Review of Preparation Methods for Supported Metal Catalysts". In: *Advances in Catalysis*. Ed. by C. Song. Vol. 61. Jan. 1, 2017, pp. 1–35. DOI: 10.1016/bs.acat.2017.10.001.

[183] T. Lazaridis, B. M. Stühmeier, H. A. Gasteiger, et al. "Capabilities and Limitations of Rotating Disk Electrodes versus Membrane Electrode Assemblies in the Investigation of Electrocatalysts". In: *Nature Catalysis* 5.5 (2022), pp. 363–373. DOI: 10.1038/s41929-022-00776-5.

[184] T. J. Schmidt, H. A. Gasteiger, G. D. Stäb, et al. "Characterization of High-Surface-Area Electrocatalysts Using a Rotating Disk Electrode Configuration". In: *Journal of The Electrochemical Society* 145.7 (1998), p. 2354. DOI: 10.1149/1.1838642.

[185] N. Wakabayashi, M. Takeichi, M. Itagaki, et al. "Temperature-Dependence of Oxygen Reduction Activity at a Platinum Electrode in an Acidic Electrolyte Solution Investigated with a Channel Flow Double Electrode". In: *Journal of Electroanalytical Chemistry* 574.2 (2005), pp. 339–346. DOI: 10.1016/j.jelechem.2004.08.013.

[186] J. Schröder, V. A. Mints, A. Bornet, et al. "The Gas Diffusion Electrode Setup as Straightforward Testing Device for Proton Exchange Membrane Water Electrolyzer Catalysts". In: *Journal of Chemical Society Au* 1.3 (2021), pp. 247–251. DOI: 10.1021/jacsau.1c00015.

[187] S. M. Alia and G. C. Anderson. "Iridium Oxygen Evolution Activity and Durability Baselines in Rotating Disk Electrode Half-Cells". In: *Journal of The Electrochemical Society* 166.4 (2019), F282–F294. DOI: 10.1149/2.0731904jes.

[188] Y. Garsany, I. L. Singer, and K. E. Swider-Lyons. "Impact of Film Drying Procedures on RDE Characterization of Pt/VC Electrocatalysts". In: *Journal of Electroanalytical Chemistry* 662.2 (2011), pp. 396–406. DOI: 10.1016/j.jelechem.2011.09.016.

[189] A. J. Bard, L. R. Faulkner, and H. S. White. *Electrochemical Methods: Fundamentals and Applications*. John Wiley & Sons, 2022.

[190] S. Geiger, O. Kasian, A. M. Mingers, et al. "Catalyst Stability Benchmarking for the Oxygen Evolution Reaction: The Importance of Backing Electrode Material and Dissolution in Accelerated Aging Studies". In: *ChemSusChem* 10.21 (2017), pp. 4140–4143. DOI: 10.1002/cssc.201701523.

[191] S. M. Alia and N. Danilovic. "Rotating Disk Electrode Standardization and Best Practices in Acidic Oxygen Evolution for Low-Temperature Electrolysis". In: *Frontiers in Energy Research* 10 (2022). DOI: 10.3389/fenrg.2022.857663.

[192] *What Is iR Drop?* Pine Research Instrumentation Store. 2019. URL: https://pineresearch.com/shop/kb/theory/general-electrochemistry/ir-compensation/.

[193] G. Jerkiewicz. "Standard and Reversible Hydrogen Electrodes: Theory, Design, Operation, and Applications". In: *ACS Catalysis* 10.15 (2020), pp. 8409–8417. DOI: 10.1021/acscatal.0c02046.

[194] J. Lee and J. H. Bang. "Reliable Counter Electrodes for the Hydrogen Evolution Reaction in Acidic Media". In: *ACS Energy Letters* 5.8 (2020), pp. 2706–2710. DOI: 10.1021/acsenergylett.0c01537.

[195] Xiaojuan Ma, Chenlu Yang, Fengru Zhang, et al. "Oxygen-Vacancy-Rich Tungsten Oxide Boosted Ultrasmall Iridium Nanoparticles for Acidic Oxygen Evolution". In: *International Journal of Hydrogen Energy* (2023). DOI: 10.1016/j.ijhydene.2023.06.068.

[196] Z. Wang, Z. Zheng, Y. Xue, et al. "Acidic Water Oxidation on Quantum Dots of IrO_x/Graphdiyne". In: *Advanced Energy Materials* 11.32 (2021), p. 2101138. DOI: 10.1002/aenm.202101138.

[197] C. Baik, S. W. Lee, and C. Pak. "Glycine-Induced Ultrahigh-Surface-Area IrO_2@IrO_x Catalyst with Balanced Activity and Stability for Efficient Water Splitting". In: *Electrochimica Acta* 390 (2021), p. 138885. DOI: 10.1016/j.electacta.2021.138885.

[198] C. Sun, X. Chen, C. Ma, et al. "Pr-Si Co-Doped IrO_x as Promoted Anode for Refractory SDZ Degradation". In: *Journal of Electroanalytical Chemistry* 881 (2021), p. 114954. DOI: 10.1016/j.jelechem.2020.114954.

[199] J. Qi, M. Yang, H. Zeng, et al. "Understanding the Stabilization Effect of the Hydrous IrO_x Layer Formed on the Iridium Oxide Surface during the Oxygen Evolution Reaction in Acid". In: *Inorganic Chemistry Frontiers* 10.3 (2023), pp. 776–786. DOI: 10.1039/D2QI02214A.

[200] W. Gou, Z. Xia, X. Tan, et al. "Highly Active and Stable Amorphous IrO_x/CeO_2 Nanowires for Acidic Oxygen Evolution". In: *Nano Energy* 104 (2022), p. 107960. DOI: 10.1016/j.nanoen.2022.107960.

[201] Z. Yu, J. Xu, Y. Li, et al. "Ultrafine Oxygen-Defective Iridium Oxide Nanoclusters for Efficient and Durable Water Oxidation at High Current Densities in Acidic Media". In: *Journal of Materials Chemistry A* 8.46 (2020), pp. 24743–24751. DOI: 10.1039/D0TA07093A.

[202] S. Zhao, H. Yu, R. Maric, et al. "Calculating the Electrochemically Active Surface Area of Iridium Oxide in Operating Proton Exchange Membrane Electrolyzers". In: *Journal of The Electrochemical Society* 162.12 (2015), F1292. DOI: 10.1149/2.0211512jes.

[203] T. Shinagawa, A. T. Garcia-Esparza, and K. Takanabe. "Insight on Tafel Slopes from a Microkinetic Analysis of Aqueous Electrocatalysis for Energy Conversion". In: *Scientific Reports* 5.1 (2015), p. 13801. DOI: 10.1038/srep13801.

[204] U. Babic, M. Tarik, T. J. Schmidt, et al. "Understanding the Effects of Material Properties and Operating Conditions on Component Aging in Polymer Electrolyte Water Electrolyzers". In: *Journal of Power Sources* 451 (2020), p. 227778. DOI: 10.1016/j.jpowsour.2020.227778.

[205] Q. Feng, X.Z. Yuan, G. Liu, et al. "A Review of Proton Exchange Membrane Water Electrolysis on Degradation Mechanisms and Mitigation Strategies". In: *Journal of Power Sources* 366 (2017), pp. 33–55. DOI: 10.1016/j.jpowsour.2017.09.006.

[206] C. C. L. McCrory, S. Jung, I. M. Ferrer, et al. "Benchmarking Hydrogen Evolving Reaction and Oxygen Evolving Reaction Electrocatalysts for Solar Water Splitting Devices". In: *Journal of the American Chemical Society* 137.13 (2015), pp. 4347–4357. ISSN: 1520-5126. DOI: 10.1021/ja510442p.

[207] N. Trogisch, M. Koch, E. N. El Sawy, et al. "Microscopic Bubble Accumulation: The Missing Factor in Evaluating Oxygen Evolution Catalyst Stability during Accelerated Stress Tests". In: *ACS Catalysis* 12.21 (2022), pp. 13715–13724. DOI: 10.1021/acscatal.2c03881.

[208] M. F. Tovini, A. Hartig-Weiß, H. A. Gasteiger, et al. "The Discrepancy in Oxygen Evolution Reaction Catalyst Lifetime Explained: RDE vs MEA - Dynamicity within the Catalyst Layer Matters". In: *Journal of The Electrochemical Society* 168.1 (2021), p. 014512. DOI: 10.1149/1945-7111/abdcc9.

[209] A. Hartig-Weiss, M. F. Tovini, H.t A. Gasteiger, et al. "OER Catalyst Durability Tests Using the Rotating Disk Electrode Technique: The Reason Why This Leads to Erroneous Conclusions". In: *ACS Applied Energy Materials* 3.11 (2020), pp. 10323–10327. DOI: 10.1021/acsaem.0c01944.

[210] S. Kim, C. Ahn, Y. Cho, et al. "Suppressing Buoyant Force: New Avenue for Long-Term Durability of Oxygen Evolution Catalysts". In: *Nano Energy* 54 (2018), pp. 184–191. DOI: 10.1016/j.nanoen.2018.10.009.

[211] Y. Zhou, N. Jin, Y. Ma, et al. "Tube-Sponge-Inspired Hierarchical Electrocatalysts with Boosted Mass and Electron Transfer for Efficient Oxygen Evolution". In: *Advanced Materials* 35.8 (2023), p. 2209500. DOI: 10.1002/adma.202209500.

[212] Gh. Barati Darband, M. Aliofkhazraei, and A. Sabour Rouhaghdam. "Nickel Nanocones as Efficient and Stable Catalyst for Electrochemical Hydrogen Evolution Reaction". In: *International Journal of Hydrogen Energy* 42.21 (2017), pp. 14560–14565. DOI: 10.1016/j.ijhydene.2017.04.120.

[213] M. S. Faber, R. Dziedzic, M. A. Lukowski, et al. "High-Performance Electrocatalysis Using Metallic Cobalt Pyrite (CoS_2) Micro- and Nanostructures". In: *Journal of the American Chemical Society* 136.28 (2014), pp. 10053–10061. DOI: 10.1021/ja504099w.

[214] J. A. Koza, S. Mühlenhoff, P. Żabiński, et al. "Hydrogen Evolution under the Influence of a Magnetic Field". In: *Electrochimica Acta* 56.6 (Feb. 15, 2011), pp. 2665–2675. ISSN: 0013-4686. DOI: 10.1016/j.electacta.2010.12.031. URL: https://www.sciencedirect.com/science/article/pii/S0013468610016646 (visited on 03/04/2023).

[215] H. Matsushima, T. Iida, and Y. Fukunaka. "Gas Bubble Evolution on Transparent Electrode during Water Electrolysis in a Magnetic Field". In: *Electrochimica Acta* 100 (2013), pp. 261–264. DOI: 10.1016/j.electacta.2012.05.082.

[216] M. Wang, Z. Wang, and Z. Guo. "Understanding of the Intensified Effect of Super Gravity on Hydrogen Evolution Reaction". In: *International Journal of Hydrogen Energy* 34.13 (2009), pp. 5311–5317. DOI: 10.1016/j.ijhydene.2009.05.043.

[217] H Cheng and K Scott. "An Empirical Model Approach to Gas Evolution Reactions in a Centrifugal Field". In: *Journal of Electroanalytical Chemistry* 544 (2003), pp. 75–85. DOI: 10.1016/S0022-0728(03)00078-0.

[218] G. B. Darband, M. Aliofkhazraei, and S. Shanmugam. "Recent Advances in Methods and Technologies for Enhancing Bubble Detachment during Electrochemical Water Splitting". In: *Renewable and Sustainable Energy Reviews* 114 (2019), p. 109300. DOI: 10.1016/j.rser.2019.109300.

[219] *Geopolitics of the Energy Transformation: The Hydrogen Factor*. 2022. URL: https://www.irena.org/publications/2022/Jan/Geopolitics-of-the-Energy-Transformation-Hydrogen.

[220] *Electrolyser Costs*. URL: https://www.irena.org/Energy-Transition/Technology/Hydrogen/Electrolyser-costs.

[221] S. Lee, Y.-J. Lee, G. Lee, et al. "Activated Chemical Bonds in Nanoporous and Amorphous Iridium Oxides Favor Low Overpotential for Oxygen Evolution Reaction". In: *Nature Communications* 13.1 (2022), p. 3171. DOI: 10.1038/s41467-022-30838-y.

[222] C. Gutsche, C. J. Moeller, M. Knipper, et al. "Synthesis, Structure, and Electrochemical Stability of Ir-Decorated RuO_2 Nanoparticles and Pt Nanorods as Oxygen Catalysts". In: *The Journal of Physical Chemistry C* 120.2 (2016), pp. 1137–1146. DOI: 10.1021/acs.jpcc.5b11437.

[223] S. Park, N. Utsch, M. Carmo, et al. "Iridium–Nickel Nanoparticle-Based Aerogels for Oxygen Evolution Reaction". In: *ACS Applied Nano Materials* 5.12 (2022), pp. 18060–18069. DOI: 10.1021/acsanm.2c04000.

[224] D. Chandra, N. Abe, D. Takama, et al. "Open Pore Architecture of an Ordered Mesoporous IrO_2 Thin Film for Highly Efficient Electrocatalytic Water Oxidation". In: *ChemSusChem* 8.5 (2015), pp. 795–799. DOI: 10.1002/cssc.201402911.

[225] J. Gao, X. Huang, W. Cai, et al. "Rational Design of an Iridium–Tungsten Composite with an Iridium-Rich Surface for Acidic Water Oxidation". In: *ACS Applied Materials & Interfaces* 12.23 (2020), pp. 25991–26001. DOI: 10.1021/acsami.0c05906.

[226] S.A. Park, K. Kim, and Y. Kim. "Electrochemically Activated Iridium Oxide Black as Promising Electrocatalyst Having High Activity and Stability for Oxygen Evolution Reaction". In: *ACS Energy Letters* 3.5 (2018), pp. 1110–1115. DOI: 10.1021/acsenergylett.8b00368.

[227] J. J. Podestá, R. C. V. Piatti, and A. J. Arvia. "The Influence of Iridium, Ruthenium and Palladium on the Electrochemical Behaviour of Co-P and Ni-Co-P Base Amorphous Alloys for Water Electrolysis in KOH Aqueous Solutions". In: *International Journal of Hydrogen Energy* 20.2 (1995), pp. 111–122. DOI: 10.1016/0360-3199(94)E0006-K.

[228] J. Liu, Y. Zheng, Y. Jiao, et al. "NiO as a Bifunctional Promoter for RuO_2 toward Superior Overall Water Splitting". In: *Small* 14.16 (2018), p. 1704073. DOI: 10.1002/smll.201704073.

[229] L. Yang, H. Chen, L. Shi, et al. "Enhanced Iridium Mass Activity of 6H-Phase, Ir-Based Perovskite with Nonprecious Incorporation for Acidic Oxygen Evolution Electrocatalysis". In: *ACS Applied Materials & Interfaces* 11.45 (2019), pp. 42006–42013. DOI: 10.1021/acsami.9b11287.

[230] L. Ai, Y. Luo, W. Huang, et al. "Cobalt/Cerium-Based Metal-Organic Framework Composites for Enhanced Oxygen Evolution Electrocatalysis". In: *International Journal of Hydrogen Energy* 47.26 (2022), pp. 12893–12902. DOI: 10.1016/j.ijhydene.2022.02.043.

[231] L. Wang, F. Song, G. Ozouf, et al. "Improving the Activity and Stability of Ir Catalysts for PEM Electrolyzer Anodes by SnO_2:Sb Aerogel Supports: Does V Addition Play an Active Role in Electrocatalysis?" In: *Journal of Materials Chemistry A* 5.7 (2017), pp. 3172–3178. DOI: 10.1039/C7TA00679A.

[232] D. Böhm, M. Beetz, M. Schuster, et al. "Efficient OER Catalyst with Low Ir Volume Density Obtained by Homogeneous Deposition of Iridium Oxide Nanoparticles on Macroporous Antimony-Doped Tin Oxide Support". In: *Advanced Functional Materials* 30.1 (2020), p. 1906670. DOI: 10.1002/adfm.201906670.

[233] S. B. Han, Y. H. Mo, Y. S. Lee, et al. "Mesoporous Iridium Oxide/Sb-doped SnO_2 Nanostructured Electrodes for Polymer Electrolyte Membrane Water Electrolysis". In: *International Journal of Hydrogen Energy* 45.3 (2020), pp. 1409–1416. DOI: 10.1016/j.ijhydene.2019.11.109.

[234] N. J. Pérez-Viramontes, I. L. Escalante-García, C. Guzmán-Martínez, et al. "Electrochemical Study of Ir–Sn–Sb–O Materials as Catalyst-Supports for the Oxygen Evolution Reaction". In: *Journal of Applied Electrochemistry* 45.11 (2015), pp. 1165–1173. DOI: 10.1007/s10800-015-0875-3.

[235] H. Jang, J. H. Lee, J. R. Lee, et al. "Metal–Support Interaction Can Deactivate IrO_x/Sb:SnO_2 OER Catalysts in Polyol Process". In: *ACS Applied Energy Materials* 5.8 (2022), pp. 9297–9302. DOI: 10.1021/acsaem.2c01765.

[236] P. Mazúr, J. Polonský, M. Paidar, et al. "Non-Conductive TiO_2 as the Anode Catalyst Support for PEM Water Electrolysis". In: *International Journal of Hydrogen Energy* 37.17 (2012), pp. 12081–12088. DOI: 10.1016/j.ijhydene.2012.05.129.

[237] A. V. Nikiforov, A. L. Tomás García, I. M. Petrushina, et al. "Preparation and Study of IrO_2/SiC–Si Supported Anode Catalyst for High Temperature PEM Steam Electrolysers". In: *International Journal of Hydrogen Energy* 36.10 (2011), pp. 5797–5805. DOI: 10.1016/j.ijhydene.2011.02.050.

[238] J. Polonský, I. M. Petrushina, E. Christensen, et al. "Tantalum Carbide as a Novel Support Material for Anode Electrocatalysts in Polymer Electrolyte Membrane Water Electrolysers". In: *International Journal of Hydrogen Energy*. 2010 AIChE Annual Meeting Topical Conference on Hydrogen Production and Storage Special Issue 37.3 (2012), pp. 2173–2181. DOI: 10.1016/j.ijhydene.2011.11.035.

[239] S. Daolio, J. Kristóf, J. Mink, et al. "Secondary Ion Mass Spectrometric Studies on the Formation Mechanism of IrO_2/ZrO_2 Based Electrocatalytic Thin Films". In: *Rapid Communications in Mass Spectrometry* 10.15 (1996), pp. 1881–1886. DOI: 10.1002/(SICI)1097-0231(199612)10:15<1881::AID-RCM766>3.0.CO;2-C.

[240] B. Liu, C. Wang, Y. Chen, et al. "Effects of Calcination Temperature on the Surface Morphology and Electrocatalytic Properties of Ti/IrO_2-ZrO_2 Anodes in an Oxygen Evolution Application". In: *Journal of The Electrochemical Society* 165.14 (2018), F1192. DOI: 10.1149/2.0701814jes.

[241] Y. Q. Shao, Z. J. Chen, J. Q. Zhu, et al. "Relationship Between Electronic Structures and Capacitive Performance of the Electrode Material IrO_2–ZrO_2". In: *Journal of the American Ceramic Society* 99.7 (2016), pp. 2504–2511. DOI: 10.1111/jace.14219.

[242] F. Zhao, B. Wen, W. Niu, et al. "Increasing Iridium Oxide Activity for the Oxygen Evolution Reaction with Hafnium Modification". In: *Journal of the American Chemical Society* 143.38 (2021), pp. 15616–15623. DOI: 10.1021/jacs.1c03473.

[243] M. M. Jakšić. "Advances in Electrocatalysis for Hydrogen Evolution in the Light of the Brewer-Engel Valence-Bond Theory". In: *Journal of Molecular Catalysis* 38.1 (1986), pp. 161–202. DOI: 10.1016/0304-5102(86)87056-0.

[244] C. Lee, K. Shin, Y. Park, et al. "Catalyst-Support Interactions in Zr_2ON_2-Supported IrO_x Electrocatalysts to Break the Trade-Off Relationship Between the Activity and Stability in the Acidic Oxygen Evolution Reaction". In: *Advanced Functional Materials* 33.25 (2023), p. 2301557. DOI: 10.1002/adfm.202301557.

[245] F. Claudel, L. Dubau, S. Sunde, et al. "Degradation of IrO_x Nanoparticles Supported Onto Sb-Doped SnO_2 Aerogel Monitored By Dynamic Electrochemical Impedance Spectroscopy and Identical-Location TEM". In: *ECS Meeting Abstracts* MA2018-01.29 (2018), p. 1668. DOI: 10.1149/MA2018-01/29/1668.

[246] H. A. El-Sayed, A. Weiß, L. F. Olbrich, et al. "OER Catalyst Stability Investigation Using RDE Technique: A Stability Measure or an Artifact?" In: *Journal of The Electrochemical Society* 166.8 (2019), F458. DOI: 10.1149/2.0301908jes.

[247] G. C. da Silva, N. Perini, and E. A. Ticianelli. "Effect of Temperature on the Activities and Stabilities of Hydrothermally Prepared IrO_x Nanocatalyst Layers for the Oxygen Evolution Reaction". In: *Applied Catalysis B: Environmental* 218 (2017), pp. 287–297. DOI: 10.1016/j.apcatb.2017.06.044.

[248] B. G. Pollet and J. T. E. Goh. "The Importance of Ultrasonic Parameters in the Preparation of Fuel Cell Catalyst Inks". In: *Electrochimica Acta* 128 (2014), pp. 292–303. DOI: 10.1016/j.electacta.2013.09.160.

[249] Ming Gong and Hongjie Dai. "A Mini Review of NiFe-based Materials as Highly Active Oxygen Evolution Reaction Electrocatalysts". In: *Nano Research* 8.1 (2015), pp. 23–39. DOI: 10.1007/s12274-014-0591-z.

[250] S. Cherevko, S. Geiger, O. Kasian, et al. "Oxygen Evolution Activity and Stability of Iridium in Acidic Media. Part 2. – Electrochemically Grown Hydrous Iridium Oxide". In: *Journal of Electroanalytical Chemistry* 774 (2016), pp. 102–110. DOI: 10.1016/j.jelechem.2016.05.015.

[251] E. Willinger, C. Massué, R. Schlögl, et al. "Identifying Key Structural Features of IrO_x Water Splitting Catalysts". In: *Journal of the American Chemical Society* 139.34 (2017), pp. 12093–12101. DOI: 10.1021/jacs.7b07079.

[252] J. Kondoh. "Origin of the Hump on the Left Shoulder of the X-ray Diffraction Peaks Observed in Y_2O_3-fully and Partially Stabilized ZrO_2". In: *Journal of Alloys and Compounds* 375.1 (2004), pp. 270–282. DOI: 10.1016/j.jallcom.2003.11.129.

[253] E. A. Klop and M. Lammers. "XRD Study of the New Rigid-Rod Polymer Fibre PIPD". In: *Polymer* 39.24 (1998), pp. 5987–5998. DOI: 10.1016/S0032-3861(97)10187-2.

[254] V. Stanev, V. V. Vesselinov, A. G. Kusne, et al. "Unsupervised Phase Mapping of X-ray Diffraction Data by Nonnegative Matrix Factorization Integrated with Custom Clustering". In: *npj Computational Materials* 4.1 (2018), pp. 1–10. DOI: 10.1038/s41524-018-0099-2.

[255] R. D. Shannon. "Revised Effective Ionic Radii and Systematic Studies of Interatomic Distances in Halides and Chalcogenides". In: *Acta Crystallographica Section A* 32.5 (1976), pp. 751–767. DOI: 10.1107/S0567739476001551.

[256] H. T. Chung, J. G. Kim, and H. G Kim. "Dependence of the Lithium Ionic Conductivity on the B-site Ion Substitution in $(Li_{0.5}La_{0.5})Ti_{1-x}M_xO_3$ (M=Sn, Zr, Mn, Ge)". In: *Solid State Ionics* 107.1 (1998), pp. 153–160. DOI: 10.1016/S0167-2738(97)00525-0.

[257] A. Minguzzi, O. Lugaresi, E. Achilli, et al. "Observing the Oxidation State Turnover in Heterogeneous Iridium-Based Water Oxidation Catalysts". In: *Chemical Science* 5.9 (2014), p. 3591. DOI: 10.1039/C4SC00975D.

[258] G. K. Wertheim and H. J. Guggenheim. "Conduction-Electron Screening in Metallic Oxides: IrO_2". In: *Physical Review B* 22.10 (1980), pp. 4680–4683. DOI: 10.1103/PhysRevB.22.4680.

[259] A. Kramida and Y. Ralchenko. *NIST Atomic Spectra Database, NIST Standard Reference Database 78*. National Institute of Standards and Technology, 1999. DOI: 10.18434/T4W30F.

[260] PubChem. *Ionization Energy | Periodic Table of Elements*. URL: https://pubchem.ncbi.nlm.nih.gov/periodic-table/ionization-energy.

[261] M. Scohy, S. Abbou, V. Martin, et al. "Probing Surface Oxide Formation and Dissolution on/of Ir Single Crystals via X-ray Photoelectron Spectroscopy and Inductively Coupled Plasma Mass Spectrometry". In: *ACS Catalysis* 9.11 (2019), pp. 9859–9869. DOI: 10.1021/acscatal.9b02988.

[262] A. BalaKrishnan, N. Blanc, U. Hagemann, et al. "Direct Detection of Surface Species Formed on Iridium Electrocatalysts during the Oxygen Evolution Reaction". In: *Angewandte Chemie International Edition* 60.39 (2021), pp. 21396–21403. DOI: 10.1002/anie.202106790.

[263] F. Hegge, F. Lombeck, E. Cruz Ortiz, et al. "Efficient and Stable Low Iridium Loaded Anodes for PEM Water Electrolysis Made Possible by Nanofiber Interlayers". In: *ACS Applied Energy Materials* 3.9 (2020), pp. 8276–8284. DOI: 10.1021/acsaem.0c00735.

[264] E. Fabbri, A. Rabis, R. Kötz, et al. "Pt Nanoparticles Supported on Sb-doped SnO_2 Porous Structures: Developments and Issues". In: *Physical Chemistry Chemical Physics* 16.27 (2014), pp. 13672–13681. DOI: 10.1039/C4CP00238E.

[265] G. Cognard, G. Ozouf, C. Beauger, et al. "Benefits and Limitations of Pt Nanoparticles Supported on Highly Porous Antimony-Doped Tin Dioxide Aerogel as Alternative Cathode Material for Proton-Exchange Membrane Fuel Cells". In: *Applied Catalysis B: Environmental* 201 (2017), pp. 381–390. DOI: 10.1016/j.apcatb.2016.08.010.

[266] V. Pfeifer, T. E. Jones, J. J. Velasco Vélez, et al. "The Electronic Structure of Iridium and Its Oxides". In: *Surface and Interface Analysis* 48.5 (2016), pp. 261–273. DOI: 10.1002/sia.5895.

[267] M. Bernt, C. Schramm, J. Schröter, et al. "Effect of the IrO_x Conductivity on the Anode Electrode/Porous Transport Layer Interfacial Resistance in PEM Water Electrolyzers". In: *Journal of The Electrochemical Society* 168.8 (2021), p. 084513. DOI: 10.1149/1945-7111/ac1eb4.

[268] R. A. Krivina, M. Zlatar, T. N. Stovall, et al. "Oxygen Evolution Electrocatalysis in Acids: Atomic Tuning of the Stability Number for Submonolayer IrO_x on Conductive Oxides from Molecular Precursors". In: *ACS Catalysis* 13.2 (2023), pp. 902–915. DOI: 10.1021/acscatal.2c04439.

[269] A. Lončar, D. Escalera-López, S. Cherevko, et al. "Inter-Relationships between Oxygen Evolution and Iridium Dissolution Mechanisms". In: *Angewandte Chemie International Edition* 61.14 (2022), e202114437. DOI: 10.1002/anie.202114437.

[270] S. Siracusano, N. Van Dijk, E. Payne-Johnson, et al. "Nanosized IrO_x and $IrRuO_x$ Electrocatalysts for the O_2 Evolution Reaction in PEM Water Electrolysers". In: *Applied Catalysis B: Environmental* 164 (2015), pp. 488–495. DOI: 10.1016/j.apcatb.2014.09.005.

[271] P. Satjaritanun, M. O'Brien, D. Kulkarni, et al. "Observation of Preferential Pathways for Oxygen Removal through Porous Transport Layers of Polymer Electrolyte Water Electrolyzers". In: *iScience* 23.12 (2020), p. 101783. DOI: 10.1016/j.isci.2020.101783.

[272] A. Minguzzi, C. Locatelli, O. Lugaresi, et al. "Easy Accommodation of Different Oxidation States in Iridium Oxide Nanoparticles with Different Hydration Degree as Water Oxidation Electrocatalysts". In: *ACS Catalysis* 5.9 (2015), pp. 5104–5115. DOI: 10.1021/acscatal.5b01281.

[273] T. Naito, T. Shinagawa, T. Nishimoto, et al. "Recent Advances in Understanding Oxygen Evolution Reaction Mechanisms over Iridium Oxide". In: *Inorganic Chemistry Frontiers* 8.11 (2021), pp. 2900–2917. DOI: 10.1039/D0QI01465F.

[274] H. G. Sanchez Casalongue, M. L. Ng, S. Kaya, et al. "In Situ Observation of Surface Species on Iridium Oxide Nanoparticles during the Oxygen Evolution Reaction". In: *Angewandte Chemie International Edition* 53.28 (2014), pp. 7169–7172. DOI: 10.1002/anie.201402311.

[275] S. Fierro, A. Kapałka, and C. Comninellis. "Electrochemical Comparison between IrO_2 Prepared by Thermal Treatment of Iridium Metal and IrO_2 Prepared by Thermal Decomposition of H_2IrCl_6 Solution". In: *Electrochemistry Communications* 12.1 (2010), pp. 172–174. DOI: 10.1016/j.elecom.2009.11.018.

[276] W. Huo, X. Zhou, Y. Jin, et al. "Rhenium Suppresses Iridium (IV) Oxide Crystallization and Enables Efficient, Stable Electrochemical Water Oxidation". In: *Small* 19.19 (2023), p. 2207847. DOI: 10.1002/smll.202207847.

[277] K. Schweinar, B. Gault, I. Mouton, et al. "Lattice Oxygen Exchange in Rutile IrO_2 during the Oxygen Evolution Reaction". In: *The Journal of Physical Chemistry Letters* 11.13 (2020), pp. 5008–5014. DOI: 10.1021/acs.jpclett.0c01258.

[278] S. Siahrostami and A. Vojvodic. "Influence of Adsorbed Water on the Oxygen Evolution Reaction on Oxides". In: *The Journal of Physical Chemistry C* 119.2 (2015), pp. 1032–1037. DOI: 10.1021/jp508932x.

[279] P. Rüetschi and P. Delahay. "Influence of Electrode Material on Oxygen Overvoltage: A Theoretical Analysis". In: *Journal of Chemical Physics* 23 (1955), pp. 556–560. DOI: 10.1063/1.1742029.

[280] J. A. Gauthier, C. F. Dickens, L. D. Chen, et al. "Solvation Effects for Oxygen Evolution Reaction Catalysis on IrO_2 (110)". In: *The Journal of Physical Chemistry C* 121.21 (2017), pp. 11455–11463. DOI: 10.1021/acs.jpcc.7b02383.

[281] John Meurig Thomas and W. John Thomas. *Principles and Practice of Heterogeneous Catalysis*. John Wiley & Sons, Dec. 11, 2014. ISBN: 978-3-527-68380-2.

[282] M. Egashira, M. Nakashima, S. Kawasumi, et al. "Temperature Programmed Desorption Study of Water Adsorbed on Metal Oxides. Tin Oxide Surfaces". In: *The Journal of Physical Chemistry* 85.26 (1981), pp. 4125–4130. DOI: 10.1021/j150626a034.

[283] W. Cao, J. Kang, G. Fan, et al. "Fabrication of Porous ZrO_2 Nanostructures with Controlled Crystalline Phases and Structures via a Facile and Cost-Effective Hydrothermal Approach". In: *Industrial & Engineering Chemistry Research* 54.51 (2015), pp. 12795–12804. DOI: 10.1021/acs.iecr.5b03114.

[284] J. Liao, Y. Wang, M. Chen, et al. "IrO_x Supported onto Niobium-Doped Titanium Dioxide as an Anode Reversal Tolerant Electrocatalyst for Proton Exchange Membrane Fuel Cells". In: *ACS Applied Energy Materials* 5.3 (2022), pp. 3259–3268. DOI: 10.1021/acsaem.1c03873.

[285] Q. Deng, Y. Sun, J. Wang, et al. "Boosting OER Performance of IrO_2 in Acid via Urchin-like Hierarchical-Structure Design". In: *Dalton Transactions* 50.18 (2021), pp. 6083–6087. DOI: 10.1039/D1DT00329A.

[286] M. Gollasch, J. Schmeling, C. Harms, et al. "Comparative Analysis of Synthesis Routes for Antimony-Doped Tin Oxide-Supported Iridium and Iridium Oxide Catalysts for OER in PEM Water Electrolysis". In: *Advanced Materials Interfaces* 10.15 (), p. 2300036. DOI: 10.1002/admi.202300036.

[287] J. Lim, G. Kang, J. W. Lee, et al. "Amorphous Ir Atomic Clusters Anchored on Crystalline IrO_2 Nanoneedles for Proton Exchange Membrane Water Oxidation". In: *Journal of Power Sources* 524 (2022), p. 231069. ISSN: 0378-7753. DOI: 10.1016/j.jpowsour.2022.231069.

[288] S. Ardizzone, C. L. Bianchi, L. Borgese, et al. "Physico-Chemical Characterization of IrO_2–SnO_2 Sol-Gel Nanopowders for Electrochemical Applications". In: *Journal of Applied Electrochemistry* 39.11 (2009), pp. 2093–2105. DOI: 10.1007/s10800-009-9895-1.

[289] Y. Hu, C. Ma, G. Du, et al. "Toward Efficient Electrocatalytic Oxygen Evolution with a Low Concentration Baking Soda Activated IrO_x Surface in a Hydrothermal Medium". In: *Materials Chemistry Frontiers* 6.10 (2022), pp. 1282–1291. DOI: 10.1039/D2QM00121G.

[290] S. Siracusano, V. Baglio, A. Di Blasi, et al. "Electrochemical Characterization of Single Cell and Short Stack PEM Electrolyzers Based on a Nanosized IrO_2 Anode Electrocatalyst". In: *International Journal of Hydrogen Energy* 35.11 (2010), pp. 5558–5568. DOI: 10.1016/j.ijhydene.2010.03.102.

[291] F. Farges, J. A. Sharps, and G. E. Brown. "Local Environment around Gold (III) in Aqueous Chloride Solutions: An EXAFS Spectroscopy Study". In: *Geochimica et Cosmochimica Acta* 57.6 (1993), pp. 1243–1252. DOI: 10.1016/0016-7037(93)90061-Z.

[292] B. S Uphade, M Okumura, S Tsubota, et al. "Effect of Physical Mixing of CsCl with Au/Ti-MCM-41 on the Gas-Phase Epoxidation of Propene Using H_2 and O_2:: Drastic Depression of H_2 Consumption". In: *Applied Catalysis A: General* 190.1 (2000), pp. 43–50. DOI: 10.1016/S0926-860X(99)00285-9.

[293] E. del Río, D. Gaona, J.C. Hernández-Garrido, et al. "Speciation-Controlled Incipient Wetness Impregnation: A Rational Synthetic Approach to Prepare Sub-Nanosized and Highly Active Ceria–Zirconia Supported Gold Catalysts". In: *Journal of Catalysis* 318 (2014), pp. 119–127. DOI: 10.1016/j.jcat.2014.07.001.

[294] M. Hargittai, A. Schulz, B. Réffy, et al. "Molecular Structure, Bonding, and Jahn-Teller Effect in Gold Chlorides: Quantum Chemical Study of $AuCl_3$, Au_2Cl_6, $AuCl_4$-, AuCl, and $Au2Cl_2$ and Electron Diffraction Study of Au_2Cl_6". In: *Journal of the American Chemical Society* 123.7 (2001), pp. 1449–1458. DOI: 10.1021/ja003038k.

[295] G. A. Lindquist, Q. Xu, S. Z. Oener, et al. "Membrane Electrolyzers for Impure-Water Splitting". In: *Joule* 4.12 (2020), pp. 2549–2561. DOI: 10.1016/j.joule.2020.09.020.

[296] Fanghao Zhang, Luo Yu, Libo Wu, et al. "Rational Design of Oxygen Evolution Reaction Catalysts for Seawater Electrolysis". In: *Trends in Chemistry* 3.6 (June 1, 2021), pp. 485–498. ISSN: 2589-5974. DOI: 10.1016/j.trechm.2021.03.003. URL: https://www.sciencedirect.com/science/article/pii/S2589597421000551 (visited on 04/24/2023).

[297] G. Liu, Y. Xu, T. Yang, et al. "Recent Advances in Electrocatalysts for Seawater Splitting". In: *Nano Materials Science* 5.1 (2023), pp. 101–116. DOI: 10.1016/j.nanoms.2020.12.003.

[298] J. E. Bennett. "Electrodes for Generation of Hydrogen and Oxygen from Seawater". In: *International Journal of Hydrogen Energy* 5.4 (1980), pp. 401–408. DOI: 10.1016/0360-3199(80)90021-X.

[299] J. G. Vos, A. Venugopal, W. A. Smith, et al. "Competition and Selectivity during Parallel Evolution of Bromine, Chlorine and Oxygen on IrO_x Electrodes". In: *Journal of Catalysis* 389 (2020), pp. 99–110. DOI: 10.1016/j.jcat.2020.05.024.

[300] M. Haruta. "Size-and Support-Dependency in the Catalysis of Gold". In: *Catalysis Today* 36.1 (1997), pp. 153–166. DOI: 10.1016/S0920-5861(96)00208-8.

[301] D. Xu, P. Diao, T. Jin, et al. "Iridium Oxide Nanoparticles and Iridium/Iridium Oxide Nanocomposites: Photochemical Fabrication and Application in Catalytic Reduction of 4-Nitrophenol". In: *ACS Applied Materials & Interfaces* 7.30 (2015), pp. 16738–16749. DOI: 10.1021/acsami.5b04504.

[302] PubChem. *Ammonia*. URL: https://pubchem.ncbi.nlm.nih.gov/compound/222.

[303] PubChem. *Nitrogen Dioxide*. URL: https://pubchem.ncbi.nlm.nih.gov/compound/3032552.

[304] J. Gao, C. Q. Xu, S. F. Hung, et al. "Breaking Long-Range Order in Iridium Oxide by Alkali Ion for Efficient Water Oxidation". In: *Journal of the American Chemical Society* 141.7 (2019), pp. 3014–3023. DOI: 10.1021/jacs.8b11456.

[305] S. J. Freakley, J. Ruiz-Esquius, and D. J. Morgan. "The X-ray Photoelectron Spectra of Ir, IrO_2 and $IrCl_3$ Revisited". In: *Surface and Interface Analysis* 49.8 (2017), pp. 794–799. ISSN: 1096-9918. DOI: 10.1002/sia.6225.

[306] N. Diklić, A. H. Clark, J. Herranz, et al. "Surface Ir^{+5} Formation as a Universal Prerequisite for O_2 Evolution on Ir Oxides". In: *ACS Catalysis* 13.16 (2023), pp. 11069–11079. DOI: 10.1021/acscatal.3c01448.

[307] C. D. Wagner, D. A. Zatko, and R. H. Raymond. "Use of the Oxygen KLL Auger Lines in Identification of Surface Chemical States by Electron Spectroscopy for Chemical Analysis". In: *Analytical Chemistry* 52.9 (1980), pp. 1445–1451. DOI: 10.1021/ac50059a017.

[308] R. V. Mom, L. J. Falling, O. Kasian, et al. "Operando Structure–Activity–Stability Relationship of Iridium Oxides during the Oxygen Evolution Reaction". In: *ACS Catalysis* 12.9 (2022), pp. 5174–5184. DOI: 10.1021/acscatal.1c05951.

[309] D. J. Morgan. "Resolving Ruthenium: XPS Studies of Common Ruthenium Materials". In: *Surface and Interface Analysis* 47.11 (2015), pp. 1072–1079. DOI: 10.1002/sia.5852.

[310] G. W. Jang. "Thermal and Electrochemical Analyses of Noble Metal Compounds". D.Sc. United States – Texas: The University of Texas at Arlington.

[311] J. Liao, S. Zaman, Y. Wang, et al. "Improved Reversal Tolerant Properties of IrO_x as an Anode Electrocatalyst in Proton Exchange Membrane Fuel Cells". In: *ACS Applied Materials & Interfaces* 15.3 (2023), pp. 4092–4100. DOI: 10.1021/acsami.2c20246.

[312] Ge Meng, Wenming Sun, Aye Aye Mon, et al. "Strain Regulation to Optimize the Acidic Water Oxidation Performance of Atomic-Layer IrO_x". In: *Advanced Materials* 31.37 (2019), p. 1903616. DOI: 10.1002/adma.201903616.

[313] C. Massué, V. Pfeifer, M. van Gastel, et al. "Reactive Electrophilic O^{I-} Species Evidenced in High-Performance Iridium Oxohydroxide Water Oxidation Electrocatalysts". In: *ChemSusChem* 10.23 (2017), pp. 4786–4798. DOI: 10.1002/cssc.201701291.

[314] K. S. Exner. "Overpotential-Dependent Volcano Plots to Assess Activity Trends in the Competing Chlorine and Oxygen Evolution Reactions". In: *ChemElectroChem* 7.6 (2020), pp. 1448–1455. DOI: 10.1002/celc.202000120.

[315] J. M. Hu, J. Q. Zhang, and C. N. Cao. "Oxygen Evolution Reaction on IrO_2-based DSA Type Electrodes: Kinetics Analysis of Tafel Lines and EIS". In: *International Journal of Hydrogen Energy* 29.8 (2004), pp. 791–797. DOI: 10.1016/j.ijhydene.2003.09.007.

[316] V. A. Alves, L. A. da Silva, J. F. C. Boodts, et al. "Kinetics and Mechanism of Oxygen Evolution on IrO_2-based Electrodes Containing Ti and Ce Acidic Solutions". In: *Electrochimica Acta* 39.11 (1994), pp. 1585–1589. DOI: 10.1016/0013-4686(94)85139-5.

[317] C. Angelinetta, S. Trasatti, Lj. D. Atanasoska, et al. "Effect of Preparation on the Surface and Electrocatalytic Properties of RuO_2 + IrO_2 Mixed Oxide Electrodes". In: *Materials Chemistry and Physics* 22.1 (1989), pp. 231–247. DOI: 10.1016/0254-0584(89)90039-4.

[318] Y. Liu, A. Ishihara, S. Mitsushima, et al. "Zirconium Oxide for PEFC Cathodes". In: *Electrochemical and Solid-State Letters* 8.8 (2005), A400. ISSN: 1944-8775. DOI: 10.1149/1.1943550.

[319] Y. Wang, T. Brezesinski, M. Antonietti, et al. "Ordered Mesoporous Sb-, Nb-, and Ta-Doped SnO_2 Thin Films with Adjustable Doping Levels and High Electrical Conductivity". In: *ACS Nano* 3.6 (2009), pp. 1373–1378. DOI: 10.1021/nn900108x.

[320] Sieghard E. Wanke. "Introduction to Characterization and Testing of Catalysts". In: *The Canadian Journal of Chemical Engineering* 66.2 (1988), pp. 349–349. DOI: 10.1002/cjce.5450660229.

[321] K. Zhang, W. Mai, J. Li, et al. "Highly Scattered Ir Oxides on TiN as an Efficient Oxygen Evolution Reaction Electrocatalyst in Acidic Media". In: *Journal of Materials Science* 55.8 (2020), pp. 3507–3520. DOI: 10.1007/s10853-019-04201-4.

[322] X. Zheng, M. Qin, S. Ma, et al. "Strong Oxide-Support Interaction over IrO_2/V_2O_5 for Efficient pH-Universal Water Splitting". In: *Advanced Science* 9.11 (2022), p. 2104636. DOI: 10.1002/advs.202104636.

[323] S. S. Karade, R. Sharma, S. Gyergyek, et al. "IrO_2/Ir Composite Nanoparticles (IrO_2@Ir) Supported on TiN_xO_y Coated TiN: Efficient and Robust Oxygen Evolution Reaction Catalyst for Water Electrolysis". In: *ChemCatChem* 15.4 (2023), e202201470. DOI: 10.1002/cctc.202201470.

[324] E. J. Kim, J. Shin, J. Bak, et al. "Stabilizing Role of Mo in TiO_2-MoO_x Supported Ir Catalyst toward Oxygen Evolution Reaction". In: *Applied Catalysis B: Environmental* 280 (2021), p. 119433. DOI: 10.1016/j.apcatb.2020.119433.

[325] M. Bele, K. Stojanovski, P. Jovanovič, et al. "Towards Stable and Conductive Titanium Oxynitride High-Surface-Area Support for Iridium Nanoparticles as Oxygen Evolution Reaction Electrocatalyst". In: *ChemCatChem* 11.20 (2019), pp. 5038–5044. DOI: 10.1002/cctc.201901487.

[326] L. Moriau, M. Bele, Ž. Marinko, et al. "Effect of the Morphology of the High-Surface-Area Support on the Performance of the Oxygen-Evolution Reaction for Iridium Nanoparticles". In: *ACS Catalysis* 11.2 (2021), pp. 670–681. DOI: 10.1021/acscatal.0c04741.

[327] L. Moriau, G. Koderman Podboršek, A. K. Surca, et al. "Enhancing Iridium Nanoparticles' Oxygen Evolution Reaction Activity and Stability by Adjusting the Coverage of Titanium Oxynitride Flakes on Reduced Graphene Oxide Nanoribbons' Support". In: *Advanced Materials Interfaces* 8.17 (2021), p. 2100900. ISSN: 2196-7350. DOI: 10.1002/admi.202100900.

[328] J. M. Kanervo and A. Krause. "Kinetic Analysis of Temperature-Programmed Reduction: Behavior of a CrO_x/Al_2O_3 Catalyst". In: *The Journal of Physical Chemistry B* 105.40 (2001), pp. 9778–9784. DOI: 10.1021/jp0114079.

Appendix A: Strong metal - support interactions in ZrO_2-supported IrO_X catalyst for efficient oxygen evolution reaction

A.1 Materials characterization

A.1.1 Nitrogen (N_2) adsorption-desorption isotherm for $ZrO_{2(L)}$

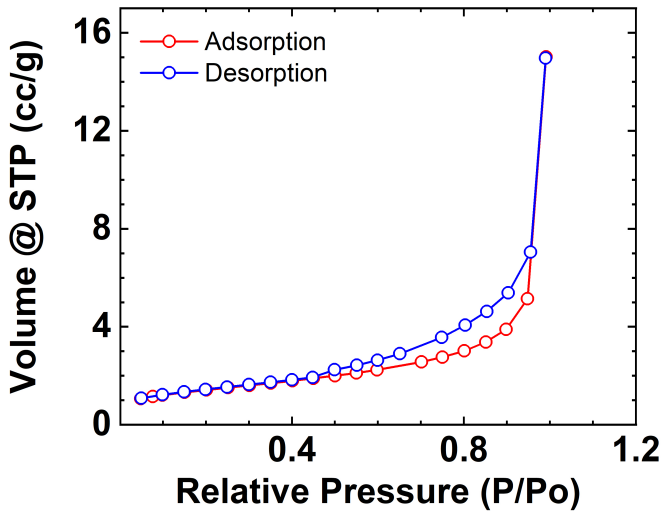

Figure A.1: N_2 adsorption-desorption isotherm for $ZrO_{2(L)}$.

A.1.2 Microstructural characterization: Transmission electron microscopy (TEM), energy-dispersive X-ray analysis (EDX) mapping, selected area electron diffraction (SAED)

The commercial software ImageJ was used to estimate the particle size of IrO_x nanoparticles. The volume mean averaged diameter of IrO_x particles (in nm) was calculated using the formula [320]:

$$đ_{\mathrm{vol}} = \left[\frac{\sum_{i=1}^{N} n_{\mathrm{i}} (d_{\mathrm{i}})^3}{\sum_{i=1}^{N} n_{\mathrm{i}}} \right]^{\frac{1}{3}} \tag{A.1}$$

where,

n_i is number of particles in the size range defined by size d_i, and

N is number of size increments.

The skewness was calculated using the skew function in Excel.

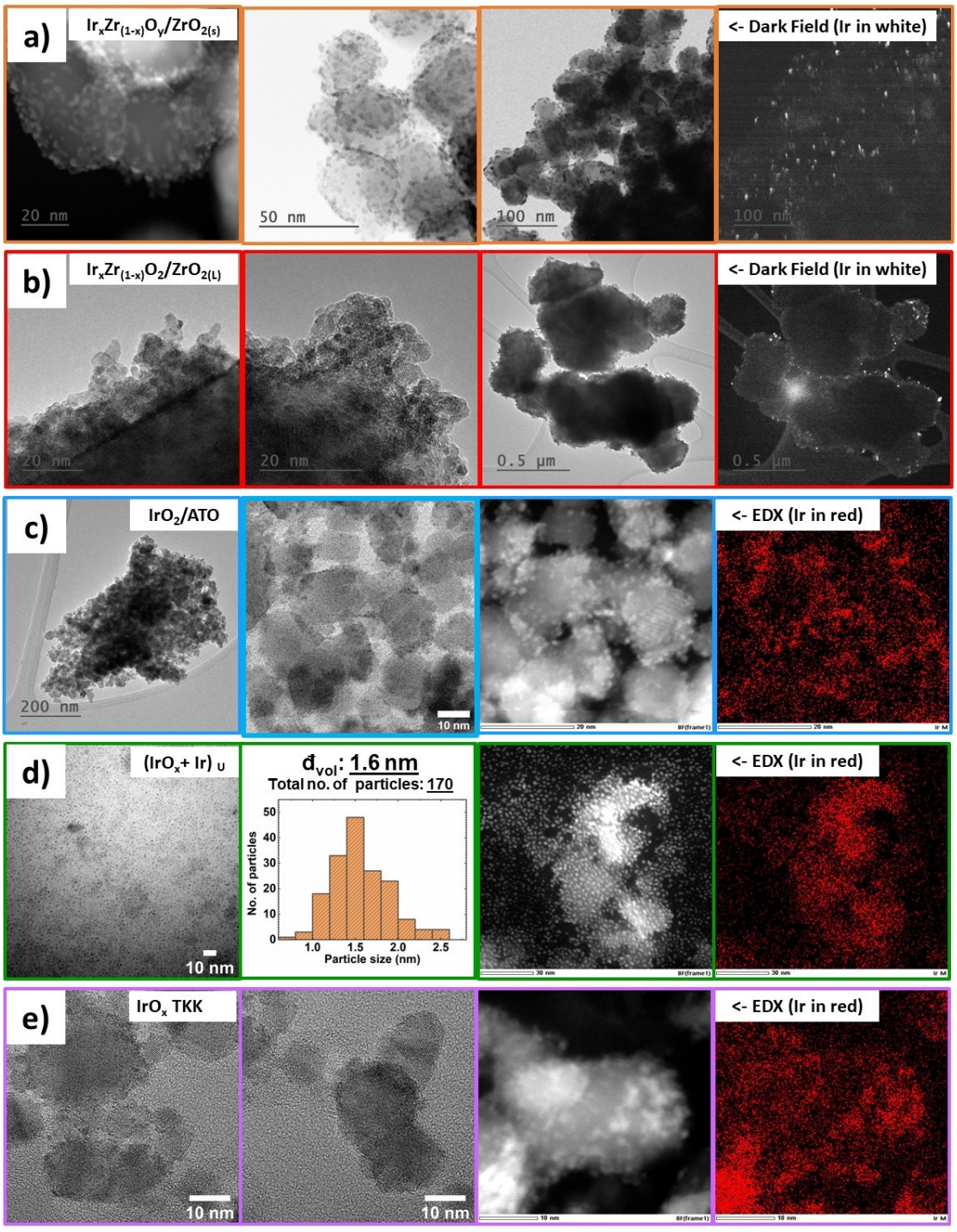

Figure A.2: TEM and EDX mapping images of the electrocatalysts (a) $Ir_xZr_{(1-x)}O_y/ZrO_{2(S)}$, (b) $Ir_xZr_{(1-x)}O_2/ZrO_{2(L)}$, (c) IrO_2/ATO, (d) $(IrO_2 + Ir)_U$, and (e) IrO_x TKK with corresponding particle-size distribution, where $\bar{d}_{vol}$ is the volume mean particle size of the catalysts.

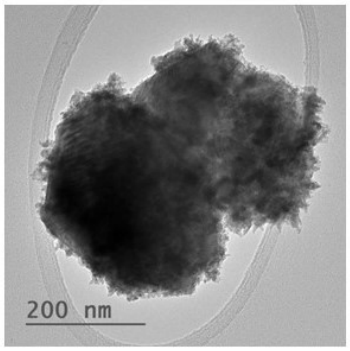

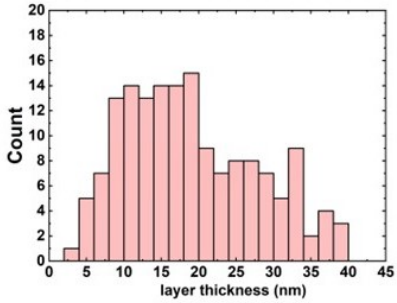

Avg. $Ir_xZr_{(1-x)}O_2$ layer thickness: 23 nm

No. of data points: 152

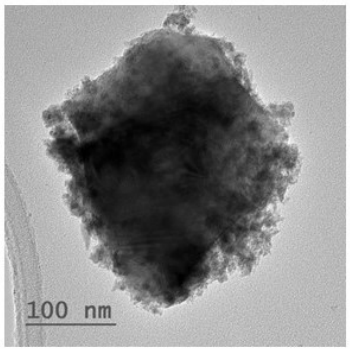

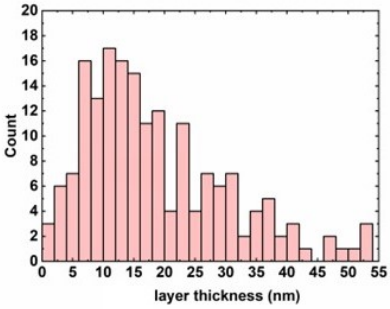

Avg. $Ir_xZr_{(1-x)}O_2$ layer thickness: 25 nm

No. of data points: 179

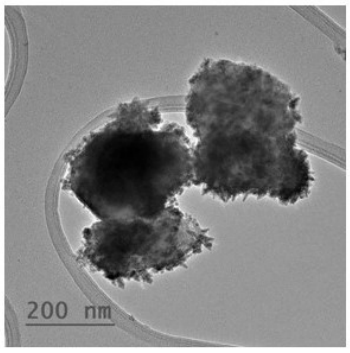

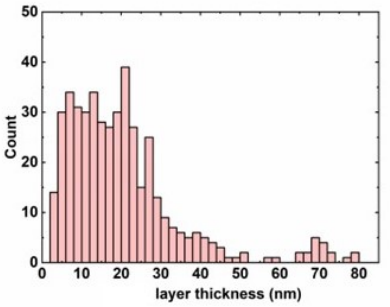

Avg. $Ir_xZr_{(1-x)}O_2$ layer thickness: 30 nm

No. of data points: 446

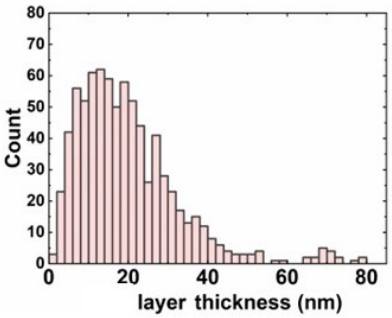

Avg. $Ir_xZr_{(1-x)}O_2$ layer thickness: 28 nm

No. of data points: 788

Figure A.3: Thickness of Ir oxide layer around $ZrO_{2(L)}$ observed in $Ir_xZr_{(1-x)}O_2$ /$ZrO_{2(L)}$ particles (in nm).

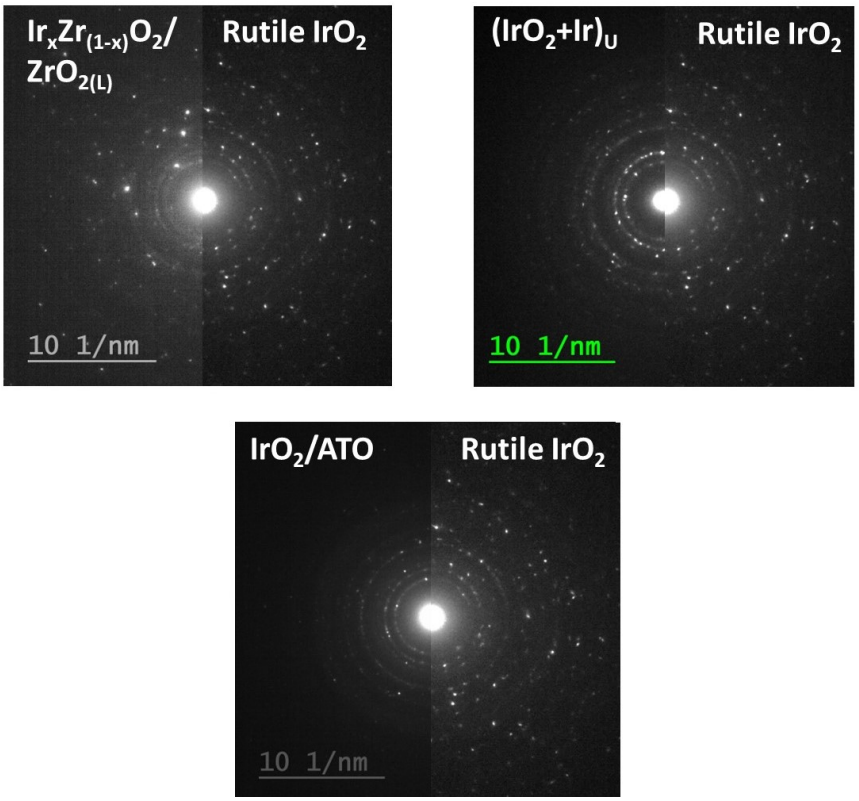

Figure A.4: SAED images of IrO_x in $Ir_xZr_{(1-x)}O_2/ZrO_{2(L)}$, $(IrO_2 + Ir)_U$, IrO_2/ATO resembling rutile IrO_2 (Alfa Aesar).

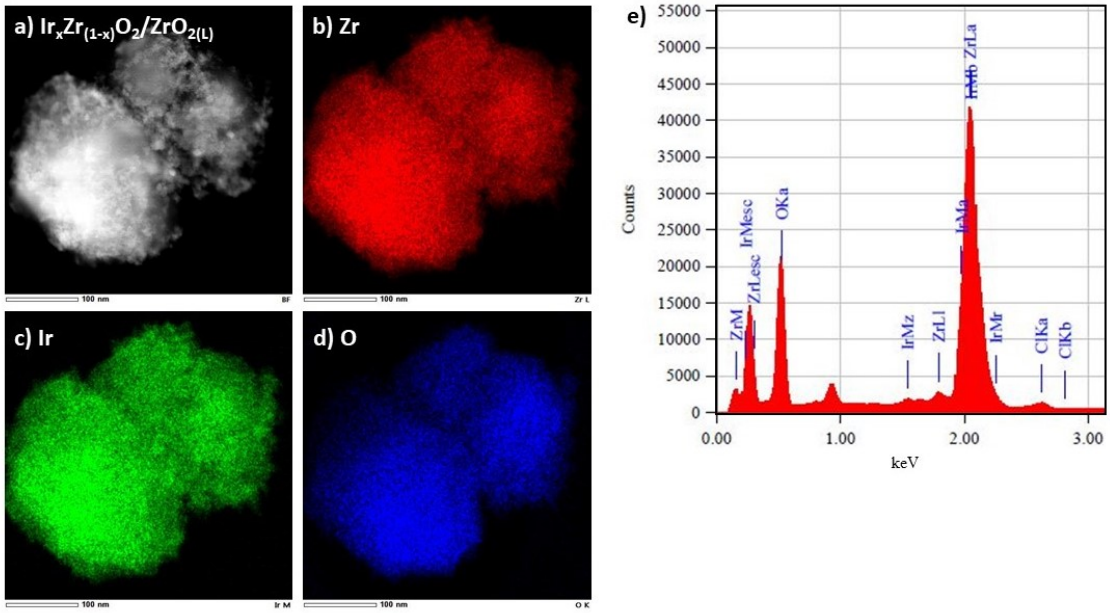

Figure A.5: (a-d) Dark field TEM of $Ir_xZr_{(1-x)}O_2/ZrO_{2(L)}$ and EDS elemental mapping of Zr, Ir, and O, (e) spectrum showcasing overlapping peaks of Zr La and Ir Mb at 2 keV.

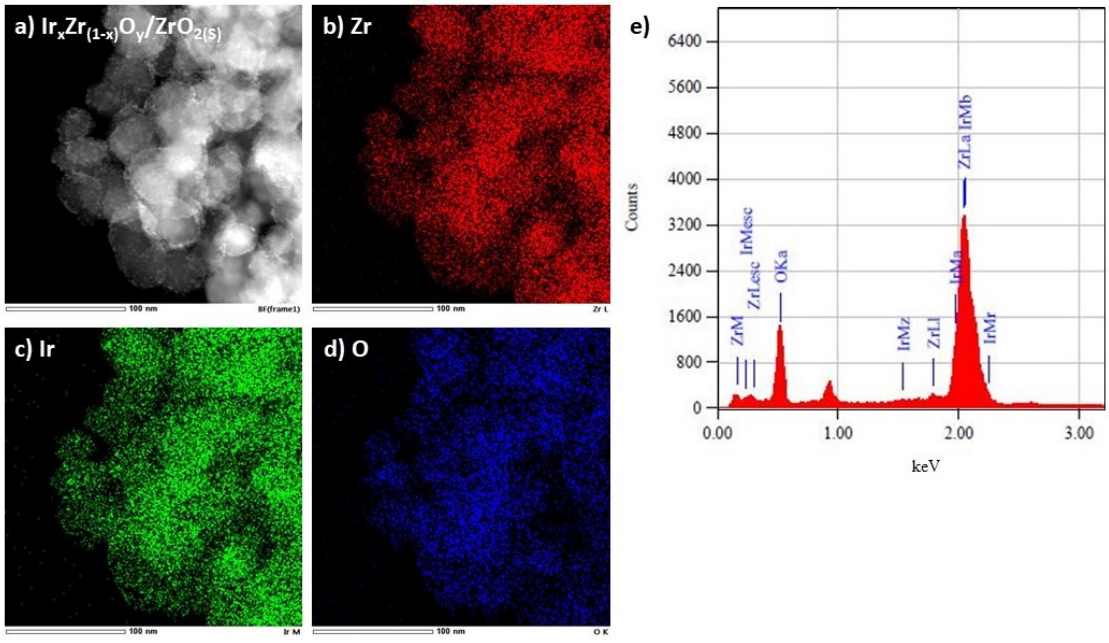

Figure A.6: (a-d) Dark field TEM of $Ir_xZr_{(1-x)}O_y/ZrO_{2(S)}$ and EDS elemental mapping of Zr, Ir, and O, (e) spectrum showcasing overlapping peaks of Zr La and Ir Mb at 2 keV.

A.1.3 X-ray diffraction (XRD)

Instrument specifications for XRD of $Ir_xZr_{(1-x)}O_2/ZrO_{2(L)}$ and $Ir_xZr_{(1-x)}O_y/ZrO_{2(S)}$

- Rigaku Ultima IV - Co radiation (λ= 0.178900 nm)
- Focusing Geometry: Bragg Brentano Mode
- Detector: D/Tex Ultra with Fe Filter (K-beta filter)
- Slit sizes used are: Divergence Slit - 2/3 deg, Divergence Height Limiting Slit - 10mm, Scattering slit - open, Receiving Slit - open

Instrument specifications for XRD of IrO_2/ATO, $(IrO_2 + Ir)_U$, IrO_x TKK

- Rigaku Ultima IV - Cu-Kα radiation (λ = 0.15406 nm)
- Detector: Scintillation Counter plus graphite crystal monochromator or a Nickel K- filter
- Slit sizes used are: Divergence slit: 2/3 deg, Scattering slit: 2/3 deg, Receiving slit: 0.3 mm

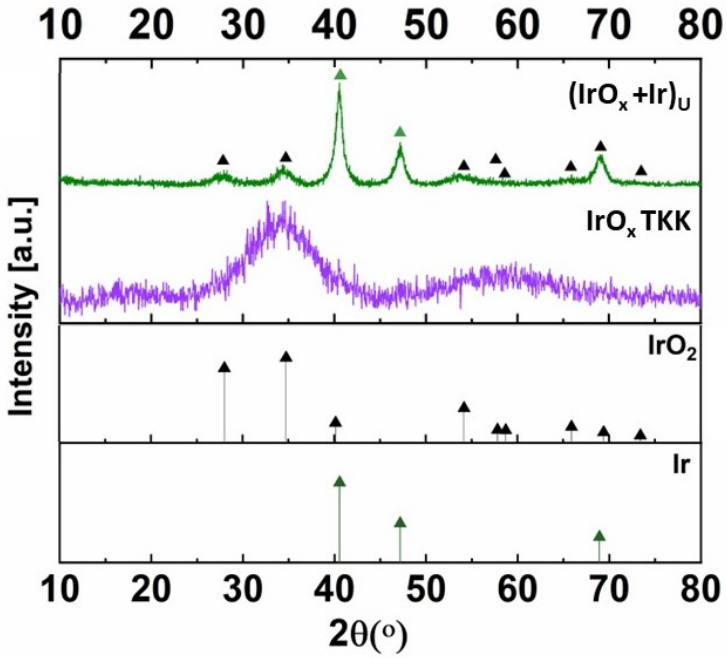

Figure A.7: X-ray diffraction profiles of $(IrO_2 + Ir)_U$, IrO_x TKK. References for IrO_2 (JCPDS 15870, X-ray: Cu-Kα radiation ($\lambda = 0.15406$ nm)), and Ir (JCPDS 6598, X-ray: Cu-Kα radiation ($\lambda = 0.15406$ nm)).

A.1.4 X-ray photoelectron spectroscopy (XPS)

The XPS spectra were analyzed using CasaXPS, where all peaks were calibrated to the C 1s signal at 284.8 eV. A Shirley-type background was applied and the peaks were fitted with a DS(0.05,230) SGL(55) profile and the satellite peaks were fitted using GL(0). All the Ir 4f peaks were constrained to a doublet separation of 3 eV, the area ratio of $4f_{7/2}$:$4f_{5/2}$ = 4:3, and a doublet FWHM ratio of 1.

Table A.1: Fit parameters for Ir 4f of $Ir_xZr_{(1-x)}O_y/ZrO_{2(S)}$

$Ir_xZr_{(1-x)}O_y/ZrO_{2(S)}$	**Ir $4f_{7/2}$** Ir(IV)	**Ir $4f_{5/2}$** Ir(IV)	**Ir $4f_{7/2}$** Ir(IV) sat 1	**Ir $4f_{5/2}$** Ir(IV) sat 1	**Ir $4f_{5/2}$** Ir(IV) sat 2	**Ir $4f_{7/2}$** Ir(III)	**Ir $4f_{5/2}$** Ir(III)	**Ir $4f_{7/2}$** Ir(III) sat 1	**Ir $4f_{5/2}$** Ir(III) sat 1
B.E. (eV)	62.0	65.0	63.0	66.0	68.0	62.4	65.4	63.4	66.4
Conc. (%)	14	10.5	11	8.3	4.2	17	13	13	9
FWHM	0.7	0.7	2.3	2.3	2.8	1	1	2.7	2.7

Table A.2: Fit parameters for Ir 4f of $Ir_xZr_{(1-x)}O_2/ZrO_{2(L)}$

$Ir_xZr_{(1-x)}O_2/ZrO_{2(L)}$	**Ir $4f_{7/2}$** Ir(IV)	**Ir $4f_{5/2}$** Ir(IV)	**Ir $4f_{7/2}$** Ir(IV) sat 1	**Ir $4f_{5/2}$** Ir(IV) sat 1	**Ir $4f_{5/2}$** Ir(IV) sat 2	**Ir $4f_{7/2}$** Ir(III)	**Ir $4f_{5/2}$** Ir(III)	**Ir $4f_{7/2}$** Ir(III) sat 1	**Ir $4f_{5/2}$** Ir(III) sat 1
B.E. (eV)	61.8	64.8	62.8	65.8	67.8	62.4	65.4	63.4	66.4
Conc. (%)	24	17.5	7.3	5.4	2.5	15	11	10	7.3
FWHM	0.8	0.8	2.3	2.3	2.5	1.1	1.1	2.7	2.7

Table A.3: Fit parameters for Ir 4f of IrO_x TKK

IrO_x TKK	**Ir $4f_{7/2}$** Ir(IV)	**Ir $4f_{5/2}$** Ir(IV)	**Ir $4f_{7/2}$** Ir(IV) sat 1	**Ir $4f_{5/2}$** Ir(IV) sat 1	**Ir $4f_{5/2}$** Ir(IV) sat 2	**Ir $4f_{7/2}$** Ir(III)	**Ir $4f_{5/2}$** Ir(III)	**Ir $4f_{7/2}$** Ir(III) sat 1	**Ir $4f_{5/2}$** Ir(III) sat 1
B.E. (eV)	61.8	64.8	62.8	65.8	67.8	62.4	65.4	63.4	66.4
Conc. (%)	24.8	18.6	7	5.2	1.1	13.6	10.2	11.1	8.4
FWHM	0.9	0.9	2.5	2.5	2.9	1	1	2.8	2.8

Table A.4: Fit parameters for Ir 4f of IrO_2/ATO

IrO_2/ATO	**Ir $4f_{7/2}$** Ir(IV)	**Ir $4f_{5/2}$** Ir(IV)	**Ir $4f_{7/2}$** Ir(IV) sat 1	**Ir $4f_{5/2}$** Ir(IV) sat 1	**Ir $4f_{5/2}$** Ir(IV) sat 2	**Ir $4f_{7/2}$** Ir(III)	**Ir $4f_{5/2}$** Ir(III)	**Ir $4f_{7/2}$** Ir(III) sat 1	**Ir $4f_{5/2}$** Ir(III) sat 1
B.E. (eV)	61.8	64.8	62.8	65.8	67.8	62.4	65.4	63.4	66.4
Conc. (%)	18.4	15	10.5	8	1.7	18.5	14	8	6
FWHM	0.8	0.8	2.1	2.1	2.5	1	1	2.8	2.8

Table A.5: Fit parameters for Ir 4f of $(IrO_2 + Ir)_U$

$IrO_{x(U)}$	**Ir $4f_{7/2}$** Ir(0)	**Ir $4f_{5/2}$** Ir(0)	**Ir $4f_{7/2}$** Ir(IV)	**Ir $4f_{5/2}$** Ir(IV)	**Ir $4f_{7/2}$** Ir(IV) sat 1	**Ir $4f_{5/2}$** Ir(IV) sat 1	**Ir $4f_{5/2}$** Ir(IV) sat 2
B.E. (eV)	60.9	63.9	61.8	64.8	62.8	65.8	67.8
Conc. (%)	15	11	30	23	12	9	1
FWHM	0.7	0.7	1.5	1.5	2.6	2.6	2.9

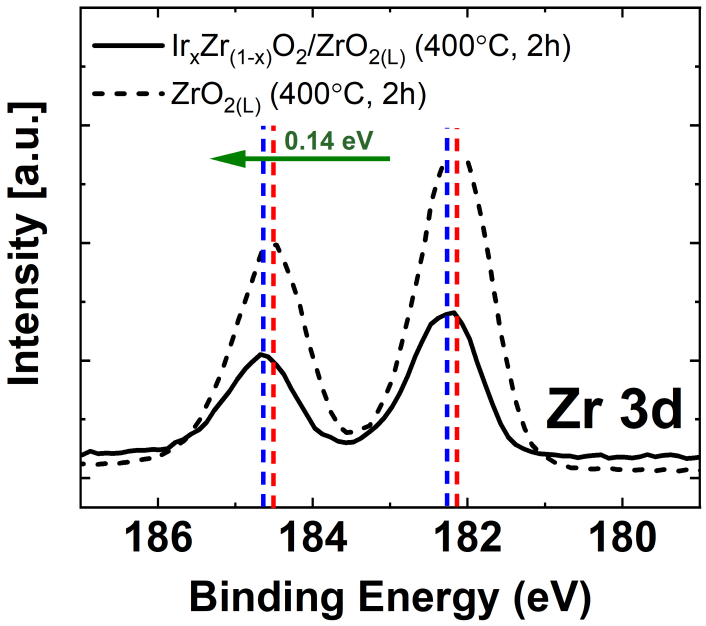

Figure A.8: Zr 3d XPS spectra of $Ir_xZr_{(1-x)}O_2/ZrO_{2(L)}$ and $ZrO_{2(L)}$ calcined in the air at 400°C for 2 h showing binding energy shift.

Table A.6: Fit parameters for Ir 4f of spent $Ir_xZr_{(1-x)}O_2/ZrO_{2(L)}$ after stability test

	Ir 4f$_{7/2}$ Ir(IV)	**Ir 4f$_{5/2}$** Ir(IV)	**Ir 4f$_{7/2}$** Ir(IV) sat 1	**Ir 4f$_{5/2}$** Ir(IV) sat 1	**Ir 4f$_{5/2}$** Ir(IV) sat 2	**Ir 4f$_{7/2}$** Ir(III)	**Ir 4f$_{5/2}$** Ir(III)	**Ir 4f$_{7/2}$** Ir(III) sat 1	**Ir 4f$_{5/2}$** Ir(III) sat 1	**Ir 4f$_{7/2}$** Ir (post-OER)	**Ir 4f$_{5/2}$** Ir (post-OER)	**Ir 4f$_{7/2}$** Ir (post-OER)	**Ir 4f$_{5/2}$** Ir (post-OER)
B.E. (eV)	61.9	64.9	62.9	65.9	67.9	62.4	65.4	63.4	66.4	63.1	66.1	64.1	67.1
Conc. (%)	5.8	4.3	0.56	0.42	2	29	21.7	11.8	8.8	5.1	3.8	3.8	2.8
FWHM	0.8	0.8	2.3	2.3	2.5	1	1	2.7	2.7	0.9	0.9	2.4	2.4

Table A.7: Fit parameters for Ir 4f of spent $Ir_xZr_{(1-x)}O_y/ZrO_{2(S)}$ after stability test

	Ir 4f$_{7/2}$ Ir(IV)	**Ir 4f$_{5/2}$** Ir(IV)	**Ir 4f$_{7/2}$** Ir(IV) sat 1	**Ir 4f$_{5/2}$** Ir(IV) sat 1	**Ir 4f$_{5/2}$** Ir(IV) sat 2	**Ir 4f$_{7/2}$** Ir(III)	**Ir 4f$_{5/2}$** Ir(III)	**Ir 4f$_{7/2}$** Ir(III) sat 1	**Ir 4f$_{5/2}$** Ir(III) sat 1	**Ir 4f$_{7/2}$** Ir (post-OER)	**Ir 4f$_{5/2}$** Ir (post-OER)	**Ir 4f$_{7/2}$** Ir (post-OER)	**Ir 4f$_{5/2}$** Ir (post-OER)
B.E. (eV)	62.0	65.0	63	66	68	62.4	65.4	63.4	66.4	63.1	66.1	64.1	67.1
Conc. (%)	4.3	3.2	1.1	0.8	3.4	20.6	15.4	8.5	6.3	16.6	12.4	4.2	3.2
FWHM	0.7	0.7	2.3	2.3	2.8	1	1	2.8	2.8	1.5	1.5	2.9	2.9

Table A.8: Fit parameters for Ir 4f of spent $(IrO_2 + Ir)_U$ after stability test

	Ir 4f$_{7/2}$ Ir(IV)	**Ir 4f$_{5/2}$** Ir(IV)	**Ir 4f$_{7/2}$** Ir(IV) sat 1	**Ir 4f$_{5/2}$** Ir(IV) sat 1	**Ir 4f$_{5/2}$** Ir(IV) sat 2	**Ir 4f$_{7/2}$** Ir(III)	**Ir 4f$_{5/2}$** Ir(III)	**Ir 4f$_{7/2}$** Ir(III) sat 1	**Ir 4f$_{5/2}$** Ir(III) sat 1	**Ir 4f$_{7/2}$** Ir (post-OER)	**Ir 4f$_{5/2}$** Ir (post-OER)	**Ir 4f$_{7/2}$** Ir (post-OER)	**Ir 4f$_{5/2}$** Ir (post-OER)
B.E. (eV)	61.8	64.8	62.8	65.8	67.8	62.4	65.4	63.4	66.4	63.0	66.0	64.0	67.0
Conc. (%)	3.9	2.9	2.1	1.6	2.2	24.1	18	6.7	5	18.6	14	0.6	0.5
FWHM	0.9	0.9	2.3	2.3	2.8	0.8	0.8	2.3	2.3	0.9	0.9	2.5	2.5

A.2 Electrochemical characterization

A.2.1 Reference electrode calibration against hydrogen reference electrode

It is important to note that the reference hydrogen electrode required initial 30-40 minutes to equilibrate and for the potential to stabilize. All measurements in this work were performed only after a stable potential was obtained.

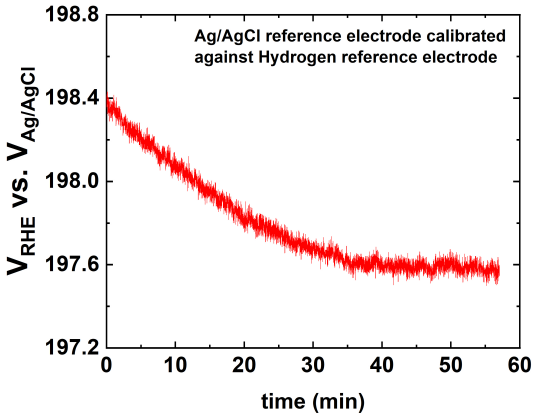

Figure A.9: Ag/AgCl electrode (Pine Research) calibrated against hydrogen reference electrode (ET070 Hydroflex™) in 1.0 M H_2SO_4 electrolyte solution. A drift of 1.4 mV was observed from the standard value of 199 mV, which lies within the typical variance range of ± 5 mV.

A.2.2 Shift in y-axis of current vs. potential graph during preconditioning cycles

During the 500 preconditioning cycles performed prior to ECSA estimation, a shift along the -y direction was observed. Since the ECSA is calculated by measuring the total area under the anodic CV, the cyclic voltammogram was also corrected for the shift along the normalized current density (y-axis) Fig. A.10 shows an example of the shift in y-axis for IrO_x TKK.

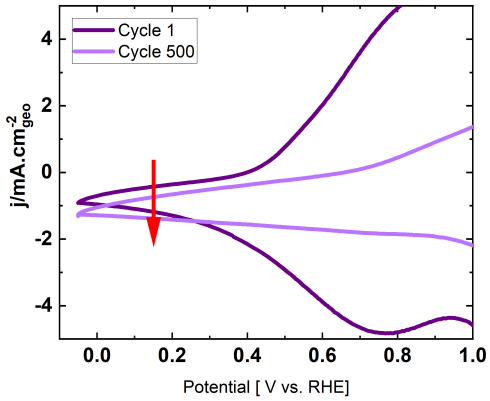

Figure A.10: Shift in y-axis for IrO_x/TKK during preconditioning cycles between 0-1.53 V_{RHE} in nitrogen-saturated environment. The figure represents an observable shift towards the negative y-axis over 500 preconditioning cycles.

A.2.3 Determining electrochemical surface area (ECSA) of Ir for supported and unsupported catalysts

The ECSA of the catalysts was calculated by estimating the total anodic charges under the CV (forward sweep) in the potential range of 0.4 V_{RHE} - 1.25 V_{RHE}, which corresponds to the area under the CV curve which was calculated using the EC-Lab software. The total charge accumulated was then appropriately corrected for a double layer based on the work of Tan et al.[6] The cyclic voltammogram was also corrected

for the shift along the normalized current density (y-axis).

$$\text{ECSA}\left(\frac{m^2}{g}\right) = \frac{\text{Charge}(A{\cdot}V)}{\text{Scan Rate}\left(\frac{V}{s}\right){\times}\text{Geometric Area}\left(cm^2_{\text{geo}}\right){\times}q_{\text{dep}}\left(\frac{C}{m^2_{\text{ECSA}}}\right){\times}\text{Loading}\left(\frac{g}{cm^2_{\text{geo}}}\right)} \quad \text{(A.2)}$$

The scan rate is 0.04 V.s^{-1}, q_{dep} was taken as 440 $\pm$ 14 $\mu\text{C.cm}^{-2}{}_{\text{ECSA}}$ based on the work of Tan et al.[6]. Geometric iridium loading ($\mu\text{g/cm}^2{}_{\text{geo}}$) was calculated based on the bulk elemental composition of Ir in the catalysts (weight %) obtained by performing EDX on the powdered catalyst samples, and the amount of the catalyst dissolved in the catalyst ink.

A.2.4 Calculating the weight of the catalyst on the working electrode

$$\text{Weight of catalyst on W.E. } (\mu\text{g}) = \text{Weight of ink on W.E. } (\mu\text{g}) \times \frac{\text{Weight of catalyst in ink (mg)}}{\text{Weight of ink (IPA + Water + Nafion + Catalyst, mg)}} \quad \text{(A.3)}$$

$$\text{Ir geometric loading } \left(\mu\text{g} \cdot \text{cm}^{-2}_{\text{geo}}\right) = \frac{\text{Weight of catalyst on W.E. } (\mu\text{g}){\times}\text{Ir wt.\% (Based on EDX)}}{\text{Surface area of W.E. } (\text{cm}^2)} \quad \text{(A.4)}$$

W.E. refers to the working electrode. Ir weight percent was obtained by performing elemental mapping of all the catalyst samples using SEM-EDX.

Geometric iridium loading ($\mu\text{g}{\cdot}\text{cm}^2_{\text{geo}}$) was calculated based on the bulk elemental composition of Ir in the catalysts (weight %) obtained by performing EDX on the powdered catalyst samples, and the amount of the catalyst dissolved in the catalyst ink.

A.2.5 Cyclic voltammogram (CV) of $Ir_xZr_{1-x}O_2/ZrO_{2(L)}$ vs. $ZrO_{2(L)}$

In order to decouple the charge accumulation of the supports from the active metal Ir, the supports were calcined at 400°C and tested under the aforementioned conditions in a rotating disk electrode set-up with a comparable support geometric loading as the synthesized catalyst. The charge accumulated was observed to be negligible compared to that of the supported catalyst as shown in Figure A.11.

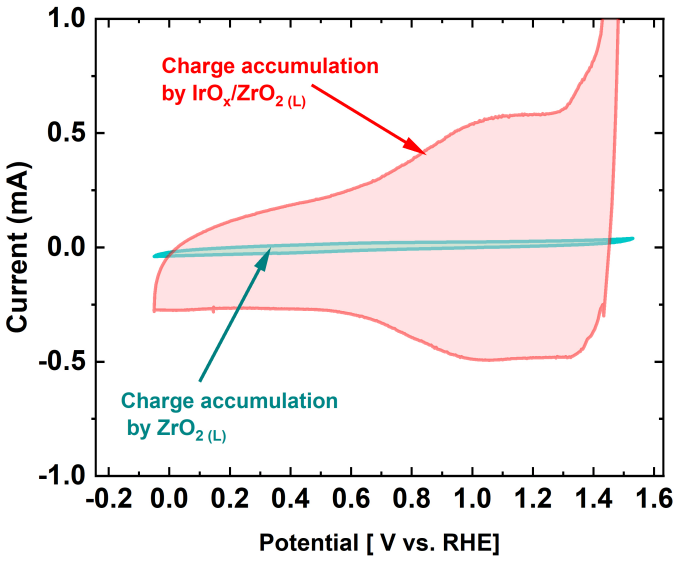

Figure A.11: Schematic diagram displaying the charge accumulation by $Ir_xZr_{(1-x)}O_2/ZrO_{2(L)}$, charge accumulated by calcined ZrO_2 and double layer correction for $Ir_xZr_{(1-x)}O_2/ZrO_{2(L)}$.

A.2.6 Variation in Ir loading on ATO support

In the supplementary study using different Ir loadings on ATO, the catalysts were exposed to 500 preconditioning cycles between 0 V_{RHE}-1.53 V_{RHE} before activity measurement.

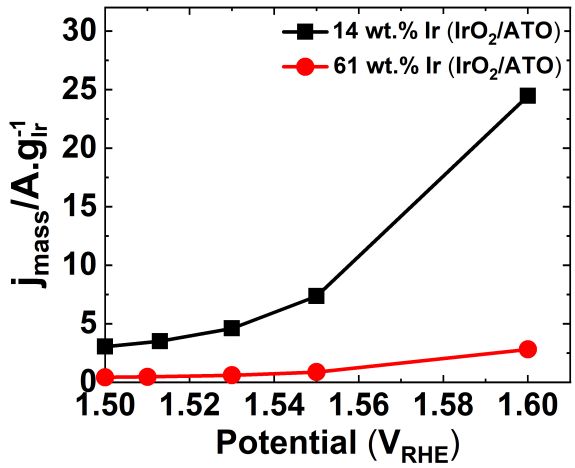

Figure A.12: Mass normalized activity of IrO_2/ATO with 14 and 60 Ir wt.% loading.

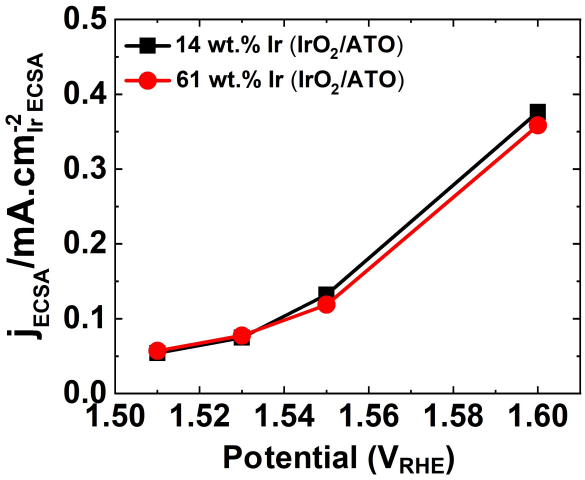

Figure A.13: ECSA normalized activity of IrO_2/ATO with 14 and 60 Ir wt. % loading.

A.2.7 Electrochemical impedance spectroscopy (EIS) measured before and after chronoamperometry (CA) cycle-2

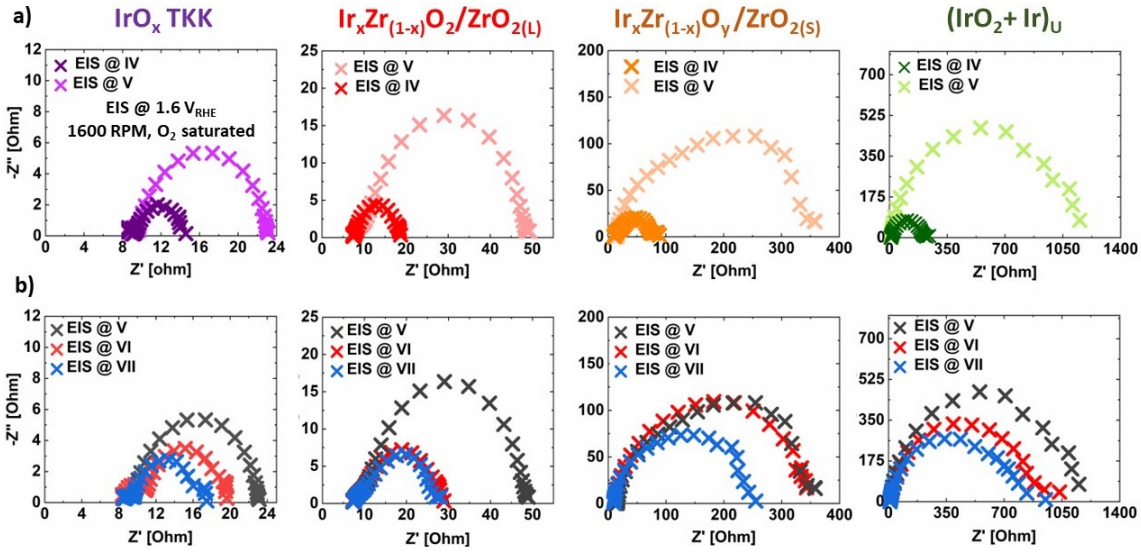

Figure A.14: a) Electrochemical impedance spectroscopy (EIS), measured before and after the second 2-h CA analysis with minimal interference in the applied potential of the CA analysis; b) partial recovery of charge transfer from the removal of accumulated microscopic bubbles and CV regeneration.

A.3 Comparison of $Ir_xZr_{(1-x)}O_2/ZrO_{2(L)}$ performance with literature data

Table A.9: Comparison of intrinsic activity with literature data

S.No.	Sample	Intrinsic activity ($mA.cm^{-2}_{Ir\ ECSA}$)	Potential (V_{RHE})	Citation
1.	$Ir_xZr_{(1-x)}O_2/ZrO_{2(L)}$	0.2	1.51	This work
		0.5	1.53	
		1.1	1.55	
		4.8	1.60	
2.	$Ir@WO_{(3-x)}(H_2)$	0.076	1.55	[195]
	Ir black	0.032	1.55	
	$IrO_2@TiO_2$	0.023	1.55	
3.	IrO_x/Graphdiyne	0.021	1.58	[196]
4.	$IrO_2@IrO_x$(G-350)	0.01	1.55	[197]
5.	$(Ir_{0.3}Pr_{0.3}Si_{0.4})O_x$	0.10	1.509	[198]
6.	$BaIrO_3$	0.154	1.55	[199]
	$SrIrO_3$	0.025	1.55	

*ECSA normalized activity is challenging to compare due to the different methods used in the literature to calculate ECSA

Table A.10: Comparison of intrinsic activity with literature data

S.No.	Sample	Intrinsic activity ($mA.cm^{-2}_{Ir\ ECSA}$)	Potential (V_{RHE})	Citation
7.	Ir (TKK)	0.809	1.55	[187]
	Ir (JM)	1.3	1.55	
	IrO_2 Alfa Aesar	0.643	1.55	
8.	IrO_x/CeO_2	0.3	1.6	[200]
9.	H-Ti@IrO_x	0.04	1.58	[201]
10.	Umicore Ir black	2.4	1.53	[6]
	50 nm Ir PPs	1.5	1.53	
11.	Li-IrO_x	0.44	1.51	[304]

*ECSA normalized activity is challenging to compare due to the different methods used in the literature to calculate ECSA

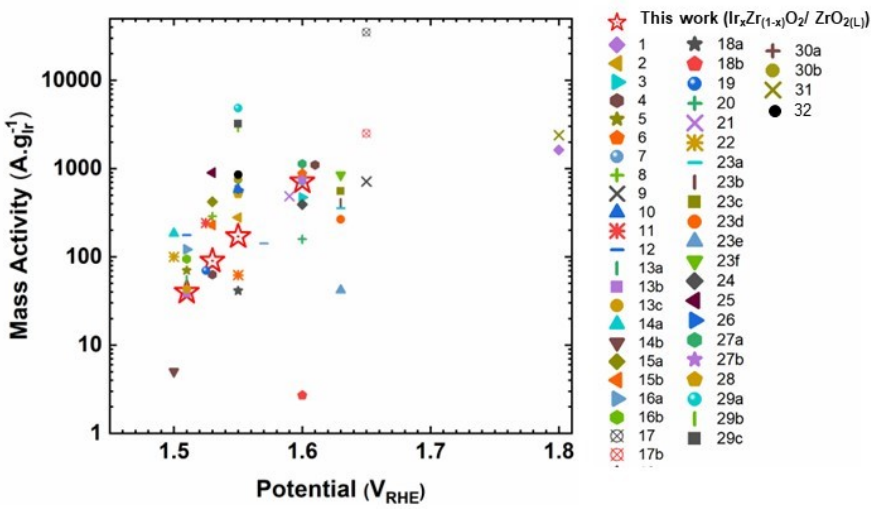

Figure A.15: Comparison of mass (specific) activity of $Ir_xZr_{(1-x)}O_2/ZrO_{2(L)}$ with supported Ir/IrO_x catalysts in literature synthesized using wet-chemistry methods.

Table A.11: Comparison of mass (specific) activity with literature data- Part 1

S.No.	Sample	Mass activity ($A.g_{Ir}^{-1}$)	Potential (V_{RHE})	Citation
+	$Ir_xZr_{(1-x)}O_2/ZrO_{2(L)}$	30	1.51	This work
		71	1.53	
		200	1.55	
		712	1.60	
1	IrO_2-ATO	1625	1.8	[145]
2	$IrO_x/N–TiO_2$	278.7	1.55	[152]
3	$IrO_2/Nb–TiO_2$ (26 wt%)	471	1.6	[153]
4	Ir/ATO(25 wt%)	1100	1.61	[232]
		63	1.53	

Table A.12: Comparison of mass (specific) activity with literature data- Part 2

S.No.	Sample	Mass activity ($A.g_{Ir}^{-1}$)	Potential (V_{RHE})	Citation
5	Ir ND/ATO	70	1.51	[79]
6	IrO_2:TiN (31 wt% Ir)	874.0*	1.6	[321]
7	IrO_2/TSO	714.85	1.6	[147]
8	IrO_2/V_2O_5 (20.8 wt%)	287	1.53	[322]
9	IrO_2@Ir/TiN-40 (Initial)	715	1.65	[323]
10	IrO_2/TiB_xO_2	583	1.55	[154]
11	IrO_x/ITO	207 ± 34	1.525	[148]
12	IrO_2/ITO	176	1.51	[137]
13	(a) IrO_x/Tin oxide	54.9	1.51	[138]
	(b) IrO_x/ ATO	38.2	1.51	
	(c) IrO_x/TaTO	42.8	1.51	
14	(a)Ir/ATO (80 °C)	185	1.5	[139]
		1100	1.53	
	(b) Umicore IrO_2/TiO_2	5	1.5	

+ Value measured in $V_{Ag/AgCl}$ *Data corresponds to the mass activity of IrO_x

Table A.13: Comparison of mass (specific) activity with literature data- Part 3

S.No.	Sample	Mass activity ($A.g_{Ir}^{-1}$)	Potential (V_{RHE})	Citation
15	(a) $IrNiO_x$/ATO (DD)	420	1.53	[140]
	(b) $IrNiO_x$/comm. ATO	230	1.53	
16	(a) Ir/SnO_2:Sb-mod-V	121.5	1.51	[231]
	(b) Ir/SnO_2:Sb	94.6	1.51	
17	(a) IrO_x/ITO	35000	1.65	[141]
	(b) IrO_x/FTO	2500	1.65	
18	(a) IrO_x@(SnO_2/ATO/FTO/ITO)	41.3	1.55	[142]
	(b) IrO_x@(SnO_2/ATO/FTO/ITO) (600 ° C)	2.7	1.60	
19	IrO_2-TiO_2	70 ± 3	1.525	[155]
20	Mesoporous Ir/TiO_x	158.3	1.60	[156]
21	$IrOOH_x$/TiO_2	487	1.592	[151]
22	Ir/$W_xTi_{1-x}O_2$	100	1.5	[150]
23	(a) Ir/WC	355 ± 124	1.48 $^+$	[158]
	(b) Ir/TaC	410 ± 39	1.48 $^+$	
	(c) Ir/NbO_2	554 ± 39	1.48 $^+$	
	(d) Ir/NbC	266 ± 75	1.48 $^+$	
	(e) Ir/TiC	42 ± 26	1.48 $^+$	
	(f) Ir/ATO	845 ± 159	1.48 $^+$	

$^+$ Value measured in $V_{Ag/AgCl}$ *Data corresponds to the mass activity of IrO_x

Table A.14: Comparison of mass (specific) activity with literature data- Part 4

S.No.	Sample	Mass activity ($A.g_{Ir}^{-1}$)	Potential (V_{RHE})	Citation
24	IrO_x/Nb-Ti-O_2	393*	1.6	[284]
25	Ir/Nb_2O_{5-x}	900	1.53	[159]
26	Ir/TiO_2-MoO_x	573	1.55	[324]
27	(a) Ir/$TiON_x$-P25	1130	1.60	[325]
	(b) Ir/$TiON_x$-NR	754	1.60	
28	$TiON_x$-Ir	520.3 ± 50.6	1.55	[326]
29	(a) Ir/middle-$TiON_x$/rGONRs	4820 ± 310	1.55	[327]
	(b) Ir/low-$TiON_x$/rGONRs	2910 ± 120	1.55	
	(c) Ir/high-$TiON_x$/rGONRs	3200 ± 250	1.55	
30	(a) Ir/TiON (Before degradation)	582	1.55	[149]
	(b) Ir/TiON (After degradation)	745	1.55	
31	Ir/ATO	2400	1.8	[132]
32	IrO_x/Zr_2ON_2	849	1.55	[244]

A.4 Temperature-programmed desorption (TPD) and temperature-programmed reduction (TPR)

A.4.1 TPD of H_2O and O_2

$ZrO_{2(L)}$

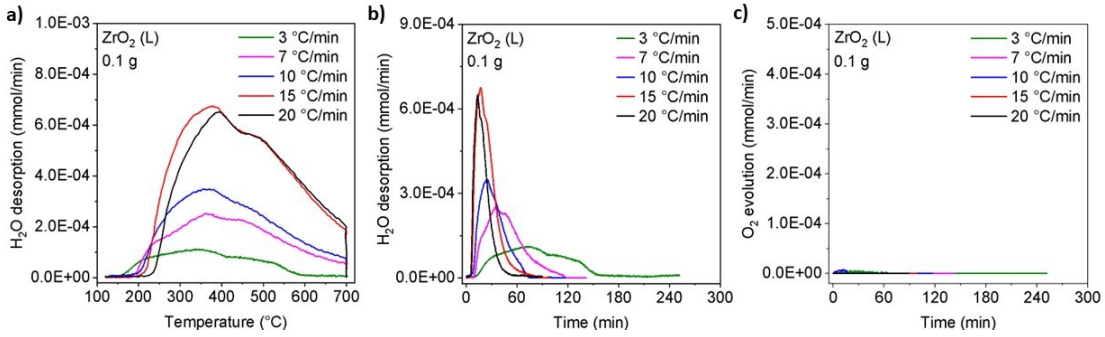

Figure A.16: TPD of H_2O and O_2 was performed at 5 different heating rates (β = 3, 7, 10, 15, 20° C/min) in He (50 mL/min): (a) H_2O desorption from $ZrO_{2(L)}$ as a function of temperature; (b) H_2O desorption as a function of time. (c) O_2 desorption from $ZrO_{2(L)}$ in the temperature window of 120°C-700°C at different β in the as a function of time.

Table A.15: Desorbed H_2O and O_2 amounts from $ZrO_{2(L)}$ at different heating rates

Heating rate (β)	H_2O	O_2
°C/min	mmol·$g_{cat.}^{-1}$	mmol·$g_{cat.}^{-1}$
5	0.130	0.0000
7	0.124	0.0000
10	0.115	0.0000
15	0.166	0.0000
20	0.119	0.0000
Average (Standard deviation)	**0.131 (0.021)**	**0.000 (0.000)**

$Ir_xZr_{(1-x)}O_2/ZrO_{2(L)}$

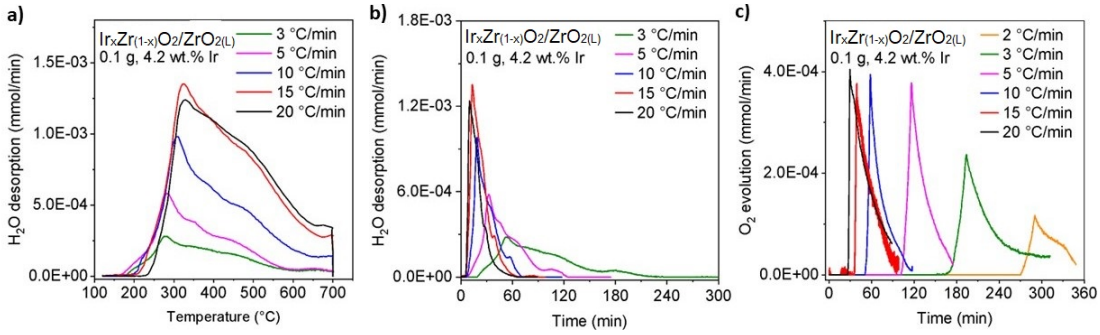

Figure A.17: TPD of H_2O and O_2 was performed at 5 different heating rates (β = 3, 5, 7, 10, 15, 20° C/min) in He (50 mL/min): (a) H_2O desorption from $Ir_xZr_{(1-x)}O_2/ZrO_{2(L)}$ as a function of temperature; (b) H_2O desorption as a function of time; (c) O_2 desorption from $Ir_xZr_{(1-x)}O_2/ZrO_{2(L)}$ in the temperature window of 120°C-700°C at different β as a function of time.

Table A.16: Desorbed H_2O and O_2 amounts from $Ir_xZr_{(1-x)}O_2/ZrO_{2(L)}$ at different heating rates

Heating rate (β)	H_2O	O_2
°C/min	$mmol \cdot g_{cat.}^{-1}$	$mmol \cdot g_{cat.}^{-1}$
2	0.198	NA
3	0.216	0.116
5	0.273	0.111
10	0.267	0.117
15	0.2	0.085
20	0.199	0.114
Average (Standard deviation)	**0.237 (0.054)**	**0.109 (0.013)**

$Ir_xZr_{(1-x)}O_y/ZrO_{2(S)}$

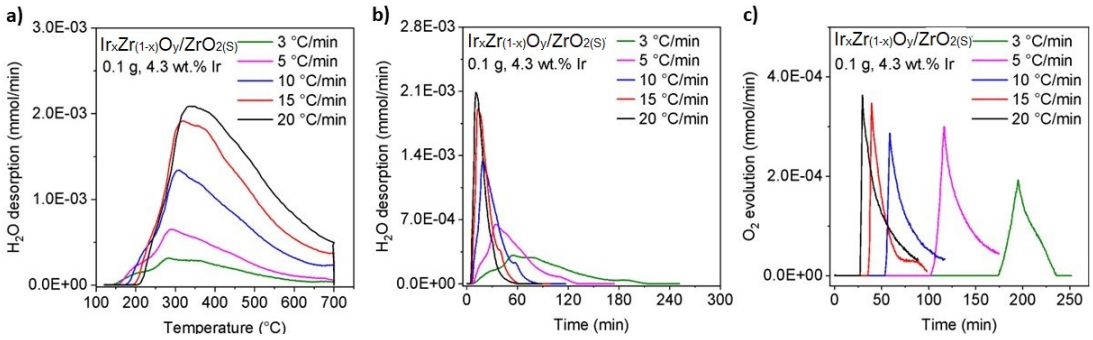

Figure A.18: TPD of H_2O and O_2 was performed at 5 different heating rates (β = 3, 5, 7, 10, 15, 20° C/min) in He (50 mL/min): (a) H_2O desorption from $Ir_xZr_{(1-x)}O_y/ZrO_{2(S)}$ as a function of temperature; (b) H_2O desorption as a function of time; (c) O_2 desorption from $Ir_xZr_{(1-x)}O_y/ZrO_{2(S)}$ in the temperature window of 120°C-700°C at different β as a function of time.

Table A.17: Desorbed H_2O and O_2 amounts from $Ir_xZr_{(1-x)}O_y/ZrO_{2(S)}$ at different heating rates

Heating rate (β)	H_2O	O_2
°C/min	$mmol \cdot g_{cat.}^{-1}$	$mmol \cdot g_{cat.}^{-1}$
3	0.291	0.051
5	0.321	0.080
10	0.356	0.063
15	0.366	0.053
20	0.338	0.074
Average (Standard deviation)	**0.328 (0.031)**	**0.062 (0.012)**

IrO_x TKK+$ZrO_{2(L)}$ (Physical mixture)

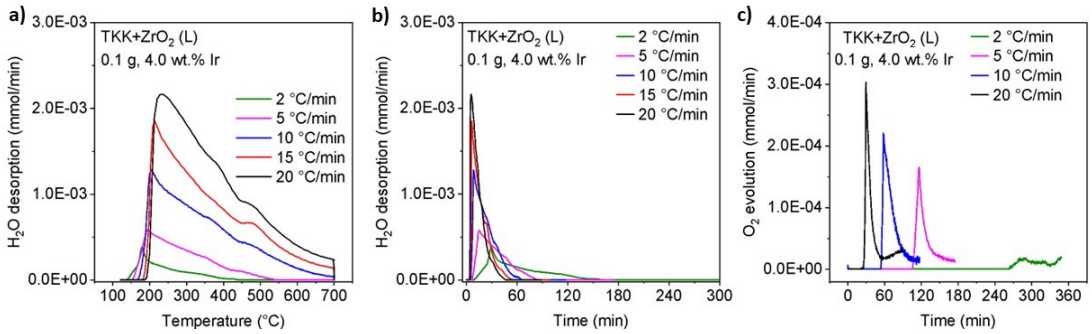

Figure A.19: TPD of H_2O and O_2 was performed at 5 different heating rates (β = 2, 5, 10, 15, 20° C/min) in He (50 mL/min): (a) H_2O desorption from IrO_x TKK+$ZrO_{2(L)}$ as a function of temperature; (b) H_2O desorption as a function of time; (c) O_2 desorption from IrO_x TKK+$ZrO_{2(L)}$ in the temperature window of 120°C-700°C at different β as a function of time.

Table A.18: Desorption of H_2O and O_2 amounts from IrO_x TKK+$ZrO_{2(L)}$ at different heating rates

Heating rate (β)	H_2O	O_2
°C/min	$mmol \cdot g_{cat.}^{-1}$	$mmol \cdot g_{cat.}^{-1}$
2	0.157	NA
5	0.187	0.030
10	0.266	0.041
15	0.263	NA
20	0.277	0.035
Average (Standard deviation)	**0.230 (0.054)**	**0.035 (0.006)**

$(IrO_2 + Ir)_U$+$ZrO_{2(L)}$ (Physical mixture)

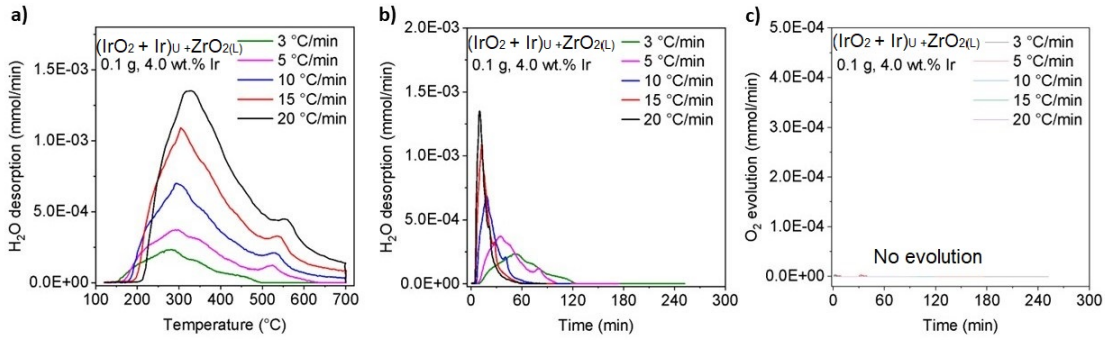

Figure A.20: TPD of H_2O and O_2 was performed at 5 different heating rates (β = 3, 5, 7, 10, 15, 20° C/min) in He (50 mL/min): (a) H_2O desorption from $(IrO_2 + Ir)_U$+$ZrO_{2(L)}$; (b) H_2O desorption as a function of time; (c) O_2 desorption from $(IrO_2 + Ir)_U$+$ZrO_{2(L)}$ in the temperature window of 120°C-700°C at different β as a function of time.

Table A.19: Desorbed H_2O and O_2 amounts from $(IrO_2 + Ir)_U$+$ZrO_{2(L)}$ at different heating rates

Heating rate (β)	H_2O	O_2
°C/min	mmol·$g_{cat.}^{-1}$	mmol·$g_{cat.}^{-1}$
3	0.133	0.000
5	0.174	0.000
10	0.154	0.000
15	0.163	0.000
20	0.170	0.000
Average (Standard deviation)	**0.161 (0.017)**	**0.000 (0.000)**

ATO support

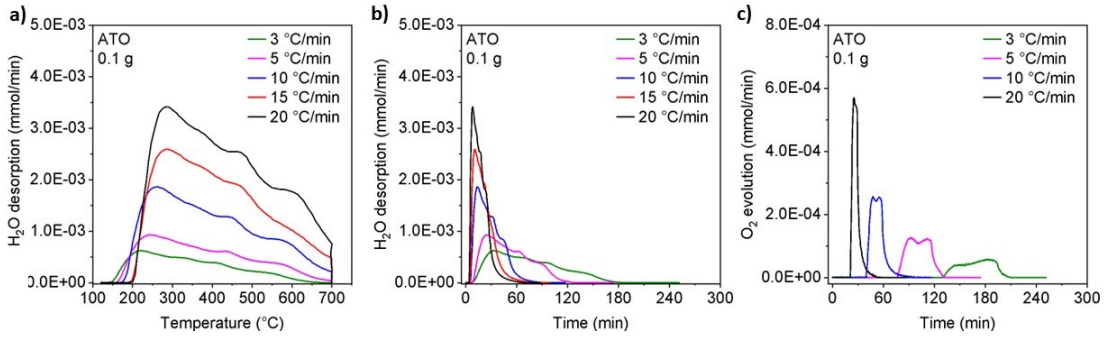

Figure A.21: TPD of H_2O and O_2 was performed at 5 different heating rates (β = 3, 5, 7, 10, 15, 20° C/min) He (50 mL/min): (a) H_2O desorption from ATO as a function of temperature; (b) H_2O desorption as a function of time; (c) O_2 desorption from ATO in the temperature window of 120°C-700°C at different β as a function of time.

Table A.20: Desorbed H_2O and O_2 amounts from ATO at different heating rates

Heating rate (β)	H_2O	O_2
°C/min	mmol·$g_{cat.}^{-1}$	mmol·$g_{cat.}^{-1}$
3	0.555	0.029
5	0.572	0.048
10	0.590	0.049
15	0.582	NA
20	0.603	0.049
Average (Standard deviation)	**0.580 (0.018)**	**0.044 (0.010)**

IrO_2/ATO

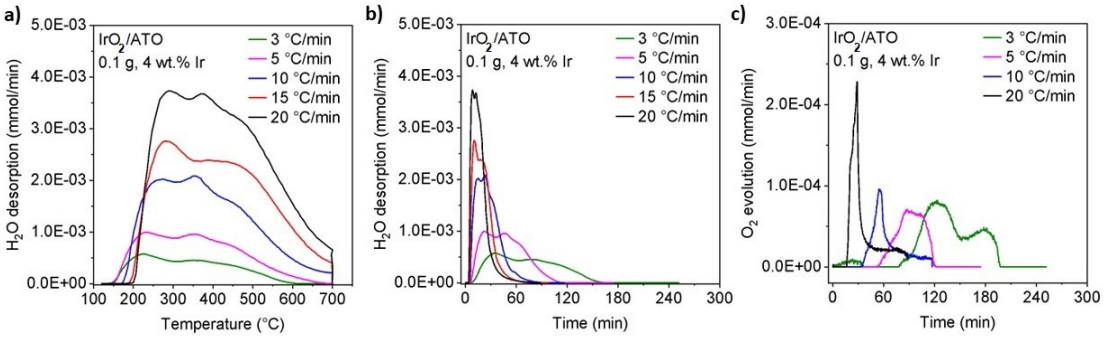

Figure A.22: TPD of H_2O and O_2 was performed at 5 different heating rates (β = 3, 5, 7, 10, 15, 20° C/min) in He (50 mL/min): (a) H_2O desorption from IrO_2/ATO as a function of temperature; (b) H_2O desorption as a function of time; (c) O_2 desorption from IrO_2/ATO in the temperature window of 120°C-700°C at different β as a function of time.

Table A.21: Desorbed H_2O and O_2 amounts from IrO_2/ATO at different heating rates

Heating rate (β)	H_2O	O_2
°C/min	mmol·$g_{cat.}^{-1}$	mmol·$g_{cat.}^{-1}$
3	0.518	0.052
5	0.612	0.028
10	0.664	0.022
15	0.640	NA
20	0.695	0.034
Average (Standard deviation)	**0.626 (0.068)**	**0.034 (0.013)**

A.4.2 Calculation for activation energy of H_2O desorption

To find the activation energy of water desorption, TPD was performed at 5 different heating rates (β = 3, 5, 7, 10, 15, 20° C/min) for each iridium sample and supports. The activation energy (E_a) was determined using the following equation, which is based on the shift of the temperature of the rate maximum as a function of the heating rate. [328]

$$\ln\left(\frac{\beta}{T_{max}^2}\right) = \ln\left(\frac{AR}{Ea}\right) - \frac{Ea}{RT_{max}} \tag{A.5}$$

The activation energy of water desorption was determined from the slope of ln (β/T_{max}^2) vs. $1/T_{max}$; where T_{max} is the maximum temperature of the water desorption peak; β is the heating rate. The slope of the plot, -Ea/R, was used to calculate the activation energy of water desorption.

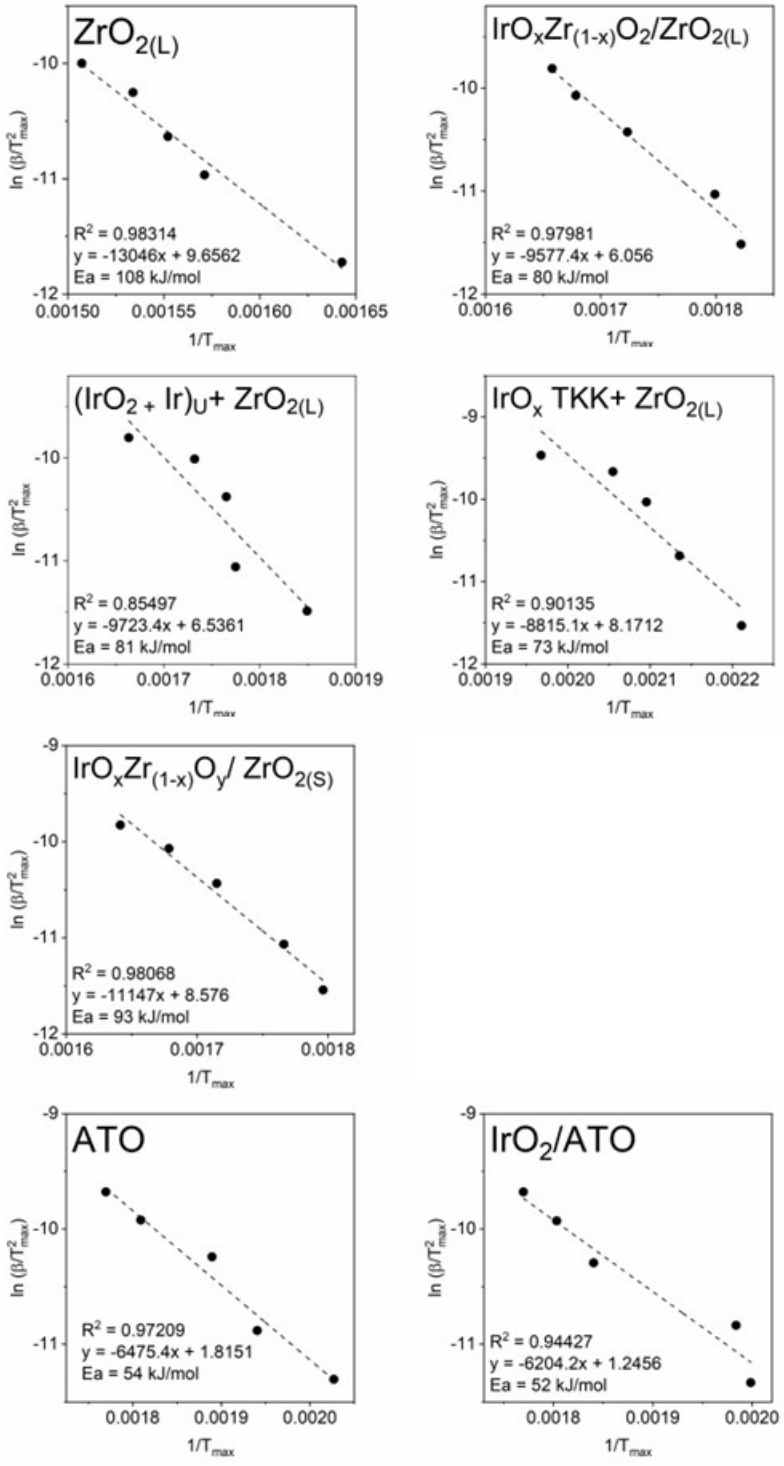

Figure A.23: Activation energy of water desorption.

A.4.3 TPR performed after TPD of H_2O and O_2

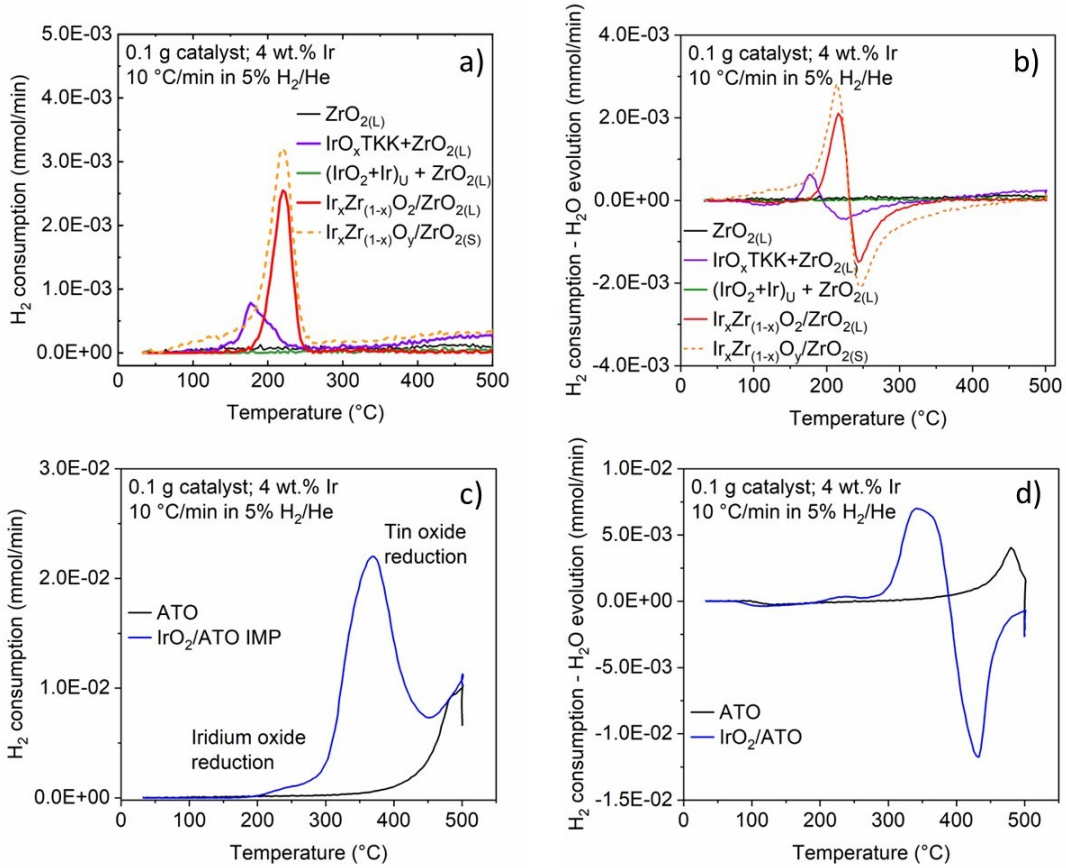

Figure A.24: (a,c) H_2 consumption and (b,d) H_2 consumption-H_2O evolution detected by performing TPR (10°C/min in 5% H_2/He gas mixture (20 mL/min)) on spent catalysts: $ZrO_{2(L)}$, $Ir_xZr_{(1-x)}O_2/ZrO_{2(L)}$, $Ir_xZr_{(1-x)}O_y$ /$ZrO_{2(S)}$, IrO_x TKK+$ZrO_{2(L)}$, $(IrO_2 + Ir)_U$+$ZrO_{2(L)}$, ATO and IrO_2/ ATO after TPD experiments.

Table A.22: Summary of H_2 consumption and H_2O evolution from TPR shown in Figure A.24.

Sample	$\mathbf{T_{max}}$ **(°C)**	$\mathbf{H_2}$ **(mmol·g$_{cat}^{-1}$)**	$\mathbf{H_2O}$ **(mmol·g$_{cat}^{-1}$)**
$ZrO_{2(L)}$	NA	NA	NA
$Ir_xZr_{(1-x)}O_2/ZrO_{2(L)}$	220	2.11	2.11
$Ir_xZr_{(1-x)}O_y/ZrO_{2(S)}$	220	5.67	5.69
IrO_x TKK+$ZrO_{2(L)}$	177	2.57	1.75
$(IrO_2 + Ir)_U$+$ZrO_{2(L)}$	NA	0	0
ATO	NA	NA	NA
IrO_2/ATO	370	NA	NA

Appendix B: Effect of residual chlorine from catalyst precursors during the synthesis of Ir-based catalysts

B.1 Materials characterization

B.1.1 Scanning electron microscopy (SEM)

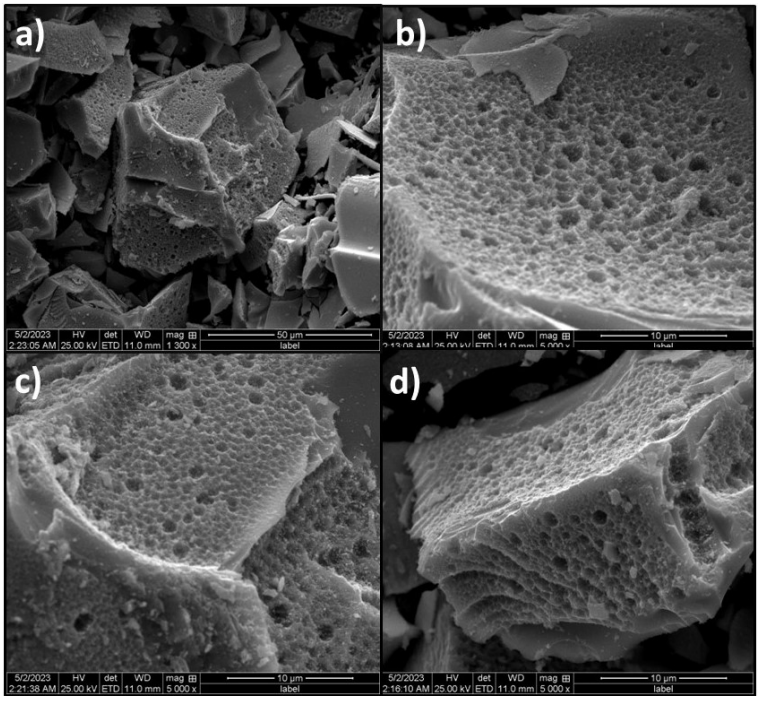

Figure B.1: SEM images of IrO_2-HCl sample showing porous nature of the catalyst produced potentially by the evaporation of HCl.

Table B.1: Summary of the elemental composition of catalysts obtained using SEM-EDX

Samples	Atomic %			Weight %			Atomic ratio	
	Ir	Cl	O	Ir	Cl	O	Cl:Ir	O:Ir
IrO_x TKK	22±3	–	78±3	77±3	–	23±3	–	3.5
IrO_2 AA	37±2	3±0	60±2	87±1	1±0	12±1	0.1	1.6

Atomic and weight percentages are calculated by averaging 10 values of the bulk composition obtained by performing SEM-EDX on the powdered samples.

B.1.2 Transmission electron microscopy (TEM): IrO_x particle size distribution and average size

The volume mean averaged diameter of IrO_x particles (in nm) was calculated using the formula [320]:

$$đ_{\mathrm{vol}} = \left[\frac{\sum_{i=1}^{N} n_{\mathrm{i}}(d_{\mathrm{i}})^3}{\sum_{i=1}^{N} n_{\mathrm{i}}}\right]^{\frac{1}{3}}$$

where,

n_i is number of particles in the size range defined by size d_i, and

N is number of size increments.

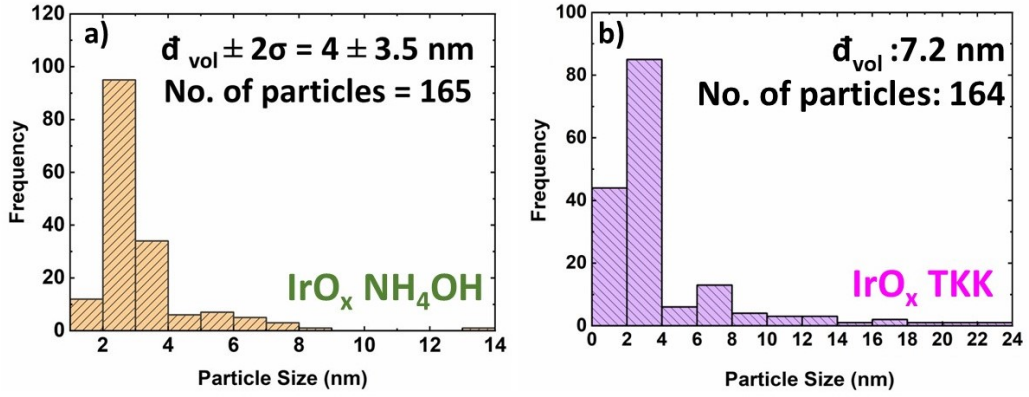

Figure B.2: Particle size distribution of (a) IrO_x-NH_4OH, and (b) IrO_x TKK nanoparticles showing mean volume diameter ($đ_{vol}$).

B.1.3 X-ray diffraction (XRD): instrument specifications

- Focusing Geometry: Bragg Brentano Mode
- Detector: D/Tex Ultra with Fe Filter (K-beta filter)
- Slit sizes used are: Divergence Slit - 2/3 deg, Divergence Height Limiting Slit - 10mm, Scattering slit - open, Receiving Slit - open

B.1.4 X-ray photoelectron spectroscopy (XPS)

Fit parameters for Ir 4f

Table B.2: Fit parameters for Ir 4f of IrO_2

	Ir 4f$_{7/2}$ Ir(IV)	**Ir 4f$_{5/2}$** Ir(IV)	**Ir 4f$_{7/2}$** Ir(IV) sat 1	**Ir 4f$_{5/2}$** Ir(IV) sat 1	**Ir 4f$_{5/2}$** Ir(IV) sat 2	**Ir 4f$_{7/2}$** Ir(III)	**Ir 4f$_{5/2}$** Ir(III)	**Ir 4f$_{7/2}$** Ir(III) sat 1	**Ir 4f$_{5/2}$** Ir(III) sat 1
B.E. (eV)	62.1	65.1	63.1	66.1	68	62.6	65.6	63.6	66.6
Conc. (%)	18.6	14	11.4	8.6	1.2	23.9	17.9	2.5	1.9
FWHM	0.7	0.7	2.3	2.3	2.8	0.9	0.9	2.5	2.5

Table B.3: Fit parameters for Ir 4f of IrO_2-HCl

	Ir 4f$_{7/2}$ Ir(IV)	**Ir 4f$_{5/2}$** Ir(IV)	**Ir 4f$_{7/2}$** Ir(IV) sat 1	**Ir 4f$_{5/2}$** Ir(IV) sat 1	**Ir 4f$_{5/2}$** Ir(IV) sat 2	**Ir 4f$_{7/2}$** Ir(III)	**Ir 4f$_{5/2}$** Ir(III)	**Ir 4f$_{7/2}$** Ir(III) sat 1	**Ir 4f$_{5/2}$** Ir(III) sat 1
B.E. (eV)	62.1	65.1	63.1	66.1	68	62.6	65.6	63.6	66.6
Conc. (%)	5.3	4	2.1	1.7	0.4	47	35	2.5	2
FWHM	0.7	0.7	2.3	2.3	2.8	0.9	0.9	2.5	2.5

Table B.4: Fit parameters for Ir 4f of IrO_x-NH_4OH

	Ir $4f_{7/2}$ Ir(IV)	**Ir $4f_{5/2}$** Ir(IV)	**Ir $4f_{7/2}$** Ir(IV) sat 1	**Ir $4f_{5/2}$** Ir(IV) sat 1	**Ir $4f_{5/2}$** Ir(IV) sat 2	**Ir $4f_{7/2}$** Ir(III)	**Ir $4f_{5/2}$** Ir(III)	**Ir $4f_{7/2}$** Ir(III) sat 1	**Ir $4f_{5/2}$** Ir(III) sat 1
B.E. (eV)	62	65	63	66	68	62.5	65.5	63.5	66.5
Conc. (%)	14	10	2.6	2.0	1.4	28	21	12	9
FWHM	0.8	0.8	2	2	2.8	1.1	1.1	2.7	2.7

Table B.5: Fit parameters for Ir 4f of IrO_2 Alfa Aesar (IrO_2 AA)

	Ir $4f_{7/2}$ Ir(IV)	**Ir $4f_{5/2}$** Ir(IV)	**Ir $4f_{7/2}$** Ir(IV) sat 1	**Ir $4f_{5/2}$** Ir(IV) sat 1	**Ir $4f_{5/2}$** Ir(IV) sat 2	**Ir $4f_{7/2}$** Ir(III)	**Ir $4f_{5/2}$** Ir(III)	**Ir $4f_{7/2}$** Ir(III) sat 1	**Ir $4f_{5/2}$** Ir(III) sat 1
B.E. (eV)	62	65	63	66	68	62.5	65.5	63.5	66.5
Conc. (%)	20.5	15.3	17.7	13.2	5.5	11.5	8.6	4.4	3.3
FWHM	0.7	0.7	2.6	2.6	2.9	1.3	1.3	2.8	2.8

Table B.6: Fit parameters for Ir 4f of IrO_x TKK

	Ir $4f_{7/2}$ Ir(IV)	**Ir $4f_{5/2}$** Ir(IV)	**Ir $4f_{7/2}$** Ir(IV) sat 1	**Ir $4f_{5/2}$** Ir(IV) sat 1	**Ir $4f_{5/2}$** Ir(IV) sat 2	**Ir $4f_{7/2}$** Ir(III)	**Ir $4f_{5/2}$** Ir(III)	**Ir $4f_{7/2}$** Ir(III) sat 1	**Ir $4f_{5/2}$** Ir(III) sat 1
B.E. (eV)	61.8	64.8	62.8	65.8	67.8	62.4	65.4	63.4	66.4
Conc. (%)	24.8	18.6	7	5.2	1.1	13.6	10.2	11.1	8.4
FWHM	0.9	0.9	2.5	2.5	2.9	1	1	2.8	2.8

Fit parameters for O 1s

Table B.7: Fit parameters for O 1s of IrO_2

	Lattice oxygen (O_{Ir-O})	Surface Hydroxide (O_{OH})	Water (O_{H2O})
B.E. (eV)	530.4	531.6	533.4
% conc.	27	48	25
FWHM	0.8	1.8	1.8

Table B.8: Fit parameters for O 1s of IrO_2-HCl

	Lattice oxygen (O_{Ir-O})	Surface Hydroxide (O_{OH})	Water (O_{H2O})
B.E. (eV)	530.4	531.7	533.4
% conc.	20	47	33
FWHM	1.0	1.9	1.9

Table B.9: Fit parameters for O 1s of IrO_x-NH_4OH

	Lattice oxygen (O_{Ir-O})	Surface Hydroxide (O_{OH})	Water (O_{H2O})
B.E. (eV)	530.3	531.5	533.3
% conc.	20	60	20
FWHM	0.9	1.9	1.9

Table B.10: Fit parameters for O 1s of IrO_2 Alfa Aesar (IrO_2 AA)

	Lattice oxygen (O_{Ir-O})	Surface Hydroxide (O_{OH})	Water (O_{H2O})
B.E. (eV)	530.2	531.2	533.0
% conc.	36	44	20
FWHM	0.8	1.6	1.6

Table B.11: Fit parameters for O 1s of IrO_x TKK

	Lattice oxygen (O_{Ir-O})	Surface Hydroxide (O_{OH})	Water (O_{H2O})
B.E. (eV)	530.1	531.4	533.2
% conc.	5	79	16
FWHM	1	2	2

Fit parameters for Cl 2p

Table B.12: Fit parameters for Cl 2p of IrO_2

	Cl $2p_{3/2}$ HCl	Cl 2p $_{1/2}$ HCl	Cl $2p_{3/2}$ Ir-Cl	Cl $2p_{3/2}$ Ir-Cl
B.E. (eV)	197.7	199.3	199.2	200.8
% conc.	5.2	2.6	61.5	30.7
FWHM	0.9	0.9	1.4	1.4

Table B.13: Fit parameters for Cl 2p of IrO_2-HCl

	Cl $2p_{3/2}$ HCl	Cl 2p $_{1/2}$ HCl	Cl $2p_{3/2}$ Ir-Cl	Cl $2p_{3/2}$ Ir-Cl
B.E. (eV)	198.1	199.7	199.3	200.9
% conc.	8	4	61.4	30.6
FWHM	1	1	1.3	1.3

Table B.14: Fit parameters for Cl 2p of IrO_x-NH_4OH

	Cl $2p_{3/2}$ HCl	Cl 2p $_{1/2}$ HCl	Cl $2p_{3/2}$ Ir-Cl	Cl $2p_{3/2}$ Ir-Cl
B.E. (eV)	197.7	199.3	199.2	200.8
% conc.	7	3.5	60	29.5
FWHM	0.85	0.85	1.4	1.4

B.2 Thermogravimetric analysis (TGA)

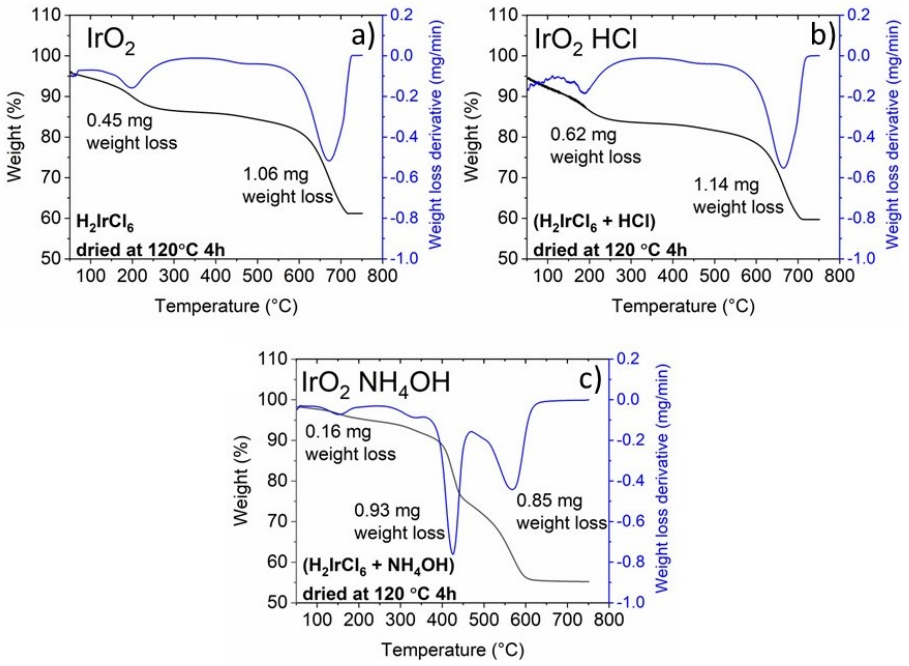

Figure B.3: (TGA and Derivative thermogravimetry (DTG) of (a) IrO_2 (H_2IrCl_6 heated at 120°C for 4 h), (b) IrO_2 -HCl (H_2IrCl_6 + HCl heated at 120°C for 4 h), and (c) IrO_x-NH_4OH (H_2IrCl_6 + NH_4OH heated at 120°C for 4 h). Decomposition of 20 mg of the dried precursor samples in the air (flow rate = 50 ml/min) from room temperature to 750 °C, at the heating rate of 10 °C·min^{-1}.